

Advances in Meteorology

Satellite Observation of Atmospheric Compositions for Air Quality and Climate Study

Guest Editors: Xiaozhen Xiong, Liangfu Chen, Yang Liu, Ugo Cortesi, and Pawan Gupta





Satellite Observation of Atmospheric Compositions for Air Quality and Climate Study

Advances in Meteorology

Satellite Observation of Atmospheric Compositions for Air Quality and Climate Study

Guest Editors: Xiaozhen Xiong, Liangfu Chen, Yang Liu, Ugo Cortesi, and Pawan Gupta



Copyright © 2015 Hindawi Publishing Corporation. All rights reserved.

This is a special issue published in “Advances in Meteorology.” All articles are open access articles distributed under the Creative Commons Attribution License, which permits unrestricted use, distribution, and reproduction in any medium, provided the original work is properly cited.

Editorial Board

José Antonio Adame, Spain
Cesar Azorin-Molina, Spain
Guillermo Baigorria, USA
Marina Baldi, Italy
Abderrahim Bentamy, France
Massimo A. Bollasina, UK
Stefania Bonafoni, Italy
Isabella Bordi, Italy
Alex Cannon, Canada
Claudio Carbone, Italy
Dominique Carrer, France
Charles Chemel, UK
Annalisa Cherchi, Italy
James Cleverly, Australia
Jill S. M. Coleman, USA
Gabriele Curci, Italy
Mladjen Ćurić, Serbia
Maher A. Dayeh, USA
Klaus Dethloff, Germany
Panuganti C. S. Devara, India
Julio Diaz, Spain
Arona Diedhiou, France
Stefano Dietrich, Italy
Eugenio Domínguez Vilches, Spain
Antonio Donateo, Italy
Igor Esau, Norway
Stefano Federico, Italy
Enrico Ferrero, Italy
Rossella Ferretti, Italy
Roberto Fraile, Spain
Charmaine Franklin, Australia
Jan Friesen, Germany

María Ángeles García, Spain
Herminia García Mozo, Spain
Eduardo García-Ortega, Spain
Luis Gimeno, Spain
Jorge E. Gonzalez, USA
Ismail Gultepe, Canada
Rafiq Hamdi, Belgium
Adel Hanna, USA
Hiroyuki Hashiguchi, Japan
Tareq Hussein, Jordan
Bradley G. Illston, USA
Ivar S A Isaksen, Norway
Yasunobu Iwasaka, Japan
Pedro Jiménez-Guerrero, Spain
Kuruvilla John, USA
Charles Jones, USA
Hann-Ming H. Juang, USA
George Kallos, Greece
Harry D. Kambezidis, Greece
Nir Y. Krakauer, USA
Simon O. Krichak, Israel
Hisayuki Kubota, Japan
Haim Kutiel, Israel
Richard Leaitch, Canada
Monique Leclerc, USA
Ilan Levy, Israel
Gwo-Fong Lin, Taiwan
Anthony R. Lupo, USA
Paolo Madonia, Italy
Andreas Matzarakis, Germany
Samantha Melani, Italy
Nicholas Meskhidze, USA

Christophe Messenger, France
Mario Marcello Miglietta, Italy
Takashi Mochizuki, Japan
Andrea Montani, Italy
Goro Mouri, Japan
Brian R. Nelson, USA
Efthymios I. Nikolopoulos, USA
Sandip Pal, USA
Giulia Panegrossi, Italy
Giulia Pavese, Italy
Kyaw T. Paw, USA
Olivier P. Prat, USA
Sara C. Pryor, USA
Philippe Ricaud, France
Tomeu Rigo, Spain
Filomena Romano, Italy
Jose Antonio Ruiz-Arias, Spain
Haydee Salmun, USA
Pedro Salvador, Spain
Arturo Sanchez-Lorenzo, Spain
Andres Schmidt, USA
Shraddhanand Shukla, USA
Fiona Smith, UK
Francisco J. Tapiador, Spain
Yoshihiro Tomikawa, Japan
Tomoo Ushio, Japan
Rogier Van Der Velde, Netherlands
Sergio M. Vicente-Serrano, Spain
Francesco Viola, Italy
Alastair Williams, Australia
Olga Zolina, France

Contents

Investigation of Precipitation Variations over Wet and Dry Areas from Observation and Model,
James H. Trammell, Xun Jiang, Liming Li, Maochang Liang, Mao Li, Jing Zhou, Eric Fetzer, and Yuk Yung
Volume 2015, Article ID 981092, 9 pages

Tropospheric NO₂ Trends over South Asia during the Last Decade (2004–2014) Using OMI Data,
Zia ul-Haq, Salman Tariq, and Muhammad Ali
Volume 2015, Article ID 959284, 18 pages

Analysis of Long-Range Transport of Carbon Dioxide and Its High Concentration Events over East Asian Region Using GOSAT Data and GEOS-Chem Modeling, Seung-Yeon Kim, Sang-Deok Lee, Jae-Bum Lee, Deok-Rae Kim, Jin-Seok Han, Kwang-Ho Choi, and Chang-Keun Song
Volume 2015, Article ID 680264, 13 pages

Preliminary Assessment of Methane Concentration Variation Observed by GOSAT in China,
Xiuchun Qin, Liping Lei, Zhonghua He, Zhao-Cheng Zeng, Masahiro Kawasaki, Masafumi Ohashi, and Yutaka Matsumi
Volume 2015, Article ID 125059, 11 pages

Optical Properties of the Urban Aerosol Particles Obtained from Ground Based Measurements and Satellite-Based Modelling Studies, Genrik Mordas, Nina Prokopciuk, Steigvilė Byčėnkiėnė, Jelena Andriejauskienė, and Vidmantas Ulevicius
Volume 2015, Article ID 898376, 12 pages

Satellite Observed Aerosol Optical Thickness and Trend around Megacities in the Coastal Zone,
Xuepeng Zhao
Volume 2015, Article ID 170672, 7 pages

Operational Monitoring of Trace Gases over the Mediterranean Sea, Giuseppe Grieco, Guido Masiello, and Carmine Serio
Volume 2015, Article ID 318608, 9 pages

Dominant Modes of Tropospheric Ozone Variation over East Asia from GOME Observations, Yi Liu, Yuli Zhang, Yong Wang, Chuanxi Liu, Zhaonan Cai, Paul Konopka, and Rolf Müller
Volume 2015, Article ID 879578, 10 pages

Research Article

Investigation of Precipitation Variations over Wet and Dry Areas from Observation and Model

James H. Trammell,¹ Xun Jiang,¹ Liming Li,² Maochang Liang,³ Mao Li,⁴ Jing Zhou,⁵ Eric Fetzer,⁶ and Yuk Yung⁷

¹Department of Earth and Atmospheric Sciences, University of Houston, Houston, TX, USA

²Department of Physics, University of Houston, Houston, TX, USA

³Research Center for Environmental Changes, Academia Sinica, Taipei, Taiwan

⁴Hunan Meteorological Administration, Changsha, China

⁵Department of Physics, Beijing Normal University, Beijing, China

⁶Science Division, Jet Propulsion Laboratory, California Institute of Technology, Pasadena, CA, USA

⁷Division of Geological & Planetary Sciences, California Institute of Technology, Pasadena, CA, USA

Correspondence should be addressed to Xun Jiang; xjiang7@uh.edu

Received 25 January 2015; Accepted 22 June 2015

Academic Editor: Ugo Cortesi

Copyright © 2015 James H. Trammell et al. This is an open access article distributed under the Creative Commons Attribution License, which permits unrestricted use, distribution, and reproduction in any medium, provided the original work is properly cited.

Our observational study revealed that the precipitation increased over the wet area and decreased over the dry area during the past two decades. Here, we further investigate whether the current atmospheric models can quantitatively capture the characteristics of precipitation from the observation. The NASA Goddard Institute for Space Studies (GISS) model is used to examine the historic simulation of the precipitation, in which the historic greenhouse gases and aerosols are included in the radiative forcing. The consistency between the historic GISS simulation and the Global Precipitation Climatology Project (GPCP) precipitation suggests that the model can qualitatively capture the temporal trends of precipitation over the wet and dry areas. However, the precipitation trends are weaker in the model than in the observation. The observed trends of precipitation do not appear in the control simulation with the fixed concentrations of greenhouse gases and aerosols, which suggests that the global warming due to anthropogenic forcing can influence the temporal variations of precipitation over the wet and dry areas. Diagnostic studies of other variables from the model further suggest that enhanced rising air can increase the precipitation over the wet area.

1. Introduction

The influence of greenhouse gases on global warming has been investigated in numerous studies [1–3]. This paper focuses on the effect global warming may have on the temporal variation and spatial pattern of precipitation and its possible influence on causing precipitation extremes. Compared with the Clausius-Clapeyron equation relating water vapor to the atmospheric temperature [4, 5], there is no simple relationship between precipitation and the atmospheric temperature [6–10]. This is because precipitation is influenced by more factors, such as atmospheric circulation, solar forcing, anthropogenic forcing, and cloud [11, 12]. It is also found that changes in the precipitation can be attributed

to natural climate variability and external influences [13]. Most observational studies [7, 10, 14, 15] and climate models [16–18] suggest that global precipitation is increasing more slowly than the total mass of water vapor in response to global warming. Previous studies [10, 19–23] try to separate the data into wet versus dry regions; they find that precipitation has an increasing tendency in the wet areas and has a decreasing tendency in dry areas, which is referred to as the “rich-get-richer” mechanism. Recently, Chou et al. [24] found that the wet seasons become wetter and dry seasons become dryer. Here, we will investigate whether a current climate model can capture the characteristics of the temporal variations of the precipitation by emphasizing the role of the greenhouse gases and aerosols. Quantitatively simulating the precipitation

trend will not only help predict the variation of precipitation in the future, but also provide a numerical basis to better understand the physics behind the temporal and spatial variability of precipitation.

2. Methodology and Data

Both observations and numerical simulations are employed to examine precipitation under two different regions within 40°S – 40°N : dry areas with precipitation less than 50 mm/month and wet areas with precipitation greater than 200 mm/month. By comparing the current atmospheric model to observations, we can explore how good is the model in simulating precipitation. In addition, a diagnostic analysis of the numerical simulation will be conducted to investigate the physics behind the temporal trends of precipitation over different areas.

We use the NASA Goddard Institute for Space Studies (GISS) model to study the precipitation, temperature, water vapor, and circulation. Specifically, the GISS atmospheric general circulation model coupled to the hybrid-isopycnic ocean model (HYCOM) [12] is employed. It is an updated version used for IPCC AR4 report [2]. GISS-EH Model E20/HYCOM is a $4 \times 5 \times \text{L20}$ model that uses the Model E atmospheric code (internal version number E3), with 20 layers in the vertical, a model top at 0.1 hPa, and coupled to the HYCOM ocean model (v. 0.9, $2 \times 2 \times \text{L16}$) (<http://data.giss.nasa.gov/modelE/ar4/>). The atmosphere model includes a gravity-wave drag parameterization in the stratosphere. The HYCOM dynamic ocean model can produce a reasonable magnitude of El Niño Southern Oscillation- (ENSO-) like variability [12]. This model has been utilized to study the influence of solar and anthropogenic forcing on the tropical hydrology [12] and explore the climate drift on twenty-first-century projection [25]. The control simulation starts with year 1850 atmospheric conditions containing fixed greenhouse gases and aerosols. The historic model simulation includes the historic greenhouse gases and aerosols changes in the radiative forcing.

The observational studies of precipitation are based on the data sets from the Global Precipitation Climatology Project (GPCP), which is an international project to construct the global long-term record of precipitation over the whole world on behalf of the World Meteorological Organization (WMO), the World Climate Research Programme (WCRP), and the Global Energy and Water Experiment (GEWEX) [26]. There are many investigators and organizations contributing to this project [14, 26]. The data sets of precipitation from the latest version of the GPCP (i.e., Version 2.2) are available on the public websites maintained by the Physical Sciences Division (PSD) of the Earth System Research Laboratory (ESRL) in the National Oceanic & Atmospheric Administration (NOAA) (<http://www.esrl.noaa.gov/psd/data/gridded/data.gpcp.html>). GPCP Version 2.2 precipitation data are derived from satellite and gauge measurements. It incorporates data from SSM/I emission estimates, F17 SSMIS, SSM/I scattering estimates, GPI and OPI estimates and rain gauge analysis, and TOVS estimates [27]. The spatial resolution of GPCP V2.2 precipitation is $2.5^{\circ} \times 2.5^{\circ}$ (latitude by longitude). Analyses

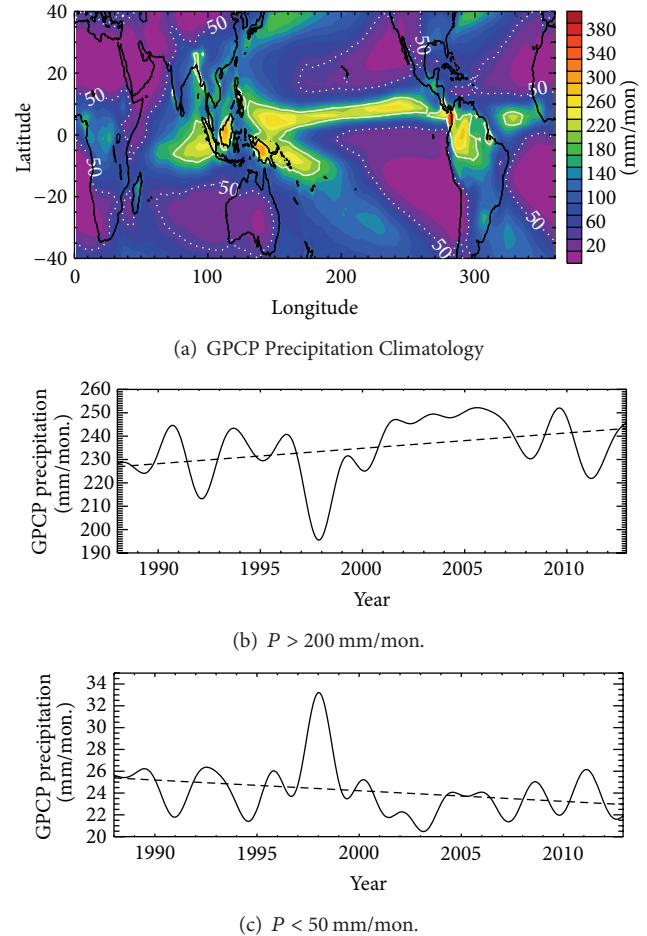


FIGURE 1: (a) Spatial pattern of the mean GPCP V2.2 precipitation (P) for 1988–2012 over the tropical and subtropical regions (40°S – 40°N). (b) Low-pass filtered time series of precipitation averaged over high-precipitation areas ($P > 200$ mm/month.). (c) Low-pass filtered time series of precipitation averaged over low-precipitation areas ($P < 50$ mm/month.). El Niño Southern Oscillation (ENSO) signals have been removed from the time series by a regression method based on the Niño3.4 index. A low-pass filter is also applied to remove the high frequency signals. Solid white contours refer to the wet area where the precipitation is higher than 200 mm/month. Dotted white contours refer to the dry area where the precipitation is lower than 50 mm/month.

based on the observational data sets are conducted to examine the consistency between the historic simulation and the observational study from 1988 to 2012, where GPCP data overlap with Special Sensor Microwave Imager data and are believed to be more reliable [28].

3. Results

The spatial pattern of the observed climatological GPCP V2.2 precipitation for 1988–2012 is shown in Figure 1(a). The high-precipitation and low-precipitation areas are defined as the areas with climatological monthly mean precipitation larger than 200 millimeter per month (mm/month) and less than 50 mm/month, respectively. The high-precipitation areas and

TABLE 1: Trends for precipitation (P), column water (W), temperature (T), and vertical pressure velocity (Ω) over wet area ($P > 200$ mm/mon.) and dry area ($P < 50$ mm/mon.).

	Wet area ($P > 200$ mm/mon.)	Dry area ($P < 50$ mm/mon.)
GPCP P	6.57 ± 0.27 mm/mon./decade	-0.98 ± 0.23 mm/mon./decade
GISS P (control simulation)	0.02 ± 0.19 mm/mon./decade	-0.03 ± 0.24 mm/mon./decade
GISS P (historic simulation)	3.8 ± 0.17 mm/mon./decade	-0.48 ± 0.21 mm/mon./decade
GISS W (control simulation)	-0.06 ± 0.18 mm/mon./decade	0.057 ± 0.20 mm/mon./decade
GISS W (historic simulation)	1.15 ± 0.21 mm/mon./decade	0.49 ± 0.20 mm/mon./decade
GISS T (control simulation)	$-0.04 \pm 0.19^\circ\text{C}/\text{decade}$	$-0.04 \pm 0.20^\circ\text{C}/\text{decade}$
GISS T (historic simulation)	$0.61 \pm 0.23^\circ\text{C}/\text{decade}$	$0.52 \pm 0.22^\circ\text{C}/\text{decade}$
GISS Ω (control simulation)	-0.016 ± 0.17 Pa/day/decade	-0.04 ± 0.18 Pa/day/decade
GISS Ω (historic simulation)	-0.32 ± 0.18 Pa/day/decade	-0.03 ± 0.21 Pa/day/decade

low-precipitation areas are highlighted by the solid white contours and dotted white contours in Figure 1(a). Figure 1(a) illustrates that the high-precipitation area is roughly the same as the Intertropical Convergence Zone (ITCZ) identified by the highly reflective clouds [29]. The low-precipitation area comprises most of the other regions in the tropics and midlatitudes. Two different approaches were attempted when evaluating these data in preparation for plotting a time series. Since the ITCZ fluctuates in position throughout the year, one way to prepare the data is to allow the wet and dry areas to change position with month to follow the movement of the ITCZ. Another way is to calculate the precipitation over the climatological wet and dry areas as shown in Figure 1(a). Both approaches yielded similar results. Time series of the observed precipitation over the climatological wet and dry areas are plotted in Figures 1(b) and 1(c), which include data over both land and ocean between 40°S and 40°N . From this temporal variation of precipitation, it is evident that the areas already receiving great precipitation tend to receive more while the areas already receiving little precipitation tend to receive less. The trend and uncertainty associated with the wet area are 6.57 ± 0.27 mm/mon./decade while for the dry area are -0.98 ± 0.23 mm/mon./decade. Details for trends are listed in Table 1. El Niño Southern Oscillation (ENSO) signals have been removed from the precipitation time series at each location by a multiple regression method to avoid large biases in the trend due to significant interannual variability. We first regress the original time series on first, second, and third Legendre polynomials, annual cycle, semiannual cycle, and ENSO signal [30]. Then we subtract the ENSO signal from the original time series. Also applied to the data was a 20-month low-pass filter to remove the high frequency signals. The low-pass filter is constructed as a convolution of a step function with a Hanning window and chosen to obtain a full signal from periods above 20 months [31]. The linear trend coefficient for the time series is calculated from the least-square fitting. The standard error of the linear trend is estimated by $SE(b) = (\sigma/\sqrt{N_1})/\sqrt{(1/N_2) \sum x_i^2}$ [32], where σ is the standard deviation of the data, N_1 is the number of degrees of freedom of the data, N_2 is the length of the data set, and x_i is the time series corresponding to a number of measurements with $\sum x_i = 0$. The number of degrees of freedom N_1 is estimated by a formula

$N_1 = N_2[1 - r(\Delta x)^2]/[1 + r(\Delta x)^2]$ suggested by Bretherton et al. [33], where $r(\Delta x)$ is the autocorrelation corresponding to a lag of time interval Δx .

Next, we use the NASA GISS/HYCOM model to investigate whether the model can capture the overall trends seen in the observations and reproduce the characteristics of precipitation. We conduct experimental simulations in a control simulation where the greenhouse gases and aerosols are fixed and a historic simulation where the historic greenhouse gases and aerosols are included. Figure 2 illustrates the identified areas of high and low precipitation and contains each of their precipitation trends for both the control and historic simulations. Corresponding trends and uncertainties in the control simulation for the wet area are 0.02 ± 0.19 mm/mon./decade with -0.03 ± 0.24 mm/mon./decade for the dry area, as shown in Figures 2(a) and 2(c). There is no significant trend in the precipitation over the wet and dry areas when the greenhouse gas concentrations and aerosols are fixed. In contrast, the historic simulation demonstrates trends of 3.8 ± 0.17 mm/mon./decade and -0.48 ± 0.21 mm/mon./decade for the wet and dry areas, respectively, as shown in Figures 2(b) and 2(d). The trends (3.8 ± 0.17 mm/mon./decade and -0.48 ± 0.21 mm/mon./decade) in the GISS precipitation are smaller than those seen in the observations (Figures 1(b) and 1(c)), which might be related to the weakness of the model in simulating the Pacific decadal variability (PDV). As suggested by Gu and Adler [34], the PDV can also contribute to the long-term trend of precipitation in addition to global warming. The GISS/HYCOM model cannot simulate the PDV well, which might contribute to the weak trends in the model precipitation. We also apply similar analyses to AMIP-type CMIP5 model simulations and obtain similar results. Since most CMIP5 model simulations end at 2008 and have shorter time periods than those of observations, we do not include results from these models in this paper.

The concentration of water vapor is one factor that can influence precipitation. Figure 3 illustrates the trends of column water for both the historic and control simulations in the wet and dry areas. Corresponding trends in the control simulation for the wet area are -0.06 ± 0.18 mm/mon./decade with 0.057 ± 0.20 mm/mon./decade for the dry area. Column water trends for the historic simulation are 1.15 ± 0.21 mm/mon./decade over the wet area with 0.49 ± 0.20 mm/mon./decade for the dry area, as shown in

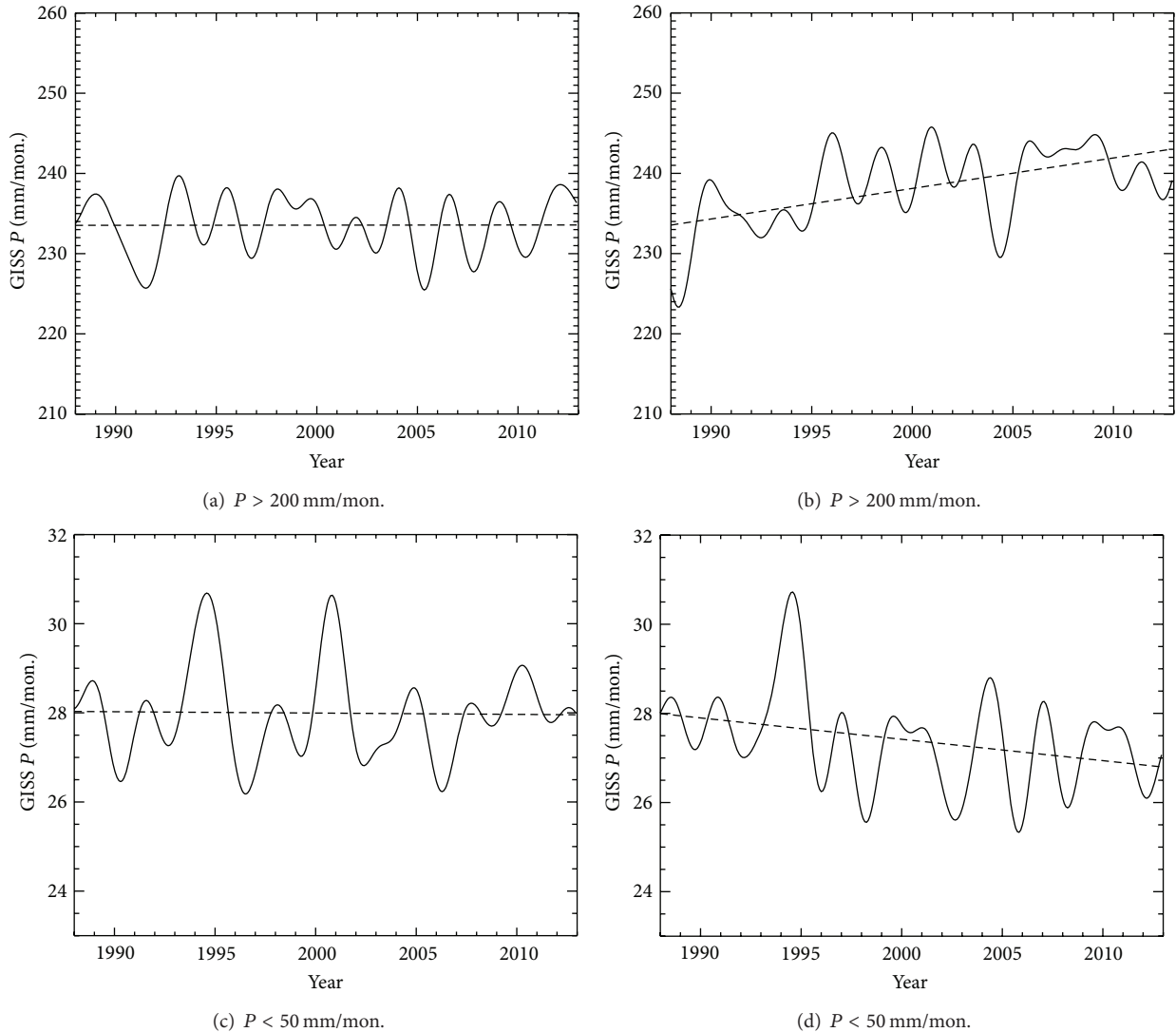


FIGURE 2: Low-pass filtered time series for precipitation (P) from GISS/HYCOM. (a) P over high-precipitation area ($P > 200$ mm/mon.) from the control simulation (solid line) and trend (dashed line). (b) P over high-precipitation area from the historic simulation (solid line) and trend (dashed line). (c) Same as (a) except for areas with precipitation < 50 mm/mon. (d) Same as (b) except for areas with precipitation < 50 mm/mon.

Figures 3(b) and 3(d). The historic simulation exhibits a strong positive trend for both the wet and dry areas while the control simulation reveals virtually no trend in either. Furthermore, of considerable note is the strength of the trend in column water in the historic simulation and the models ability to simulate it with low uncertainties and small deviations.

The concentration of water vapor is related to the atmospheric temperature by the Clausius-Clapeyron equation [35]. Therefore, we further examine the temporal variation of atmospheric temperature from the simulations by the GISS model. Results of the GISS 337 hPa temperature averaged in the identified areas of high and low precipitation are shown in Figure 4 for both the historic and control simulations. Corresponding trends and uncertainties in the control simulation for the wet area are $-0.04 \pm 0.19^\circ\text{C}/\text{decade}$

with $-0.04 \pm 0.20^\circ\text{C}/\text{decade}$ for the dry area. Trends for the 337 hPa temperature in the historic simulation are $0.61 \pm 0.23^\circ\text{C}/\text{decade}$ over the wet area and $0.52 \pm 0.22^\circ\text{C}/\text{decade}$ over the dry area, as illustrated in Figures 4(b) and 4(d). Temperature has positive trends over both wet areas and dry areas, which are responses to the anthropogenic forcing in the historic simulation. According to the Clausius-Clapeyron law, air with high temperature will hold more water vapor. Column water vapor also shows positive trends in both the wet and dry areas in Figure 3. This behavior is different from the temporal variation of precipitation for wet and dry areas.

To better understand the possible physics in the temporal variation of precipitation, we examine the vertical pressure velocity $\Omega = dP/dt$ in the GISS model over the wet and dry areas. Results for Ω at 337 hPa are given in Figure 5. Corresponding trends in the control simulation for the wet

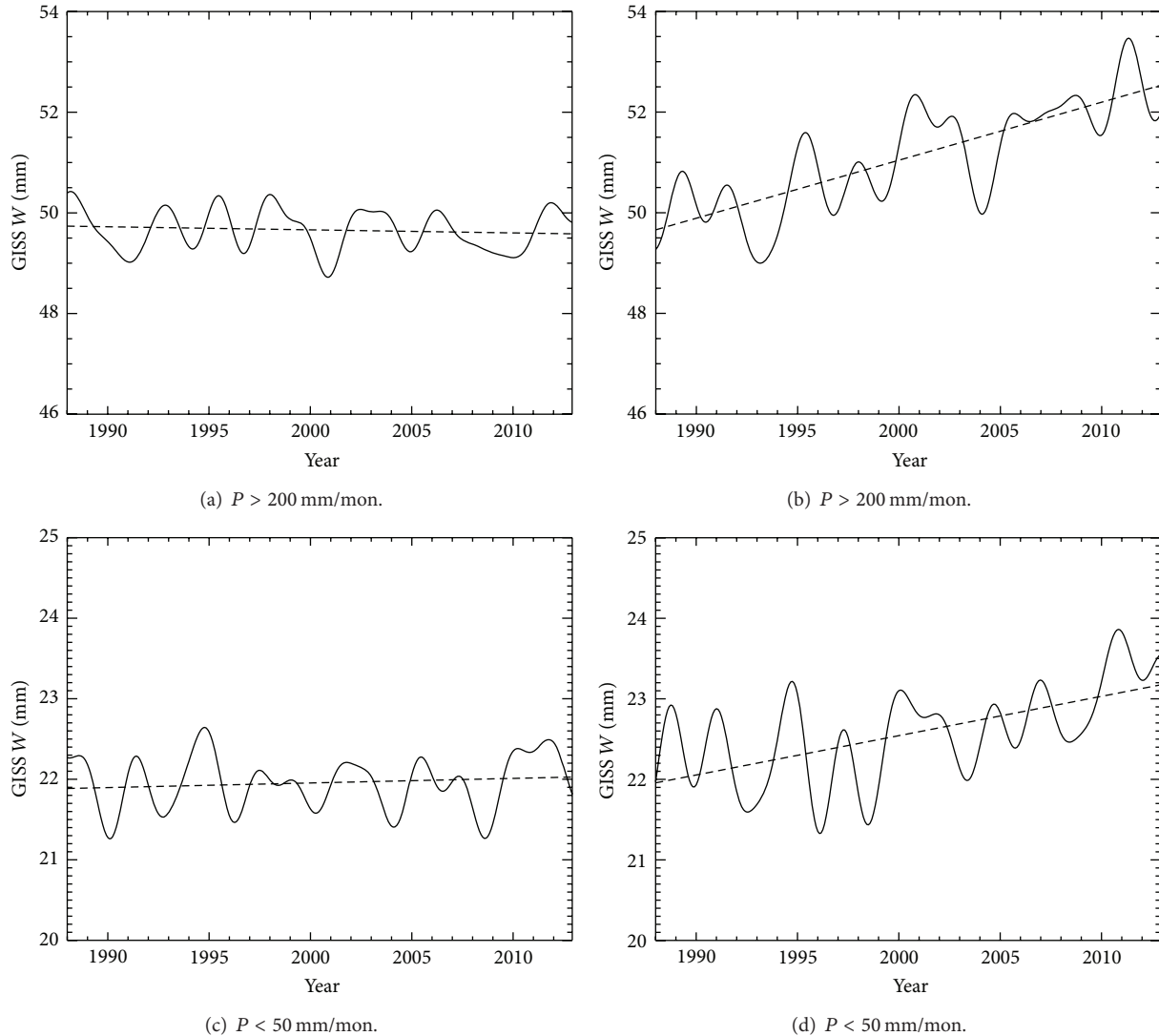


FIGURE 3: Low-pass filtered time series for column water vapor (W) from GISS/HYCOM. (a) W over high-precipitation area ($P > 200$ mm/mon.) from the control simulation (solid line) and trend (dashed line). (b) W over high-precipitation area from the historic simulation (solid line) and trend (dashed line). (c) Same as (a) except for areas with precipitation < 50 mm/mon. (d) Same as (b) except for areas with precipitation < 50 mm/mon.

area are -0.016 ± 0.17 Pa/day/decade with -0.04 ± 0.18 Pa/day/decade for the dry area. Trends for the 337 hPa Ω in the historic simulation are -0.32 ± 0.18 Pa/day/decade over the wet area and -0.03 ± 0.21 Pa/day/decade over the dry area, as demonstrated in Figures 5(b) and 5(d). Figure 5(b) illustrates a significant negative trend in the 337 hPa vertical pressure velocity. This negative trend suggests that the rising air is strengthening over the wet area and, in turn, can lead to enhanced precipitation there. The temporal variation of the vertical pressure velocity is consistent with a mechanism suggested in some previous studies [19, 21], in which the gross moist stability of the atmospheric boundary layer is reduced due to increased moisture and hence the convection and the related precipitation are amplified. Our investigation of the column water vapor and temperature suggests positive trends of column water vapor and temperature over the dry area.

Furthermore, the GISS historic simulation suggests that the vertical pressure velocity did not significantly change during the past two decades over the dry areas. The temporal trend of the precipitation over the dry area poses a challenge to our current understanding, which will be explored in the future.

The GISS/HYCOM model is also utilized to examine the temporal variation of residual meridional circulations. To explore the influence of anthropogenic forcing on the meridional circulation, we calculated the time series of 337 hPa residual vertical velocity [31] over 15°N – 15°S from the GISS/HYCOM control and historic simulations. Results are shown in Figure 6. In general, the increasing precipitation over the ITCZ area (i.e., rich-get-richer) is accompanied by an intensifying convection over the tropical region. This intensifying convection can be seen by the increasing trend of residual vertical velocity shown in Figure 6(a) of

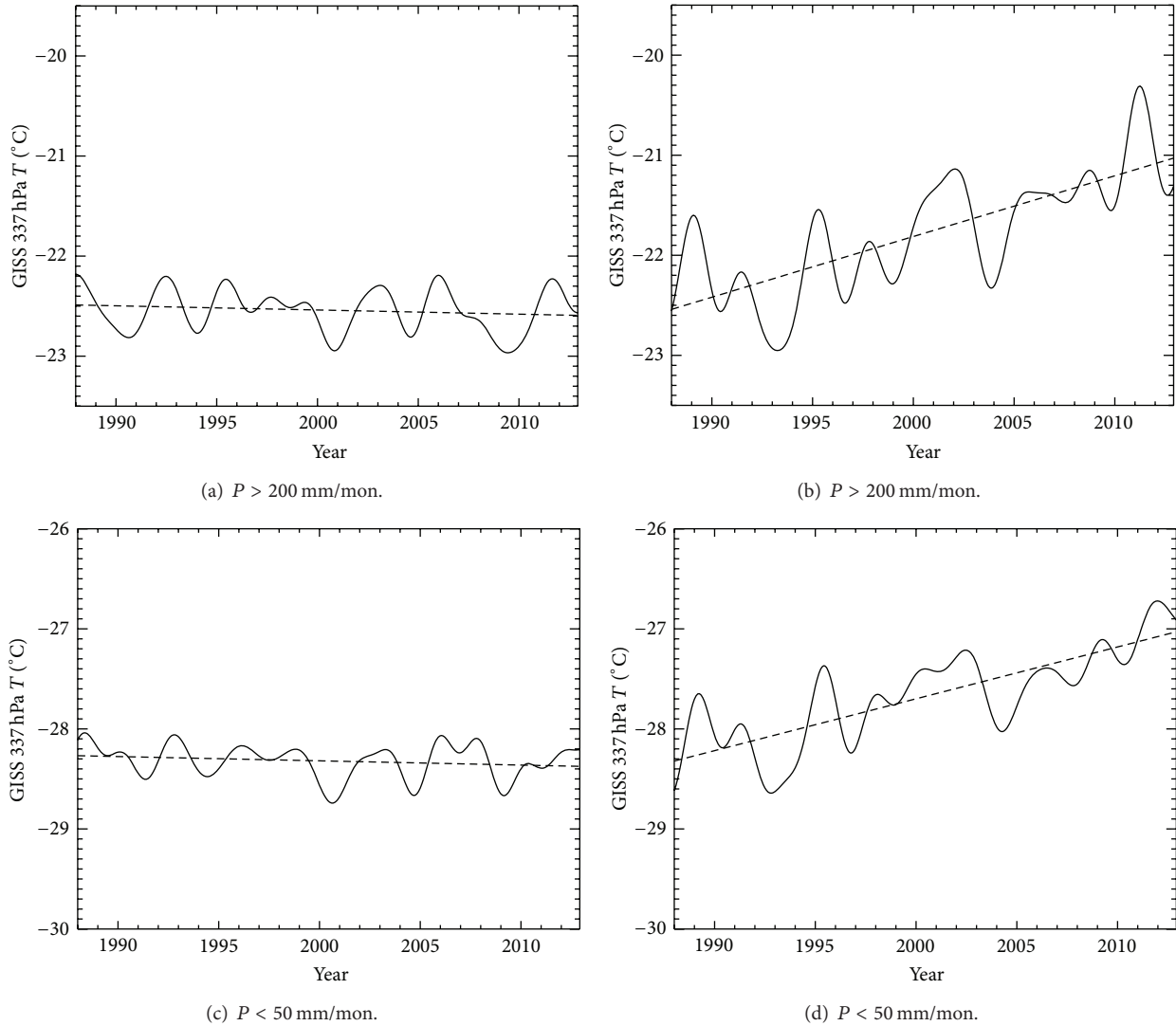


FIGURE 4: Low-pass filtered time series for 337 hPa temperature (T) from GISS/HYCOM. (a) T over high-precipitation area ($P > 200$ mm/mon.) from the control simulation (solid line) and trend (dashed line). (b) T over high-precipitation area from the historic simulation (solid line) and trend (dashed line). (c) Same as (a) except for areas with precipitation < 50 mm/mon. (d) Same as (b) except for areas with precipitation < 50 mm/mon.

the GISS/HYCOM historic model simulation. The residual vertical velocity displayed in Figure 6(a) has an increasing trend of 1.99 ± 0.82 m/day/decade. Figure 6(b) illustrates the residual vertical velocity of GISS/HYCOM control simulation. The residual vertical velocity for control simulation has a trend of -0.04 ± 0.68 m/day/decade. The historic simulation reveals a robust trend while the control simulation does not. The lack of an increasing trend in the control simulation is evidence of the influence anthropogenic forcing on the residual vertical velocity. The increasing trend demonstrated in the historic simulation suggests that an intensifying convection is occurring over the tropical region, and thus enhancing the precipitation in those regions. Such an intensifying convection is associated with a stronger meridional circulation, thus providing another perspective of the influence of

the large-scale meridional circulation on the temporal variation of tropical precipitation.

4. Conclusions

The GISS model simulations imply that the anthropogenic forcing can affect the temporal variations of precipitation over the wet and dry areas. Results from the GISS historic simulation suggest that the wet area is getting wetter while the dry area is getting drier, which are consistent with the results from observation. Precipitation from the control simulation with fixed amounts of greenhouse gases and aerosols does not demonstrate trends over the wet and dry areas. The diagnostic studies of the simulations from the GISS models reveal that the atmospheric dynamics related to the convective stability,

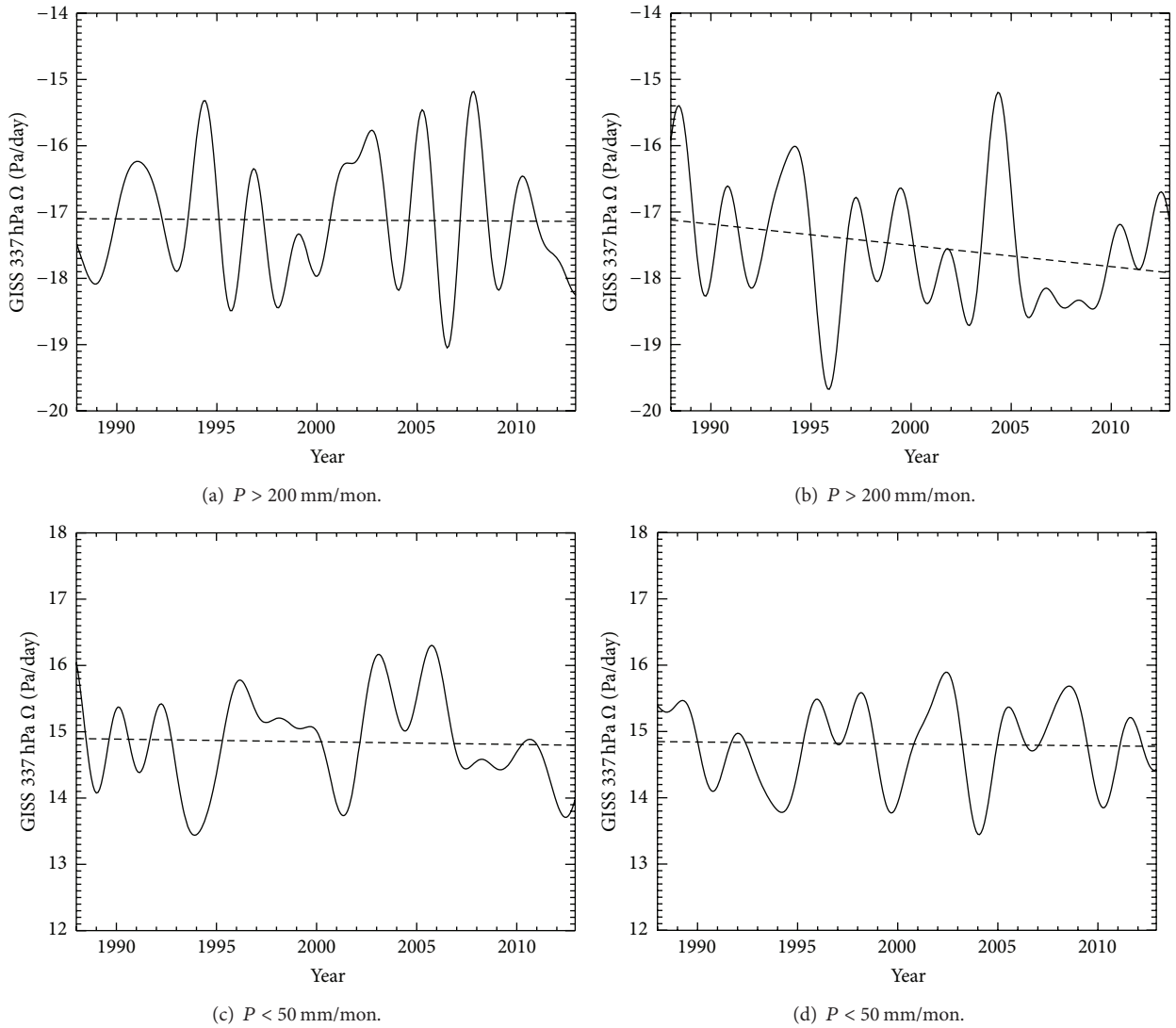


FIGURE 5: Low-pass filtered time series for 337 hPa vertical pressure velocity Ω (dP/dt) from GISS/HYCOM. (a) Ω over high-precipitation area ($P > 200$ mm/mon.) from the control simulation (solid line) and trend (dashed line). (b) Ω over high-precipitation area from the historic simulation (solid line) and trend (dashed line). (c) Same as (a) except for areas with precipitation < 50 mm/mon. (d) Same as (b) except for areas with precipitation < 50 mm/mon.

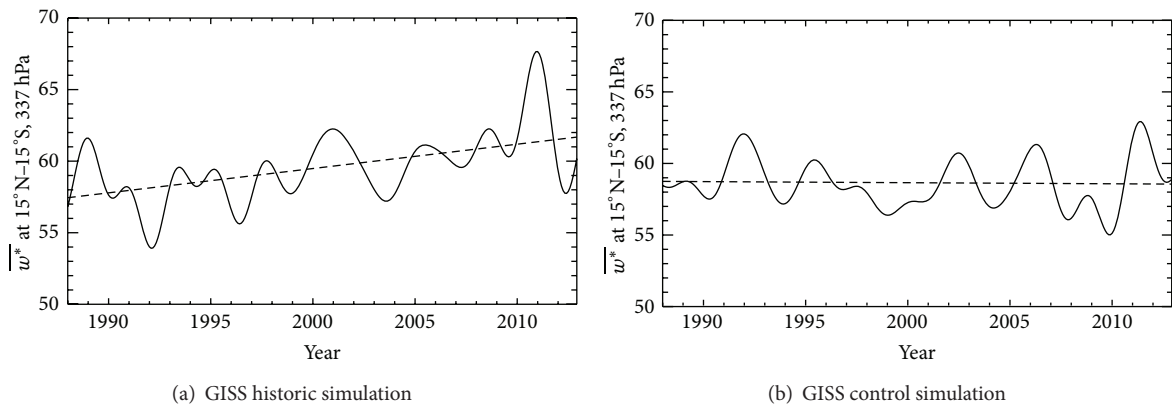


FIGURE 6: (a) Residual vertical velocity ($\overline{w^*}$) averaged over $15^\circ\text{N}-15^\circ\text{S}$ at 337 hPa from historic simulation (solid line) and trend (dashed line). (b) Same as (a) except for control simulation.

and hence the vertical motions, contribute to the increased precipitation over the wet area. Comparison of residual vertical velocity from the control and historic simulations also illustrates variations in meridional circulation as a result of global warming, which can further drive the increased precipitation over the tropical regions. Correct simulation of these important features by the climate model can help to elucidate the physics behind the temporal variations of precipitation, paving the way for more accurate prediction of future climate change due to anthropogenic activities.

With increasing numbers of weather extremes related to climate change, it is important to investigate precipitation, temperature, and water vapor trends and their associated spatial distribution. The significance and broader impacts are evident when we look at the consequences of increased drought in some areas and flooding in other areas. Droughts create a heightened threat for fire weather, diminishing the water supply, and recovery from the economic impact could take years. On the other hand, rapid and abundant rainfall could cause flooding and economic damages. These may be related to the influence of global warming.

Conflict of Interests

The authors declare that there is no conflict of interests regarding the publication of this paper.

Acknowledgments

The authors thank two anonymous reviewers for helpful comments. This work was supported by the NASA ROSES-2010 NEWS Grant NNX13AC04G. Part of the research was carried out at the Jet Propulsion Laboratory, California Institute of Technology, under a contract with the National Aeronautics and Space Administration.

References

- [1] R. E. Dickinson and R. J. Cicerone, "Future global warming from atmospheric trace gases," *Nature*, vol. 319, no. 6049, pp. 109–115, 1986.
- [2] IPCC, *Climate Change 2007: The Physical Science Basis*, Cambridge University Press, Cambridge, UK, 2007.
- [3] IPCC, *Climate Change 2013: The Physical Science Basis*, IPCC Secretariat, World Meteorological Organization, Geneva, Switzerland, 2013.
- [4] K. E. Trenberth, J. Fasullo, and L. Smith, "Trends and variability in column-integrated atmospheric water vapor," *Climate Dynamics*, vol. 24, no. 7–8, pp. 741–758, 2005.
- [5] B. D. Santer, C. Mears, F. J. Wentz et al., "Identification of human-induced changes in atmospheric moisture content," *Proceedings of the National Academy of Sciences of the United States of America*, vol. 104, no. 39, pp. 15248–15253, 2007.
- [6] K. E. Trenberth and D. J. Shea, "Relationships between precipitation and surface temperature," *Geophysical Research Letters*, vol. 32, no. 14, Article ID L14703, 2005.
- [7] R. F. Alder, G. J. Gu, J.-J. Wang, G. J. Huffman, S. Curtis, and D. Bolvin, "Relationships between global precipitation and surface temperature on interannual and longer timescales (1979–2006)," *Journal of Geophysical Research: Atmospheres*, vol. 113, no. 22, Article ID D22104, 2008.
- [8] R. P. Allan and B. J. Soden, "Atmospheric warming and the amplification of precipitation extremes," *Science*, vol. 321, no. 5895, pp. 1481–1484, 2008.
- [9] S. C. Liu, C. B. Fu, C. J. Shiu, J. P. Chen, and F. T. Wu, "Temperature dependence of global precipitation extremes," *Geophysical Research Letters*, vol. 36, no. 17, Article ID L17702, 2009.
- [10] L. Li, X. Jiang, M. T. Chahine et al., "The recycling rate of atmospheric moisture over the past two decades (1988–2009)," *Environmental Research Letters*, vol. 6, no. 3, Article ID 034018, 2011.
- [11] S. Bony, G. Bellon, D. Klocke, S. Sherwood, S. Fermepin, and S. Denvil, "Robust direct effect of carbon dioxide on tropical circulation and regional precipitation," *Nature Geoscience*, vol. 6, no. 6, pp. 447–451, 2013.
- [12] D. T. Shindell, G. Faluvegi, R. L. Miller, G. A. Schmidt, J. E. Hansen, and S. Sun, "Solar and anthropogenic forcing of tropical hydrology," *Geophysical Research Letters*, vol. 33, no. 24, 2006.
- [13] K. Marvel and C. Bonfils, "Identifying external influences on global precipitation," *Proceedings of the National Academy of Sciences of the United States of America*, vol. 110, no. 48, pp. 19301–19306, 2013.
- [14] R. F. Adler, G. J. Huffman, A. Chang et al., "The version-2 global precipitation climatology project (GPCP) monthly precipitation analysis (1979–present)," *Journal of Hydrometeorology*, vol. 4, no. 6, pp. 1147–1167, 2003.
- [15] G. J. Gu, R. F. Adler, G. J. Huffman, and S. Curtis, "Tropical rainfall variability on interannual-to-interdecadal and longer time scales derived from the GPCP monthly product," *Journal of Climate*, vol. 20, no. 15, pp. 4033–4046, 2007.
- [16] M. R. Allen and W. J. Ingram, "Constraints on future changes in climate and the hydrologic cycle," *Nature*, vol. 419, no. 6903, pp. 224–232, 2002.
- [17] I. M. Held and B. J. Soden, "Robust responses of the hydrological cycle to global warming," *Journal of Climate*, vol. 19, no. 21, pp. 5686–5699, 2006.
- [18] G. L. Stephens and T. D. Ellis, "Controls of global-mean precipitation increases in global warming GCM experiments," *Journal of Climate*, vol. 21, no. 23, pp. 6141–6155, 2008.
- [19] C. Chou and J. D. Neelin, "Mechanisms of global warming impacts on regional tropical precipitation," *Journal of Climate*, vol. 17, no. 13, pp. 2688–2701, 2004.
- [20] R. P. Allan and B. J. Soden, "Large discrepancy between observed and simulated precipitation trends in the ascending and descending branches of the tropical circulation," *Geophysical Research Letters*, vol. 34, no. 18, Article ID L18705, 2007.
- [21] C. Chou, J. D. Neelin, C.-A. Chen, and J.-Y. Tu, "Evaluating the 'rich-get-richer' mechanism in tropical precipitation change under global warming," *Journal of Climate*, vol. 22, no. 8, pp. 1982–2005, 2009.
- [22] P. J. Durack, S. E. Wijffels, and R. J. Matear, "Ocean salinities reveal strong global water cycle intensification during 1950 to 2000," *Science*, vol. 336, no. 6080, pp. 455–458, 2012.
- [23] D. Polson, G. C. Hegerl, R. P. Allan, and B. B. Sarojini, "Have greenhouse gases intensified the contrast between wet and dry regions?" *Geophysical Research Letters*, vol. 40, no. 17, pp. 4783–4787, 2013.

- [24] C. Chou, J. C. H. Chiang, C.-W. Lan, C.-H. Chung, Y.-C. Liao, and C.-J. Lee, "Increase in the range between wet and dry season precipitation," *Nature Geoscience*, vol. 6, no. 4, pp. 263–267, 2013.
- [25] M.-C. Liang, L.-C. Lin, K.-K. Tung, Y. L. Yung, and S. Sun, "Impact of climate drift on twenty-first-century projection in a coupled atmospheric-ocean general circulation model," *Journal of the Atmospheric Sciences*, vol. 70, no. 10, pp. 3321–3327, 2013.
- [26] G. J. Huffman, R. F. Adler, P. Arkin et al., "The global precipitation climatology project (GPCP) combined precipitation dataset," *Bulletin of the American Meteorological Society*, vol. 78, no. 1, pp. 5–20, 1997.
- [27] G. J. Huffman, D. T. Bolvin, and R. F. Adler, *GPCP Version 2.2 Combined Precipitation Data Set*, NCDC, Asheville, NC, USA, 2012.
- [28] R. P. Allan, B. J. Soden, V. O. John, W. Ingram, and P. Good, "Current changes in tropical precipitation," *Environmental Research Letters*, vol. 5, no. 2, Article ID 025205, 2010.
- [29] D. E. Waliser and C. Gautier, "A satellite-derived climatology of the ITCZ," *Journal of Climate*, vol. 6, no. 11, pp. 2162–2174, 1993.
- [30] X. Jiang, J. Wang, E. T. Olsen et al., "Influence of EL Niño on midtropospheric CO₂ from Atmospheric infrared sounder and model," *Journal of the Atmospheric Sciences*, vol. 70, no. 1, pp. 223–230, 2013.
- [31] X. Jiang, C. D. Camp, R. Shia, D. Noone, C. Walker, and Y. L. Yung, "Quasi-biennial oscillation and quasi-biennial oscillation-annual beat in the tropical total column ozone: a two-dimensional model simulation," *Journal of Geophysical Research D: Atmospheres*, vol. 109, no. 16, 2004.
- [32] P. R. Bevington and D. K. Robinson, *Data Reduction and Error Analysis for the Physical Sciences*, McGraw-Hill, New York, NY, USA, 3rd edition, 2003.
- [33] C. S. Bretherton, M. Widmann, V. P. Dymnikov, J. M. Wallace, and I. Bladé, "The effective number of spatial degrees of a time varying field," *Journal of Climate*, vol. 12, no. 7, pp. 1990–2009, 1999.
- [34] G. J. Gu and R. F. Adler, "Interdecadal variability/long-term changes in global precipitation patterns during the past three decades: global warming and/or pacific decadal variability?" *Climate Dynamics*, vol. 40, no. 11-12, pp. 3009–3022, 2013.
- [35] M. Salby, *Physics of the Atmosphere and Climate*, Cambridge University Press, 2012.

Research Article

Tropospheric NO₂ Trends over South Asia during the Last Decade (2004–2014) Using OMI Data

Zia ul-Haq, Salman Tariq, and Muhammad Ali

Remote Sensing and GIS Group, Department of Space Science, University of the Punjab, New Campus, Lahore 54590, Pakistan

Correspondence should be addressed to Zia ul-Haq; zia.spssc@yahoo.com

Received 18 February 2015; Revised 12 May 2015; Accepted 7 June 2015

Academic Editor: Pawan Gupta

Copyright © 2015 Zia ul-Haq et al. This is an open access article distributed under the Creative Commons Attribution License, which permits unrestricted use, distribution, and reproduction in any medium, provided the original work is properly cited.

The focus of this study is to assess spatiotemporal variability of tropospheric NO₂ over South Asia using data from spaceborne OMI during the past decade (2004–2015). We find an average value of NO₂ $1.0 \pm 0.05 \times 10^{15}$ molec/cm² and a significant decadal increase of 14%. The elevating NO₂ pollution over the region is linked to rise in motor vehicles and industrial and agricultural activities and increase in biomass fuel usage. The observed seasonality of NO₂ is associated with change in meteorological conditions and seasonal cycles of anthropogenic emissions. OMI data reveal a seasonal peak in spring followed by winter largely linked to meteorological conditions and anthropogenic emissions from crop residue and biomass burning for heating purpose, and low concentration in summer is mostly attributed to meteorological conditions. Significant increase, up to 42%, in NO₂ concentrations over northwestern IGB, is observed connected to large scale postmonsoon crop residue events of 2010 and 2012. It is seen that NO₂ is mounting over all the hotspot locations and most of the cities. Dhaka shows the highest increase of 77% followed by Islamabad (69%), Kabul (68%), Korba (64%), Bardhaman (47%), and Lahore (40%). On the contrary, DG Khan has shown negative trend of -11%.

1. Introduction

Nitrogen dioxide (NO₂) plays an important role in the modification of radiative balance of the Earth's atmosphere by changing its oxidizing capacity and chemistry and by influencing the lifetimes of important greenhouse gases. Its high concentration in the troposphere adversely impacts inhabitants of the planet [1, 2]. NO₂ is mainly emitted during industrial burning, vehicle combustion, biomass fuel and crop residue burning, direct soil emissions, and natural lightning [3, 4]. The dominant sink of NO₂ is its oxidation process, involving hydroxyl radical (OH) and solar ultraviolet (UV) radiations, by which secondary pollutants such as ozone, nitric acid, methane, and aldehydes are produced [5–9].

Tropospheric NO₂ shows high spatiotemporal variability mainly modulated by local emission changes, seasonal cycles, and meteorological conditions. South Asia is experiencing severe air quality degradation due to high population growth rate, burgeoning urbanization and industrialization, expanding demand of agricultural products, and exponentially increasing energy consumption rate (e.g., [10–14]). Therefore,

in order to develop the effective strategies to reduce its emissions, it is necessary to assess spatiotemporal distribution of NO₂ and identify its emission sources over the study region.

As far as tropospheric NO₂ assessments are concerned, no study has so far been carried out over the whole South Asian region. However, a few studies have been conducted only on some parts of South Asia to investigate spatiotemporal variations and to identify NO₂ emission hotspots using satellite remote sensing technique [15–20]. Recently, Ul-Haq et al. [20] assessed spatial and temporal patterns of NO₂ over Pakistan using Ozone Monitoring Instrument (OMI) retrieved data for the period 2004–2008. Renuka et al. [19] analyzed long-term changes of tropospheric NO₂ over south India using retrievals from GOME/ERS-2 and OMI/Aura during 1996–2014. They reported an increase in NO₂ column over Gadanki (13.48°N, 79.18°E). In spite of increase in anthropogenic emissions (e.g., population and vehicular traffic), these authors also found decreasing trend between eastern and western Ghats possibly linked with changes in land-use pattern limiting the soil emissions of NO₂. Ramachandran et al. [18] studied tropospheric NO₂ over India and identified NO₂ hotspots during 2002–2012 based



FIGURE 1: Geographical map of South Asia identifying locations of the NO_2 hotspots (image source: Google Earth).

on measurements from SCanning Imaging Absorption spectroMeter for Atmospheric CHartography (SCIAMACHY, on board Envisat satellite; [21, 22]). The study of David and Nair [17] was based on OMI data to detect seasonal changes and trends over Indian region for a period from 2007 to 2008. Ten-year (1996–2006) data obtained from Global Ozone Monitoring Experiment (GOME) and SCIAMACHY were used to study trends and seasonality over India [15] and to detect and analyze global NO_2 hotspots [16].

However, compared to previous studies, the present study offers two advancements, that is, complete coverage of the South Asian region for the first time and usage of higher spatial resolution data from OMI to identify small and localized emission sources of NO_2 . In this study, spatiotemporal distribution of tropospheric NO_2 and identification of hotspots in South Asia are presented by using OMI data for a period from October 2004 to January 2015.

2. Geography and Meteorology of South Asia

South Asia is the second most populous region in the world having population over 1667.8 million with land surface area of approximately $5,134,613 \text{ km}^2$. According to the South Asian Association for Regional Cooperation (SAARC), this region consists of eight countries: Afghanistan, Pakistan, India, Nepal, Maldives, Sri Lanka, Bangladesh, and Bhutan [23] (Figure 1).

The study region can be divided into five extensive physical subregions: the high Himalayan and Karakoram mountains in the north; the southern lowlands (Indus-Ganges-Brahmaputra) that expand from Pakistan to the delta lands of Bangladesh making up the core and densely populated areas; Balochistan Plateau, the most dry area of the

study region that covers the Suleman and Kirthar mountains in southern boundary of Afghanistan and Pakistan; the peninsular India, dominated by the Deccan Plateau bordered by narrow and fertile coastal plains backed by elongated north-south mountain ranges called western Ghats and eastern Ghats; and the island realm that includes Sri Lanka and Maldives [24].

Monsoon weather systems are the dominant climatic factors for the most of South Asia especially in Pakistan and India. In winter season cold and dry winds flow outward due to a large high-pressure system over the Himalayas and down across South Asia causing small amount of rain, whereas, in spring, these winds diminish, resulting in hot and dry season. In June low pressure over landmass draws in clean, warm, and moist air from the Arabian Sea (ArS), Bay of Bengal (BoB), and Indian Ocean (InO). The uplifting and cooling of these moist monsoon winds result in heavy rain fall, but not all of South Asia receives substantial rainfall from the southwest monsoon. In much of Pakistan and the Indian state of Rajasthan, precipitation is low and variable, resulting in steppe and desert climates [25–28].

Eleven statistical significant hotspots of NO_2 concentration have been identified which include Delhi, Mumbai, Kolkata, Korba, Singrauli, Bardhaman, Pakur, and Angul located in India, Lahore and Karachi from Pakistan, and Dhaka sited in Bangladesh. The basic climatic parameters of these hotspots are shown in Figure 2.

3. Materials and Methods

3.1. NO_2 Retrievals by OMI/Aura. NASA's Aura satellite team, celebrating its 10th anniversary of operations, has provided vital data about the chemistry and dynamics of Earth's atmosphere from the surface through the mesosphere. This satellite carries four instruments, that is, High Resolution Dynamics Limb Sounder (HIRDLS), Tropospheric Emission Spectrometer (TES), Microwave Limb Sounder (MLS), and Ozone Monitoring Instrument (OMI). In this study, because of improved algorithms and sensitivity of OMI for NO_2 detection at lower atmosphere, we have used its tropospheric NO_2 daily averaged product (OMNO2d.003, level 3). This sensor is a wide-field-imaging grating spectrometer with horizontal resolution of $13 \times 24 \text{ km}^2$ at the nadir point and it uses push-broom mode to measure the backscattered solar radiations (270–500 nm with spectral resolution of about 0.5 nm, [29–31]). Tropospheric NO_2 columns are retrieved by using Differential Optical Absorption Spectroscopy (DOAS) analysis in the 405–465 nm spectral range [32, 33]. Details of data filtering, DOAS analysis and algorithm, and data quality control procedures can be found in NASA's online user's manual for OMI products (<https://earthdata.nasa.gov/>).

It has been well established that NO_2 measurements retrieved from satellites are in good agreement with *in situ* measurements and bottom-up emission inventories [34–40]. The studies of Boersma et al. [41] and Celarier et al. [42] reviewed and validated the OMI- NO_2 with ground (MAX-DOAS instruments) and aircraft (DC-8 aircraft) measurements. They showed a good agreement between the tropospheric OMI- NO_2 column and ground-based measurements,

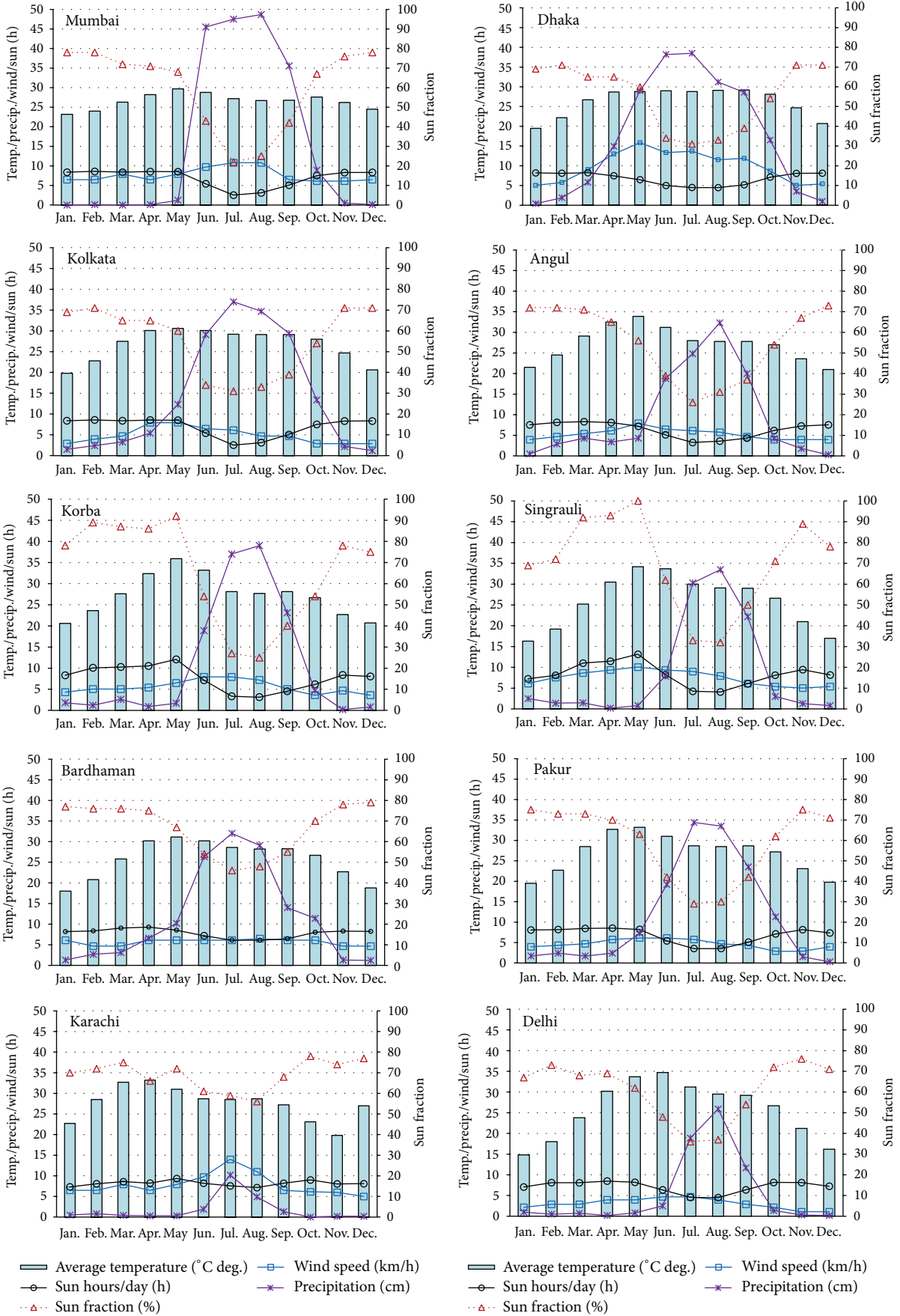


FIGURE 2: Continued.

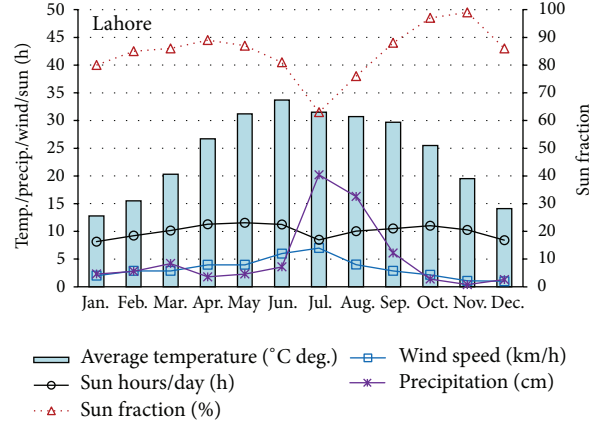


FIGURE 2: Climographs showing average temperature, sun fraction, precipitation, wind speed, and sun hours per day over NO₂ hotspots. Dotted line corresponds to secondary vertical axis.

with OMI-NO₂ columns underestimated by 15–30%. They also found a good correlation ($r = 0.83$) between the aircraft based NO₂ and OMI-NO₂ datasets. The observed OMI-NO₂ columns were smaller at about 15% (with uncertainty of $\pm 10\%$ and large scatter in the data) than the integrated *in situ* aircraft profiles. In a recent study, Ul-Haq et al. [20] found a good correlation ($r = 0.845$) between tropospheric OMI-NO₂ and SCIAMACHY-NO₂ columns using overpass data for the megacity Lahore (Pakistan).

3.2. Climate Data by Food and Agriculture Organization of United Nations (FAO). Monthly averaged climate data for NO₂ hotspots have been obtained from Food and Agriculture Organization of United Nations (FAO) global climate database using FAO Local Climate Estimator software New_LocClim, version 1.10 [43]. FAO has been using data from satellites and agrometeorological models [44, 45].

3.3. NO₂ Hotspots Identification. Higher values of a measurement may be very significant statistically but their spatial patterns are equally important if the data in hand is geographical in nature. In such a case spatial clustering of higher or lower values is of real importance to explain the phenomenon rather than the statistics of values only. In geostatistics, a feature will be significant if it has a high value and is surrounded by other features with high values as well. Geostatistical hotspot analysis compares proportionally local sum of NO₂ concentration for a feature and its defined neighborhood with sum of all the features in the study area.

In this study, geospatial statistic tool Getis-Ord G_i^* [46, 47] is used to identify statistically significant NO₂ concentration hotspots. The Getis-Ord G_i^* tool can be utilized for spatial clustering and autocorrelation [48]. This tool has been applied by using ArcGIS's Spatial Statistics tools and described in the following equations:

$$G_i^* = \frac{\sum_{j=1}^n w_{i,j} x_j - \bar{X} \sum_{j=1}^n w_{i,j}}{S \sqrt{\left[n \sum_{j=1}^n w_{i,j}^2 - \left(\sum_{j=1}^n w_{i,j} \right)^2 \right] / (n-1)}}$$

$$\bar{X} = \frac{\sum_{j=1}^n x_j}{n},$$

$$S = \sqrt{\frac{\sum_{j=1}^n x_j^2}{n} - (\bar{X})^2}, \quad (1)$$

where x_j is the attributive value for a point j , $w_{i,j} = 1/r_{i,j}$ is distance of j th measurement point from i th measurement point, and n is the total number of measurement points (i.e., 23712 in this study). The calculated values of \bar{X} are 0.724356 and 0.782528 for the years 2005–2008 and 2011–2014, respectively. Similarly, we find S values to be 0.665821 and 0.587949 for the data during 2005–2008 and 2011–2014, respectively. Getis-Ord G_i^* creates a new output feature class with z -score for each feature in the input feature class which indicates the place of a particular value in a dataset relative to the mean, standardized with respect to the standard deviation. The z -score represents the statistical significance (90% significant at $z \geq 1.645$, 95% significant at $z \geq 1.960$, 99% significant at $z \geq 2.576$, and 99.9% significant at $z \geq 3.291$) of clustering for a specified distance. For statistically significant positive z -scores, the larger the z -score, the more intense the clustering of high values (hotspot) [49]. A high z -score for a point indicates its neighbors have high attribute values and z -score near zero indicates that neighboring points have a range of values [50]. The Inverse Distance Squared Method, appropriate for this type of data where the closer features influence each other, with threshold distance of 1° has been used in hotspot identification [49]. We have obtained z -score values ranging from -4.43 to 22.18 . Any location with its surrounding areas having sufficiently extreme z -score ($z \geq 10$) is selected to be a real statistically significant hotspot of NO₂ concentration.

In the present work, we have used annual mean values of OMI-NO₂ to calculate NO₂ average values, and the percentage increase calculation is based on linear trend line equation; that is, y -intercept represents initial concentration value. The correlations of hotspots are based on monthly mean values.

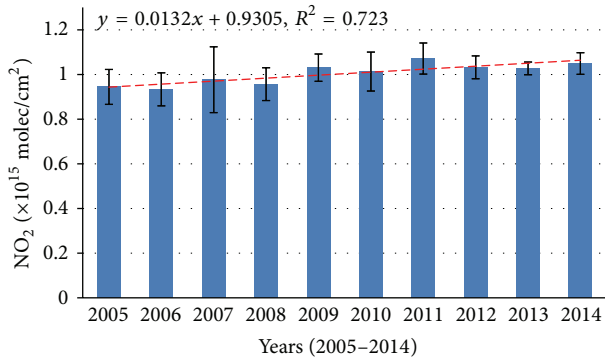


FIGURE 3: Area averaged annual distribution of OMI-NO₂ (×10¹⁵ molec/cm²) over the study region during 2005–2014.

4. Results and Discussion

4.1. Temporal Distribution of NO₂. The OMI retrievals show annual average value of tropospheric NO₂ column to be $1.0 \pm 0.05 \times 10^{15}$ molec/cm² over South Asia during the study period. A linear regression on the annual mean data shows a statistically significant (at confidence level of 99.9%) decadal increase of 14% with a slope of 0.013 (±0.002), correlation coefficient (R^2) 0.723, and y intercept at $0.930 (\pm 0.017) \times 10^{15}$ molec/cm². This positive trend is quite consistent with the trend ($1.76 \pm 1.1\%$ per year) reported by Ghude et al. [16] for a region consisting of India, Pakistan, Bangladesh, and Nepal and trend reported by Ghude et al. [15] for India (1.67% per year). During the study period the highest annual value of 1.07×10^{15} molec/cm² is found in 2011 and lowest value of 0.93×10^{15} molec/cm² in 2006 (Figure 3).

The observed increase of NO₂ in the region may be attributed to increase in anthropogenic emissions due to expansion in traffic volume, increasing power generation, flourishing industries, rapid urbanization, more demand of agricultural products, and more biomass fuel usage (e.g., [10–16, 19, 20, 51–54]).

The main sources of NO₂ are different for South Asian countries. The level of urbanization in Pakistan is now the highest in South Asia [55]. During this period the escalating urban population, coupled with more demand in some sectors such as cement production, industrial expansion, motor vehicles usage, and electricity generation, has resulted in elevated levels of NO₂ emissions. In Pakistan road transport is the dominant mode of passengers that is responsible for carrying 91% of the national passenger traffic and 96% of the freight movements. During 2000 to 2010, the number of vehicles on the roads has grown from 4 to 9.8 million showing an increase of 145% [56]. The factors that are responsible for this huge increase are the import of reconditioned vehicles, popularity of vehicle financing schemes, and the President and the Prime Minister's Rozgar schemes (self-employment schemes) with heavy investments at low mark-up to purchase small auto vehicles like rickshaws and taxis [53]. The economy of Pakistan is heavily dependent on the agricultural sector. The total agricultural waste burnt is estimated to be 1704.9 thousand tons per year in the rice-wheat cropping

system in Pakistan [57] contributing significant emissions of NO₂.

In India, the road transport is the dominant source of NO₂ emissions as compared to industry and power sector. The number of vehicles, registered in India, was 55 million in 2001 which has grown to around 159.5 million by 2012 [58]. Another important source of NO₂ emissions is the industrial process, especially the production of nitric acid, used in fertilizer manufacturing. India is an agrarian country and generates a large quantity of agricultural wastes. The annual crop residue generated in India for 2008–2009 is found to be about 620 Mt/year of which 15% is burnt on farms emitting huge amount of NO_x for the 2008–2009 [59]. Significant amount of NO₂ is emitted from coal fired power plants. India is the biggest energy user, followed by Iran and Pakistan. Coal is India's most abundant source of energy and currently almost 60% of its commercial energy needs are fulfilled by it. Lastly, widespread use of traditional sources of energy such as fuel wood and animal dung has also been contributing to NO₂ emissions. Estimates indicate that nearly 3 in 4 rural households depend on traditional sources of energy for cooking, heating, and so forth [60].

In Afghanistan, usage of electricity generators, biomass burning, and vehicular traffic are important sources of NO₂. The use of portable generators during power outages is a major source of NO₂ in the country. In Kabul alone, there are about 173,755 diesel and gasoline power generators in which 99.5% are used by households. Animal dung is also used in 85% of rural homes and in about 15% of urban homes for heating and cooking. The transport sector faces challenges of illegal import of used vehicles, continued use of very old and poorly maintained vehicles, poor quality of transport fuel, and limited road capacity leading to high emissions of air pollutants [61].

In Bangladesh, NO₂ is mainly emitted from energy transformation industries, motor vehicles, biomass burning for industrial processing and home cooking, burning of agricultural residues, and iron and steel industries. In Bhutan, the sector-wise emissions estimates of NO₂ indicate that domestic sources and vehicles are responsible for NO₂ emissions. As per Male Declaration-2000 [62], the sources of NO₂ in Sri Lanka include transport (46.8%), domestic use (37.1%), power generation (13.7%), industry (2.3%), and fuel conversion (0.1%). Bhutan is one of the few countries in the world where the environment is still protected largely due to its vast forest cover and widespread use of hydropower and biomass energy. Forest fires are the biggest sources of air pollution in Bhutan [63]. In Maldives, road traffic and domestic combustions are mostly responsible for NO_x air pollution. In Nepal, major NO_x sources are associated with the combustion of fossil fuels in industries, especially in the cement industry.

The estimated lifetime of NO₂ in the Planetary Boundary Layer (PBL) is 18–27 hours with considerable diurnal and seasonal variations [7, 64, 65]. However, in the middle and upper troposphere, NO₂ lifetime varies from several days to a week due to decreased OH and aerosol concentrations [6, 66, 67]. The NO₂ lifetime depends on meteorological conditions, its photolysis rate, surface emissions, length of day and night,

aerosols abundance, and OH and H₂O concentrations [18, 68, 69]. The meteorological conditions such as wind speed, temperature, humidity, and solar radiations flux affect NO₂ concentration via removal, transformation, and transport processes [68]. The hot and humid atmosphere enhances the removal of NO₂ through photolysis [18]. Also low wind speeds reduce NO₂ transport and its vertical air mixing thus elevating NO₂ concentration near emission sources [69].

OMI data show large seasonal amplitude with a monthly highest value of 1.58×10^{15} molec/cm² (in March 2011) and lowest value of 0.76×10^{15} molec/cm² (in July 2006). We also find high fluctuations in daily average values ranging from 2.01×10^{15} molec/cm² to 0.22×10^{15} molec/cm². The 10-year monthly mean (October 2004–January 2015) NO₂ behavior is presented in Figure 4.

The monthly pattern shows NO₂ maximum in spring season with a primary peak in March 1.22×10^{15} molec/cm² and secondary peak in May 1.13×10^{15} molec/cm². March peak is mainly attributed to low humidity, low wind speeds, and mild temperatures causing reduction in photolysis removal process of NO₂ hence stabilizing its concentration. Because of these factors, the NO₂ stability dominates the NO₂ removal through photolysis process of NO₂ due to the availability of more solar radiations in this month. In March, the lower concentration of OH (if the water vapor concentration is low enough) is considered a limiting factor of NO₂ photolysis to form HNO₃, the principal sink for NO₂ (e.g., [5]).

Relatively high values in March–May and October–November are also associated with emissions of NO₂ from large scale open field crop residue burning (nearly 7–10 tons of crop waste per hectare) in the study area during wheat-rice rotation periods [12, 70–72]. In the study region, the main area for crop residue burning is IGB consisting of Lahore, Dera Ghazi Khan, Narowal, Hafizabad, and Faisalabad in Pakistan and states of Uttar Pradesh, Punjab, and Haryana in India [13, 53, 73].

A winter season high with a peak in December 1.07×10^{15} molec/cm², is due to meteorology (weak winds and dry weather conditions), heavy usage of biomass fuel for wintertime home heating especially in the northern areas, and less UV radiations available for the initialization of photolysis reactions that break down NO₂ [8, 20, 74, 75]. In winter, shallower boundary layer results in lower vertical dispersion which reduces the dilution and removal rates of NO₂. This may also contribute to NO₂ enhancement in wintertime [76].

Low NO₂ during wet summer, with a notable dip in August 0.80×10^{15} molec/cm², is linked to massive advection of moist clean air mass, increased actinic fluxes enhancing the photodissociation of NO₂, elevated levels of OH radical helping NO₂ removal from the atmosphere via HNO₃, and presumably less traffic activity due to reduced social and educational activities during very hot summer [16, 20, 77, 78]. During the rainy season, effect of lightning on the increase of NO₂ concentration is not clearly seen due to the opposing influence of rain washout discussed by Yoo et al. [78]. The washout of the SO₂ and NO₂ by rainfall has been a global and regional concern, since it plays an important role in

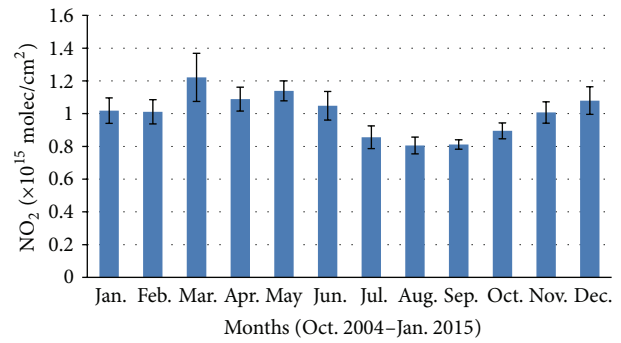


FIGURE 4: Area averaged monthly mean distribution of OMI-NO₂ (×10¹⁵ molec/cm²) over the study region during October 2004–January 2015.

producing acidic precipitation [78]. In the atmosphere, NO₂ reacts with water to form nitric or nitrous acid [79]. A number of previous studies have demonstrated significant negative correlation between NO₂ and rainfall (e.g., [77, 80, 81]). Martin [80] showed the washout coefficient for NO₂ is about 80% of that for SO₂. However, the washout effects on the NO₂ and SO₂ concentrations by daily cumulative rainfall are comparable over India, resulting in the reduction (40–45%) of these pollutants [77]. Yoo et al. [78] demonstrated the scavenging of air pollutants (CO, NO₂, SO₂, and PM₁₀) by summertime precipitation based on the three washout effect indicators such as Absolute Washout Index (AWI), Negative Correlation Fraction (NCF), and Relative Washout Index (RWI). They showed that the washout effect is in the descending magnitude order of PM₁₀ > SO₂ > NO₂ > CO > O₃.

We discuss two crop residue burning events of postmonsoon 2010 [82] and postmonsoon 2012 [83]. South Asia is the principal niche of rice-wheat system that occupies a total of 13.5 million ha in rice-wheat consortium countries such as India, Pakistan, Bangladesh, and Nepal with rice cultivation areas of 10, 2.2, 0.8, and 0.5 million ha, respectively [57, 84]. In this regard, South Asian farmers need to manage 5–7 t ha⁻¹ of rice residues and overcome the problems for planting wheat. There are various options for crop waste management out of which the burning of crop residue is one of the most common practices.

Elevated NO₂ concentrations have been found over northwestern parts of IGB including Punjab, Haryana, and western Uttar Pradesh regions as a direct consequence of the crop residue burning emissions (Figures 5(a)–5(c)). In Figure 4, NO₂ enhancements (10–42% on average) can be seen over the rice residue burning areas during the postmonsoon period of 2012, compared with the average value of postmonsoon periods during study years except 2010 and 2012, especially in Pakistani and Indian Punjab and their adjoining territories famous for rice cultivation. For the postmonsoon 2012, we find 15–35% increment in NO₂ levels showing close agreement with the results of Kaskaoutis et al. [83]. In a previous study, Kaskaoutis et al. [83] examined the impact of paddy crop residue burning over northern

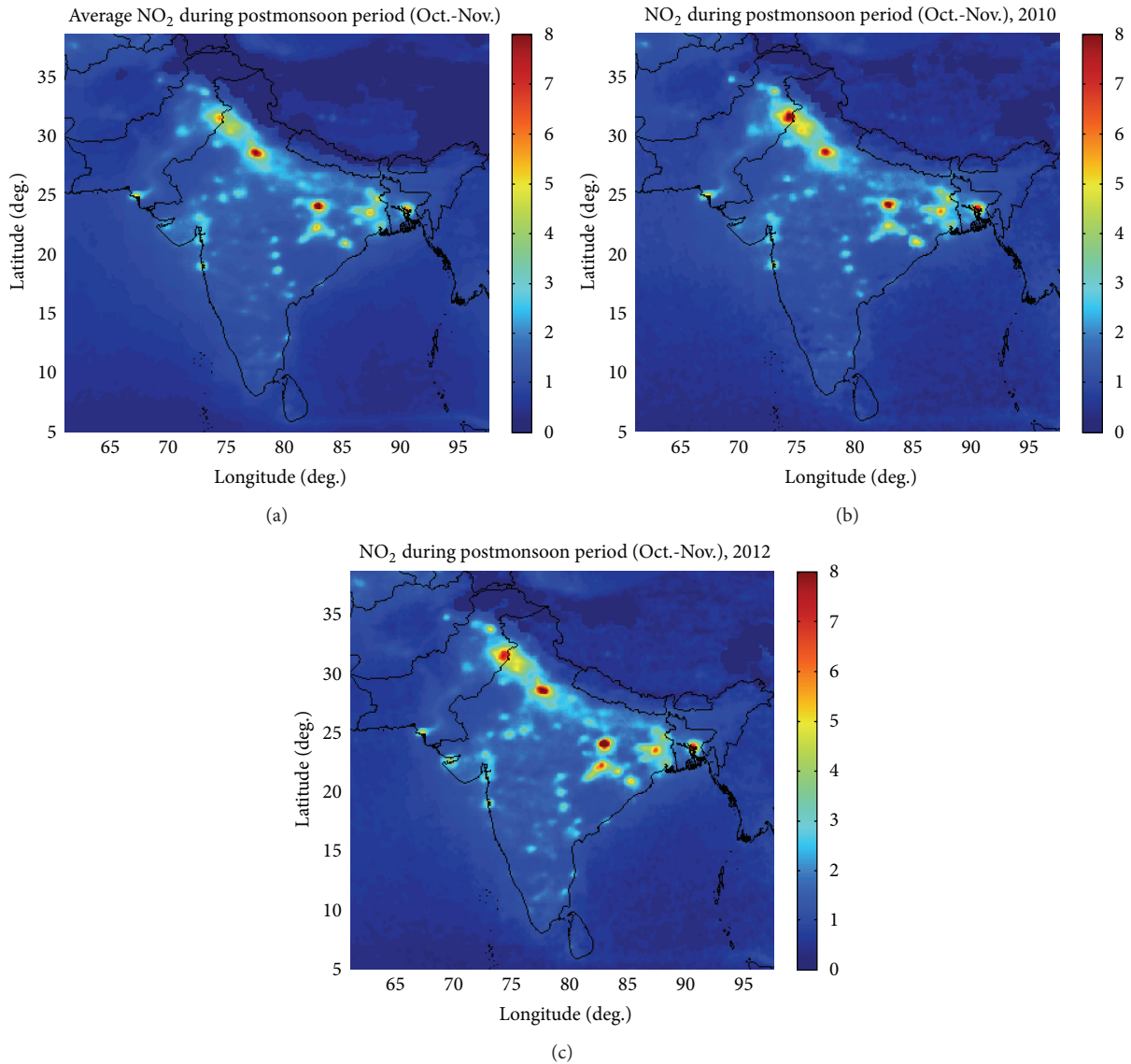


FIGURE 5: (a) Average NO₂ after monsoon for all years except 2010 and 2012. (b) NO₂ during postmonsoon 2010. (c) NO₂ during postmonsoon 2012.

India during the postmonsoon (October–November) season of 2012. They showed about 34–40% increase in NO₂ levels as a direct consequence of these crop residue burning events.

4.2. Spatial Distribution of NO₂. In Figure 6, an enhanced value of NO₂ observed over IGB is mainly coupled with high human settlement, coal based thermal power plants, industrialization and urbanization, more agricultural activity, large scale crop residue, and biomass mass burning previously reported by many studies (e.g., [3, 12, 19, 71, 85, 86]). It is evident from the figure that IGB section consisting of Punjab (from India and Pakistan) and eastern region of India show consistent high values due to high population density, crop residue and biomass burning events, power plants, and mining activities. In addition, low population and rural areas scattered all over the region also contribute to NO₂ emissions from domestic cooking, small and medium

industries, transport, and open burning of litter and biofuels. NO₂ masking is also observed over marine areas that is associated with NO₂ emissions due to seaport activities and urban pollution.

Our analysis shows significant decadal increasing trend of 17% (slope of 0.02428 ± 0.00657 and y intercept at $1.24751 \pm 0.03695 \times 10^{15}$ molec/cm²) with average of $1.36 \pm 0.01 \times 10^{15}$ molec/cm² over a region between eastern and western Ghats (12.57–17.58°N to 76.05–79.00°E). This finding differs with the results by Renuka et al. [19] who reported a decreasing trend over the region between the two Ghats. The disparity in the results may be attributed to the difference in spatial and temporal domains.

4.3. NO₂ Hotspots in South Asia. In Figure 7(a), NO₂ hotspots have been identified and visualized during 2005–2014 using Getis-Ord G_i^* statistic hotspot analysis tool.

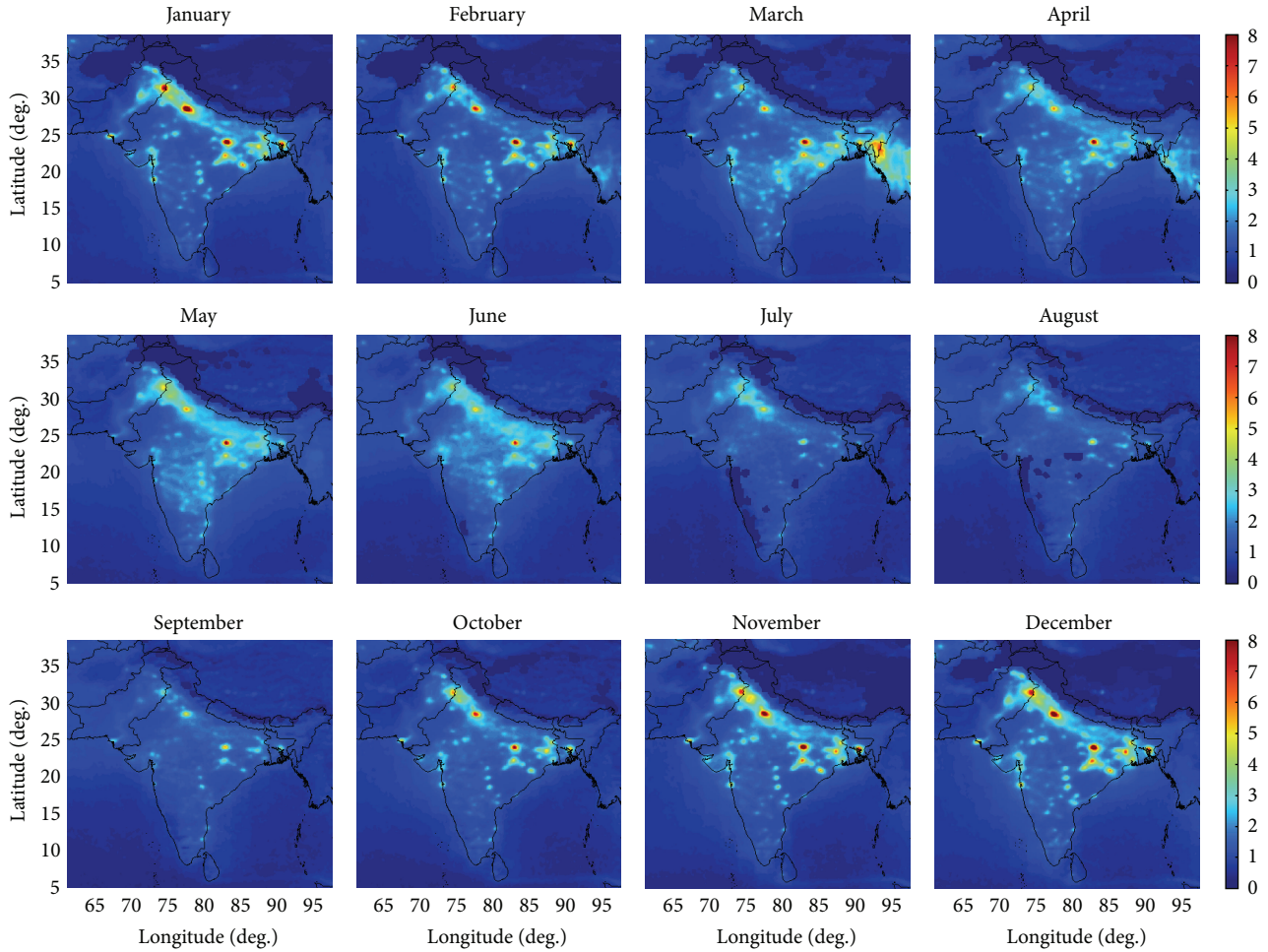


FIGURE 6: 10-year monthly mean spatial and temporal distribution of OMI/Aura tropospheric NO_2 ($\times 10^{15}$ molec/ cm^2) over the study region during October 2004–January 2015.

These hotspots include megacities of Karachi and Mumbai located along the coastal belt of ArS, Lahore and Delhi sited in IGB, and Kolkata and Dhaka situated in eastern region of the study area.

It is evident from Figure 7(a) that high values of NO_2 are found over most of the hotspots observed in the northern areas. This NO_2 pollution appears more widespread over Lahore and Delhi as compared to other hotspots. This may be related to large scale crop residue burning and high population density in the surrounding territory. The lower NO_2 value over southern part of South Asia is due to a number of factors: small number of large point sources, low population density, less amount of biomass burning and vehicular population, and the hot and humid climate which leads to enhanced NO_2 photolysis.

In order to perform a more meaningful analysis of hotspots, we have created two time zones, namely, first four years (2005–2008) and last four years (2011–2014). The tendencies in the NO_2 -hotspots are expressed in terms of differences in z -score values (Δz -score) and are calculated from the linear regression (Δz -score = $a * \Delta t$) to the time series for 2005–2008 and 2011–2014 periods individually. The averaged z -score values of the two periods are used to

calculate the trends of hotspots. Δz -score actually represents the slope of the z -score regression line in each pixel starting in 01–01–2005 to 31–12–2008 (first period) and 01–01–2011 to 31–12–2014 (second period). From Figures 7(b)–7(d), it is revealed that negative trends of z -score cover some parts of IGB and central areas of India. The hotspots of Lahore, Delhi, Dhaka, Bardhaman, Pakur, and Korba are strengthening and expanding in geographical extent during both the periods. On the other hand, Mumbai, Karachi, Singrauli, Angul, and Kolkata are found to have decreasing trends. Cities of Islamabad, Kabul, and Ahmedabad also appear with significant increasing trends.

OMI data reveal that NO_2 columns are mounting over all the hotspots and most of the selected cities. However, the difference in increasing rates is mainly attributed to levels of the industrial activity, traffic volume, urban and rural background, and local meteorological conditions. Dhaka is the fastest growing city among all the hotspots and selected cities [87] linked to the highest increase (77%) in NO_2 column with an average of $3.15 \pm 0.51 \times 10^{15}$ molec/ cm^2 . After Dhaka, we find high growth rates for Islamabad 69%, Kabul 68%, Korba 64%, Bardhaman 47%, and Lahore 40%. On the other hand, DG Khan is found with negative trend at -11% .

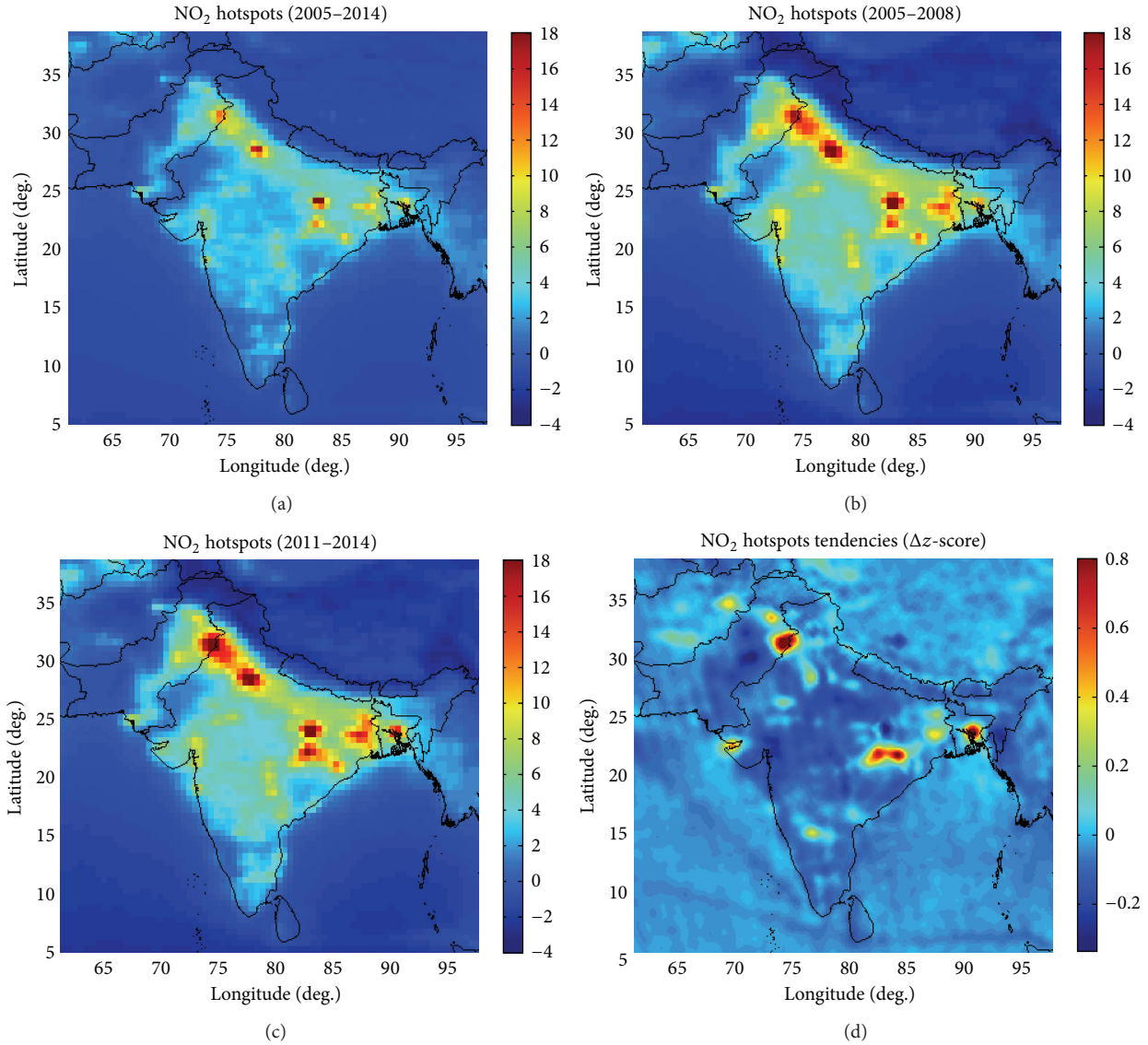


FIGURE 7: Spatial distribution of (a) hotspots during 2005–2014, (b) hotspots during 2005–2008, (c) hotspots during 2011–2014, and (d) hotspots tendencies (Δz -score) for 2005–2008 and 2011–2014.

The average value of NO₂ column over Singrauli is the highest $3.71 \pm 0.27 \times 10^{15}$ molec/cm² followed by Bardhaman $3.23 \pm 0.44 \times 10^{15}$ molec/cm² and Korba $3.23 \pm 0.44 \times 10^{15}$ molec/cm², whereas Karachi has exhibited the lowest average value of $2.00 \pm 0.10 \times 10^{15}$ molec/cm² with decadal increase at 6% (Table 1).

Figures 8 and 9 show the seasonality and intercomparison of the hotspots in the region. The megacities of Lahore and Delhi are located in IGB and experience almost the same meteorological conditions (Figure 2), large crop residue burning in surrounding areas, and extremity of monsoon which result in similarity in NO₂ seasonal patterns showing $R^2 = 0.865$ (Figures 7 and 8). Over Lahore and Delhi, higher NO₂ values are found during the winter months followed by spring season (Figure 6). Winter peak is mainly due to biomass burning for domestic heating [20], stable winds, less daily sun hours and sun fraction, and low temperature

(Figure 2). In May, a surge in NO₂ over Lahore and Delhi is linked to large scale crop residue burning from wheat fields in the neighboring rural areas of Kasur, Shiekhpura, Narowal, Hafizabad, Mianchannu, and Uttar Pradesh regions. In this month, high temperature also contributes to soil emissions which are further enhanced by the application of fertilizers in the rice fields. The low NO₂ column over these cities during the period of monsoon season is mostly coupled with heavy rains, high humidity, and strong winds (Figure 2).

Some important anthropogenic emission sources of NO₂ in Lahore are industrial zones (e.g., Sundar industrial estate, Kot Lakhpat industrial area, Shahdara tractors manufacturing units, steel mills, and refrigerator manufacturing units), power plants (SEPCO, Kohinoor, Japan Power, and Nishat) and large scale crop residue burning events. Also a notable source of high NO₂, over Lahore, is the usage of diesel and petrol electricity generators during the heavy electric power

TABLE 1: Statistics of tropospheric NO_2 ($\times 10^{15}$ molec/cm 2) over South Asian countries, hotspots, and some major cities using OMI/Aura data during 2005–2014.

Name of the country/hotspot area/city	Location	Population (million)	Area (km 2)	Average ($\times 10^{15}$ molec/cm 2)	Decadal trend (%)	Trend parameters $a = \text{slope} \pm \text{error}$ $b = y \text{ intercept} \pm \text{error}$ ($\times 10^{15}$ molec/cm 2) $R^2 =$	Highest monthly value ($\times 10^{15}$ molec/cm 2)	Lowest monthly value ($\times 10^{15}$ molec/cm 2)
Bangladesh	23.70°N, 90.35°E	156.6	147,570	1.75 \pm 0.13	23	$a = 0.04039 \pm 0.01063$, $b = 1.54966 \pm 0.05983$, $R^2 = 0.67337$	2.95 (Mar.-11)	0.95 (Jul.-05)
India	21.00°N, 78.00°E	1252	3,287,590	1.66 \pm 0.08	17	$a = 0.02912 \pm 0.00452$, $b = 1.51498 \pm 0.02541$, $R^2 = 0.85592$	1.16 (Jul.-06)	2.36 (Mar.-11)
Afghanistan	34.53°N, 69.13°E	31	652,864	0.81 \pm 0.04	16	$a = 0.01362 \pm 0.00358$, $b = 0.74361 \pm 0.02012$, $R^2 = 0.67459$	1.25 (Jul.-10)	0.49 (Oct.-05)
Nepal	26.53°N, 86.73°E	27	147,181	1.05 \pm 0.05	13	$a = 0.01452 \pm 0.00464$, $b = 0.98200 \pm 0.02614$, $R^2 = 0.58262$	1.70 (Apr.-09)	0.71 (Jan.-06)
Pakistan	33.66°N, 73.16°E	182	796,095	1.24 \pm 0.05	13	$a = 0.01706 \pm 0.00383$, $b = 1.15578 \pm 0.02154$, $R^2 = 0.73952$	1.53 (Jul.-10)	0.94 (Nov.-05)
Maldives	3.20°N, 73.22°E	0.3	300	0.20 \pm 0.01	10	$a = 0.00239 \pm 0.00098$, $b = 0.19713 \pm 0.00549$, $R^2 = 0.46181$	0.33 (Feb.-06)	0.09 (Sep.-05)
Sri Lanka	7.00°N, 81.00°E	20.4	65,610	0.71 \pm 0.01	6	$a = 0.00471 \pm 0.00203$, $b = 0.68708 \pm 0.01141$, $R^2 = 0.43601$	0.88 (May.-06)	0.582 (Oct.-07)
Bhutan	27.41°N, 90.43°E	0.7	38,394	0.83 \pm 0.04	5	$a = 0.00464 \pm 0.00628$, $b = 0.80861 \pm 0.03533$, $R^2 = 0.07251$	1.63 (Mar.-09)	0.48 (Aug.-05)
Dhaka (Dhaka Division, Bangladesh)	23.48°N, 90.24°E	14.39	815	3.15 \pm 0.51	77	$a = 0.190 \pm 0.02121$, $b = 2.2012 \pm 0.119355$, $R^2 = 0.9198$	6.25 (Jan.-11)	1.31 (Jul.-06)
Islamabad (Capital of Pakistan)	33.40°N, 73.00°E	2.1	1060	2.32 \pm 0.43	69	$a = 0.12912 \pm 0.03554$, $b = 1.67488 \pm 0.19997$, $R^2 = 0.65351$	4.68 (Dec.-10)	1.19 (Sep.-06)
Kabul (Capital of Afghanistan)	34.33°N, 69.08°E	3.5	425	1.74 \pm 0.27	68	$a = 0.09677 \pm 0.01071$, $b = 1.26159 \pm 0.06026$, $R^2 = 0.92105$	5.03 (Jan.-13)	1.01 (Mar.-05)
Korba (Chhattisgarh, India)	22.35°N, 82.68°E	1.01	6,598	3.23 \pm 0.44	64	$a = 0.1699 \pm 0.012827$, $b = 2.3838 \pm 0.072183$, $R^2 = 0.9616$	5.82 (Jun.-08)	1.44 (Feb.-05)

TABLE 1: Continued.

Name of the country/hotspot area/city	Location	Population (million)	Area (km ²)	Average ($\times 10^{15}$ molec/cm ²)	Decadal trend (%)	Trend parameters $a = \text{slope} \pm \text{error}$ $b = y\text{-intercept} \pm \text{error}$ ($\times 10^{15}$ molec/cm ²)	Highest monthly value ($\times 10^{15}$ molec/cm ²)	Lowest monthly value ($\times 10^{15}$ molec/cm ²)
Bardhaman (West Bengal, India)	23.33°N, 87.30°E	0.34	56	3.23 ± 0.38	47	$a = 0.1363 \pm 0.011839$, $b = 2.5578 \pm 0.066623$, $R^2 = 0.9498$	5.89 (Dec.-13)	1.47 (Aug.-06)
Lahore (Punjab, Pakistan)	31.32°N, 74.22°E	10.23	1,172	3.22 ± 0.31	40	$a = 0.1176 \pm 0.013978$, $b = 2.6338 \pm 0.078661$, $R^2 = 0.91$	5.95 (Oct.-13)	1.82 (Sep.-06)
Pakur (Jharkhand, India)	23.30°N, 86.40°E	0.89	686	3.07 ± 0.26	35	$a = 0.102 \pm 0.008346$, $b = 2.5619 \pm 0.046963$, $R^2 = 0.9552$	5.19 (Sep.-12)	1.58 (May.-05)
Chittagong (Chittagong Div, Bangladesh)	22.36°N, 91.80°E	4.6	157	1.61 ± 0.15	31	$a = 0.04878 \pm 0.01076$, $b = 1.37594 \pm 0.06054$, $R^2 = 0.74601$	4.03 (Mar.-11)	0.58 (Jul.-09)
Faisalabad (Punjab, Pakistan)	31.41°N, 73.07°E	6.5	5,856	2.48 ± 0.21	29	$a = 0.06997 \pm 0.01379$, $b = 2.13633 \pm 0.07759$, $R^2 = 0.78626$	3.79 (Jan.-11)	1.54 (Sep.-11)
Rajshahi (Rajshahi Division, Bangladesh)	24.36°N, 88.60°E	0.8	2,407	2.43 ± 0.19	26	$a = 0.06211 \pm 0.01320$, $b = 2.12518 \pm 0.07426$, $R^2 = 0.75987$	4.27 (Dec.-12)	1.16 (Jul.-10)
Bengaluru (Karnataka, India)	12.96°N, 77.56°E	4.30	741	1.88 ± 0.11	21	$a = 0.04048 \pm 0.00602$, $b = 1.67940 \pm 0.03390$, $R^2 = 0.86579$	3.33 (Mar.-11)	0.99 (Jul.-06)
Delhi (National Capital Region of India)	28.67°N, 77.22°E	16.31	1,484	3.20 ± 0.19	21	$a = 0.0697 \pm 0.008978$, $b = 2.8575 \pm 0.050523$, $R^2 = 0.896$	5.31 (Jan.-08)	1.99 (Aug.-06)
Singrauli (Madhya Pradesh, India)	24.12°N, 82.39°E	1.17	2,200	3.71 ± 0.27	21	$a = 0.0783 \pm 0.02638$, $b = 3.3193 \pm 0.148447$, $R^2 = 0.5574$	5.55 (Aug.-13)	1.55 (Aug.-11)
Angul (Odisha, India)	20.83°N, 85.01°E	1.27	6,232	2.73 ± 0.16	19	$a = 0.0527 \pm 0.013024$, $b = 2.4762 \pm 0.073292$, $R^2 = 0.7001$	4.59 (Mar.-11)	1.12 (Jul.-06)
Hyderabad (Telangana, India)	17.37°N, 78.48°E	9.5	650	2.06 ± 0.15	19	$a = 0.04071 \pm 0.01533$, $b = 1.86456 \pm 0.08629$, $R^2 = 0.50165$	3.6 (Mar.-11)	1.06 (Aug.-13)
Chennai (Tamil Nadu, India)	13.08°N, 80.27°E	4.34	426	2.33 ± 0.21	19	$a = 0.04669 \pm 0.02416$, $b = 2.10360 \pm 0.13594$, $R^2 = 0.34802$	3.31 (Mar.-11)	1.93 (Jul.-13)

TABLE 1: Continued.

Name of the country/hotspot area/city	Location	Population (million)	Area (km ²)	Average ($\times 10^{15}$ molec/cm ²)	Decadal trend (%)	Trend parameters $a = \text{slope} \pm \text{error}$ $b = y \text{ intercept} \pm \text{error}$ ($\times 10^{15}$ molec/cm ²) $R^2 =$	Highest monthly value ($\times 10^{15}$ molec/cm ²)	Lowest monthly value ($\times 10^{15}$ molec/cm ²)
Lucknow (Uttar Pradesh, India)	26.80°N, 80.90°E	3.7	2,528	2.14 \pm 0.10	15	$a = 0.03362 \pm 0.00609$, $b = 1.97686 \pm 0.03427$, $R^2 = 0.81324$	2.99 (Jan.-12)	1.35 (Jul.-08)
Kolkata (West Bengal, India)	22.55°N, 88.31°E	14.11	1,886	2.63 \pm 0.13	15	$a = 0.0411 \pm 0.011804$, $b = 2.4314 \pm 0.066426$, $R^2 = 0.6343$	4.27 (Oct.-10)	1.43 (Jul.-12)
Kathmandu (Capital of Nepal)	27.27°N, 85.33°E	0.7	50.67	1.03 \pm 0.05	13	$a = 0.01412 \pm 0.00630$, $b = 0.96398 \pm 0.03546$, $R^2 = 0.41776$	1.85 (Apr.-09)	0.485 (Jan.-06)
Sylhet (Sylhet Division, Bangladesh)	24.90°N, 91.86°E	2.6	26.5	1.35 \pm 0.01	12	$a = 0.01765 \pm 0.01109$, $b = 1.26824 \pm 0.06240$, $R^2 = 0.26568$	2.98 (Mar.-09)	0.61 (Jul.-05)
Gadanki (Andhra Pradesh, India)	13.48°N, 79.20°E	Few thousands	Few acres	1.16 \pm 0.06	9	$a = 0.01194 \pm 0.00784$, $b = 1.10182 \pm 0.04410$, $R^2 = 0.24890$	2.16 (Mar.-11)	0.44 (Jul.-13)
Mumbai (Maharashtra, India)	19.04°N, 72.52°E	12.47	4,355	2.14 \pm 0.08	7	$a = 0.0163 \pm 0.011462$, $b = 2.0635 \pm 0.064502$, $R^2 = 0.2243$	4.08 (Sep.-12)	0.48 (Aug.-09)
Karachi (Sindh, Pakistan)	24.51°N, 67.72°E	16.05	3,527	2.00 \pm 0.10	6	$a = 0.0144 \pm 0.014674$, $b = 1.9283 \pm 0.082573$, $R^2 = 0.1211$	3.36 (Feb.-08)	1.08 (Sep.-11)
Ahmedabad (Gujarat, India)	23.03°N, 72.78°E	3.52	464	3.03 \pm 0.10	4	$a = 0.01725 \pm 0.01369$, $b = 3.12073 \pm 0.07701$, $R^2 = 0.18491$	4.28 (Dec.-10)	1.727 (Jul.-05)
Colombo (Capital of Sri Lanka)	6.93°N, 79.84°E	6.4	37.31	1.32 \pm 0.15	3	$a = 0.00503 \pm 0.02161$, $b = 1.30349 \pm 0.12158$, $R^2 = 0.00769$	3.3 (Jan.-12)	0.39 (Jul.-13)
Kanpur (Uttar Pradesh, India)	26.28°N, 80.24°E	2.5	1,680	2.17 \pm 0.04	2	$a = 0.00442 \pm 0.00584$, $b = 2.15486 \pm 0.03285$, $R^2 = 0.07553$	2.99 (Dec.-13)	1.18 (Mar.-12)
DG Khan (Punjab, Pakistan)	30.03°N, 70.38°E	2.12	11,294	1.80 \pm 0.12	-11	$a = -0.02401 \pm 0.01464$, $b = 1.92591 \pm 0.08238$, $R^2 = 0.27753$	2.53 (Jan.-08)	1.12 (Oct.-11)

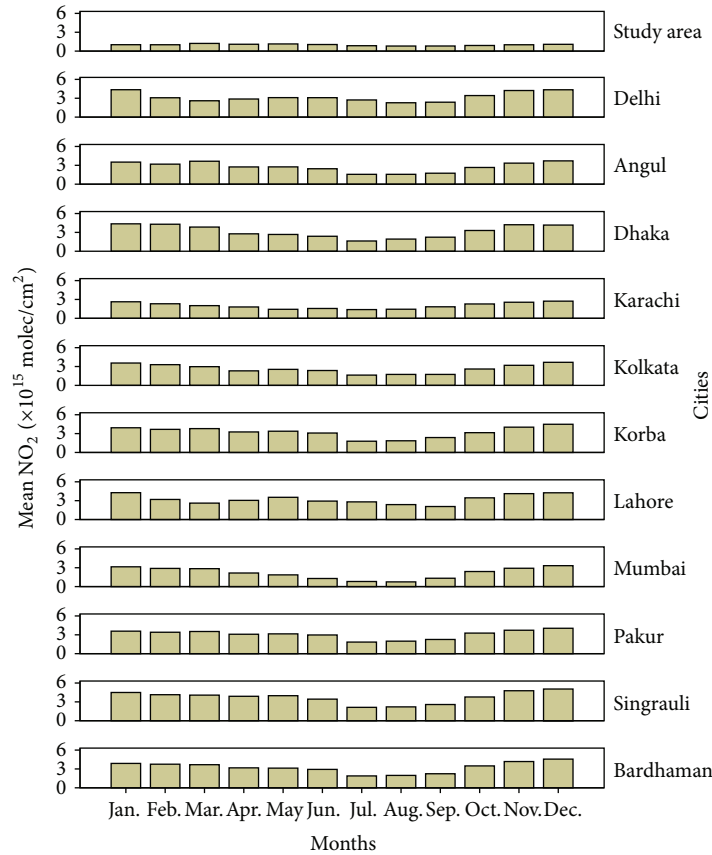


FIGURE 8: Monthly mean values of OMI/Aura tropospheric NO_2 ($\times 10^{15}$ molec/ cm^2) over the study area and hotspots during October 2004–January 2015.

load shedding (average 10–16 hours daily in city area) [53]. In Delhi, power plants (Badarpur, Rajghat, Pragati, and IPGCL), industrial estates (Badli, Wazirpur, Mangolpuri, Lawrance, Jhilmil Industrial Area, Patparganj, etc.), and biomass and crop residue burning are the notable contributors of NO_2 emissions. We find higher (17%) annual average value of tropospheric NO_2 $3.22 \pm 0.31 \times 10^{15}$ molec/ cm^2 than the previously reported value $2.74 \pm 0.79 \times 10^{15}$ molec/ cm^2 by Ul-Haq et al. [20] over Lahore for 2004–2008 using OMI data. The discrepancy between these two reported values is mainly due to the difference in time periods and increasing growth of anthropogenic emissions in the past few years.

The megacities of Karachi and Mumbai are considered as financial hubs of Pakistan and India, respectively. These cities are located in the coastal belt of ArS and show large similarity ($R^2 = 0.800$) in NO_2 column values, trends, and temporal variability (Table 1, Figure 9) mainly associated to matching meteorological and urban conditions. Karachi showed the lowest average value $2.00 \pm 0.10 \times 10^{15}$ molec/ cm^2 with the lowest increase at 6% followed by Mumbai $2.14 \pm 0.08 \times 10^{15}$ molec/ cm^2 with 7% increase during the study period. Ul-Haq et al. [20] reported higher $3.63 \pm 2.19 \times 10^{15}$ molec/ cm^2 value of NO_2 over Karachi during 2004–2008 than our computed value. This decrease in NO_2 concentration over Karachi may be associated with the political instability and economic downturn in recent years. In Karachi and Mumbai,

more than 80% of total NO_2 emissions come from industrial sector and fugitive emissions from oil and gas activities [18, 20]. It is clear from Figure 8 that high NO_2 occurs in winter over Karachi and Mumbai. These cities have poor conditions for NO_2 removal, transformation, and transport processes (low rainfall, low wind speed, and low ambient temperature) in winter months. Other contributing factor for high NO_2 may be NO_2 carrying wind (NW-NE) from Indian landmass areas amplified by local emissions. On the other hand, low values are observed in summer linked to more rain wash-out and high humidity and strong and clean sea breeze (Figure 2) from ArS. Major sectors of NO_2 emissions in Karachi are power plants (Bin Qasim I&II, Gul Ahmed, and Tapal), textile industry, steel and iron factories, chemical industry, oil refineries, and seaport activities. The core industrial area of major emissions in Mumbai and surrounding areas is the Mumbai-Pune belt that includes textiles, chemicals, engineering, electrical, drugs, transport equipment, plastic and synthetic goods, leather goods, and ship-building.

We find high correlation ($R^2 = 0.864$) between the NO_2 seasonality for Dhaka and Kolkata. NO_2 is found high over these cities throughout the dry season (October–March) and low for the rest of the year (April–September). Gurjar et al. [14] have reported that the ambient NO_2 level in Dhaka is $83 \mu\text{g}/\text{m}^3$ which exceeds the World Health Organization (WHO) guideline concentration ($40 \mu\text{g}/\text{m}^3$). Annual 7–16%

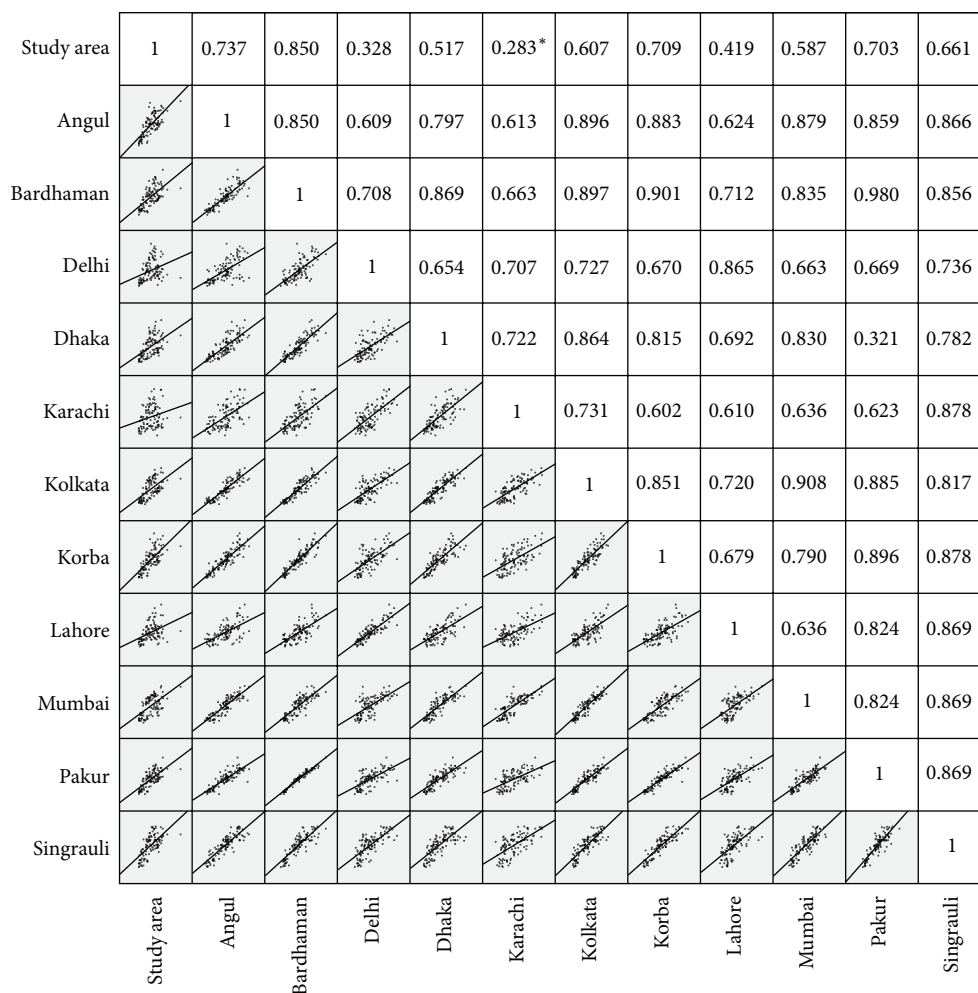


FIGURE 9: Correlation matrix of eleven NO_2 hotspots and study region with best fit curve. Pearson correlations values R^2 are also shown. All correlations are significant at the 0.01 level (2-tailed) except correlation between Karachi and the study area indicated by * which is significant at the 0.05 level (2-tailed).

increase of vehicles has been observed for the last 10 years that has worsened the air quality as vehicular emissions are the single largest contributor of NO_2 in Dhaka [10, 88, 89]. The ambient NO_2 in Kolkata is observed to be $37 \mu\text{g}/\text{m}^3$ [14] with the major emission sources of moderate to heavy vehicular traffic, power generation plants, rapid and unplanned urbanization and industrialization, and railway yard [11]. In Dhaka, a substantial part of total traffic is nonmotorized vehicles that produce severe congestion and pollution problem especially in road intersections. Other notable sectors which contribute to high NO_2 emissions are brick kilns, urban residential combustion, gas processing and refineries, and energy and manufacturing industries [90].

The highest correlation ($R^2 = 0.980$) is observed for Pakur and Bardhaman and surrounding rural areas. These areas have very similar topography, low population, and meteorological conditions in agreement with Ramachandran et al. [18]. These hotspots have major sources of emissions as steel plants, major coal fields (Raniganj and Jharia), and crop residue burning in the adjoining territory. Singrauli, Korba,

and Angul hotspots are located in the eastern mining region (Singrauli coalfield, Talchar coalfield, and Korba coalfields) of India [18]. Most of the mining processes and associated industries exist along with many of the major power plants and refineries in this region and cause high emissions and spread of NO_2 in this area [18, 85, 91, 92]. We have also found a similar seasonality ($R^2 = 0.908$) between NO_2 column over Mumbai and Kolkata as well, because both cities lie on almost similar latitude range and have tropical climate. Lower NO_2 values are observed over Mumbai compared to Kolkata primarily linked to strong winds (Table 1).

From Figure 7, it may be noted that there exists some difference between the NO_2 seasonality between the hotspots and South Asia. The NO_2 column over hotspots generally shows peak in December, while over South Asia it exhibits its elevated level in March. This is because of the fact that anthropogenic emissions dominate NO_2 seasonality over hotspots. On the other hand, March peak in South Asia, as a whole, is due to the dominance of natural factors discussed in Section 4.1.

5. Conclusions

OMI measurements over South Asia have been used to analyze spatial and temporal variability of tropospheric NO₂ column during October 2004 to January 2015. NO₂ emission hotspots and some important cities have been discussed for trends and seasonal cycles. An average value of $1.0 \pm 0.05 \times 10^{15}$ molec/cm² with 14% decadal increase has been reported over the study region. This positive trend is linked to the increasing anthropogenic emissions from power generation, urbanization, and vehicular and industrial sectors. Significant increase has been observed in NO₂ concentrations over some parts of IGB connected to large scale postmonsoon crop residue events of 2010 and 2012. Strong seasonality of NO₂ concentration is observed with the highest value in March and the lowest in August. Statistically significant NO₂ hotspots have been identified and discussed. OMI data reveal that the NO₂ columns are mounting at considerable rates over all the hotspot locations and most of the major cities. Dhaka (Bangladesh) showed the highest decadal increase, whereas Karachi (Pakistan) has exhibited the lowest average value of $2.00 \pm 0.10 \times 10^{15}$ molec/cm² with the lowest decadal increase at 6%. The highest average value is observed over Singrauli (India).

Conflict of Interests

The authors declare that there is no conflict of interests regarding the publication of this paper.

Acknowledgments

The authors thank three anonymous reviewers and the editor for improving the original paper. They greatly acknowledge NASA's team for OMI data (<http://earthdata.com/>) and FAO's team for New_LocClim, version 1.10.

References

- [1] WHO, *Guidelines for Air Quality*, World Health Organization, Geneva, Switzerland, 2000.
- [2] IPCC, "Climate change 2007: the physical science basis," in *Contribution of Working Group I to the Fourth Assessment Report of the Intergovernmental Panel on Climate Change*, S. Solomon, D. Qin, M. Manning et al., Eds., p. 996, Cambridge University Press, Cambridge, UK, 2007.
- [3] A. Richter and J. P. Burrows, "Tropospheric NO₂ from GOME measurements," *Advances in Space Research*, vol. 29, no. 11, pp. 1673–1683, 2002.
- [4] M. M. Cheng, H. Jiang, Z. Guo, and M. M. Cheng, "Evaluation of long-term tropospheric NO₂ columns and the effect of different ecosystem in Yangtze River Delta," *Procedia Environmental Sciences*, vol. 13, pp. 1045–1056, 2012.
- [5] D. J. Jacob, *Introduction to Atmospheric Chemistry*, Princeton University Press, Princeton, NJ, USA, 1999.
- [6] P. Warneck, *Chemistry of the Natural Atmosphere*, Academic Press, London, UK, 2000.
- [7] T. Kunhikrishnan, M. G. Lawrence, R. Von Kuhlmann, A. Richter, A. Ladstätter-Weißenmayer, and J. P. Burrows, "Analysis of tropospheric NO_x over Asia using the model of atmospheric transport and chemistry (MATCH-MPIC) and GOME-satellite observations," *Atmospheric Environment*, vol. 38, no. 4, pp. 581–596, 2004.
- [8] A. Richter, J. P. Burrows, H. Nüß, C. Granier, and U. Niemeier, "Increase in tropospheric nitrogen dioxide over China observed from space," *Nature*, vol. 437, no. 7055, pp. 129–132, 2005.
- [9] Y. Kanaya, H. Tanimoto, J. Matsumoto et al., "Diurnal variations in H₂O₂, O₃, PAN, HNO₃ and aldehyde concentrations and NO/NO₂ ratios at Rishiri Island, Japan: potential influence from iodine chemistry," *Science of the Total Environment*, vol. 376, no. 1–3, pp. 185–197, 2007.
- [10] A. K. Azad and T. Kitada, "Characteristics of the air pollution in the city of Dhaka, Bangladesh in winter," *Atmospheric Environment*, vol. 32, no. 11, pp. 1991–2005, 1998.
- [11] M. K. Ghose, R. Paul, and S. K. Banerjee, "Assessment of the impacts of vehicular emissions on urban air quality and its management in Indian context: the case of Kolkata (Calcutta)," *Environmental Science and Policy*, vol. 7, no. 4, pp. 345–351, 2004.
- [12] K. V. S. Badarinath, T. R. Kiran Chand, and V. Krishna Prasad, "Agriculture crop residue burning in the Indo-Gangetic Plains—a study using IRS-P6 AWiFS satellite data," *Current Science*, vol. 91, no. 8, pp. 1085–1089, 2006.
- [13] K. V. S. Badarinath, S. K. Kharol, A. R. Sharma, and V. K. Prasad, "Analysis of aerosol and carbon monoxide characteristics over Arabian Sea during crop residue burning period in the Indo-Gangetic Plains using multi-satellite remote sensing datasets," *Journal of Atmospheric and Solar-Terrestrial Physics*, vol. 71, no. 12, pp. 1267–1276, 2009.
- [14] B. R. Gurjar, T. M. Butler, M. G. Lawrence, and J. Lelieveld, "Evaluation of emissions and air quality in megacities," *Atmospheric Environment*, vol. 42, no. 7, pp. 1593–1606, 2008.
- [15] S. D. Ghude, S. Fadnavis, G. Beig, S. D. Polade, and R. J. van der A, "Detection of surface emission hot spots, trends, and seasonal cycle from satellite-retrieved NO₂ over India," *Journal of Geophysical Research: Atmospheres*, vol. 113, no. 20, 2008.
- [16] S. D. Ghude, R. J. Van der A, G. Beig, S. Fadnavis, and S. D. Polade, "Satellite derived trends in NO₂ over the major global hotspot regions during the past decade and their inter-comparison," *Environmental Pollution*, vol. 157, no. 6, pp. 1873–1878, 2009.
- [17] L. M. David and P. R. Nair, "Tropospheric column O₃ and NO₂ over the Indian region observed by Ozone Monitoring Instrument (OMI): seasonal changes and long-term trends," *Atmospheric Environment*, vol. 65, pp. 25–39, 2013.
- [18] A. Ramachandran, N. K. Jain, S. A. Sharma, and J. Pallipad, "Recent trends in tropospheric NO₂ over India observed by SCIAMACHY: identification of hot spots," *Atmospheric Pollution Research*, vol. 4, no. 4, pp. 354–361, 2013.
- [19] K. Renuka, H. Gadhavi, A. Jayaraman, S. Lal, M. Naja, and S. V. B. Rao, "Study of ozone and NO₂ over Gadanki—a rural site in South India," *Journal of Atmospheric Chemistry*, vol. 71, no. 2, pp. 95–112, 2014.
- [20] Z. Ul-Haq, S. Tariq, M. Ali, K. Mahmood, S. A. Batool, and A. D. Rana, "A study of tropospheric NO₂ variability over Pakistan using OMI data," *Atmospheric Pollution Research*, vol. 5, no. 4, pp. 709–720, 2014.
- [21] J. P. Burrows, E. Hölzle, A. P. H. Goede, H. Visser, and W. Fricke, "SCIAMACHY—scanning imaging absorption spectrometer for atmospheric cartography," *Acta Astronautica*, vol. 35, no. 7, pp. 445–451, 1995.

- [22] H. Bovensmann, J. P. Burrows, M. Buchwitz et al., "SCIAMACHY: mission objectives and measurement modes," *Journal of the Atmospheric Sciences*, vol. 56, no. 2, pp. 127–150, 1999.
- [23] R. M. Joshi, "Education in South Asia," in *International Encyclopedia of the Social & Behavioral Sciences*, pp. 194–197, 2nd edition, 2015.
- [24] UNEP, *United Nations Environment Programme and Development Alternatives (2008), South Asia Environment Outlook 2009: UNEP, SAARC and DA*, United Nations Environment Programme (UNEP), 2008.
- [25] J. E. Schwartzberg, *A Historical Atlas of South Asia*, Oxford University Press, Oxford, UK, 1992.
- [26] S. Bose and J. Ayesha, *Modern South Asia: History, Culture, and Political Economy*, Oxford University Press, Delhi, India, 2002.
- [27] J. S. Bandara and Y. Cai, "The impact of climate change on food crop productivity, food prices and food security in South Asia," *Economic Analysis and Policy*, vol. 44, no. 4, pp. 451–465, 2014.
- [28] R. Zhang, D. Jiang, Z. Zhang, and E. Yu, "The impact of regional uplift of the tibetan plateau on the asian monsoon climate," *Palaeogeography, Palaeoclimatology, Palaeoecology*, vol. 417, no. 1, pp. 137–150, 2015.
- [29] P. F. Levelt, G. H. J. van den Oord, M. R. Dobber et al., "The ozone monitoring instrument," *IEEE Transactions on Geoscience and Remote Sensing*, vol. 44, no. 5, pp. 1093–1100, 2006.
- [30] P. F. Levelt, E. Hilsenrath, G. W. Leppelmeier et al., "Science objectives of the ozone monitoring instrument," *IEEE Transactions on Geoscience and Remote Sensing*, vol. 44, no. 5, pp. 1199–1208, 2006.
- [31] I. Zyrichidou, M. E. Koukouli, D. S. Balis et al., "Evaluation of high resolution simulated and OMI retrieved tropospheric NO₂ column densities over Southeastern Europe," *Atmospheric Research*, vol. 122, pp. 55–66, 2013.
- [32] H. J. Eskes and K. F. Boersma, "Averaging kernels for DOAS total-column satellite retrievals," *Atmospheric Chemistry and Physics*, vol. 3, no. 5, pp. 1285–1291, 2003.
- [33] J. Wallace and P. Kanaroglou, "The sensitivity of OMI-derived nitrogen dioxide to boundary layer temperature inversions," *Atmospheric Environment*, vol. 43, no. 22-23, pp. 3596–3604, 2009.
- [34] K. F. Boersma, D. J. Jacob, M. Trainic et al., "Validation of urban NO₂ concentrations and their diurnal and seasonal variations observed from the SCIAMACHY and OMI sensors using in situ surface measurements in Israeli cities," *Atmospheric Chemistry and Physics*, vol. 9, no. 12, pp. 3867–3879, 2009.
- [35] M. Hayn, S. Beirle, F. A. Hamprecht, U. Platt, B. H. Menze, and T. Wagner, "Analysing spatio-temporal patterns of the global NO₂-distribution retrieved from GOME satellite observations using a generalized additive model," *Atmospheric Chemistry and Physics*, vol. 9, no. 17, pp. 6459–6477, 2009.
- [36] L. N. Lamsal, R. V. Martin, A. van Donkelaar et al., "Indirect validation of tropospheric nitrogen dioxide retrieved from the OMI satellite instrument: insight into the seasonal variation of nitrogen oxides at northern midlatitudes," *Journal of Geophysical Research: Atmospheres*, vol. 115, no. 5, Article ID D05302, 2010.
- [37] V. Sheel, S. Lal, A. Richter, and J. P. Burrows, "Comparison of satellite observed tropospheric NO₂ over India with model simulations," *Atmospheric Environment*, vol. 44, no. 27, pp. 3314–3321, 2010.
- [38] I. Kloog, F. Nordio, B. A. Coull, and J. Schwartz, "Incorporating local land use regression and satellite aerosol optical depth in a hybrid model of spatiotemporal PM_{2.5} exposures in the mid-atlantic states," *Environmental Science & Technology*, vol. 46, no. 21, pp. 11913–11921, 2012.
- [39] G. Prud'homme, N. A. Dobbin, L. Sun et al., "Comparison of remote sensing and fixed-site monitoring approaches for examining air pollution and health in a national study population," *Atmospheric Environment*, vol. 80, pp. 161–171, 2013.
- [40] A. Oluleye and E. C. Okogbue, "Analysis of temporal and spatial variability of total column ozone over West Africa using daily TOMS measurements," *Atmospheric Pollution Research*, vol. 4, no. 4, pp. 387–397, 2013.
- [41] K. F. Boersma, D. J. Jacob, E. J. Bucsela et al., "Validation of OMI tropospheric NO₂ observations during INTEX-B and application to constrain NO_x emissions over the eastern United States and Mexico," *Atmospheric Environment*, vol. 42, no. 19, pp. 4480–4497, 2008.
- [42] E. A. Celarier, E. J. Brinksma, J. F. Gleason et al., "Validation of ozone monitoring instrument nitrogen dioxide columns," *Journal of Geophysical Research: Atmospheres*, vol. 113, no. 15, Article ID D15S15, 2008.
- [43] FAO, *New LocClim: Local Climate Estimator*, Environment and Natural Resources Working Paper No. 20, 2005, http://www.fao.org/nr/climpag/pub/en3_051002.en.asp.
- [44] R. Gommès, F. L. Snijders, and J. Q. Rijk, *FAO Crop Forecasting Philosophy in National Food Warning Systems*, FAO, Rome, Italy, 1998.
- [45] M. Bernardi and F. L. Snijders, "ARTEMIS software used by FAO for remotely sensed data," in *Proceedings of the World Meteorological Organization Expert Group Meeting on Software for Agroclimatic Data Management*, Washington, DC, USA, October 2000.
- [46] A. Getis and J. K. Ord, "The analysis of spatial association by use of distance statistics," *Geographical Analysis*, vol. 24, no. 3, pp. 189–206, 1992.
- [47] J. K. Ord and A. Getis, "Local spatial autocorrelation statistics: distributional issues and an application," *Geographical Analysis*, vol. 27, no. 4, pp. 286–306, 1995.
- [48] T. Zhang, "Limiting distribution of the G statistics," *Statistics and Probability Letters*, vol. 78, no. 12, pp. 1656–1661, 2008.
- [49] Esri, *ArcGIS Resources*, 2015, <http://resources.arcgis.com/>.
- [50] A. Mitchell, *The Esri Guide to GIS Analysis*, vol. 2, ESRI Press, 2005.
- [51] M. Ali, S. Tariq, K. Mahmood, A. Daud, A. Batool, and Zia-ul-Haq, "A study of aerosol properties over Lahore (Pakistan) by using AERONET data," *Asia-Pacific Journal of Atmospheric Sciences*, vol. 50, no. 2, pp. 153–162, 2014.
- [52] Z. Ul-Haq, S. Tariq, A. D. Rana, M. Ali, K. Mahmood, and P. Shahid, "Satellite remote sensing of total ozone column (TOC) over Pakistan and neighbouring regions," *International Journal of Remote Sensing*, vol. 36, no. 4, 2015.
- [53] Z. ul-Haq, A. D. Rana, M. Ali, K. Mahmood, S. Tariq, and Z. Qayyum, "Carbon monoxide (CO) emissions and its tropospheric variability over Pakistan using satellite-sensed data," *Advances in Space Research*, 2015.
- [54] S. Tariq and M. Ali, "Spatio-temporal distribution of absorbing aerosols over Pakistan retrieved from OMI onboard aura satellite," *Atmospheric Pollution Research*, vol. 6, no. 2, pp. 254–266, 2015.

- [55] Sustainable Development Policy Institute (SDPI), *Quarterly Pakistan Forest Digest, Vol. 01, No. 01*, Sustainable Development Policy Institute (SDPI), 2010.
- [56] Pakistan Strategic Country Environmental Assessment, The World Bank, 2006, <http://www.environment.gov.pk/new-pdf/PK-SCE-FText-Oct-2006%20.pdf>.
- [57] A. Tanvir and A. Bashir, "Why do farmers burn rice residue? Examining farmers' choices in Punjab, Pakistan. South Asian Network for Development and Environmental Economics (SANDEE)," Working Paper 76-13, 2013.
- [58] RTYB, *Road Transport Year Book (2011-12)*, Transport Research Wing, Ministry of Road Transport & Highways, Government of India, New Delhi, India, 2013.
- [59] N. Jain, A. Bhatia, and H. Pathak, "Emission of air pollutants from crop residue burning in India," *Aerosol and Air Quality Research*, vol. 14, no. 1, pp. 422–430, 2014.
- [60] MoE, *State of the Environment*, Ministry of Environment, Government of India, New Delhi, India, 2010, <http://envfor.nic.in/soer/list.html>.
- [61] MoEP (Ministry of Economy and Planning), *Afghanistan Statistical Yearbook 2005*, 2005.
- [62] Malé Declaration, Baseline Information and Action Plan, United Nations Environment Programme Regional Resource Centre for Asia and Pacific, 2000, <http://www.rrcap.ait.asia/issues/air/maledec/baseline/indexsri.html>.
- [63] UNDP, United Nations Development Programme in Bhutan, 2015, http://www.bt.undp.org/content/bhutan/en/home/library/environment_energy/.
- [64] C. Leue, M. Wenig, T. Wagner, O. Klimm, U. Platt, and B. Jähne, "Quantitative analysis of NO_x emissions from Global Ozone Monitoring Experiment satellite image sequences," *Journal of Geophysical Research: Atmospheres*, vol. 106, no. 6, pp. 5493–5505, 2001.
- [65] D. Schaub, A. K. Weiss, J. W. Kaiser et al., "A transboundary transport episode of nitrogen dioxide as observed from GOME and its impact in the Alpine region," *Atmospheric Chemistry and Physics*, vol. 5, no. 1, pp. 23–37, 2005.
- [66] L. Jaeglé, D. J. Jacob, Y. Wang et al., "Sources and chemistry of NO_x in the upper troposphere over the United States," *Geophysical Research Letters*, vol. 25, no. 10, pp. 1705–1708, 1998.
- [67] J. H. Seinfeld and S. N. Pandis, *Atmospheric Chemistry and Physics—From Air Pollution to Climate Change*, John Wiley & Sons, New York, NY, USA, 1998.
- [68] P. S. Arya, *Air Pollution Meteorology and Dispersion*, Oxford University Press, New York, NY, USA, 1999.
- [69] A. M. Jones, R. M. Harrison, and J. Baker, "The wind speed dependence of the concentrations of airborne particulate matter and NO_x," *Atmospheric Environment*, vol. 44, no. 13, pp. 1682–1690, 2010.
- [70] S. Korontzi, J. McCarty, T. Loboda, S. Kumar, and C. Justice, "Global distribution of agricultural fires in croplands from 3 years of Moderate Resolution Imaging Spectroradiometer (MODIS) data," *Global Biogeochemical Cycles*, vol. 20, no. 2, 2006.
- [71] A. K. Mishra and T. Shibata, "Synergistic analyses of optical and microphysical properties of agricultural crop residue burning aerosols over the Indo-Gangetic Basin (IGB)," *Atmospheric Environment*, vol. 57, pp. 205–218, 2012.
- [72] H. S. Gadhavi, K. Renuka, V. Ravi Kiran et al., "Evaluation of black carbon emission inventories using a Lagrangian dispersion model—a case study over southern India," *Atmospheric Chemistry and Physics*, vol. 15, no. 3, pp. 1447–1461, 2015.
- [73] C. Sarkar, V. Kumar, and V. Sinha, "Massive emissions of carcinogenic benzenoids from paddy residue burning in north India," *Current Science*, vol. 104, no. 12, pp. 1703–1709, 2013.
- [74] I. H. Uno, Y. He, T. Ohara et al., "Systematic analysis of interannual and seasonal variations of model-simulated tropospheric NO₂ in Asia and comparison with GOME-satellite data," *Atmospheric Chemistry and Physics*, vol. 7, no. 6, pp. 1671–1681, 2007.
- [75] T. Nishanth and K. M. K. Satheesh, "Increasing trends of tropospheric ozone and NO₂ at the prominent hot spots along the coastal belt of the Arabian Sea in Indian Subcontinent," *International Journal of Environmental Sciences*, vol. 1, no. 5, pp. 860–870, 2011.
- [76] I. Barnes and K. J. Rudziński, Eds., *Disposal of Dangerous Chemicals in Urban Areas and Mega Cities: Role of Oxides and Acids of Nitrogen in Atmospheric Chemistry*, NATO Science for Peace and Security Series C: Environmental Security, Springer, Amsterdam, The Netherlands, 2013.
- [77] K. Ravindra, S. Mor, A. Ameena, J. S. Kamyotra, and C. P. Kaushik, "Variation in spatial pattern of criteria air pollutants before and during initial rain of monsoon," *Environmental Monitoring and Assessment*, vol. 87, no. 2, pp. 145–153, 2003.
- [78] J.-M. Yoo, Y.-R. Lee, D. Kim et al., "New indices for wet scavenging of air pollutants (O₃, CO, NO₂, SO₂, and PM₁₀) by summertime rain," *Atmospheric Environment*, vol. 82, pp. 226–237, 2014.
- [79] S. Zumdahl and S. Zumdahl, *Chemistry*, Cengage Learning, 7th edition, 2006.
- [80] A. Martin, "Estimated washout coefficients for sulphur dioxide, nitric oxide, nitrogen dioxide and ozone," *Atmospheric Environment*, vol. 18, no. 9, pp. 1955–1961, 1984.
- [81] M. Q. Huo, Q. Sun, Y. H. Bai et al., "Chemical character of precipitation and related particles and trace gases in the North and South of China," *Journal of Atmospheric Chemistry*, vol. 67, no. 1, pp. 29–43, 2010.
- [82] S. Tariq, Z. Ul-Haq, and M. Ali, "Analysis of optical and physical properties of aerosols during crop residue burning event of October 2010 over Lahore, Pakistan," *Atmospheric Pollution Research*. In press.
- [83] D. G. Kaskaoutis, S. Kumar, D. Sharma et al., "Effects of crop residue burning on aerosol properties, plume characteristics, and long-range transport over northern India," *Journal of Geophysical Research: Atmospheres*, vol. 119, no. 9, pp. 5424–5444, 2014.
- [84] K. G. Mandal, A. K. Misra, K. M. Hati, K. K. Bandyopadhyay, P. K. Ghosh, and M. Mohanty, "Rice residue-management options and effects on soil properties and crop productivity," *Journal of Food, Agriculture and Environment*, vol. 2, pp. 224–231, 2004.
- [85] A. Garg, P. R. Shukla, S. Bhattacharya, and V. K. Dadhwal, "Sub-region (district) and sector level SO₂ and NO_x emissions for India: assessment of inventories and mitigation flexibility," *Atmospheric Environment*, vol. 35, no. 4, pp. 703–713, 2001.
- [86] T. Kunhikrishnan, M. G. Lawrence, R. von Kuhlmann et al., "Regional NO_x emission strength for the Indian subcontinent and the impact of emissions from India and neighboring countries on regional O₃ chemistry," *Journal of Geophysical Research: Atmospheres*, vol. 111, no. 15, Article ID D15301, 2006.
- [87] CMF, 2014. City Mayors Foundation, http://www.citymayors.com/statistics/urban_growth1.html.
- [88] B. A. Begum, E. Kim, S. K. Biswas, and P. K. Hopke, "Investigation of sources of atmospheric aerosol at urban and semi-urban

- areas in Bangladesh,” *Atmospheric Environment*, vol. 38, no. 19, pp. 3025–3038, 2004.
- [89] B. A. Begum, S. K. Biswas, and P. K. Hopke, “Assessment of trends and present ambient concentrations of $PM_{2.2}$ and PM_{10} in Dhaka, Bangladesh,” *Air Quality, Atmosphere & Health*, vol. 1, no. 3, pp. 125–133, 2008.
- [90] B. Sivertsen, S. Randall, S. Ahammad, and N. D. Cruz, *Modelled Concentrations of Criteria Air Pollutants in Dhaka and Chittagong PM_{10} , $PM_{2.5}$, NO_x , and SO_x for 2013 and 2020*, Norwegian Institute for Air Research (NILU), 2015.
- [91] Z. Lu and D. G. Streets, “Increase in NO_x emissions from Indian thermal power plants during 1996–2010: Unit-based inventories and multisatellite observations,” *Environmental Science & Technology*, vol. 46, no. 14, pp. 7463–7470, 2012.
- [92] S. K. Sahu, G. Beig, and N. S. Parkhi, “Emerging pattern of anthropogenic NO_x emission over Indian subcontinent during 1990s and 2000s,” *Atmospheric Pollution Research*, vol. 3, no. 3, pp. 262–269, 2012.

Research Article

Analysis of Long-Range Transport of Carbon Dioxide and Its High Concentration Events over East Asian Region Using GOSAT Data and GEOS-Chem Modeling

Seung-Yeon Kim,¹ Sang-Deok Lee,¹ Jae-Bum Lee,¹ Deok-Rae Kim,¹
Jin-Seok Han,¹ Kwang-Ho Choi,² and Chang-Keun Song¹

¹Climate and Air Quality Research Department, National Institute of Environmental Research, Incheon 404-708, Republic of Korea

²Department of General Education, Namseoul University, Cheonan 331-707, Republic of Korea

Correspondence should be addressed to Chang-Keun Song; cksong@korea.kr

Received 30 January 2015; Revised 19 May 2015; Accepted 8 June 2015

Academic Editor: Ugo Cortesi

Copyright © 2015 Seung-Yeon Kim et al. This is an open access article distributed under the Creative Commons Attribution License, which permits unrestricted use, distribution, and reproduction in any medium, provided the original work is properly cited.

This study aims to evaluate the long-range transport of CO₂ in East Asian region, using concentration data in a surface measurement site (Gosan Station), column averaged concentration data of satellite-borne instrument (GOSAT), and GEOS-Chem modeling results for the period of June 2009 to May 2011. We perform a validation of the data from GOSAT and GEOS-Chem with total column observations (TCCON). The analysis of the long-range transport and high concentration (HC) events using surface/satellite observations and modeling results is conducted. During the HC events, the concentrations in CO₂ and other air pollutants such as SO₂ and CO are higher than that of all episodes. It means that CO₂, known as a globally well-mixed gas, may also act as a fingerprint of human activity with unique regional characteristics like other air pollutants. This comprehensive analysis, in particular with GOSAT CO₂ observation data, shows that CO₂ plume with high concentration can be long-range transported with 1-2 days' duration with regional scale. We can find out with GEOS-Chem tagging simulation that more than 45% of the elevated CO₂ concentration over central/eastern China, Korea, and Japan on high concentration days can be explained by emission sources of East Asia mainland.

1. Introduction

Since the industrial revolution, the current level of CO₂ emitted into the atmosphere has increased by nearly 41% because of fossil fuel combustion. This contributes to a higher global warming potential (approximately 82%) as compared to other greenhouse gases, such as CH₄ and N₂O [1]. In general, the global CO₂ concentration is 2.0–2.5 ppmv higher in the northern hemisphere than in the southern hemisphere because of the greater dependence on fossil fuel combustion [2]. In particular, among the countries in the northern hemisphere, the ground-based CO₂ concentration in Asia for year 2007 is relatively high (387.6 ppmv), as compared to Europe (386.3 ppmv) and North America (385.1 ppmv) because of the rapid industrialization [3]. According to the International Energy Agency report [4], the 2007 CO₂ emissions by regions

in Asia, such as China, India, Korea, and Iran, have increased by over 100%, compared to the 1990 level.

The atmospheric CO₂ concentration is determined by the average concentration and its short-term variation mainly due to the long-range transport and meteorological conditions [5]. It is reported that an increase in CO₂ concentration in the Arctic region is affected by the impact of long-range transport of CO₂ emissions from the midlatitude northern hemisphere [6–12]. In case of Asian regions, some studies [3, 13, 14] showed that long-range transport of CO₂ from the Asian continent contributed to the variations of CO₂ concentration in Japan and Korea, using surface measurement data. In addition, using airborne and model data, Shirai et al. [15] mentioned that the CO₂ concentration in the free troposphere was significantly affected by the long-range transport of CO₂.

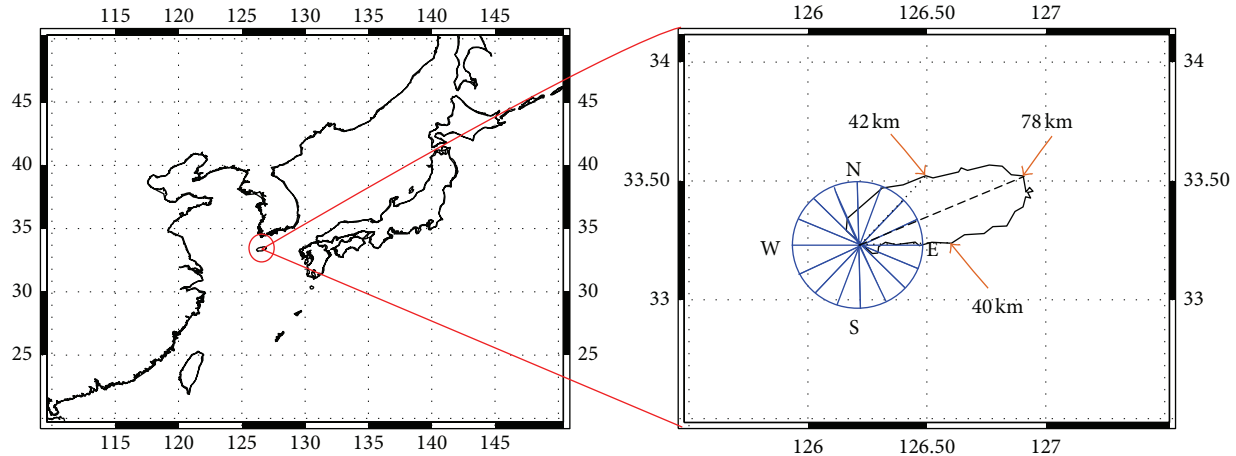


FIGURE 1: The location of Gosan site, Jeju Island in Korea.

In order to investigate the impact of global/regional carbon cycle on the regional change of CO_2 concentration and air quality [16], it is important to understand the comprehensive feature of long-range transport events utilizing the observation data on the surface level and vertically integrated column data and modeling results, simultaneously. However, the above-mentioned studies were carried out with temporally and spatially limited measurement data. For example, ground-based observations have much higher accuracy rather than the modeling approach and the satellite data, while their spatial resolution is very coarse. As for the modeling approach, there are no restrictions on spatial and temporal coverage, while it has lower confidence rather than observation data due to uncertainties in emission inventory, meteorological fields, and its initial and boundary conditions. On the other hand, the satellite data have less restriction on its spatial and temporal resolution rather than surface observations, and those are more reliable than modeling results; however, satellite data has still observational errors which are due to radiometric/geometric/atmospheric correction, surface reflection and cloud masking, and the smearing effect in high peak concentrations due to much less spatial resolution compared to that of modeling approach. Therefore, it is necessary to integrate the ground-based observations, the satellite data, and the modeling results in order to compensate possible drawbacks of the measurement and the modeling and utilize their advantages.

Although CO_2 is a globally well-mixed gas in a climatological sense, it has also the unique regional characteristics over the source and downwind area because of the same anthropogenic emission sources driven by human socioeconomic activity like other air pollutants (e.g., CO , SO_2 , and aerosols), and few studies for long-range transport of CO_2 and its high concentration events have been conducted at East Asia where it is one of the most hot spots of CO_2 emission in the world.

In this study, we investigate CO_2 long-range transport phenomena and high concentration events on the downwind regions of the Asian continent and provide observational evidences showing regionally the same behavior of CO_2 as

other air pollutants over East Asia, using all the available data, CO_2 and other air pollutants concentration data observed at surface monitoring sites, satellite data, and results of a chemical transport model.

2. Data and Methodology

This study focused on the CO_2 concentration data available for the period of June 2009 to May 2011, which was observed by the Greenhouse gases Observing SATellite (GOSAT) and surface monitoring stations. Surface observation data were collected from the Gosan site in Korea (<http://ds.data.jma.go.jp/gmd/wdcgg/cgi-bin/wdcgg/accessdata.cgi?index=GSN233N01-GERC>), which is located on the eastern side of the Asian continent. Satellite data, column-averaged CO_2 concentrations, were utilized along with GOSAT dataset L2 V02.xx (http://www.gosat.nies.go.jp/index_e.html). The Goddard Earth Observing System with Chemistry Model (GEOS-Chem, v9.1.2), a global chemical air quality transport model, was used for simulating high concentration events and their source/sink apportionment. In addition, we also evaluated satellite data and modeling results with CO_2 concentration data from the World Data Centre for Greenhouse Gases (WDCGG; <http://ds.data.jma.go.jp/gmd/wdcgg/>) and column-averaged concentration data from the Total Column Observing Network (TCCON; <http://www.tccon.caltech.edu/>). Also, the Hybrid Single Particle Lagrangian Integrated Trajectory Model (HYSPLIT) [17] was used for a trajectory analysis.

2.1. Ground-Based Observation Data. Hourly averaged CO_2 concentration and other air pollutants (SO_2 , NO_2 , CO , O_3 , PM_{10} , and $\text{PM}_{2.5}$) concentration data have been measured at Gosan Station in Korea. Gosan Station is located at the west end of Jeju Island, Korea ($33^\circ 17' \text{N}$, $126^\circ 10' \text{E}$) (Figure 1), in the middle among the Korean Peninsula, China, and Japan, so that it is well suited for the research on long-range transport of greenhouse gases and other air pollutants in East Asia. In this area, PEM-WEST A and B, ACE-Asia, and ABC's

International Joint Observational Campaign had been conducted [18–21].

The CO₂ sampling from a 10 m tower is automatically analyzed every 30 seconds, through a Nondispersive Infrared Analyzer (NDIR). All CO₂ data are reported using the WMO CO₂ mole fraction scale. We perform a statistical analysis after QA/QC (Quality Assurance/Quality Control) processes to determine whether it is a clean or a polluted atmosphere [22]. We followed Advanced Global Atmospheric Gases Experiment (AGAGE) statistical pollution identification procedure by O'Doherty et al. [22] to select clean atmosphere cases from Gosan observation data by removing polluted cases affected by local and regional sources. A polluted atmosphere is then divided as either a local atmosphere or a regional atmosphere by using the criterion according to wind direction and speed shown in Figure 1. For excluding data in a local atmosphere, the data in which wind direction is 22.5°–112.5° and the wind speed is less than 11 m/s were discarded [23]. The local atmosphere refers to areas affected by the urban scale emission sources, while the regional atmosphere reflects the effect of the East Asian regions, in which the effect of a local atmosphere could be minimized. In this study, CO₂ concentration data collected only in clean atmosphere and regional atmosphere were used to assess the effect of long-range transport.

Also, in order to make direct comparison of GOSAT data and GEOS-Chem model results with surface measurement data, we used TCCON's column-averaged concentration. TCCON is a network of ground-based Fourier transform spectrometers that measure column-averaged concentrations of CO₂, CO, CH₄, and H₂O in the atmosphere. For this study, the TCCON data were selected at each site, within about ±1 hour of the GOSAT overpass time. Also, the GOSAT and GEOS-Chem data were selected within about ±1 degree of the area centered at each TCCON site.

2.2. Satellite Data. GOSAT is a sun-synchronous satellite, which provides a global coverage in three days and crosses the equator at about 13:00 local time. Its swath width is 790 km and its spatial resolution at nadir is 10.5 km. GOSAT's wavelength ranges between 0.76 and 14.3 μm, consisting of two sensors—one is the Thermal and Near-Infrared Sensor for Carbon Observation-Fourier Transform Spectrometer (TANSO-FTS), which measures CO₂ and CH₄, and the second is the Thermal and Near-Infrared Sensor for Carbon Observation-Cloud and Aerosol Imager (TANSO-CAI), which measures clouds and aerosols. TANSO-FTS is composed of four bands. Bands 1 to 3 are Shortwave Infrared (SWIR) bands, which provide the total column amount of CO₂ and CH₄, and Band 4 is a Thermal Infrared (TIR) band, which produces a profile of CO₂ and CH₄ concentration at 1000, 700, 500, 300, 100, 50, and 10 hPa [24]. It is well known that the SWIR absorption bands near 1.6 μm and 2.0 μm provide better information on the near-surface concentrations. On the other hand, the TIR absorption band around 14 μm is used to obtain information on the profiles of CO₂ and CH₄, mainly above 2 km altitudes, so TIR data are sensitive to the middle and upper troposphere [25, 26]. With this reason, we use SWIR XCO₂ data, column-averaged concentrations,

in order to compare directly to the surface observation data of CO₂ in this study.

2.3. Modeling Data. We have used version 9-02-01 of GEOS-Chem, a global 3D atmospheric chemistry transport model developed by the National Aeronautics and Space Administration (NASA) and Harvard University. It is driven by assimilated meteorology from the NASA Global Modeling Assimilation Office (GMAO) and contains approximately 300 photochemical reaction mechanisms of the O₃-NO_x-hydrocarbon chemistry [27]. The original GEOS-Chem CO₂ simulation was developed by Suntharalingam et al. [28]. A current major update including the CO₂ source/sink inventory data has been carried out by Nassar et al. [29].

In this study, we used a globally uniform CO₂ field of 375 ppmv as an initial condition, which was measured on January 1, 2004. This simulation is performed for the target period of June 2009 to May 2011 using the GEOS-5 meteorological field with a horizontal resolution of 2° × 2.5° and 47 vertical levels that reach up to approximately 80 km above the surface of the Earth.

The CO₂ concentration (CO_{2*i*}) and air density (A_{*i*}) at each layer were used in the following equation [30] to calculate the column-averaged CO₂ concentrations (XCO₂) of GEOS-Chem [28] for comparison with CO₂ column-averaged mixing ratio of GOSAT defined as the number of gas molecules in a vertical unit column stretching from the ground surface to the top of the atmosphere [25]:

$$XCO_2 = \frac{\sum_{i=1}^{47} (A_i \times CO_{2i})}{\sum_{i=1}^{47} A_i}. \quad (1)$$

In addition, GEOS-Chem can carry out tagged simulations for CO, O_x, and CO₂ to better identify the contributions from various source regions. These contributions were calculated using tagged tracer for each geographical region and source [31, 32]. We estimated the contributions of each region and source/sink to atmospheric CO₂ concentration in East Asian regions by adding CO₂ tracer of different source produced in various geographical regions.

2.4. Selection of Long-Range Transport and High Concentration Events. It is difficult to show the long-range transport phenomena of CO₂ in the regional scale because its lifetime is very long enough to be well-mixed even globally. Moreover timely continuous CO₂ measurements with spatially wide coverage are very restricted so far. So, to distinguish each high concentration event from measurements of long-term period and to analyze the composite field of them are an easy way to identify the long-range transport phenomena.

As mentioned above, Gosan surface measurement site observed both CO₂ and other air pollutants simultaneously and its geographical location is almost a middle zone of Korean Peninsula, China, and Japan. So, this site is one of the best stations for analyzing the characteristics of a long-range transport that occurred in the East Asia regions. The observed CO₂, SO₂, and CO concentrations of Gosan site for the period of June 2009 to May 2011 were used. SO₂ and CO are well-known tracers of long-range transport, which are

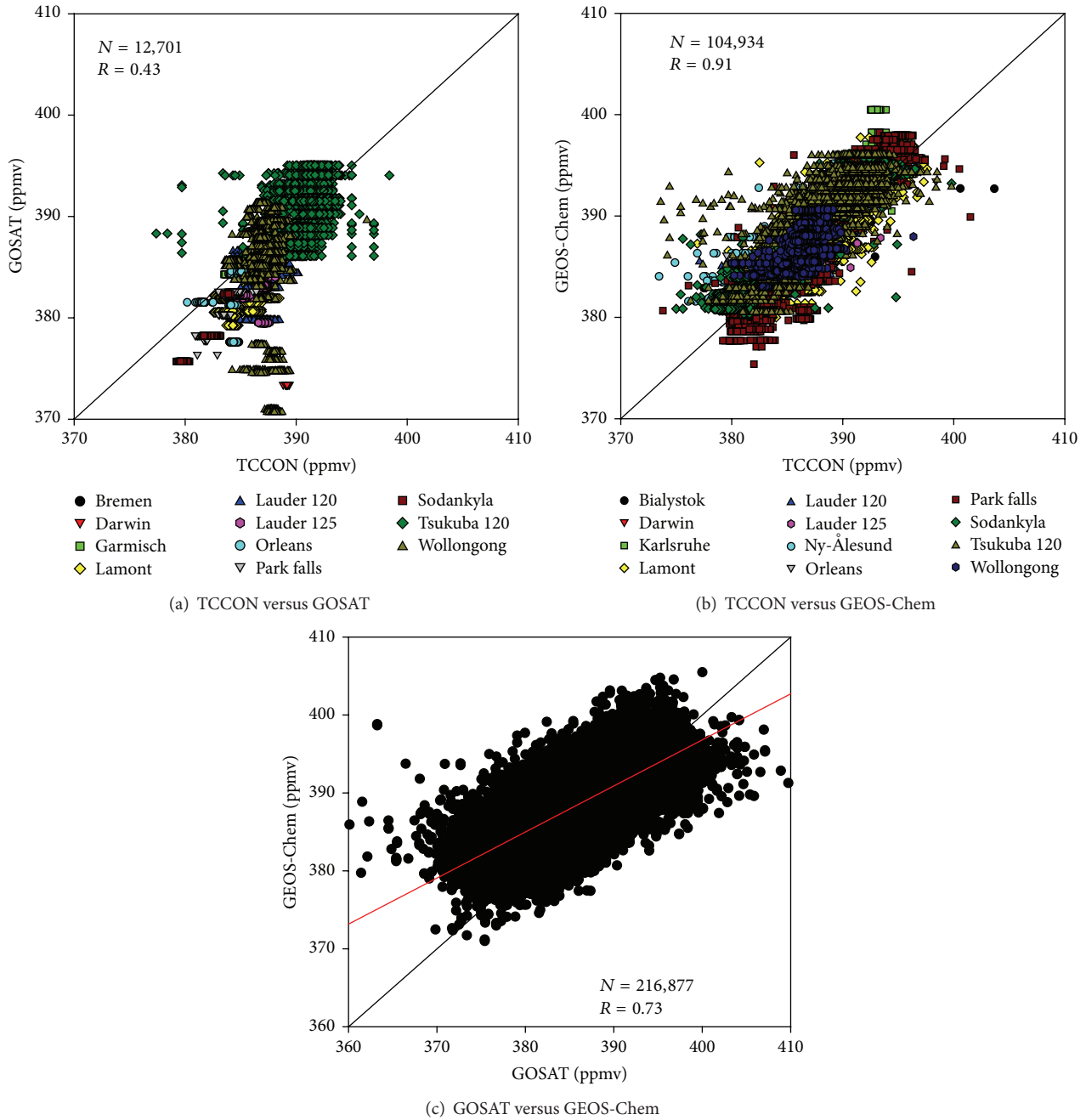


FIGURE 2: Comparison of the column-averaged CO₂ concentration (a) between TCCON and GOSAT, (b) between TCCON and GEOS-Chem, and (c) between GOSAT and GEOS-Chem. N and R indicate number and correlation coefficient of matched data, respectively.

mostly emitted by anthropogenic activities and their lifetime (several weeks to months) is long enough to trace air pollutant plumes at the intercontinental scale [33–38].

In addition, high concentration (HC) events were defined as CO₂ concentration at Gosan Station was higher than the mean + 1σ (σ : standard deviation) and the SO₂ or CO concentration was also higher than the mean + 1σ for at least three consecutive hours. The day before HC and the day after HC will be defined as HC - 1 and HC + 1, respectively.

3. Results

3.1. Evaluation of GOSAT Data and Modeling Results. Compared to TCCON's column-averaged concentration, GOSAT concentrations underestimated nearly by 2.4 ± 5.3 ppmv ($0.6 \pm 1.4\%$), while GEOS-Chem overestimated nearly 0.8 ± 1.5 ppmv ($0.2 \pm 0.4\%$) (Figures 2(a) and 2(b)). Morino et al. [25] also reported that GOSAT V01.xx data underestimated approximately 8.57 ± 4.44 ppmv ($2.2 \pm 1.2\%$) as compared

TABLE 1: Daily averaged surface concentrations of CO₂ and air pollutants on HC, HC - 1, and HC + 1 case and their occurrences.

	CO ₂ (ppmv)	SO ₂ (ppbv)	CO (ppmv)	O ₃ (ppbv)	NO ₂ (ppbv)	PM ₁₀ ($\mu\text{g}/\text{m}^3$)	PM _{2.5} ($\mu\text{g}/\text{m}^3$)	Number of days
All	395.9	2.9	0.7	43.5	3.9	49.1	27.0	606
HC - 1	398.3	2.8	1.0	44.9	3.8	48.4	22.8	25
HC	403.1	5.0	1.2	47.7	5.5	68.1	40.3	67
HC + 1	398.0	2.8	1.0	46.9	3.9	55.2	25.5	25

to TCCON due to multiple errors (e.g., solar irradiance database, handling of aerosol scattering). An improved retrieval algorithm (V02.xx) shows much smaller bias and standard deviation (-1.48 ± 2.9 ppmv) than V01.xx [39]. Fraser et al. [40] indicated that the overestimation of observed concentration under GEOS-Chem was largely due to the high anthropogenic emissions. Figure 2(c) shows a comparison result of the GOSAT and the GEOS-Chem, highlighting that GEOS-Chem generally overestimated approximately 2.6 ± 2.5 ppmv ($0.7 \pm 0.7\%$) with the relatively small spatial/temporal variation, overestimation in low concentration, but underestimation in high concentration.

Figure 3 indicates the comparison between the GOSAT SWIR measurement data and GEOS-Chem modeling results for each season. The number of GOSAT data is not enough to make comparison with the modeling results at the northern hemisphere in DJF and North Pacific in all time, because of issues regarding the elevation angle of the Sun and the effect of cloud [41, 42].

Nevertheless, the GOSAT and GEOS-Chem data showed very similar patterns of the seasonal variation and spatial distributions. The seasonal variation for both data is obvious that CO₂ decreases in summer because of photosynthesis by vegetation while it increases in winter because of the increased usage of fossil fuel and decreased vegetation. The amplitude of the CO₂ seasonal cycle is higher in the northern hemisphere than in the southern hemisphere. Also, the spatial distributions represent that CO₂ concentration is higher in the northern hemisphere than in the southern hemisphere because of the higher population and greater number of industrial activities. In addition, the spatial distribution of CO₂ concentration showed the possibility of a long-range transport of CO₂ because relatively high concentration was detected over an ocean region far from the land source. For spring and winter period of northern hemisphere (MAM and DJF), high concentration plume of CO₂ emitted from the Asian continent was expanded down to North Pacific, and for spring period of southern hemisphere (SON), the CO₂ emitted from South America and Africa has been expanded to the Atlantic and the Indian Ocean.

Through correlation analysis and comparison of spatial distribution among the comprehensive dataset, TCCON, GOSAT, and GEOS-Chem, we find that, at least in East Asian region, GOSAT and GEOS-Chem data are comparable to each other in temporal/spatial distribution with well-known differences with TCCON data, so that it might be reasonable to use those data for this study.

3.2. Analysis of the Long-Range Transport and High Concentration Event of CO₂ Using Surface Measurement. Annual averaged CO₂ concentration observed at Gosan Station in 2010 was 398.3 ppmv, which is 13.1 ppmv higher than the global average CO₂ concentration of 389.0 ppmv [43]. For the past nine years (2002–2010), its growth rate was approximately 2.2 ppmv per year, which is faster than the global average growth rate (1.98 ppmv per year).

Table 1 shows the concentrations of CO₂ and air pollutants for the HC, HC - 1, and HC + 1 days defined in Chapter 2.4. During all of the target period (June 2009 to May 2011; 606 days) of this research, the averaged CO₂ concentration observed at Gosan Station is 395.9 ppmv. The ratio of HC days to all periods is 11.1% (67 days) with the mean CO₂ concentration of 403.1 ppmv, which was 7.2 ppmv higher than that of all periods. Also, the concentration of other air pollutants was higher than that of all periods. In particular, the concentrations of SO₂ (5.0 ppbv) and CO (1.2 ppmv) were more than 1.7 times higher than those for all periods. HC was almost 5 ppmv higher than HC - 1 (398.3 ppmv) and HC + 1 (398.0 ppmv). It is obvious that Gosan Station is more directly affected by a polluted plume transported from China on HC days rather than for a day before/after HC days (HC - 1/HC + 1).

Backward trajectory and forward trajectory analyses (Figure 4) were conducted for ± 3 days on HC case, at a height of 1 km above the ground using the HYSPLIT model which was developed by NOAA to compute air trajectories and dispersion of atmospheric tracers [17]. It clearly demonstrated that the air originating from/out of Asian continent traveled through the polluted areas in China and flowed into the Korean Peninsula. Also, the analysis of the forward trajectory clearly showed that the air that once flowed into the Korean Peninsula moved away to the northwestern Pacific through Japan.

Figure 5 shows the monthly occurrence of HC case at Gosan Station. HC occurred for 48 days in winter (20 days in December, 10 days in January, and 18 days in February), for 11 days in spring (4 days in March, 5 days in April, and 2 days in May), for 7 days in autumn (5 days in October and 2 days in November), and for 1 day in summer (1 day in August). It means that long-range transport occurred mostly in winter because the CO₂ gases emitted from fuel combustion in China were affected by the continental high pressure, thus moving into the downwind regions. In summer, because the high pressure in the North Pacific expanded to the Korean Peninsula, they are mainly affected by the oceanic weather

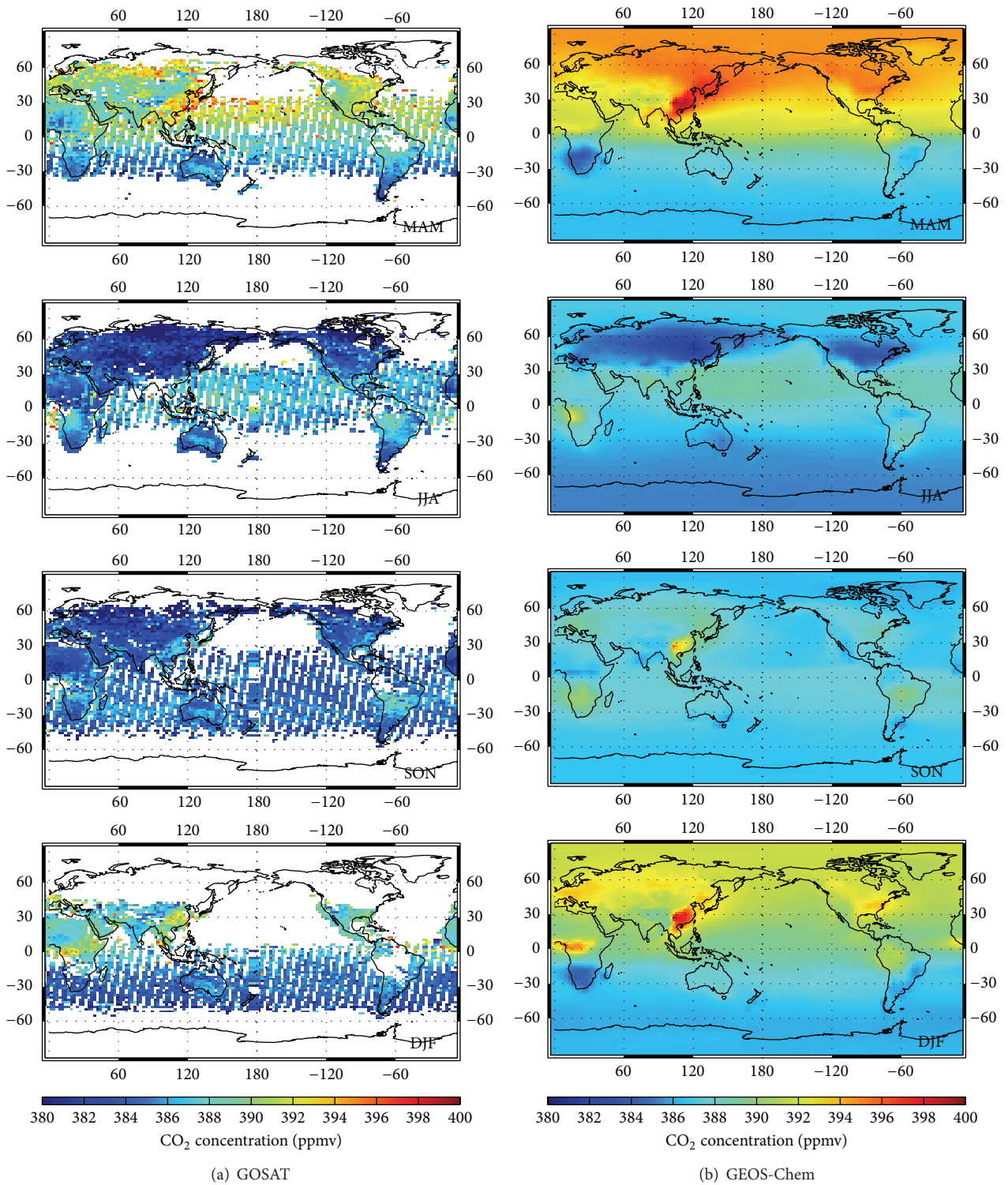


FIGURE 3: Seasonal variation and global distribution of the column-averaged CO₂ concentration (a) measured by GOSAT SWIR and (b) simulated by GEOS-Chem. MAM denotes the period from March to May, JJA from June to August, SON from September to November, and DJF from December to February.

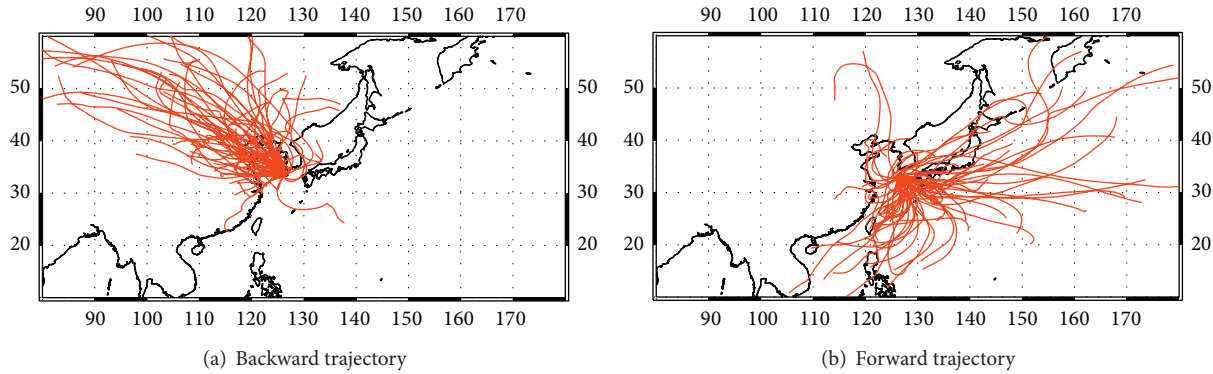


FIGURE 4: (a) Backward trajectories and (b) forward trajectories at 1 km altitude for the cases of high concentration (HC) case.

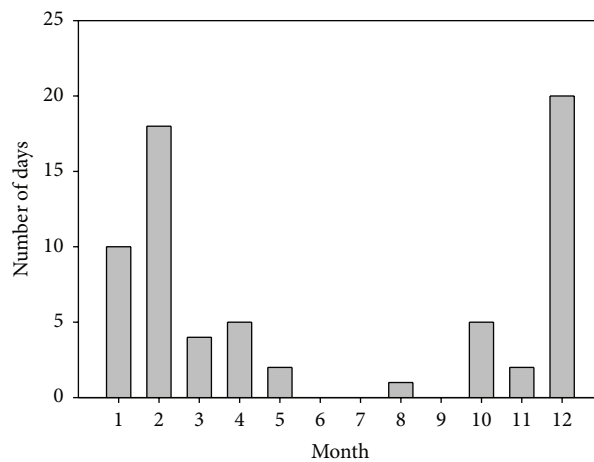


FIGURE 5: Monthly distribution in number of HC days classified from CO₂ concentration data observed at Gosan Station.

pattern, thus reducing the impact caused by the Asian continent.

3.3. Analysis of the Long-Range Transport and High Concentration Event of CO₂ Using GOSAT Data and GEOS-Chem Results. In this section, further analysis on the long-range transport of high concentration CO₂ was conducted using the GOSAT data and the GEOS-Chem modeling results, in order to expand its spatial coverage.

Figure 6 indicates the spatial distribution of the deviation of the column-averaged CO₂ concentrations for HC to those for all the periods observed by GOSAT within the area of Eastern Asia (10–70°N, 80–170°E). The mean column-averaged concentration (389.4 ppmv) for HC days was 3.6 ppmv higher than the one for all of the periods, showing a similar pattern to the result from the surface observation. As compared to the reported retrieval error (2 ppmv) of GOSAT SWIR measurement [25, 41], the increased concentration is 1.8 times higher than the measurement error. It is interesting that high concentrations are also dominating in central and eastern China and Japan when a surface site, the Gosan Station in Korea, experiences high concentration events. This means that CO₂ plume with high concentration is prevailing over those areas through long-range transport

and mixing processes like other air pollutants. It implies that the regional/national action to reduce CO₂ emission and its adverse impact might be taken with the same way/time as that of air pollutant reduction for the sake of socioeconomic cost, that is, cobenefit strategy.

We focused on 3 subregions (Region I, Region II, and Region III) for providing some observational evidence of long-range transport of high concentration CO₂ over downwind area from Asian continent; Region I (30–60°N, 110–120°E) covers the eastern region of China, and Region II (30–60°N, 120–130°E) covers the Yellow Sea and the Korean Peninsula, while Region III (30–60°N, 130–140°E) represents Japan.

Figure 7(a) shows that the concentrations on HC – 1, HC, and HC + 1 were 389.7 ppmv, 390.4 ppmv, and 390.7 ppmv in Region I, respectively. Their amplitude of variation is less than 1 ppmv, thus maintaining a certain level of concentration because Region I is one of the world most populated areas and major emission sources. However, in Region II, concentrations on HC – 1, HC, and HC + 1 were 389.3 ppmv, 391.5 ppmv, and 388.7 ppmv, respectively (Figure 7(b)). In this case, the concentration on HC is 2.2 ppmv higher than that of HC – 1 and then it dramatically decreases on HC + 1. Unlike Regions I and II, the concentration (392.2 ppmv) on HC + 1 in

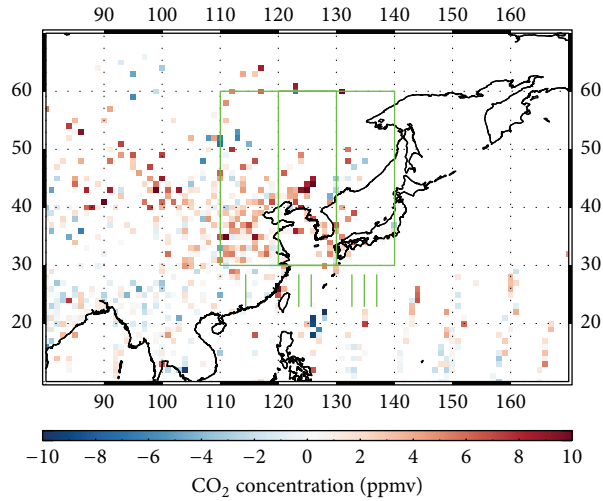


FIGURE 6: Difference in CO_2 concentration between HC and all periods of the East Asian region using GOSAT SWIR. Region I ($30\text{--}60^\circ\text{N}$, $110\text{--}120^\circ\text{E}$) covers the eastern region of China, and Region II ($30\text{--}60^\circ\text{N}$, $120\text{--}130^\circ\text{E}$) covers the Yellow Sea and the Korean Peninsula, while Region III ($30\text{--}60^\circ\text{N}$, $130\text{--}140^\circ\text{E}$) represents Japan.

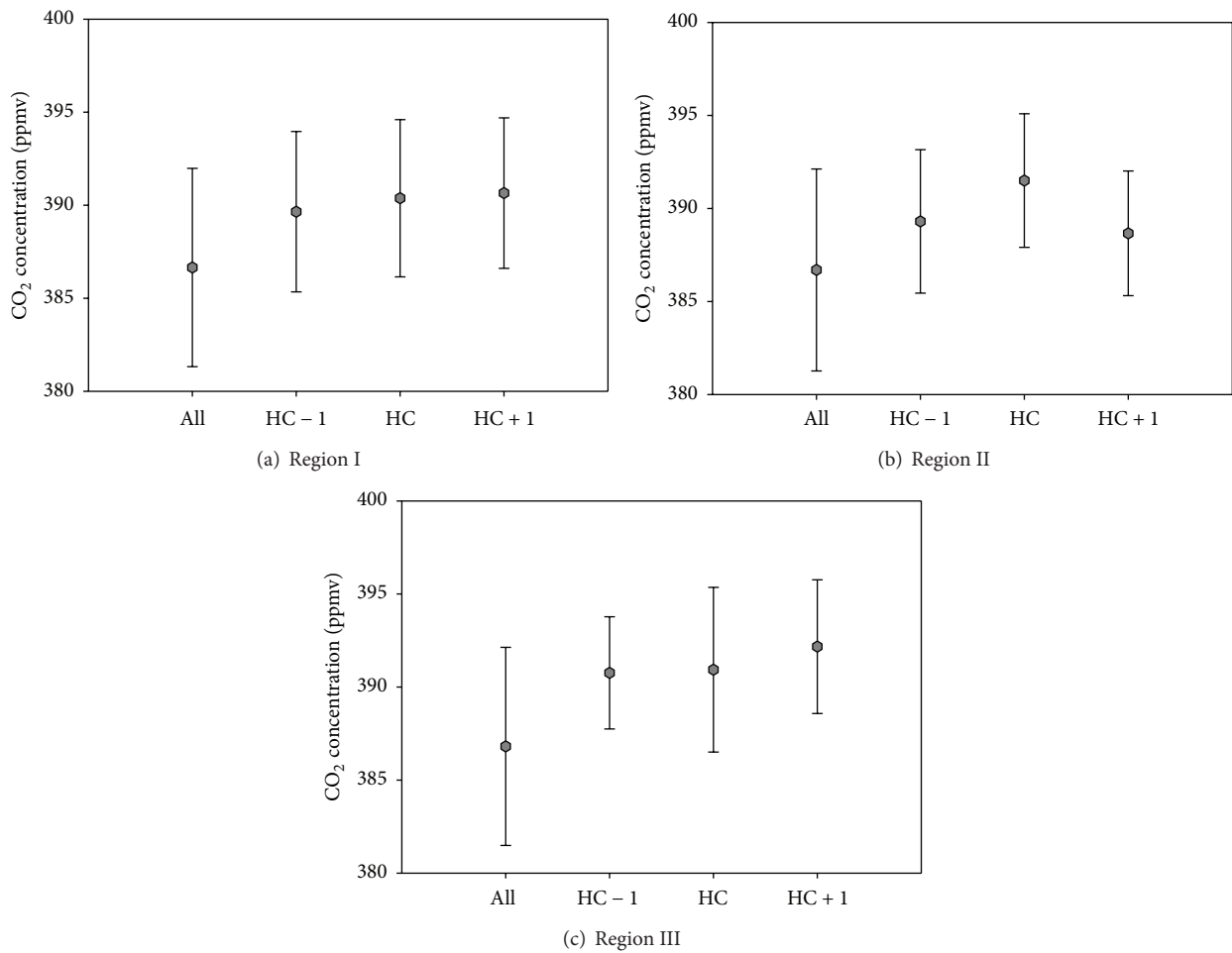


FIGURE 7: Regional mean of the column-averaged CO_2 concentration and its standard deviation on HC - 1, HC, and HC + 1 and for all periods (All) using GOSAT SWIR. (a) Region I ($30\text{--}60^\circ\text{N}$, $110\text{--}120^\circ\text{E}$), (b) Region II ($30\text{--}60^\circ\text{N}$, $120\text{--}130^\circ\text{E}$), and (c) Region III ($30\text{--}60^\circ\text{N}$, $130\text{--}140^\circ\text{E}$).

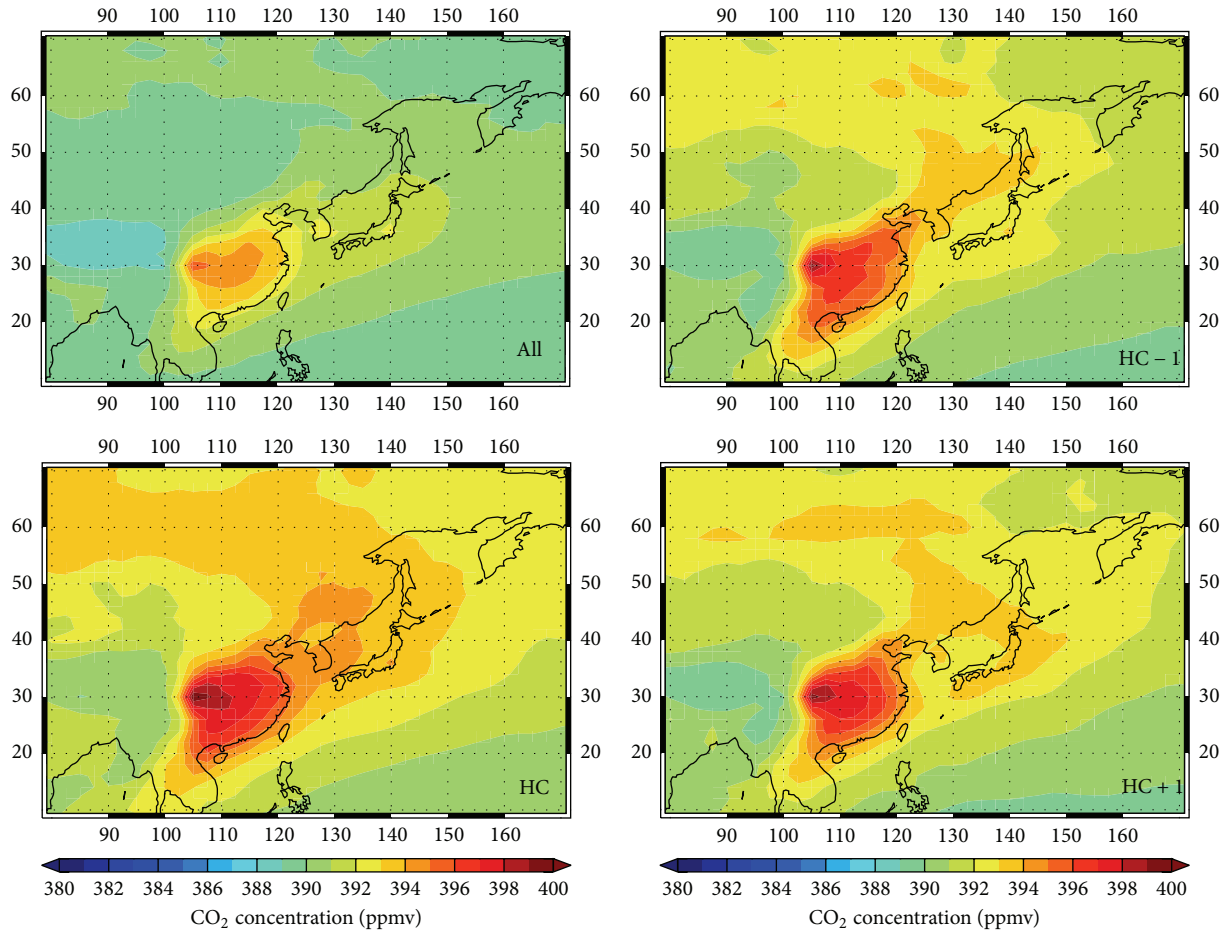


FIGURE 8: Distribution of the column-averaged CO_2 concentrations for all periods (All) and high concentration cases (HC - 1, HC, and HC + 1) simulated by GEOS-Chem.

Region III was 1.3–1.4 ppmv higher than the ones (390.8 ppmv and 390.9 ppmv) on HC - 1 and HC (Figure 7(c)). In this analysis, we can clearly find out with satellite observations that CO_2 plume with high concentration could be long-range transported with 1-2 days' duration.

Figure 8 shows the simulation results of GEOS-Chem for the same domain and period of GOSAT. Given the distribution of CO_2 concentration in all periods, most inland regions where anthropogenic emission sources are mainly concentrated, including China, Korea, and central Tokyo in Japan, reached more than 392 ppmv of CO_2 concentration. It is also shown that high concentration (almost up to 400 ppmv) plume of CO_2 emitted from China on HC - 1 days moved into the Korean Peninsula passing through the Yellow Sea on HC days and then ran away to the Pacific through the eastern coast of Korea and Japan, a day after the high concentration days (HC + 1). In particular, on HC days, high CO_2 concentrations are shown over marine area near the Korean Peninsula.

In order to clarify the source apportionment on high CO_2 concentration days, we performed the so-called tagging simulation [31, 32] using GEOS-Chem modeling.

Figures 9(a), 9(b), and 9(c) show the difference of the column-averaged CO_2 concentration between HC days and all of target periods from all sources and sinks, East Asia mainland, and South and Central Europe, respectively. Figure 10 indicates the contribution to East Asian regions as being caused by sources and sinks of 40 different regions around the world.

It is found that there are two major contributions to East Asia region for high concentration events from East Asia mainland and South/Central Europe. Over central and eastern China, Korea, and Japan, almost 45% of the contribution to China, Korea, and Japan inland area can be explained by emission sources of East Asia mainland (i.e., central/eastern China) and almost 20% to northern China by European emission sources out of the analysis domain (Figures 9(b), 9(c), and 10). In particular, it is reported from previous meteorological analysis [36] that the dynamic and meteorological mechanism for long-range transport phenomenon of high concentration CO_2 plume supposes that CO_2 emitted from China is lifted to the upper troposphere or tropopause by convection, midlatitude cyclones, and orographic lifting and is thus transported across the Pacific along with the westerlies in the upper atmosphere.

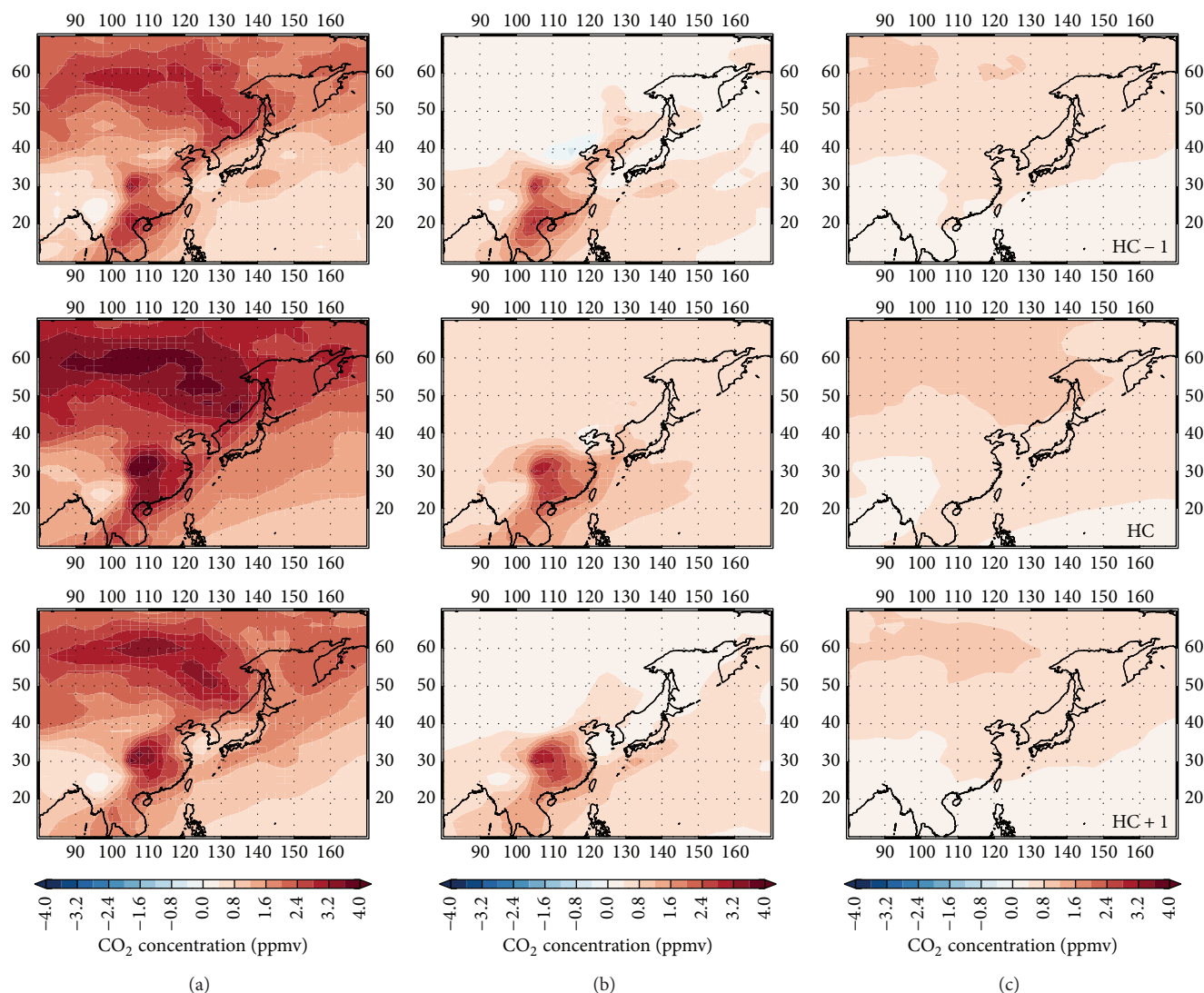


FIGURE 9: (a) Differences of the column-averaged CO_2 concentrations between high concentration cases (HC - 1, HC, and HC + 1) and all periods (All) simulated by GEOS-Chem. (b) and (c) represent differences of column-averaged CO_2 concentration contributed by emission from East Asia mainland and South and Central Europe by tagged simulation, respectively.

4. Conclusion

In this study, the ground-based data, the satellite-borne instrument (GOSAT), and the chemical transport model (GEOS-Chem) are used to investigate the long-range transport phenomena for high CO_2 concentration plume in Asian continent and the downwind regions for the period of June 2009 to May 2011. We also evaluate GOSAT data and GEOS-Chem results with TCCON data to show the reliability of the derived data. Those have very similar patterns of the seasonal variation and spatial distribution and have well-known differences with TCCON data, so that it could be reasonable to use GOSAT and GEOS-Chem data for this study.

The analysis of the long-range transport and high concentration event using observation data in a surface site, the Gosan Station in Korea, shows that the ratio of high concentration days to all periods is 11.1% with CO_2 concentration of

403.1 ppmv and 7.2 ppmv increases compared to the average CO_2 concentration (395.9 ppmv) in all periods. We can find out from backward/forward trajectory analysis that the air originating from/out of Asian continent may be transported through the polluted area in China and flowed into Korea and Japan.

The column-averaged concentration data by GOSAT and GEOS-Chem were analyzed to expand the spatial distribution of the long-range transport of high concentration CO_2 plume. With GOSAT data, concentration (389.4 ppmv) on HC days is 3.6 ppmv higher than that of all periods. It is obvious that high concentrations are also dominating in central and eastern China and Japan as a surface site, the Gosan Station in Korea, experiences high concentration events and CO_2 plume with high concentration is prevailing over those areas through long-range transport and mixing processes like other air pollutants. Also, with subregional analysis, it is found that CO_2

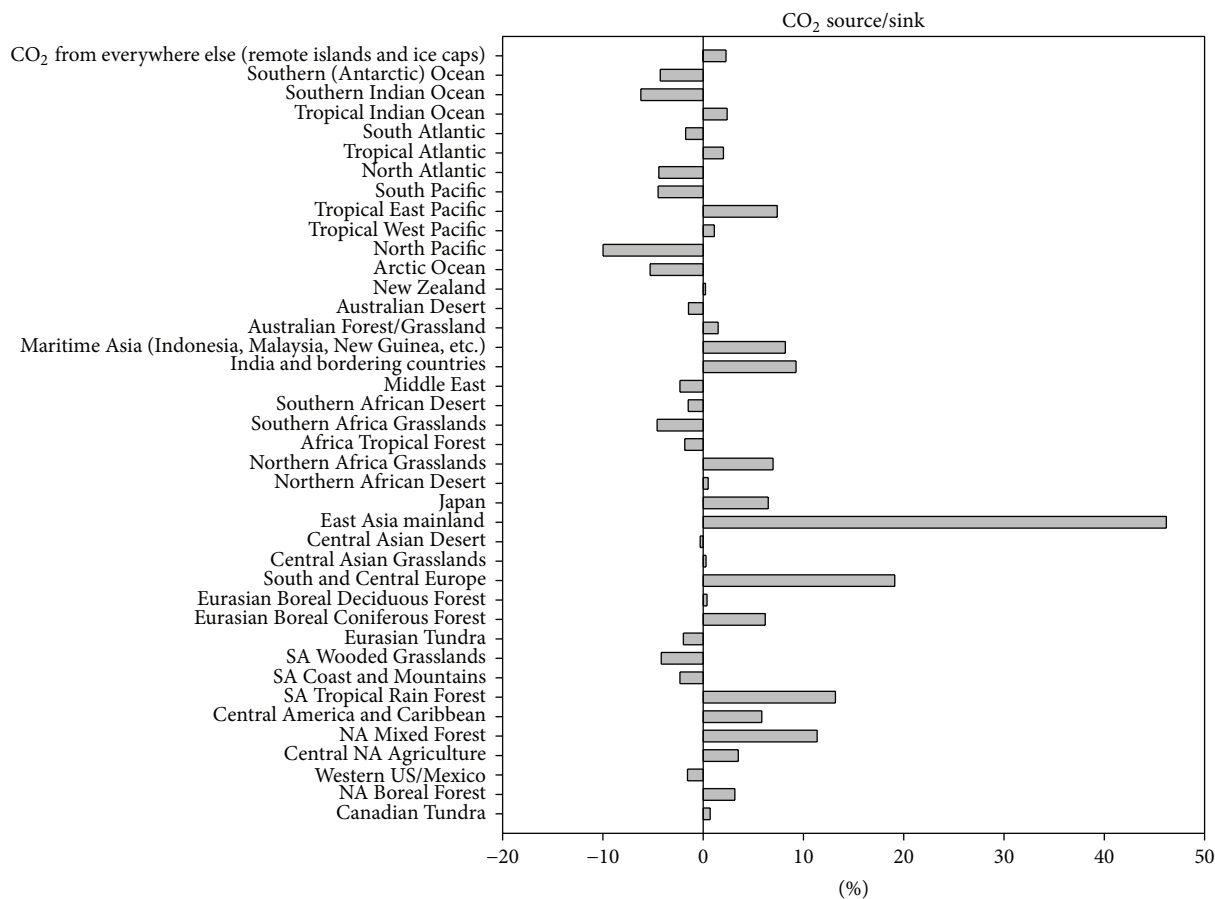


FIGURE 10: The contribution of sources and sinks to atmospheric CO₂ concentration of the East Asian regions simulated by GEOS-Chem tagged simulation.

plume with high concentration can be long-range transported with 1-2 days' duration with regional scale.

With tagging simulation using GEOS-Chem modeling, we can explain that more than 45% of the elevated CO₂ concentration over central and eastern China, Korea, and Japan on HC days may be attributed to emission sources of East Asia mainland, while almost 20% over northern China may be attributed to European emission sources.

In this study, we can understand that CO₂ which is known as a globally well-mixed gas may also act as a fingerprint of human activity with regional characteristics like other air pollutants. This comprehensive analysis with all of available data, although observational evidences are still quite few, would help better understand the long-range transport of CO₂ and its impact on climate change and the carbon cycle in the Asian regions.

Conflict of Interests

The authors declare that there is no conflict of interests regarding the publication of this paper.

Acknowledgments

The authors thank JAXA, NIES, and MOE for the GOSAT data and their continuous support as part of the Joint Research Agreement. TCCON data was obtained from the TCCON Data Archive, operated by the California Institute of Technology from the Website at <http://tcon.ipac.caltech.edu/>. They also thank WDCGG data contributors.

References

- [1] World Meteorological Organization, "WMO WDCGG data summary," WDCGG 37, World Meteorological Organization, Geneva, Switzerland, 2013.
- [2] R. J. Dargaville, S. C. Doney, and I. Y. Fung, "Inter-annual variability in the interhemispheric atmospheric CO₂ gradient: contributions from transport and the seasonal rectifier," *Tellus, Series B: Chemical and Physical Meteorology*, vol. 55, no. 2, pp. 711-722, 2003.
- [3] S.-Y. Kim, J.-B. Lee, J.-A. Yu, Y.-D. Hong, and C.-K. Song, "Analysis of the characteristics and high concentrations of carbon dioxide measured at the Gosan site in Jeju, Korea in 2007," *Climate Change Research*, vol. 2, no. 1, pp. 1-14, 2007 (Korean).

- [4] International Energy Agency, *CO₂ Emissions from Fuel Combustion (Highlights)*, International Energy Agency, 2011.
- [5] F. Artuso, P. Chamard, S. Piacentino et al., "Influence of transport and trends in atmospheric CO₂ at Lampedusa," *Atmospheric Environment*, vol. 43, no. 19, pp. 3044–3051, 2009.
- [6] T. J. Conway, L. P. Steele, and P. C. Novelli, "Correlations among atmospheric CO₂, CH₄ and CO in the Arctic, March 1989," *Atmospheric Environment*, vol. 27, no. 17-18, pp. 2881–2894, 1993.
- [7] M. Engardt and K. Holmén, "Model simulations of anthropogenic-CO₂ transport to an Arctic monitoring station during winter," *Tellus, Series B: Chemical and Physical Meteorology*, vol. 51, no. 2, pp. 194–209, 1999.
- [8] J. Brandefelt and K. Holmén, "Anthropogenic and biogenic winter sources of Arctic CO₂: a model study," *Tellus, Series B: Chemical and Physical Meteorology*, vol. 53, no. 1, pp. 10–21, 2001.
- [9] T. Aalto, J. Hatakka, I. Paatero et al., "Tropospheric carbon dioxide concentrations at a northern boreal site in Finland: basic variations and source areas," *Tellus, Series B: Chemical and Physical Meteorology*, vol. 54, no. 2, pp. 110–126, 2002.
- [10] T. Aalto, J. Hatakka, and Y. Viisanen, "Influence of air mass source sector on variations in CO₂ mixing ratio at a boreal site in northern Finland," *Boreal Environment Research*, vol. 8, no. 4, pp. 385–393, 2003.
- [11] K. Eneroth, E. Kjellström, and K. Holmén, "A trajectory climatology for Svalbard; investigating how atmospheric flow patterns influence observed tracer concentrations," *Physics and Chemistry of the Earth Parts A/B/C*, vol. 28, no. 28–32, pp. 1191–1203, 2003.
- [12] K. Eneroth, T. Aalto, J. Hatakka, K. Holmén, T. Laurila, and Y. Viisanen, "Atmospheric transport of carbon dioxide to a baseline monitoring station in northern Finland," *Tellus B: Chemical and Physical Meteorology*, vol. 57, no. 5, pp. 366–374, 2005.
- [13] Y. Tsutsumi, K. Mori, M. Ikegami, T. Tashiro, and K. Tsuboi, "Long-term trends of greenhouse gases in regional and background events observed during 1998–2004 at Yonagunijima located to the east of the Asian continent," *Atmospheric Environment*, vol. 40, no. 30, pp. 5868–5879, 2006.
- [14] Y. Tohjima, H. Mukai, S. Hashimoto, and P. K. Patra, "Increasing synoptic scale variability in atmospheric CO₂ at Hateruma Island associated with increasing East-Asian emissions," *Atmospheric Chemistry and Physics*, vol. 10, no. 2, pp. 453–462, 2010.
- [15] T. Shirai, T. MacHida, H. Matsueda et al., "Relative contribution of transport/surface flux to the seasonal vertical synoptic CO₂ variability in the troposphere over Narita," *Tellus B*, vol. 64, Article ID 19138, 2012.
- [16] US Environmental Protection Agency, "Our nation's air: status and trends through 2010," Tech. Rep. EPA-454-R-11-001, Air Quality Assessment Division, Office of Air Quality Planning and Standards, Research Triangle Park, NC, USA, 2012.
- [17] R. R. Draxler and G. D. Rolph, *HYSPLIT (Hybrid Single-Particle Lagrangian integrated Trajectory) Model*, NOAA Air Resources Laboratory, College Park, Md, USA, 2013, <http://www.arl.noaa.gov/HYSPLIT.php>.
- [18] I. M. Hoell, D. D. Davis, S. C. Liu et al., "The pacific exploratory mission-west phase B: February-March, 1994," *Journal of Geophysical Research: Atmospheres*, vol. 102, no. 23, pp. 28223–28239, 1997.
- [19] J. M. Hoell, D. D. Davis, S. C. Liu et al., "Pacific exploratory mission-west A (PEM-West A): september-october 1991," *Journal of Geophysical Research: Atmospheres*, vol. 101, no. 1, pp. 1641–1653, 1996.
- [20] B. J. Huebert, T. Bates, P. B. Russell et al., "An overview of ACE-Asia: strategies for quantifying the relationships between Asian aerosols and their climatic impacts," *Journal of Geophysical Research*, vol. 108, no. 23, p. 8633, 2003.
- [21] T. Nakajima, S.-C. Yoon, V. Ramanathan et al., "Overview of the atmospheric brown cloud East Asian regional experiment 2005 and a study of the aerosol direct radiative forcing in East Asia," *Journal of Geophysical Research: Atmospheres*, vol. 112, Article ID D24S91, 2005.
- [22] S. O'Doherty, P. G. Simmonds, D. M. Cunnold et al., "In situ chloroform measurements at Advanced Global Atmospheric Gases Experiment atmospheric research stations from 1994 to 1998," *Journal of Geophysical Research: Atmospheres*, vol. 106, no. 17, pp. 20429–20444, 2001.
- [23] National Institute Environmental Research, "Analysis of the characteristics of greenhouse gases in the background atmosphere in Korea (III)," NIER Annual Report 119, 2009, (Korean).
- [24] JAXA, NIES, and ME, *GOSAT/IBUKI Data Users Handbook*, Japan Aerospace Exploration Agency, National Institute for Environmental Studies and Ministry of the Environment, 2011.
- [25] I. Morino, O. Uchino, M. Inoue et al., "Preliminary validation of column-averaged volume mixing ratios of carbon dioxide and methane retrieved from GOSAT short-wavelength infrared spectra," *Atmospheric Measurement Techniques*, vol. 4, no. 6, pp. 1061–1076, 2011.
- [26] N. Saitoh, R. Imasu, Y. Ota, and Y. Niwa, "CO₂ retrieval algorithm for the thermal infrared spectra of the Greenhouse Gases Observing Satellite: potential of retrieving CO₂ vertical profile from high-resolution FTS sensor," *Journal of Geophysical Research: Atmospheres*, vol. 114, no. 17, Article ID D17305, 2009.
- [27] I. Bey, D. J. Jacob, R. M. Yantosca et al., "Global modeling of tropospheric chemistry with assimilated meteorology: model description and evaluation," *Journal of Geophysical Research: Atmospheres*, vol. 106, no. 19, Article ID 2001JD000807, pp. 23073–23095, 2001.
- [28] P. Suntharalingam, D. D. Jacob, P. I. Palmer et al., "Improved quantification of Chinese carbon fluxes using CO₂/CO correlations in Asian outflow," *Journal of Geophysical Research: Atmospheres*, vol. 109, no. 18, 2004.
- [29] R. Nassar, D. B. A. Jones, P. Suntharalingam et al., "Modeling global atmospheric CO₂ with improved emission inventories and CO₂ production from the oxidation of other carbon species," *Geoscientific Model Development*, vol. 3, no. 2, pp. 689–716, 2010.
- [30] D. Pillai, C. Gerbig, J. Marshall et al., "High resolution modeling of CO₂ over Europe: implications for representation errors of satellite retrievals," *Atmospheric Chemistry and Physics*, vol. 10, no. 1, pp. 83–94, 2010.
- [31] A. Kumar, S. Wu, M. F. Weise et al., "Free-troposphere ozone and carbon monoxide over the North Atlantic for 2001–2011," *Atmospheric Chemistry and Physics*, vol. 13, no. 24, pp. 12537–12547, 2013.
- [32] C.-S. Shim, R. Nassar, and J. Kim, "Comparison of model-simulated atmospheric carbon dioxide with GOSAT retrievals," *Asian Journal of Atmospheric Environment*, vol. 5, no. 4, pp. 263–277, 2011.
- [33] A. M. S. Gloudemans, M. C. Krol, J. F. Meirink et al., "Evidence for long-range transport of carbon monoxide in the Southern Hemisphere from SCIAMACHY observations," *Geophysical Research Letters*, vol. 33, no. 16, Article ID L16807, 2006.

- [34] C. C. Heald, D. J. Jacob, A. M. Fiore et al., "Asian outflow and trans-Pacific transport of carbon monoxide and ozone pollution: an integrated satellite, aircraft, and model perspective," *Journal of Geophysical Research D: Atmospheres*, vol. 108, no. 24, p. 4804, 2003.
- [35] F. H. Tu, D. C. Thornton, A. R. Bandy et al., "Dynamics and transport of sulfur dioxide over the Yellow Sea during TRACE-P" *Journal of Geophysical Research D: Atmospheres*, vol. 108, no. 20, p. 8790, 2003.
- [36] Q. Liang, L. Jaegle, D. A. Jaffe, P. Weiss-Penzias, A. Heckman, and J. A. Snow, "Long-range transport of Asian pollution to the northeast Pacific: seasonal variations and transport pathways of carbon monoxide," *Journal of Geophysical Research: Atmospheres*, vol. 109, Article ID D23S07, 2004.
- [37] C. Lee, A. Richter, H. Lee et al., "Impact of transport of sulfur dioxide from the Asian continent on the air quality over Korea during May 2005," *Atmospheric Environment*, vol. 42, no. 7, pp. 1461–1475, 2008.
- [38] J. Suthawaree, S. Kato, A. Takami et al., "Observation of ozone and carbon monoxide at Cape Hedo, Japan: seasonal variation and influence of long-range transport," *Atmospheric Environment*, vol. 42, no. 13, pp. 2971–2981, 2008.
- [39] Y. Yoshida, N. Kikuchi, I. Morino et al., "Improvement of the retrieval algorithm for GOSAT SWIR XCO₂ and XCH₄ and their validation using TCCON data," *Atmospheric Measurement Techniques*, vol. 6, no. 6, pp. 1533–1547, 2013.
- [40] A. Fraser, C. C. Miller, P. I. Palmer, N. M. Deutscher, N. B. Jones, and D. W. T. Griffith, "The Australian methane budget: interpreting surface and train-borne measurements using a chemistry transport model," *Journal of Geophysical Research: Atmospheres*, vol. 116, no. 20, Article ID D20306, 2011.
- [41] Y. Yoshida, Y. Ota, N. Eguchi et al., "Retrieval algorithm for CO₂ and CH₄ column abundances from short-wavelength infrared spectral observations by the Greenhouse gases observing satellite," *Atmospheric Measurement Techniques*, vol. 4, no. 4, pp. 717–734, 2011.
- [42] C.-S. Shim, *Sources/Sinks Analysis with Satellite Sensing for Exploring Global Atmospheric CO₂ Distributions*, Korea Environment Institute, 2010, (Korean).
- [43] World Meteorological Organization, "WMO WDCGG data summary," WDCGG 36, World Meteorological Organization, Geneva, Switzerland, 2012.

Research Article

Preliminary Assessment of Methane Concentration Variation Observed by GOSAT in China

Xiuchun Qin,¹ Liping Lei,¹ Zhonghua He,¹ Zhao-Cheng Zeng,^{1,2} Masahiro Kawasaki,³ Masafumi Ohashi,⁴ and Yutaka Matsumi³

¹Key Laboratory of Digital Earth Science, Institute of Remote Sensing and Digital Earth, Chinese Academy of Sciences, Beijing 100094, China

²Institute of Space and Earth Information Science, The Chinese University of Hong Kong, Shatin 999077, Hong Kong

³Nagoya University, Nagoya 890-0065, Japan

⁴Kagoshima University, Kagoshima 464-8601, Japan

Correspondence should be addressed to Liping Lei; leilp@radi.ac.cn

Received 16 February 2015; Accepted 18 May 2015

Academic Editor: Xiaozhen Xiong

Copyright © 2015 Xiuchun Qin et al. This is an open access article distributed under the Creative Commons Attribution License, which permits unrestricted use, distribution, and reproduction in any medium, provided the original work is properly cited.

Atmospheric column-averaged methane (XCH_4) observations from GOSAT are analyzed to study the spatiotemporal variation of XCH_4 in China. Furthermore, we investigate the driving mechanism of XCH_4 spatiotemporal variations, especially for high XCH_4 values shown over Sichuan Basin, by analyzing both the emission mechanism of rice planting process and the regional atmosphere dynamic transportation. The results indicate that spatially the Sichuan Basin presents a higher XCH_4 concentration than other regions in China and is 17 ppb higher than the paddy area in the same latitude zone. Seasonally, XCH_4 in Sichuan Basin during rice harvest season is generally higher than that in early cultivation period. However, comparing to paddy area in the same latitude zone, Sichuan Basin shows a relatively higher XCH_4 value during the winter of noncultivation period when the emissions from rice paddies are weak and surface air temperature is low. To further investigate the high XCH_4 concentration during this low-emission period, we use the HYSPLIT model to simulate the atmosphere dynamic transport process, and the result suggests that the typical closed topography of Sichuan Basin, which may lead to CH_4 accumulation and keep it from diffusion, is one possible reason for the high XCH_4 value in winter.

1. Introduction

Atmospheric methane (CH_4) is one of the most important greenhouse gases, and the greenhouse effect generated by unit molecule of CH_4 is about 23 times higher than that of atmospheric carbon dioxide (CO_2). Therefore, it will be more effective to reduce the CH_4 emissions to mitigate the potential global warming than reducing CO_2 emissions [1]. The World Meteorological Organization (WMO) indicated in the "Greenhouse Gas Bulletin" published on September 9, 2014, that, from the year 1990 to 2013, greenhouse effect had increased by 34% due to increasing concentrations of greenhouse gases such as CO_2 and CH_4 . Global warming has become one of the most important global environmental issues nowadays. Therefore, analyses of the CH_4 concentration variation and studies on its driving factors

have drawn increasing attention. However, due to limited observation capabilities and understanding of CH_4 sources and sinks, the underlying driving factors for the regional CH_4 spatiotemporal variation are still unclear [2]. The increase of global atmospheric CH_4 concentration is mainly due to agricultural activities, in which irrigated rice paddy is one of the most important sources [3]. China is the world's largest rice producer, accounting for about 22% of the rice planting area in the world and 37% of the global production. Therefore, studies of China's regional CH_4 emissions and its driving factors are of importance to understand the regional and global carbon cycle and the changing climate.

Since 1983, WMO has established a global greenhouse gases reference network for continuous observation of atmospheric greenhouse gases, including CH_4 concentration. However, due to the limited observation stations in many

parts of the world, it is still difficult to comprehensively understand the global distribution and variation of CH_4 [4, 5]. Satellite remote sensing observation of atmospheric CH_4 concentration, which provides continuous observations at the global scale, plays an increasingly important role in improving our understanding of the distribution of sources and sinks of CH_4 and the carbon cycle [6, 7]. To date, several satellites for observing CH_4 had been launched, including Atmospheric Infrared Sounder (AIRS) on the EOS/Aqua platform [8], SCanning Imaging Absorption spectroMeter for Atmospheric CHartography (SCIAMACHY) [9, 10], and the Greenhouse gases Observing SATellite (GOSAT) [11], and a lot of valuable observations have been obtained. Using AIRS data, Xiong et al. [12] investigated a strong enhancement of CH_4 over South China region during the summer, July, August, and September, in the middle to upper troposphere, and its relationship with transport and local surface CH_4 emission. Zhang et al. [13] discovered that the vertical distribution of CH_4 concentration in the troposphere of China area decreases as the altitudinal increases. Moreover, seasonal CH_4 concentration in the eastern and northern parts of China presents a double-peak variation, with the highest concentration in summer and the second highest in winter. Hayashida et al. [10] analyzed the relationship between rice paddy emission and XCH_4 concentration in Southeast Asia using satellite data obtained by SCIAMACHY and found that there is a strong correlation between the two variables in Southeast Asia. Zhang et al. [13] showed that paddy CH_4 emission is the major source of CH_4 in China and found that the air temperature, normalized difference vegetation index (NDVI), and soil total nitrogen explain more than 75% of the XCH_4 variation in China. Previous studies by [10, 12, 13] also showed that a consistently high CH_4 concentration is observed in the Sichuan Basin, including Chongqing and Sichuan regions in southwest China. These studies greatly improved the estimation of regional and national CH_4 emissions as well as our understanding of the CH_4 emission mechanism. However, most of previous studies focused on examining the correlation between the CH_4 variation and emissions from rice paddies, while potential driving factors for CH_4 variation, such as the atmospheric dynamic transport and influence from external sources, are not well analyzed, and therefore the underlying mechanism affecting the spatial and temporal distribution of CH_4 has not been comprehensively understood. Moreover, the used satellite observations of CH_4 concentration by most previous studies are primarily obtained from SCIAMACHY [12, 13], which was operational from March 2002 to April 2012. However, due to sensor problems that happened in the end of the year 2005, the SCIAMACHY observing instrument became unstable since 2006 [2]. The GOSAT, launched on January 23, 2009, is the world's first spacecraft dedicated to observing greenhouse gases, including CO_2 and CH_4 [14]. GOSAT data has been widely used in many previous studies for studying CO_2 [8, 15–17], while studies on analyzing CH_4 from GOSAT observations are still rare.

In this study, XCH_4 observations from GOSAT, spanning from January 2010 to December 2013, are analyzed to study the spatiotemporal variation of XCH_4 in China and its

relationship with regional surface emissions. Furthermore, we investigate the driving mechanism of XCH_4 spatiotemporal variations, especially for high XCH_4 values shown over Sichuan Basin in southwest China, by combining the emission mechanism of rice planting process, the meteorology data, the surface emission data, and the regional atmosphere dynamic transportation.

2. Study Area and Data

2.1. Study Area. Figure 1 shows the study area of China land region, the Sichuan Basin, and the corresponding same latitude zone in the east for comparison of XCH_4 variation. Sichuan Basin is located in the upper reaches of the Yangtze River, encompassing the eastern part of Sichuan province and most of Chongqing city, with an elevation of about 500 meters above the sea level. The basin has a close topography, in which the eastern, southern, and northern parts of the basin are surrounded by mountains, and to the western is Qinghai-Tibet Plateau, which makes it difficult for air flow diffusion. The summer season of the basin lasts for 4 to 5 months with rich rain and temperatures as high as 25~29°C during the hottest month, which is suitable for rice growing and makes the basin one of China's five major rice-producing regions [18]. The paddy region in Sichuan Basin with elevation less than 1000 meters is chosen to be the study area. In addition, Yanting county (105°27'E, 31°16'N, ~420 m in altitude), where we conducted ground-based observation of XCO_2 and XCH_4 [19, 20], and Yueyang city (116°42'E, 43°38'N, ~40 m in altitude), which is located between Hunan province and Hubei province in the same latitude paddy zone with Yanting, as shown in Figure 1, are chosen to be centers of the atmospheric molecule trajectory simulation.

2.2. Data Collection

(1) Satellite Data. In this study, 3-year GOSAT XCH_4 Level 2 data (Version 02.XX) for General User (GU) from the year 2010 to 2012 are collected. XCH_4 data are retrieved using the spectra observed from Thermal And Near-infrared Sensor for carbon Observation Fourier Transform Spectrometer (TANSO-FTS) with an orbiting period of 3 days. The nadir footprint of the instrument has a diameter of about 10.5 km at sea level [21]. Compared to early versions, these 02.xx version XCH_4 data were improved by identifying and correcting the error characteristics in retrieval, such as handling of aerosol scattering [22] which has a big impact on the GOSAT retrieval accuracy. The comparison result with data of the Total Carbon Column Observing Network (TCCON) shows the bias and standard deviation of the GOSAT XCH_4 data are -5.9 and 12.6 ppb, respectively [22]. Our ground measurement results implemented at Yanting Station using optical spectrum analyzer (OSA) [19, 20] for October–November of 2013 present 24 ppb lower deviation comparing with the GOSAT- XCH_4 data within 400 km distance from the station. Our XCH_4 data are the averaged values for the local mean solar time of 10–14 h, which show a decreasing tendency from the beginning of October to the end of November by 90 ppb and have one

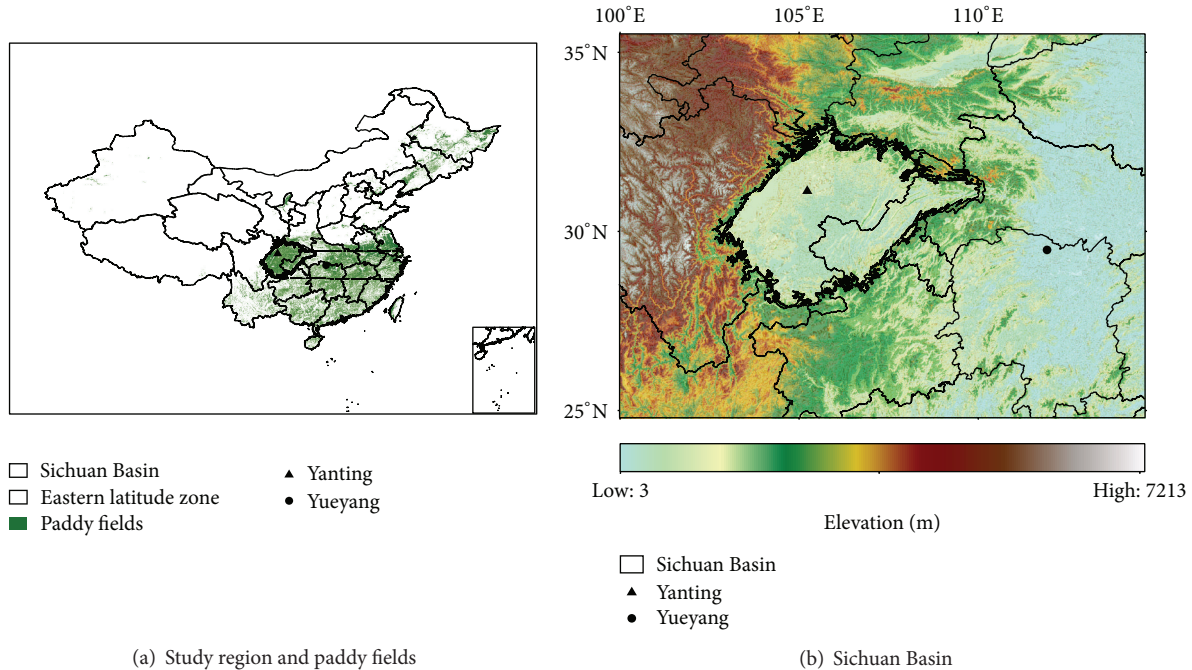


FIGURE 1: (a) Paddy fields distribution in China, the Sichuan Basin (black line polygon), and the comparative study regions (within two horizontal lines) at the same latitude zone to the east of the basin, and (b) the terrain elevation of the Sichuan Basin. Also showed in (a) and (b) are the locations of Yanting (solid triangle) and Yueyang (solid circle).

standard deviation of 70 ppb. More detailed analysis is still in process.

(2) *Meteorological Data.* To study the relationship between air temperature and satellite-observed XCH_4 concentration, monthly mean temperature data in Sichuan Basin and the paddy area in the same latitude zone are collected from the China Meteorological Data Sharing System (<http://data.cma.gov.cn/>) [23], which are based on the basic-reference surface weather observation station and automatic stations in China. We obtain the temperature data from the 19 stations in Sichuan Basin and 33 stations in the paddy areas in the same latitude zone from January 2010 to December 2013 and calculate the regional monthly mean temperature of the two areas for the following analysis.

(3) *Emission Dataset.* CH_4 emissions from human activities and natural processes correspond to anthropogenic sources and natural sources, respectively, in which anthropogenic emissions account for about 60% [24]. The anthropogenic emissions are mainly from rice cultivation, ruminants, waste disposal, biomass burning, and energy industries. The used dataset of CH_4 emissions is from the Emissions Database for Global Atmospheric Research (EDGAR) v4.2 data [25] for the year 2010 on spatial grid of $0.1^\circ \times 0.1^\circ$. EDGAR is a joint project of the European Commission JRC Joint Research Centre and the Netherlands Environmental Assessment Agency, and the data are mainly from point source emissions and global energy statistics database of the International Energy Agency (IEA). The EDGAR CH_4 emission data

include emissions from agricultural soils, gases, industrial process, and animal enteric fermentation [26]. Figure 2 shows the spatial distribution of CH_4 emissions in China for the year 2010. The area of high emission sources around the Sichuan Basin is mainly located to the east and northeast, followed by the south, whereas the emissions to the west and north are almost negligible.

2.3. *Trajectory Simulation Analysis.* In order to study the influence of nonlocal sources and atmospheric transport on CH_4 concentration, Hybrid Single-Particle Lagrangian Integrated Trajectory (HYSPPLIT) model is used to simulate the atmospheric transport by successively setting Yanting and Yueyang as center point under the weather conditions of the year 2013. The HYSPPLIT model is a complete system, developed jointly by NOAA and Australia's Bureau of Meteorology, for computing simple air parcel trajectories to complex dispersion and deposition simulations, allowing for a variety of meteorological elements in the input file, varying physical processes, and different types of emission sources. Past studies showed that 3–5-day trajectory simulation is an appropriate simulation period to study regional impact [27, 28]. Therefore, three-day (72 hours) period is chosen in this study to implement the trajectory simulation using HYSPPLIT. The simulations were started from the UTC time 00:00, 06:00, 12:00, and 18:00, respectively, with simulated height of 500 meters above the ground. The simulated trajectories are aggregated using $0.5^\circ \times 0.5^\circ$ grids to calculate the number of trajectory lines and the corresponding orientations within each grid under certain atmospheric conditions. CH_4 sources

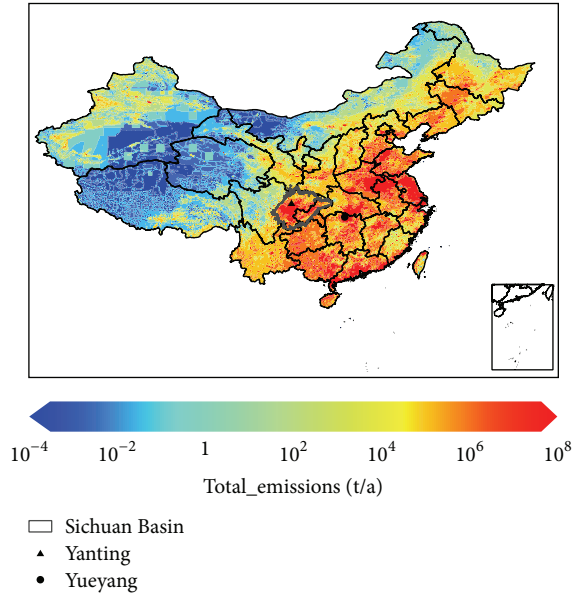


FIGURE 2: Amount of CH_4 emissions in China region in 2010 from EDGAR 4.2 data (colorbar of the emission value are shown by taking their base 10 logarithms).

and sinks can then be further analyzed by combining the simulation data and the distribution of CH_4 emissions.

3. Results and Discussions

3.1. Spatiotemporal Variability of $X\text{CH}_4$. Using the GOSAT $X\text{CH}_4$ Level 2 dataset collected from January 2010 to December 2013, we aggregated all the data into $2.5^\circ \times 2.5^\circ$ grids and calculated the averaged data within each grid to obtain the spatial distribution of $X\text{CH}_4$ in China, as shown in Figure 3. We found that the spatial variation of $X\text{CH}_4$ from GOSAT is generally consistent with $X\text{CH}_4$ bottom-up calculated emission data from EDGAR as shown in Figure 2. From Figure 3, it can be seen that west China shows a much lower value than southeast region. The lowest value exists in Qinghai-Tibet Plateau, where little CH_4 emission happens because the elevation is high (about 3000 meters on average) and there are much less human activities. However, the Sichuan Basin next to the Qinghai-Tibet Plateau presents the highest $X\text{CH}_4$ concentration in China. This overall distribution from GOSAT data shown in Figure 3 agrees with previous studies [29].

A more detailed demonstration of the $X\text{CH}_4$ seasonal variations is shown in Figure 4, in which the seasonal variation of all the GOSAT $X\text{CH}_4$ data in China region with monthly mean data, the Sichuan Basin, and the rice paddy fields in the same latitude zone is compared. The $X\text{CH}_4$ value in China land region varies from 1702 to 1917 ppb with mean value of 1794 ppb and also presents an annual increase and a seasonal cycle with the highest value in Autumn (July to September) and the lowest value in Winter (November to January). This temporal variation is consistent with ground-based observation result from Waliguan, one of the World

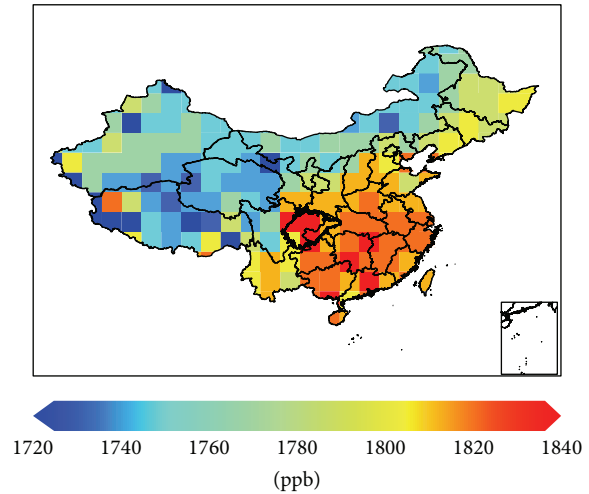


FIGURE 3: Spatial distribution of $X\text{CH}_4$ aggregated into $2.5^\circ \times 2.5^\circ$ from GOSAT observations spanning from January 2010 to December 2013.

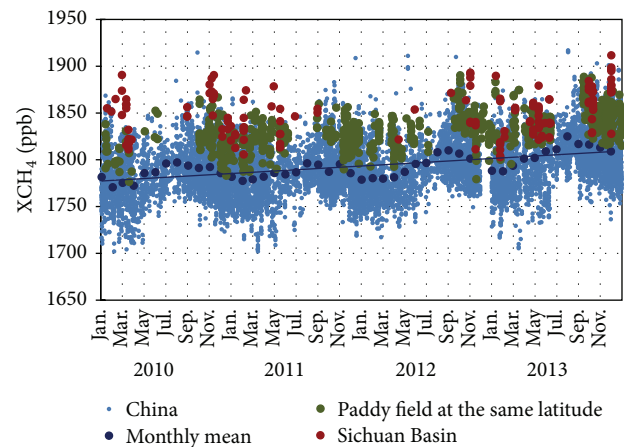


FIGURE 4: The seasonal variation of all the GOSAT $X\text{CH}_4$ data over China land region (light blue dots), the Sichuan Basin (red dots), and the rice paddy fields (dark green dots) in the same latitude zone from January 2010 to December 2013. The dark blue dots are the monthly mean for land region and the blue line shows the corresponding trend from linear fitting.

Data Centre for Greenhouse Gases (WDCGG) stations in China [30, 31]. Moreover, $X\text{CH}_4$ in both of the Sichuan Basin and the rice paddy field area in the same latitude zone of the basin presents general higher $X\text{CH}_4$ value than the average value in China land region, and $X\text{CH}_4$ value in the previous region is on average 17 ppb higher than that in latter region. The difference of 17 ppb is larger than the standard deviation (12.6 ppb) of the GOSAT $X\text{CH}_4$ data error, indicating a $X\text{CH}_4$ difference between the two regions with high confidence.

Two main factors that contribute to the $X\text{CH}_4$ concentration variability are the local surface CH_4 emission and the large scale atmosphere dynamic transport. Among the CH_4 emissions, more than 60% percent are from human activities, in which agriculture related emissions are the main

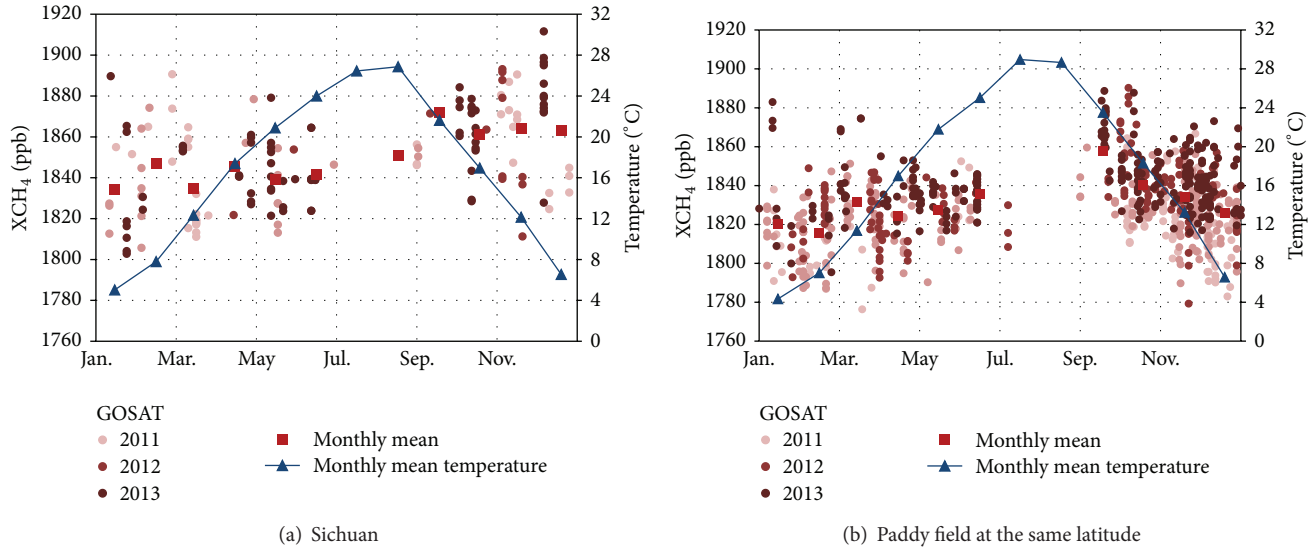


FIGURE 5: Comparison of XCH_4 value from GOSAT and the corresponding surface air temperature values from weather stations in (a) the Sichuan Basin and (b) the rice paddy fields in the same latitude region. The time table of months in x-axis indicates the beginning of each month.

component. According to statistics from EDGAR, as shown in Figure 2, in the Sichuan Basin the proportions of CH_4 emissions from agriculture related emission, fuel gas, and waste water are 44%, 14%, and 13%, respectively. On the other hand, the typical closed topography of Sichuan Basin, which results in low surface wind speed and CH_4 accumulation and keeps it from outward diffusion, together with high CH_4 emissions from large area of rice paddy fields in the Sichuan Basin is possibly the main reasons for the high XCH_4 value in region [29]. To further investigate the high XCH_4 value in this region, two factors, including the emission mechanism of rice paddy which is the main CH_4 emission source and the regional atmosphere dynamic transportation, are analyzed to investigate the underlying processes leading to XCH_4 variability in the Sichuan Basin.

3.1.1. Relationship between Seasonal Variation of XCH_4 and Emissions from Rice Paddies. Emissions of CH_4 from rice paddies become active through soil CH_4 production, reoxidation, and transmission and release from plant through the aeration organizations [30]. The emission process of CH_4 is influenced by many factors including weather, water management, fertilization, soil respiration, and rice growth [30, 32, 33]. As shown by previous studies, the temperature is one of the most important factors influencing the CH_4 emissions from rice paddies [34, 35] and the CH_4 emission will increase 3 times as the temperature increases by $10^\circ C$ [36]. The Sichuan Basin paddy region mainly includes winter rice paddy, which is characterized by irrigation in March, planting in May, and rice harvesting in September. Afterwards the land keeps soil moisture and remains arable until transplanting rice in the following May [29, 33]. This kind of paddy field is flooded during all four seasons to keep the soil in a reduced state.

Figures 5(a) and 5(b) show the relationship between the monthly averaged surface air temperature from weather stations and the XCH_4 values in the Sichuan Basin and the corresponding paddy fields in the same latitude zone, respectively. From Figure 5(a), in the Sichuan basin region the averaged XCH_4 value in September is generally higher than that in May, as expected according to the seasonal variation of CH_4 emissions due to rice paddy cultivation with planting in May and harvest in September. However, XCH_4 value during the noncultivation season, especially from November to December and January to February, is unexpectedly higher than that in September which is the harvest month in cultivation. As shown in Figure 5(b), paddy rice regions in the same latitude zone show a different feature from the Sichuan Basin. From the available monthly mean XCH_4 data shown in Figure 5, we can see that both regions present an annual maximum of XCH_4 concentration in September. Moreover, we found the seasonal variation of XCH_4 of paddy regions in the latitude zone as shown in Figure 5(b) agrees well with the seasonal variation of surface air temperature, while the Sichuan Basin in Figure 5(a) presents a relatively higher XCH_4 value during low temperature period in winter. For the period during July and August, unfortunately, almost no GOSAT XCH_4 data are available during this rainy season because of the frequency clouds. As presented by Hayashida et al. [10] using the SCIAMACHY data, this period, which is right before the paddy harvest time, presents the highest CH_4 concentration, corresponding to the highest surface air temperature.

It can be concluded that, in the Sichuan Basin region as in Figure 5(a), the seasonal variation of XCH_4 is generally consistent with CH_4 emissions from cultivation of rice paddy fields. However, higher XCH_4 is unexpectedly observed during the low temperature period in winter, which will be

further investigated in the following sections in this paper. For the rice paddy fields located in the same latitude zone in Figure 5(b), the seasonal variation of XCH₄ generally agrees with CH₄ emissions from cultivation of rice paddy fields and is consistent with the surface air temperature variation.

3.1.2. Relationship between XCH₄ Variation and Atmospheric Transport. HYSPLIT model is used to simulate atmospheric transport and trajectories to investigate the influence of transport on high XCH₄ concentration in January, February, November, and December in the Sichuan Basin. Based on the source of gas molecules, a simulation can be categorized into backward trajectory simulation and forward trajectory simulation. A backward track simulation can be used to analyze the impact of external sources on local circumstances, and a forward trajectory simulation can be used to examine atmospheric dynamics and transport in a specific region. In this study, we chose Yanting and Yueyang in Sichuan Basin, as shown in Figure 1, as the target regions and implemented both the forward and backward simulation every three days beginning, respectively, from the two target regions at four UTC times (00:00, 06:00, 12:00, 18:00) each day for the year 2013. There are in total 4 trajectories for each target regions each day. Figure 6 shows gridded results from the backward simulation of the Sichuan Basin for each month in 2013. Figure 7 shows the results from forward trajectory simulation by setting Yanting and Yueyang city as the target regions in the year 2013.

Using all the trajectories from HYSPLIT forward simulation, as shown in Figure 7, we calculate the number of trajectories that remains in the target regions within different time ranges, to study the atmospheric transport and diffusion of CH₄ molecules from the study regions. Each trajectory line from the HYSPLIT output is a series of 73 hourly trajectory points, including the initial time (0 hours) and all hourly output of the 3-day simulation (3 day × 24 hours). For each trajectory line, the time when the line intersects with the study region boundary is obtained and then used to calculate the staying time of the molecule inside the study area. The total number of daily trajectories inside the study region is grouped into 4 different time lengths (0, 12, 24, and 48 hours) and then further grouped into monthly statistics using the following equation:

$$L_m = \sum_{j=1}^{m_d} \sum_{i=1}^4 n_{ij} \begin{cases} n_{ij} = 1 & (h_{ij} \geq H) \\ n_{ij} = 0 & (h_{ij} < H) \end{cases} \quad (1)$$

$$(H = 0, 12, 24, 48; h_{ij} \in (0, 72]),$$

where L_m is the number of trajectories staying inside the study area in month m , m_d is the number of days in the corresponding month, i is the daily number of trajectories, j is the j th day in month m , and h_{ij} is the time length from target point to the area boundary of the i th trajectory in j th day, which quantify the transport time by the molecules to be transported out of the study region. The value is from 0 to 72 hours. H stands for the 4 different time lengths. We define the Sichuan Basin region (Figure 7(a)) and the circle region

centering on Yueyang with 2.5° radius (Figure 7(b)) as two target regions. Figure 8 shows the number of CH₄ molecule trajectories staying inside these two target regions after 4 different transport running times in each month for the year 2013 calculated from (1) based on the forward simulations.

From Figure 8, in the Sichuan Basin region the number of staying trajectories is generally higher than Yueyang area, especially the result after 48 hours of transport, which indicates a strong gas retention phenomenon in the Sichuan Basin. For January, February, November, and December in the basin region, the number of staying trajectories inside this area is obviously larger than other months, even after 48 hours of transport. However, the number of staying trajectories in Yueyang region is smaller in these months. Comparing with seasonal variation of XCH₄ in Figure 5, we found the seasonal variation of the number of staying trajectories inside the study region agrees well with the seasonal variation of XCH₄. Moreover, from Figure 7 we found in the Sichuan Basin area the air parcel trajectories are aggregating in a volute shape, indicating a weak outward diffusion of the CH₄ molecules. However, the overall atmosphere transport in Yueyang as observed from the trajectories is distributed obviously along the northeast and southwest direction, which is very different from the Sichuan Basin possibly mainly due to their different topographies.

Compared with the backward simulation results in Figure 6, the Sichuan Basin is weakly influenced by emissions from a small part of the eastern China source region in February and from northeastern part in November and is consistently and greatly influenced from north regions all the year, where, however, almost no CH₄ emission sources exist according to EDGAR emission data shown in Figure 2. Therefore, we conclude that, in January, February, November, and December, the CH₄ in Sichuan Basin is partly affected by the CH₄ emissions from the northeast and north regions, where the emissions are small, indicating the high XCH₄ values during these four months are not results of strong influence by external emission sources.

Regarding CH₄ emission from sources other than rice paddies, which might be impacting the spring/winter high in Sichuan Basin, we examined the GISS bottom-up emission inventory data [37] as shown in Figure 8 (6-2) in Hayashida et al. [10]. We found that during the cultivation season almost all the CH₄ emission is from rice cultivation, while during the winter noncultivation season the rice emission is close to zero and the emissions from other sources are also very small that the GOSAT-observed high XCH₄ value during spring/winter is not likely from these sources.

From both the spatial and temporal variation of XCH₄ from GOSAT data as described and discussed above, it can be concluded that the typical closed topography of Sichuan Basin, which leads to CH₄ accumulation and keeps it from diffusion, is one important reason for the high XCH₄ value observed in this region.

As the main sink of atmospheric CH₄, the reaction of CH₄ with hydroxyl radicals (OH) removes almost 90% of CH₄ [38]. Because of a stronger chemical loss that happened in summer, the CH₄ concentrations are generally lowest in summer and highest in winter, as reported by [39] using

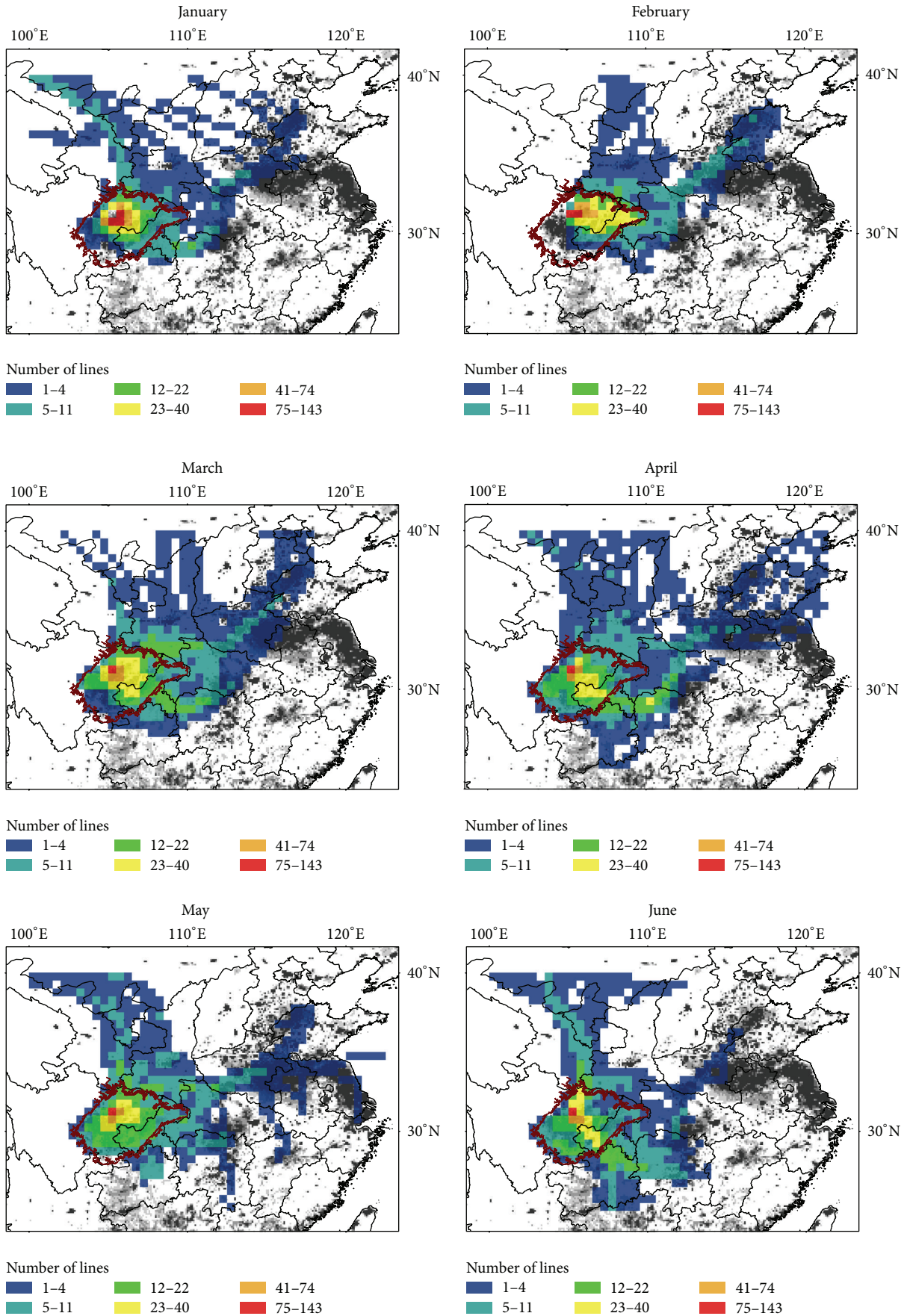


FIGURE 6: Continued.

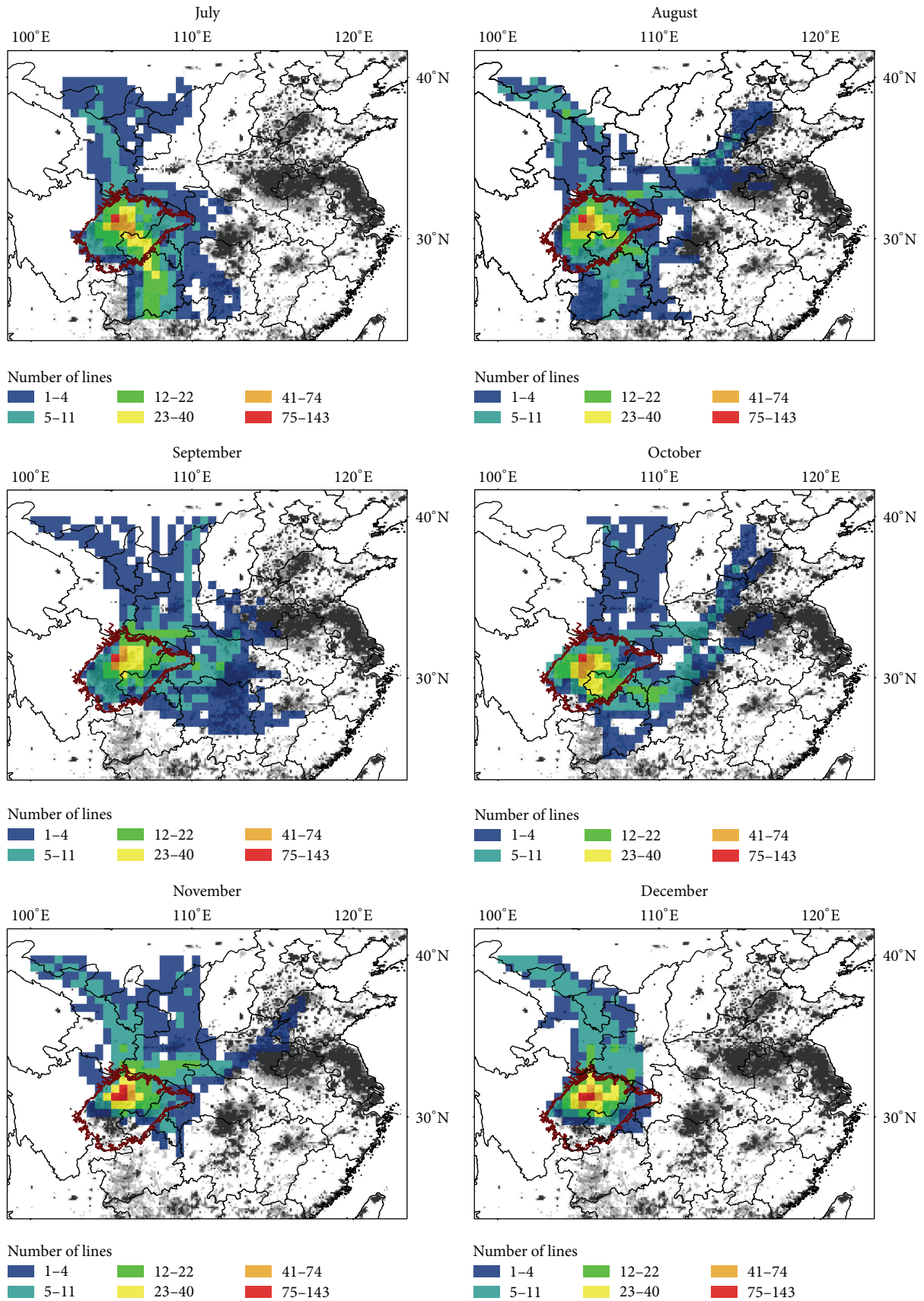


FIGURE 6: The density of the backward simulated trajectories, which are gridded into 0.5 by 0.5 degree grids, from Yanting in the Sichuan Basin for each month in 2013.

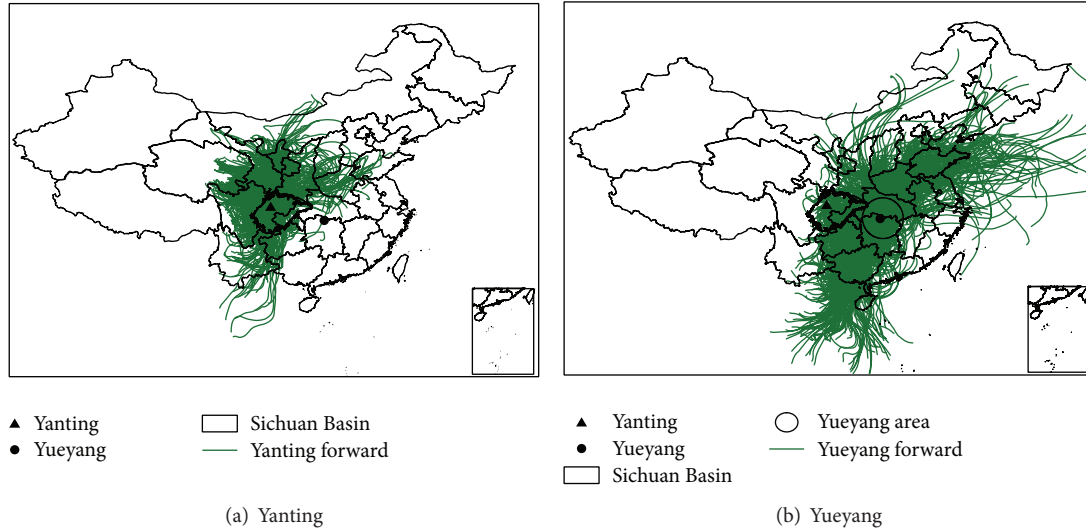


FIGURE 7: The spatial distribution of forward trajectory simulation from (a) Yanting (solid triangle) in Sichuan Basin and (b) Yueyang area (solid circle).

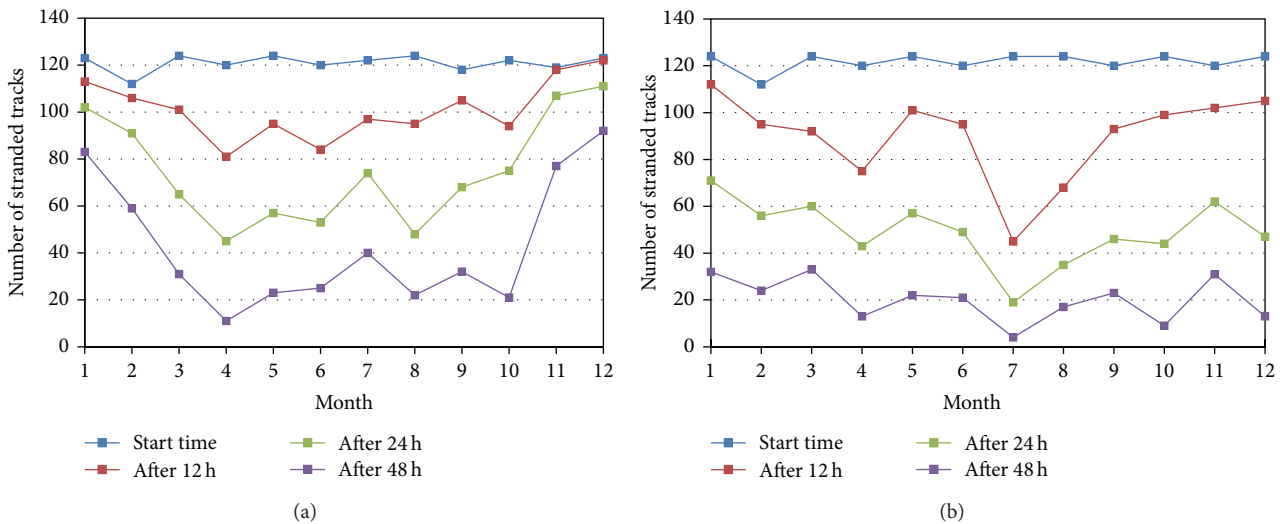


FIGURE 8: The number of trajectories that still stay inside the study area of (a) the Sichuan Basin and (b) the circle region centering on Yueyang with 2.5° radius after 4 different transport times (0, 12, 24, and 48 hours).

the background observations from the monitoring network data. However, GOSAT XCH₄ data in this study shows a different seasonal variation in Sichuan Basin characterized by higher concentration during summer and autumn (rice cultivation season) and lower concentration during winter and spring (noncultivation season), which are consistent with Hayashida et al. [10] using the SCIAMACHY XCH₄ data. Unfortunately, few XCH₄ retrievals from GOSAT during summer are available for further investigation.

4. Conclusions

In this study, GOSAT-XCH₄ data from January 2010 to December 2013 are used to study the spatiotemporal variation of XCH₄ in China, especially for Sichuan Basin where it

presents consistent higher XCH₄ values than other parts of China. We further investigate the driving factors, including the CH₄ emissions and regional atmosphere dynamic transport, to study the variations of CH₄ concentration in the basin and evaluate the potential role of satellite-observed XCH₄ data in analyzing the regional variation of CH₄.

Our results show that the spatial distribution of GOSAT-XCH₄ is generally consistent with that of CH₄ emission, and abnormal high XCH₄ values can be seen in the Sichuan Basin, which is consistent with previous results from SCIAMACHY [10, 12]. The seasonal variation of XCH₄ is highly related to the CH₄ emissions from rice paddy fields during rice growing period from April to October and presents a difference feature from background CH₄ variation related to stronger CH₄ loss in summer due to chemical reaction. During the rice

harvesting season of August to September, XCH₄ data are higher than that in early stage of rice growing in April. However, the abnormal high XCH₄ data are shown in the winter when the CH₄ emissions from rice paddy fields are weak and the surface air temperature is low. By implementing the trajectory simulation using HYSPLIT in the basin, we found the typical closed topography of Sichuan Basin, which may lead to CH₄ accumulation and keep it from diffusion, is one possible reason for the extreme high XCH₄ value in winter. The influence of CH₄ emissions from sources other than rice paddies is also discussed and bottom-up emission inventory data show that they are not likely big causes of the observed winter high XCH₄ value in Sichuan Basin. It can be indicated that the regional variations of XCH₄ observed by GOSAT in Sichuan Basin are determined by not only the CH₄ emissions from ground sources but also very likely the regional topography and the related regional air transport.

Our result from studying the CH₄ variations in Sichuan Basin, especially the abnormal higher value during winter, and their driving factors demonstrate a certain potential of using GOSAT-XCH₄ for investigating the regional CH₄ changes. This study presents preliminary results of CH₄ in China, and a further investigation of the CH₄ in the basin is still necessary as more satellite observations of CH₄ with improving accuracy are available in the coming future to further study the CH₄ variations and regional emissions [40].

Conflict of Interests

The authors declare that there is no conflict of interests regarding the publication of this paper.

Acknowledgments

This work was supported by the Strategic Priority Research Program-Climatic Change (XDA05040401) and the National High Technology Research and Development Program of China (2012AA12A301). The authors are grateful for the valuable and excellent comments from the reviewer and editor and acknowledge the data products provided by NIES GOSAT Project (<https://data.gosat.nies.go.jp/gateway/gateway/MenuPage/open.do>) and China Meteorological Data Sharing System (<http://data.cma.gov.cn/>) and EDGAR (<http://edgar.jrc.ec.europa.eu/>). Masahiro Kawasaki, Masafumi Ohashi, and Yutaka Matsumi acknowledge the financial supports from JSPS, JST, and GRENE-ei of the Ministry of Education, Science, Culture and Sports of Japan.

References

- [1] K. B. Hogan, A. M. Thompson, and J. S. Hoffman, "Methane on the greenhouse agenda," *Nature*, vol. 354, no. 6350, pp. 181–182, 1991.
- [2] Q. He, T. Yu, X. F. Gu, T. H. Cheng, Y. Zhang, and D. H. Xie, "Global atmospheric methane variation and temporal-spatial distribution analysis based on ground-based and satellite data," *Remote Sensing Informations*, vol. 27, no. 4, p. 35, 2012.
- [3] R. X. Shen, X. J. Shangguan, M. Wang et al., "Methane emission from rice fields in Guangzhou region and the spatial variation of methane emission in China," *Advances in Earth Science*, vol. 10, no. 4, pp. 387–392, 1995.
- [4] L. X. Zhou, J. Tang, Y. P. Wen et al., "Characteristics of atmospheric methane concentration variation at Mt. Waliguan," *Quarterly Journal of Applied Meteorology*, vol. 9, no. 4, pp. 385–391, 1998.
- [5] WMO, "Strategy for the Implementation of the Global Atmosphere Watch Programme (2001–2007), a contribution to the implementation of the WMO longterm plan," GAW Report 142, 2001.
- [6] S. Kirschke, P. Bousquet, P. Ciais et al., "Three decades of global methane sources and sinks," *Nature Geoscience*, vol. 6, no. 10, pp. 813–823, 2013.
- [7] F. Deng, D. B. A. Jones, D. K. Henze et al., "Inferring regional sources and sinks of atmospheric CO₂ from GOSAT XCO₂ data," *Atmospheric Chemistry and Physics*, vol. 14, no. 7, pp. 3703–3727, 2014.
- [8] X. Xiong, C. Barnet, E. Maddy et al., "Characterization and validation of methane products from the Atmospheric Infrared Sounder (AIRS)," *Journal of Geophysical Research G: Biogeosciences*, vol. 113, no. 3, Article ID G00A01, 2008.
- [9] C. Frankenberg, J. F. Meirink, P. Bergamaschi et al., "Satellite cartography of atmospheric methane from SCIAMACHY on board ENVISAT: analysis of the years 2003 and 2004," *Journal of Geophysical Research D: Atmospheres*, vol. 111, no. 7, Article ID D07303, 2006.
- [10] S. Hayashida, A. Ono, S. Yoshizaki, C. Frankenberg, W. Takeuchi, and X. Yan, "Methane concentrations over Monsoon Asia as observed by SCIAMACHY: signals of methane emission from rice cultivation," *Remote Sensing of Environment*, vol. 139, pp. 246–256, 2013.
- [11] T. Yokota, Y. Yoshida, N. Eguchi et al., "Global concentrations of CO₂ and CH₄ retrieved from GOSAT: first preliminary results," *SOLA*, vol. 5, pp. 160–163, 2009.
- [12] X. Xiong, S. Houweling, J. Wei, E. Maddy, F. Sun, and C. Barnet, "Methane plume over south Asia during the monsoon season: satellite observation and model simulation," *Atmospheric Chemistry and Physics*, vol. 9, no. 3, pp. 783–794, 2009.
- [13] X. Y. Zhang, H. Jiang, Y. Q. Wang et al., "Spatial variations of atmospheric methane concentrations in China," *International Journal of Remote Sensing*, vol. 32, no. 3, pp. 833–847, 2011.
- [14] T. Hamazaki, A. Kuze, and K. Kondo, "Sensor system for greenhouse gas observing satellite (GOSAT)," in *Infrared Spaceborne Remote Sensing XII*, vol. 5543 of *Proceedings of SPIE*, International Society for Optics and Photonics, Denver, Colo, USA, November 2004.
- [15] Z. Zeng, L. Lei, L. Guo, L. Zhang, and B. Zhang, "Incorporating temporal variability to improve geostatistical analysis of satellite-observed CO₂ in China," *Chinese Science Bulletin*, vol. 58, no. 16, pp. 1948–1954, 2013.
- [16] L. Lei, X. Guan, Z. Zeng, B. Zhang, F. Ru, and R. Bu, "A comparison of atmospheric CO₂ concentration GOSAT-based observations and model simulations," *Science China Earth Sciences*, vol. 57, no. 6, pp. 1393–1402, 2014.
- [17] Z. Zeng, L. Lei, S. Hou, F. Ru, X. Guan, and B. Zhang, "A regional gap-filling method based on spatiotemporal variogram model of CO₂ columns," *IEEE Transactions on Geoscience and Remote Sensing*, vol. 52, no. 6, pp. 3594–3603, 2014.
- [18] J. X. Xia, L. J. Deng, and S. R. Zhang, "Effects of environmental factors on the Sichuan Basin rice quality," in *Proceedings of the China to Soil Society 10th National Congress and the 5th*

Member Representative Cross-Strait Academic Exchanges and Fertilizer Symposium for Agricultural and Environmental Soil Science Topics Articles, 2004.

- [19] X. C. Qin, L. P. Lei, M. Kawasaki et al., "Retrieval and analysis of atmospheric XCO₂ using ground-based spectral observation," *Spectroscopy and Spectral Analysis*, vol. 34, no. 7, pp. 1729–1735, 2014.
- [20] M. Kawasaki, H. Yoshioka, N. B. Jones et al., "Usability of optical spectrum analyzer in measuring atmospheric CO₂ and CH₄ column densities: inspection with FTS and aircraft profiles in situ," *Atmospheric Measurement Techniques*, vol. 5, no. 11, pp. 2593–2600, 2012.
- [21] <https://data.gosat.nies.go.jp/gateway/gateway/MenuPage/open.do>.
- [22] Y. Yoshida, N. Kikuchi, I. Morino et al., "Improvement of the retrieval algorithm for GOSAT SWIR XCO₂ and XCH₄ and their validation using TCCON data," *Atmospheric Measurement Techniques*, vol. 6, no. 6, pp. 1533–1547, 2013.
- [23] <http://data.cma.gov.cn/>.
- [24] World Meteorological Organization (WMO), WMO Greenhouse Gas Bulletin, No. 10, 2014.
- [25] <http://edgar.jrc.ec.europa.eu/>.
- [26] Q. Yue, G.-J. Zhang, and Z. Wang, "Preliminary estimation of methane emission and its distribution in China," *Geographical Research*, vol. 31, no. 9, pp. 1559–1570, 2012.
- [27] A. Stohl, "Trajectory statistics—a new method to establish source-receptor relationships of air pollutants and its application to the transport of particulate sulfate in Europe," *Atmospheric Environment*, vol. 30, no. 4, pp. 579–587, 1996.
- [28] D. D. Rousseau, D. Duzer, J. L. Etienne et al., "Pollen record of rapidly changing air trajectories to the North Pole," *Journal of Geophysical Research*, vol. 109, no. 6, 2004.
- [29] G. J. Zhang, *Temporal and Spatial Distribution of Column Vertical Density and Emission of Methane in China*, East China Normal University, 2011.
- [30] C. F. Wei, M. Gao, Q. Huang et al., "Effects of tillage-cropping systems on methane emission from year-round flooded paddy field in Southwest China," *Acta Pedologica Sinica*, vol. 37, no. 2, pp. 157–165, 2000.
- [31] F. Zhang, L. Zhou, and L. Xu, "Temporal variation of atmospheric CH₄ and the potential source regions at Waliguan, China," *Science China Earth Sciences*, vol. 56, no. 5, pp. 727–736, 2013.
- [32] D. Z. Chen, M.-X. Wang, X.-J. Shangguan, and J. Huang, "Methane emission from rice fields in the south-east China," *Advances in Earth Science*, vol. 8, no. 5, pp. 47–54, 1993.
- [33] Y. Y. Wang, W. W. Chen, Z. C. Zhao, and J.-X. Gu, "Characteristics and emission from cold paddy field in the Sanjiang Plain," *Transactions of the Chinese Society of Agricultural Engineering*, vol. 24, no. 10, pp. 170–176, 2008.
- [34] X. J. Shangguan, M. X. Wang, and R. X. Shen, "Regularity of methane emission from rice paddy fields," *Advance in Earth Science*, vol. 8, no. 5, p. 23, 1993.
- [35] X. K. Yu, N. Li, C. Y. Li, B. Shao, W. D. Wang, and X. L. Xie, "Effect of temperature on methane emissions from rice paddies," *Advances in Earth Science*, vol. 9, no. 5, pp. 54–56, 1994.
- [36] W.-D. Wang, X.-L. Xie, X.-J. Shangguan, D.-Z. Chen, and M.-X. Wang, "Laws of methane production in paddy soil in red earth hilly area of South China," *Rural Eco-Environment*, vol. 11, no. 3, pp. 11–14, 1995.
- [37] E. Matthews, I. Fung, and J. Lerner, "Methane emission from rice cultivation: geographic and seasonal distribution of cultivated areas and emissions," *Global Biogeochemical Cycles*, vol. 5, no. 1, pp. 3–24, 1991.
- [38] Intergovernmental Panel on Climate Change (IPCC), *Climate Change 2001: The Scientific Basis*, Cambridge University Press, New York, NY, USA, 2001.
- [39] World Meteorological Organization, WDCGG Data Report no. 36, 2012.
- [40] R. Parker, H. Boesch, and A. Cogan, "Methane observations from the Greenhouse Gases Observing SATellite: comparison to ground-based TCCON data and model calculations," *Geophysical Research Letters*, vol. 38, no. 15, Article ID L15807, 2011.

Research Article

Optical Properties of the Urban Aerosol Particles Obtained from Ground Based Measurements and Satellite-Based Modelling Studies

**Genrik Mordas, Nina Prokopciuk, Steigvilė Byčėnkiėnė,
Jelena Andriejauskienė, and Vidmantas Ulevicius**

SRI Center for Physical Sciences and Technology, Savanorių Avenue 231, LT-02300 Vilnius, Lithuania

Correspondence should be addressed to Steigvilė Byčėnkiėnė; steigvile.bycenkiene@ftmc.lt

Received 29 January 2015; Revised 29 April 2015; Accepted 2 May 2015

Academic Editor: Yang Liu

Copyright © 2015 Genrik Mordas et al. This is an open access article distributed under the Creative Commons Attribution License, which permits unrestricted use, distribution, and reproduction in any medium, provided the original work is properly cited.

Applications of satellite remote sensing data combined with ground measurements and model simulation were applied to study aerosol optical properties as well as aerosol long-range transport under the impact of large scale circulation in the urban environment in Lithuania (Vilnius). Measurements included the light scattering coefficients at 3 wavelengths (450, 550, and 700 nm) measured with an integrating nephelometer and aerosol particle size distribution (0.5–12 μm) and number concentration ($D_{\text{pa}} > 0.5 \mu\text{m}$) registered by aerodynamic particle sizer. Particle number concentration and mean light scattering coefficient varied from relatively low values of 6.0 cm^{-3} and 12.8 Mm^{-1} associated with air masses passed over Atlantic Ocean to relatively high value of 119 cm^{-3} and 276 Mm^{-1} associated with South-Western air masses. Analysis shows such increase in the aerosol light scattering coefficient (276 Mm^{-1}) during the 3rd of July 2012 was attributed to a major Sahara dust storm. Aerosol size distribution with pronounced coarse particles dominance was attributed to the presence of dust particles, while resuspended dust within the urban environment was not observed.

1. Introduction

The atmospheric aerosol particles have significant direct and indirect effects on air quality, climate, and human health [1]. The impacts of particles depend on their physical and chemical properties [2–4]. Thus, the characterization of the aerosol properties is crucial to understand many important processes in the atmosphere and to examine the energy balance of the Earth. The coming solar radiation is modified when it passes through the atmosphere by two main processes: the light scattering and the light absorption. The attenuation of the light by these processes has important climatic consequences [5, 6]. Aerosol particles both absorb and scatter the light, with the efficiency of the processes being highly dependent on their size and shape, chemical composition, morphology, and the wavelength of the incident radiation [7–9]. The maximum in scattering efficiency is found for aerosol particles in a range from 0.1 to $1 \mu\text{m}$ [7]. The integrating nephelometer is widely used for the measurement of the light scattering coefficient

[8, 9] in the marine boundary layer [10, 11] and in the urban environment [12].

Most studies have examined parameters, which depend on the quantity of aerosol, such as AOD, and parameters depend on the aerosol characteristics, such as the scattering Ångström exponent [13, 14]. Aerosol optical properties at regional scale have been studied since 1990s with model simulations [15–17] and satellite-based retrievals [18–20]. Satellite data from MODIS have been used to retrieve the AOD measurements of dust storm events [21, 22] as aerosol particles may be transported over long distances. Long-range transport of Saharan dust to the Northern parts of Europe was observed [23]. The climate and aerosol communities are increasingly relying on satellite-derived aerosol data for research as well as for monitoring [24]. Aerosol products from NASA's Moderate Imaging Spectrometer (MODIS) [25] sensor were utilized in the latest IPCC (AR5) assessment of climate (IPCC, 2014) [26]. Satellite-derived aerosol products, including those from MODIS, have been used for air quality

monitoring on both regional and local scales [27, 28]. One important and common aerosol parameter retrieved from satellite sensors is the aerosol optical depth (AOD). Generally, a higher AOD value indicates higher aerosol loading and therefore low visibility. It should be noted that the AOD values represent vertical column properties, whereas the PM_{2.5} or PM₁₀ data are the “surface” data. The AOD data do not always have good correlation with the PM data measured at the ground station. AOD is not an ideal indicator of the exact average size of particles as it depends on the absorption property of aerosols [29]. The satellite technique proved to be a suitable tool for the study of aerosol optical properties and long-range transport. Main advantage of satellite is the real time observation, which can be used to identify the origin and the path of air mass. This technique has its uncertainty limitations, but, in combination with surface based measurements such as nephelometer, important information about aerosol origin, type, and distribution can be derived [30]. This study is focused on detailed analysis of an intensive case of air pollution in Lithuania.

The current study describes the results combining data obtained by a nephelometer, aerosol particle sizer, and satellite-based datasets. Air masses from North and Eastern Europe, from the Atlantic Ocean, and from South-Western part of Europe have been advected to the monitoring site during the study period in accordance with back-trajectories and satellite images. It is shown in the study that only the integration of data from different instruments gives the possibility to properly characterize the contribution of different aerosol types (sizes) during long-range transport. A description of the experiment methodology is given in Section 2. Results are analyzed and discussed in Section 3.

2. Instrumentation and Methods

2.1. Sampling Location. Ground based measurements of the aerosol physical and optical properties were performed during July 2012 in Vilnius (Lithuania) (54°38′36″N, 25°10′58″E) at the top floor of the academic building of the Center for Physical Sciences and Technology campus. The inlet of sampling system was placed on the top floor about 12 m above the ground level. The location can be described as an urban background.

2.2. Nephelometer. The light scattering coefficient was measured at three wavelengths, $\lambda = 450, 550,$ and 700 nm, using an integrating nephelometer TSI model 3563. The nephelometer geometry restricts the sensing of the total aerosol scattering to angles between 7° and 170°. The nephelometer was operated at a 30 L/min flow rate. The measured values of the aerosol scattering coefficients (σ_{sp}) are recorded every 5 min and an automatic calibration is performed every 60 min for setting the instrument background level. The instrument background determines the detection limit of the light scattering measurement and it has been assessed as the standard deviation (SD) of the zero baseline measurements. The investigation of the nephelometer performance characteristics is presented by [31, 32]. On the front of the nephelometer was installed a 15 cm long stainless steel tube with a diameter of

30 mm in 60 degrees from horizontal and a connected vertical ~5 m length stainless steel tube with a diameter of 30 mm with open conductive inlet protection from precipitation. The sampled aerosol losses and the instrument cut-size were estimated by empirical relationship [33, 34]. The resulting calculated cut-size was 10 μm at a typical measured wind speed of 3 m/s.

The particle scattering coefficient σ_{sp} decreases with wavelength and can be described as

$$\sigma_{sp} = B\lambda^{-\alpha}, \quad (1)$$

where B is a constant known as the turbidity coefficient, λ is wavelength of light, and α is an Ångström exponent coefficient. Using the measured light scattering coefficient data at 450 and 700 nm wavelength pair, the corresponding values of the Ångström exponent can be calculated by the following equation:

$$\alpha = \frac{-\ln[\sigma_{sp}^{700}/\sigma_{sp}^{450}]}{\ln(700/450)}, \quad (2)$$

where σ_{sp}^{700} is the measured light scattering coefficient at the wavelength of 700 nm and σ_{sp}^{450} is the measured light scattering coefficient at the wavelength of 450 nm. The wavelength pair of 450 and 700 nm gives more accurate determination of the Ångström exponent because of the larger difference in the values of the measured light scattering coefficients. The calculated Ångström exponent describes the domination of the fine or coarse particles on the measured integrated light scattering coefficient. So, if there are high values of the Ångström exponent, then the fine particles of 0.1–1.0 μm had larger domination on the value of the measured date. Low α values (close to zero) indicate domination by coarse particles of 1.0–10 μm [35]. The determination of the Ångström exponent allows characterizing and selecting different sources of the aerosol particles. The light scattering coefficient is dependent on the aerosol particle number concentration and the particle size. However, if the particle size is smaller than the used wavelength, the efficiency of the light scattering is very low. Thus, the measured integrated light scattering coefficient is determined only by the optically detectable particles.

2.3. Aerodynamic Particle Sizer. The aerosol particle number concentration and the particle size distribution were investigated with the aerodynamic particle sizer of TSI model 3321. The APS measures the aerodynamic diameter of individual particles (from 0.5 to 20 μm) based on the particle velocities immediately downstream of a flow accelerating nozzle. The instrument was operated using the high total flow rate of 5 L/min (an aerosol flow is 1 L/min and a clean sheath flow is 4 L/min). The aerosol particle size distribution and the particle number concentration ($D_{pa} > 0.5 \mu\text{m}$) were determined in real time averaging the measured data every 5 minutes. The APS used individual sampling line. The sampling aerosol flow passed through PM10 impactor and a vertical ~2.5 m long stainless steel sampling tube (6 mm i.d.) before reaching the instruments. Particle losses in the line were estimated to be lower than 2%.

2.4. Air Mass Backward Trajectories Analysis. The air mass trajectories were calculated using the Hybrid Single-Particle Lagrangian Integrated Trajectories model Version 4 (HYSPPLIT4) [36]. 96-h backward trajectories at 500, 1500, and 2500 m a.g.l. were calculated to identify the origin of the air masses. The analysis of air masses allowed determining the most important sectors, which have an effect on the air quality in Lithuania. The dispersion model used meteorological data fields that were obtained from dataset archives.

2.5. CALIPSO, NAAPS, and MODIS Retrievals. The Navy Aerosol Analysis and Prediction System (NAAPS) has been used to explore the spatial distribution of the AOD. NAAPS was developed at the Naval Research Laboratory in Monterey, USA, based on the Danish Eulerian Hemispheric Model (DENM). The offline model NAAPS utilizes the meteorological analysis and forecast field from 0.5-degree Navy's Operational Global Analysis and Prediction System (NOGAPS) [37, 38]. The model calculation result is an optical depth at a wavelength of 550 nm for three components (sulphate, dust, and smoke). The dust distribution was simulated for aerosol particles of 1.0 μm in the diameter having a refractive index of $1.55 + 0.001i$. As a result, the dust distribution is illustrated by a common modeling parameter, an aerosol optical depth. Additionally, the AOD was determined by MODIS Terra and Aqua satellites using the calculation algorithm over land surface [39–42]. The aerosol optical depth is computed at 470, 550, and 660 nm wavelengths [43, 44]. However, the wavelength of 550 nm is more useful for our investigations because the same wavelength is used by the nephelometer and the NAAPS model. Dust plume layers were evaluated by the Cloud-Aerosol Lidar and Infrared Pathfinder Satellite Observation (CALIPSO) Level-2 aerosol products (Version-3.01) such as aerosol layer identification by total attenuated backscatter. Vertical feature masks were used to determine the heights of structures and to distinguish aerosols from cloud; the 532 nm total attenuated backscatter and depolarization ratio were checked.

3. Results and Discussion

3.1. Ground Based Measurements. The light scattering coefficients at 450, 550, and 700 nm and Ångström exponent are illustrated in Figure 1. Figure 1(a) shows that the 1 h averaged scattering coefficient values varied in the range from 4.0 to 369.0 Mm^{-1} . There is a similar trend in the variations of the light scattering coefficients at different wavelength. The average of the light scattering coefficient at 450, 550, and 700 nm was found to be 30.5 (SD = 23.8), 20.2 (SD = 16.7), and 12.8 (SD = 11.3) Mm^{-1} , respectively. The highest values for $\sigma_{\text{sp}}^{450} = 369$ and $\sigma_{\text{sp}}^{700} = 195 \text{ Mm}^{-1}$ were observed mostly at the beginning of the month. High positive correlations of 0.99 and 0.98 were found between 450 and 550 nm and 450 and 700 nm wavelengths. In order to use ground based measurements, data of the light scattering coefficient at 550 nm were selected investigating the trends of the particle optical properties and comparing the ground based measurements with the satellite determined AOD. Meanwhile, the light scattering coefficients at wavelength of 450 and 700 nm were

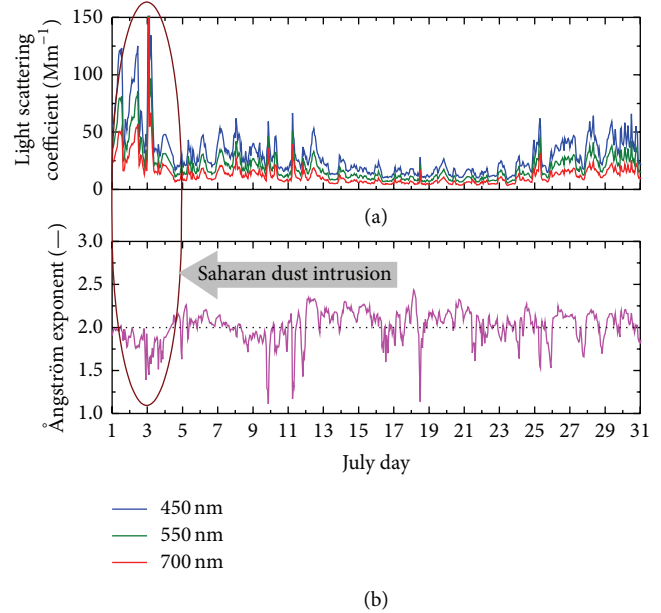


FIGURE 1: (a) The light scattering coefficient for the wavelength of 450, 550, and 700 nm during July 2012. (b) The calculated Ångström exponent for 450 and 700 nm wavelength pair filtered with a 2-point moving average filter. The oval highlighted area shows Saharan dust intrusion.

useful characterizing aerosol particle sources by Ångström exponent values.

The Ångström exponent (Figure 1(b)) analysis allowed us to determine the domination of the aerosol fine and coarse modes using scattering coefficient data [45]. Figure 1(b) shows that the typical Ångström exponent values were ranged from 1.1 to 2.4 with the average of ~ 2.0 (SD = 0.2). The positive fluctuation of the Ångström exponent up to averaged value was about 15% and presented the domination of the coarse particles. It is seen that the fluctuations of Ångström exponent values below average value were more pronounced ($\sim 45\%$) compared with the typical Ångström exponent mean value. The statistical analysis of the frequency distribution of Ångström exponent showed a peak of 2.0 that is typical for places affected by the urban or continental pollution [12, 46]. It is also shown that the aerosol particle optical properties during the 3rd of July could be strongly affected by the long-range transport (discussion in Section 3.3). It should be noted that extreme light scattering values at 700 nm occurred influencing aerosol number concentration as well (Figure 2). Consequently, the light scattering coefficients in conjunction with Ångström exponent and number concentration analysis can be helpful in determining the influence of the far located pollution sources on the regional air quality. The variation of the total particle number concentration and light scattering coefficient is presented in Figure 2.

Figure 2 shows that the typical number concentration varies between several particles and 40 cm^{-3} . The statistical examination showed that the mean aerosol number concentration was found to be 12 cm^{-3} (SD = 9 cm^{-3}) during the study period. However, several high peaks of the particle

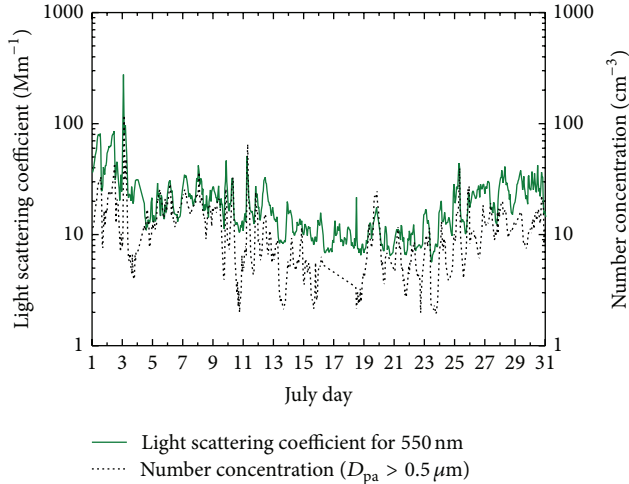


FIGURE 2: The variations of the light scattering coefficient (at 550 nm) and the particle number concentration ($D_{pa} > 0.5 \mu\text{m}$).

number concentration were observed on 1st (33 cm^{-3}), 2nd (43 cm^{-3}), 3rd (118 cm^{-3}), 11th (65 cm^{-3}), 19th (24 cm^{-3}), and 25th (39 cm^{-3}) of July. Therefore, below we focused our study on relationship between the particle number concentration and the light scattering coefficient (Figure 2). Statistical analysis of data showed a positive correlation ($R^2 = 0.82$) between light scattering coefficient and particle number concentration. The relationship between the light scattering coefficient (at 550 nm) and the particle number concentration ($D_{pa} > 0.5 \mu\text{m}$) is shown in Figure 3 as a solid line with top and bottom dot lines, which characterize the critical ranges of particle refractive indexes. A solid line with top and bottom dot lines characterizes the critical ranges of dispersion. The middle line, the so-called “bisector” (Figure 3), describes a linear dependence of the light scattering coefficient on the particle number concentration. Presumably, the urban aerosol is more heterogeneous according to the particle chemical composition. As a result, the refractive index varies in a wide range. Two dominating types of the urban aerosol particles were determined (Figure 3). Most important parameters for scattering, holding the refractive index constant, allowed exploring observed changes in scattering/absorption due to changes in particle size. The measured optical properties and the relationship between the light scattering coefficient (at 550 nm) and the particle number concentration ($D_{pa} > 0.5 \mu\text{m}$) in different air masses (Figure 3) arriving from different areas showed that the changes in particle size explain most of the variability in scattering. It is shown that increasing particle number concentration in the “low scattering sector” has a little effect on the value of the light scattering coefficient. The angle between two bisectors characterizes the homogeneity of the aerosol optical properties. Thus, the aerosol optical properties can be characterized by three empirical parameters: (1) the angle α_H between the “bisector” of “high scattering sector” and x -axis, (2) the angle α_L between the “bisector” of “low scattering sector” and x -axis, and (3) the angle β between two

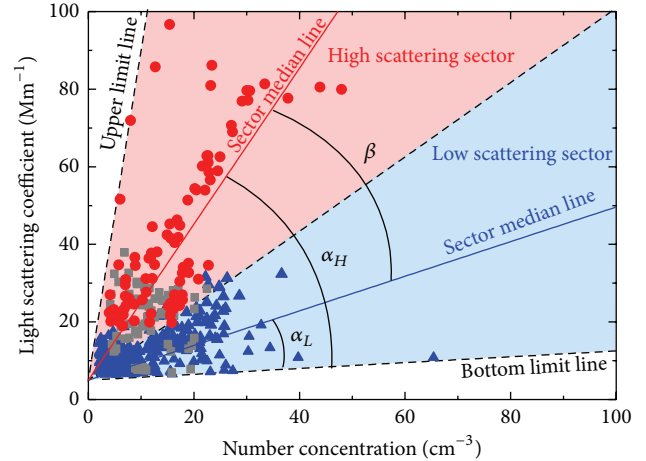


FIGURE 3: The relationship between the light scattering coefficient (at 550 nm) and the particle number concentration ($D_{pa} > 0.5 \mu\text{m}$) in different air masses arriving from Sahara storm area (red), Atlantic Ocean (blue), and continent (grey).

bisectors. We suggest that the data dispersion is dependent mainly on particle refractive indexes. So the homogeneous particles have a single refractive index. More detailed analysis of both sectors allowed concluding that the particles from “high scattering sector” were observed during the air mass transport from the Mediterranean Sea basin and the Sahara desert (Section 3.3).

The air masses arriving from Atlantic Ocean and continent sector are presented in “low scattering sector”

Contrary to the urban environment and for products of the burning processes, the Ångström exponent of the desert aerosol has very low values ($\alpha < 1$) [47]. For example, during the Saharan dust intrusion into Europe in October–November 2001, the Ångström exponent decreased up to 0.68, when its variation varied from 1.20 to 1.45 before and after the dust event in Kishinev [47]. The Ångström exponents lower than 0.5 during the Saharan dust events were also observed at the Global Atmospheric Watch (GAW) laboratory at the high alpine research station Jungfraujoch (3580 m above sea level) in Switzerland [48]. It should be noted that Ångström values of < 0.5 also can indicate the presence of sea salt particles in the clean marine environment [49]. Close to the dust source region (Sahara desert), the aerosol optical properties show mostly pure dust particles. However, after a long-range transport of the air masses, a vapour condensation, particle coagulation, sedimentation, and mixing with the other aerosol types could modify aerosol physical, chemical, and, as a result, optical properties [50] (Figure 3) (grey square dots). It is known that the mixing of the Sahara dust particles with anthropogenic aerosol has the largest effect on the aerosol properties [51, 52]. So it can be pointed out that the influence of the anthropogenic particles on the direct radiative forcing needs to take into account analyzing Sahara desert dust intrusions over the Mediterranean basin and continental Europe [53, 54].

TABLE 1: The comparison of the aerosol optical depth, the light scattering coefficient (at 550 nm), and the particle number concentration ($D_{pa} > 0.5 \mu\text{m}$) averaged daily.

July 2012	AOD, —	Light scat. coef., Mm^{-1}	Number conc., cm^{-3}
01	0.32	50.3	19
03	0.35	50.1	19
07	0.10	25.9	20
09	0.30	23.0	15
11	0.12	19.7	15
24	0.02	14.9	7
25	0.12	20.2	15
26	0.02	24.0	11
28	0.20	26.3	14
29	0.22	28.0	11
30	0.26	27.9	15

3.2. Satellite Data

3.2.1. Aerosol Optical Depth. The cloudy atmosphere prevented the continuous satellite measurements of the AOD over Vilnius during study period and the satellite AOD data consist of eleven events only (Table 1).

The table shows that AOD varied in a wide range from 0.02 to 0.35 compared with the typical AOD of 0.20 (Table 1, Figure 1). The satellite AOD measurements were compared with the ground based measurements of the light scattering coefficient and the particle number concentration ($D_{pa} > 0.5 \mu\text{m}$). Moderate positive correlation ($R = 0.7$, $P = 0.01$) was found between AOD and the light scattering coefficient as well as with particle number concentration ($R = 0.6$, $P = 0.01$). So the satellite measurements of the AOD are more useful for the global atmosphere aerosol distribution monitoring and the sun radiation absorption modelling. However, the characterization of optical properties of the local aerosol particles cannot be done accurately based only on the AOD satellite measurements over Lithuania. Thus, detailed characterization of the aerosol optical properties can be obtained based on the ground based measurements of the light scattering coefficient and the particle number concentration and size distribution.

3.3. Air Mass Clustering and Sahara Dust Event. By dividing the source regions into clusters (sectors), it was possible to classify and understand the relative influence of each sector in the typical characteristics of the air masses arriving over the measurement site (Vilnius) and to evaluate the dependence of these optical and physical aerosol particle properties on the dominant air mass type. To identify the origin of air masses arriving above study area, the backward trajectories were classified into five main clusters. Investigating the clusters revealed five sectors: one cluster was in the Northern direction, “N,” and two clusters were in the Western and South-Western direction, “W” and “SW.” One cluster was in the Eastern direction, “E.” Sector “N” defines continental polar air masses and includes Scandinavian region. “W”

and “SW” air masses reached Preila area from Atlantic Ocean but “W” passed dominantly through the industrial European regions (Great Britain, France, Germany, Czech Republic, and Poland), while “SW” originated over North Africa (Egypt and Morocco) and the Mediterranean Sea basin. Days under the influence of different air masses and Sahara dust outbreaks were identified by means of backward trajectories and satellite map analysis, and then aerosol number concentration and Ångström exponent levels were evaluated for these days. It was determined that cold air masses with the marine aerosol particles from the Atlantic Ocean passed over the Western region. On the contrary, sector “SW” is characterized by continental air masses with a significant load of dust due to the Saharan desert storm causing the advection of dust and aerosol particles into high-altitude layers from where they were transported to higher latitudes and study area. The air masses coming from this sector were expected to have low Ångström exponent values and a size distribution with a coarse mode dominating the accumulation mode. The industrial European region affected air masses and, as a result, aerosol particles properties; for example, East sector, “E,” combined the air masses from the continent (Ukraine, Belarus, and Russia). The “N” and “W” clusters’ air masses were influenced by cleanest conditions (especially on 20–25 July (not shown)), which were associated with the lowest light scattering coefficients and the lowest particle number concentrations ($D_{pa} > 0.5 \mu\text{m}$). The Western and Northern directions’ clusters represented 48% of the total trajectories. The South-Western cluster represented 29% and the Eastern cluster 23%. To illustrate the difference in the air mass origin, the events of each type were selected for case studies (Figures 4–6). The light scattering coefficient of 28 Mm^{-1} for 550 nm and the particle number concentration of 20 cm^{-3} were registered on 29 July (Figure 4).

Figures 4(c) and 4(d) indicate that the Ångström exponent is quite sensitive to the aerodynamic diameter of size distributions that are consistent with fine mode aerosols; that is, an increase in the Ångström exponent (9 p.m.) up to 2.2 showed increase in particles smaller than $\sim 0.4 \mu\text{m}$ (9 a.m.).

The effect of the local pollution sources can be seen on 14 July, despite the fact that the air masses from industrialized areas (sector “W”) of Europe were observed (Figure 5(a)). The aerosol number concentration increased during the morning traffic peak (5–7 a.m.) hour and again in the evening (7–10 p.m.). After the morning traffic peak hour, the number concentration rapidly decreased. This phenomenon can be explained by mixing within the developing boundary layer. Low mean light scattering coefficient of 12.8 Mm^{-1} and mean particle number concentration of 6.0 cm^{-3} were found (Figure 5(b)).

The calculated Ångström exponent varied from 2.0 to 2.3 (Figure 5(c)) with the mean value of 2.2. However, the high Ångström exponent values associated with coarse mode aerosols could significantly reduce the particle number concentration. It is also evident in Figure 5(d) that a decrease in the Ångström exponent values (3 a.m.) corresponds to an increase in number concentration in the fine mode aerodynamic diameter and coarse particles as well, highlighting

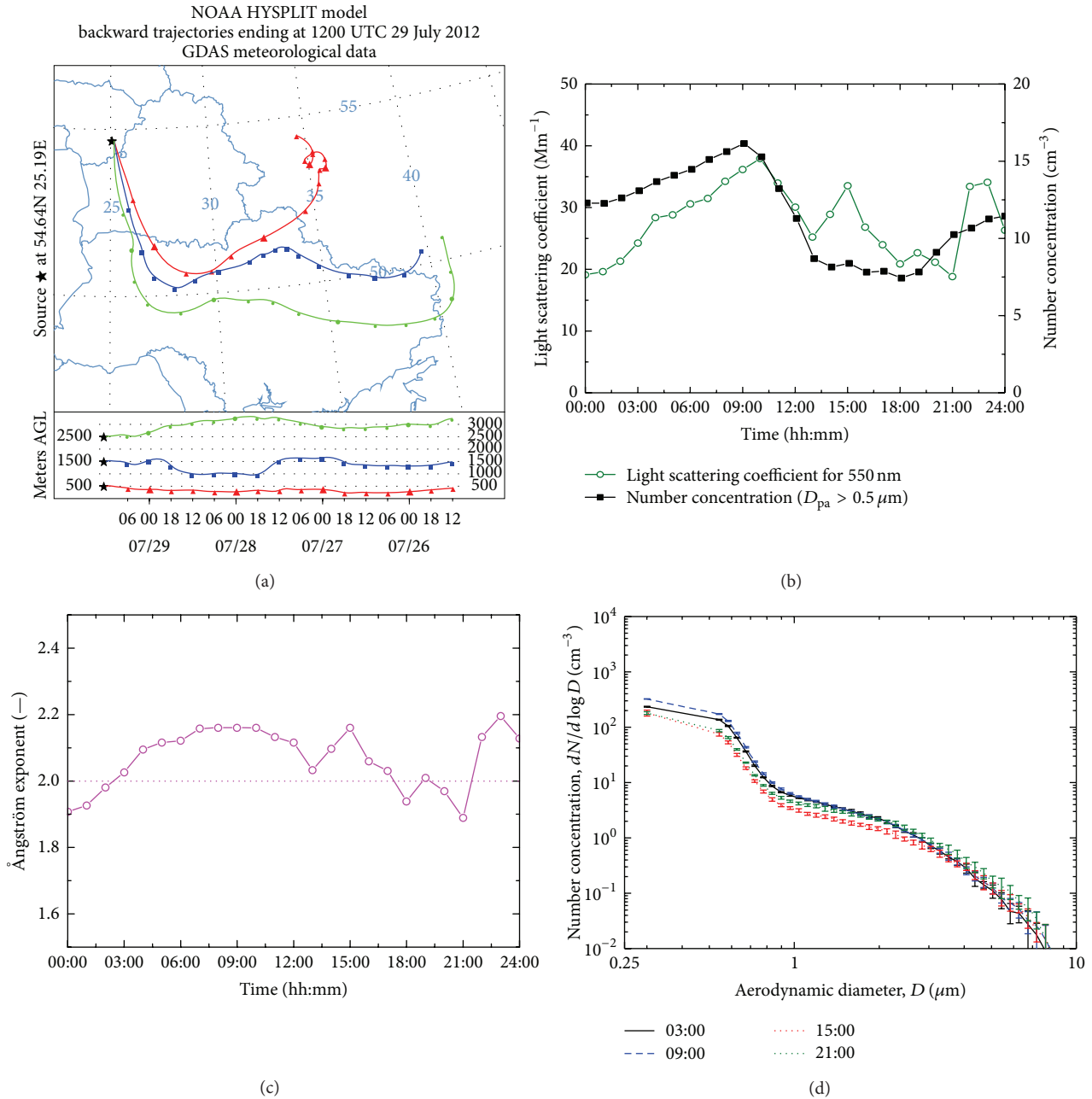


FIGURE 4: (a) Air parcel trajectory analysis from the National Oceanic and Atmospheric Administration (NOAA) Air Resources Laboratory (ARL) HYSPLIT model. For this analysis, the model was run backwards for 96 hours from 29th July 2012 at 12 UTC. Traces show the origin of air parcels at Vilnius at the 500 m (red), 1500 m (blue), and 2500 m (green) levels. (b) The variation of the measured and hourly averaged values of the light scattering coefficient at 550 nm and the particle number concentration. (c) The calculated Ångström exponent for 450 and 700 nm wavelength pair. (d) The particle size distributions.

intensive Saharan dust intrusion. The two-modal particle size distribution was observed with the mean particle diameters at 0.55 and $2 \mu m$ (Figure 5(d)).

As in the case of the 3rd of July, observations have suggested that increase of the light scattering coefficient and the particle number concentration ($D_{pa} > 0.5 \mu m$) was not influenced by local sources as the daily variation of both parameters was not pronounced (7–12 p.m.) (Figure 6(b)).

The particle number concentration started to increase at 3 a.m. when the local traffic influence was negligible. The mixing of different types of air mass (“SW” and “N” sectors) arriving at 3 a.m. could lead to a regional mixed plume with modified properties. Figure 6(a) highlights air masses arriving over Vilnius on the 3rd of July 2012 at 1500 m altitude transported from Sahara dust plume extended across the Atlantic Ocean toward Great Britain. This makes one think

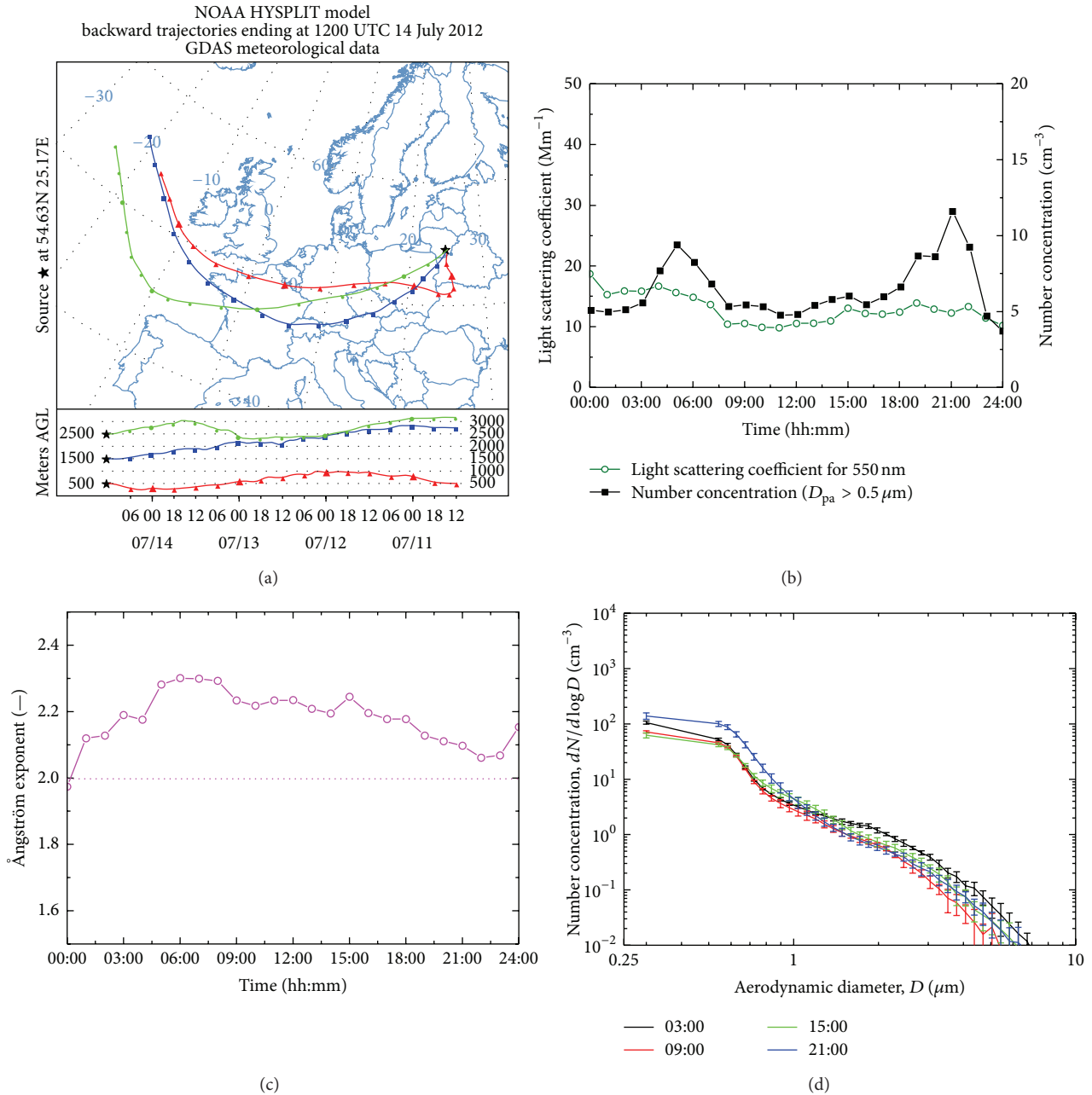


FIGURE 5: (a) Air parcel trajectory analysis from the National Oceanic and Atmospheric Administration (NOAA) Air Resources Laboratory (ARL) HYSPLIT model. For this analysis, the model was run backwards for 96 hours from 14 July 2012 at 12 UTC. Traces show the origin of air parcels at Vilnius at the 500 m (red), 1500 m (blue), and 2500 m (green) levels. (b) The variation of the measured and hourly averaged values of the light scattering coefficient at 550 nm and the particle number concentration. (c) The calculated Ångström exponent for 450 and 700 nm wavelength pair. (d) The particle size distributions.

that loading the atmosphere with coarse aerosol particles during this period is mainly Saharan dust type. Thick dust which blew through the Sahara desert in late June 2012 (<http://earthobservatory.nasa.gov/NaturalHazards/>) extended over parts of Algeria, Mali, Mauritania, Morocco, and Atlantic Ocean. To validate this idea, we used CALIPSO and NAAPS satellite data (Figures 7-8).

A sudden increase in the aerosol number concentration (118 cm^{-3}) and light scattering coefficient (276 Mm^{-1}) was

observed on 3 July over Lithuania which can be attributed to the Sahara dust event in Europe as well as to some industrial activities in that region. At the same time, Ångström exponent decreased to 1.4. The massive export of dust from Sahara is observed starting 23rd June, while the dust plume spread over Western parts of Europe including Lithuania only on the 3rd of July. Lidar data measured on 23 June 2012 between 9:30 UTC and 18:30 UTC confirm the existence of an aerosol layer in the atmosphere above Vilnius between 4 and

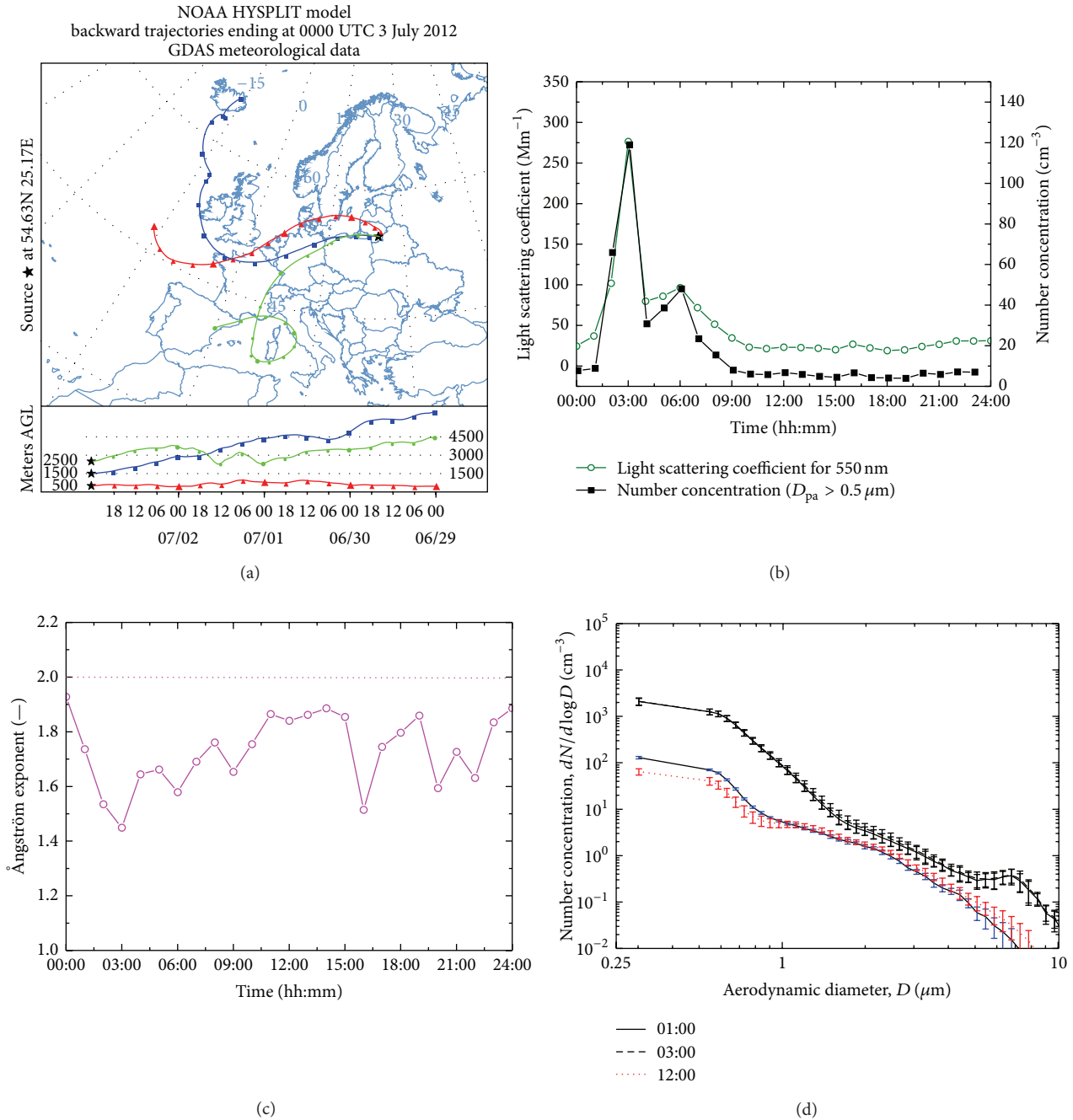


FIGURE 6: (a) Air parcel trajectory analysis from the National Oceanic and Atmospheric Administration (NOAA) Air Resources Laboratory (ARL) HYSPLIT model. For this analysis, the model was run backwards for 96 hours from 3 July 2012 at 00 UTC. Traces show the origin of air parcels at Vilnius at the 500 m (red), 1500 m (blue), and 2500 m (green) levels. (b) The variation of the measured and hourly averaged values of the light scattering coefficient at 550 nm and the particle number concentration. (c) The Ångström exponent for 450 and 700 nm wavelength pair. (d) The particle size distributions.

5 km, which descends in time below 3 km after 17:00 UTC. Grey shades indicate a change in aerosol type. Black region is due to laser stop for half an hour (Figure 7). The CALIPSO classification scheme identified two types of aerosol layers: pure dust (orange) and polluted dust (brown). In this study, aerosol (low confidence) could be defined as a mixture of pure

dust and anthropogenic pollution formed during air mass transport.

The particle size distribution showed two modes in the spectra at 0.6 and 6.70 μm . Comparing the particle size distribution at 3 a.m. and at 9 a.m., it is seen that the second mode disappeared and the particle number concentration

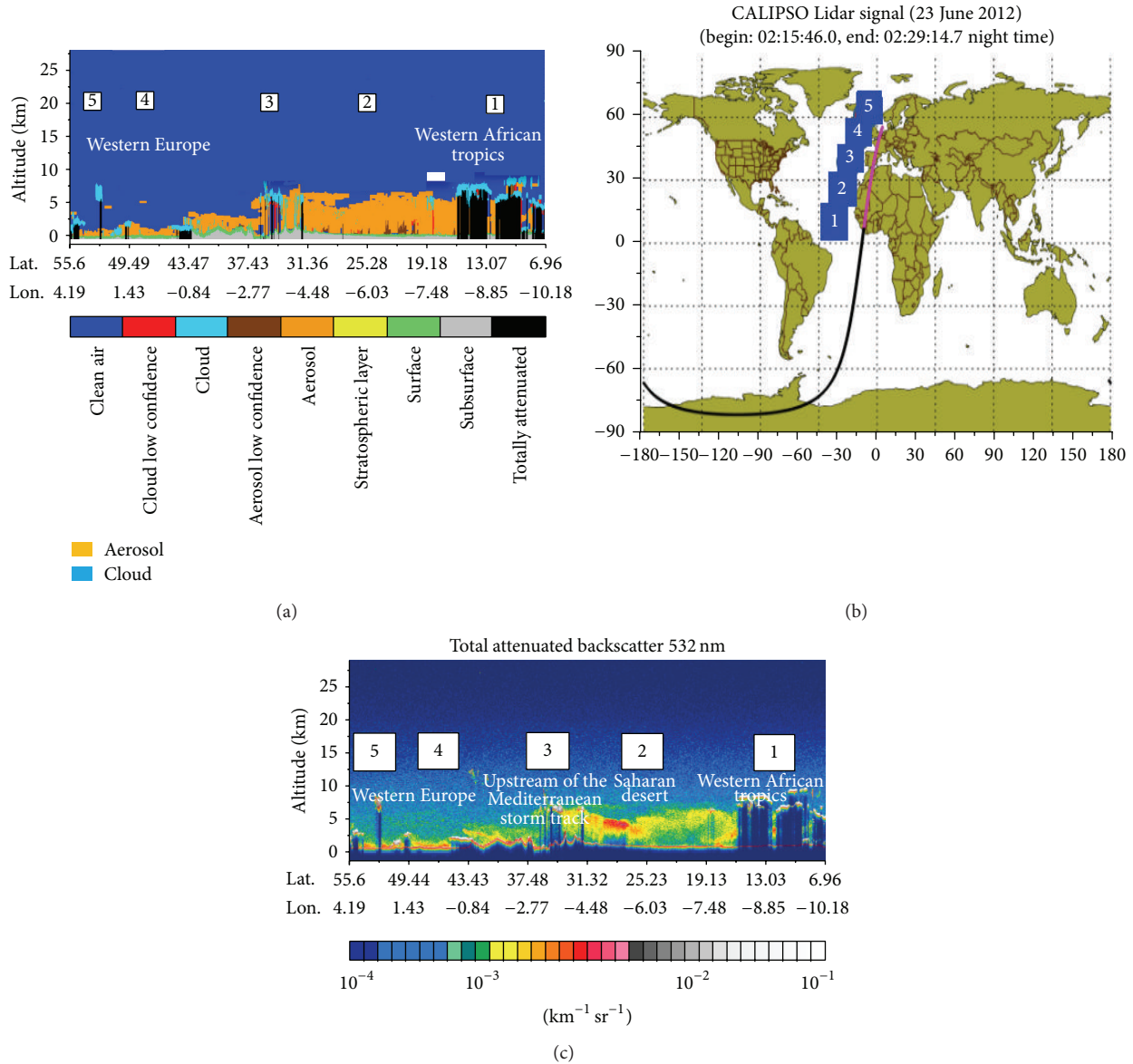


FIGURE 7: (a) Vertical feature mask shows the CALIPSO aerosol subtypes. (b-c) Total attenuated backscatter at 532 nm along with the orbit track (b) ($\text{km}^{-1} \text{sr}^{-1}$); the colour bars for attenuated backscatter show the colors assigned to ranges of attenuated backscatter, $\text{km}^{-1} \text{sr}^{-1}$; the vertical axes are annotated to indicate altitude in kilometers; the horizontal axes are annotated with latitude in kilometres (deg) and longitude (deg).

($D_{pa} > 0.5 \mu\text{m}$) and the light scattering coefficient decreased (Figure 6(d)).

AOD based on the satellite measurements shows that the penetration of the Sahara dust to the Baltic region (Figure 8) was observed from the 1st to the 8th of July 2012.

From the Atlantic Ocean, the dust formed the arc bents eastward in the direction of the Mediterranean Sea. Thus, the dust has spread over the Atlantic and turned to the North getting the UK islands. Another part of the dust crossed Europe directly from the Mediterranean Sea region through Italy, Germany, and Poland. Arriving air masses were mixed with the air from other regions. As a result, the aerosol was diluted with the clean air decreasing the high values

of the particle number concentration and light scattering coefficients. However, the event on the 3rd of July clearly illustrates increasing of the particle number concentration ($D_{pa} > 0.5 \mu\text{m}$) correlating with the rapid light scattering coefficient increasing. Also, the appearance of the second particle mode with the peak at $7 \mu\text{m}$ of the particle size distribution was observed. That presents the appearance of the dust particles in the local ambient air at the time when the local pollution sources have a minimal influence. The Sahara dust intrusions are very frequent in South Europe. In Spain, Italy, and Greece, the number of days when carrying of a dust from Northern Africa is observed makes up 20–30%. In the region of Belarus, such episodes make up 5–10% [55].

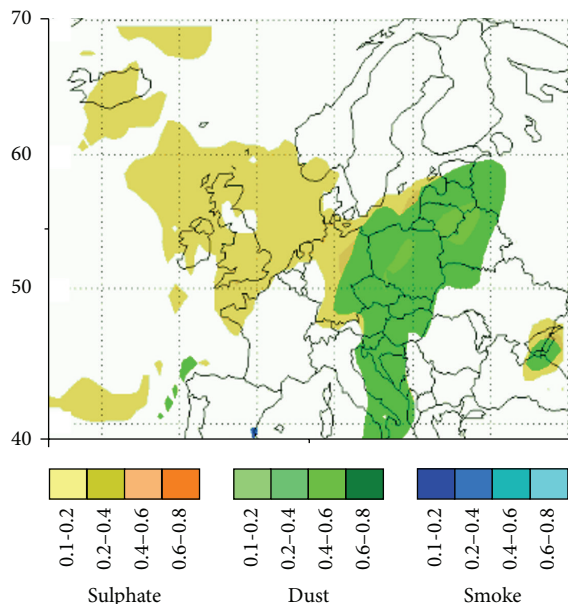


FIGURE 8: The dust distribution over Europe on the 3rd of July by satellite measurements and NAAPS distribution model.

The high dust particle number concentrations are observed close to the Mediterranean Sea region and they decreased over West and Central Europe coming highly diluted in the East region. The vertical profile of the Sahara dust over South Europe is distributed mainly at heights of 1.5–8 km [56]. With an increase in the distance from Sahara storm location, the average height of the dust layer increased. For example, in the region of Belarus, the dust layer concentrates at a height of 3–8 km [56]. Thus, the air masses from the Sahara region transported the sand dust over Lithuania in the middle free troposphere.

4. Conclusions

The ground based measurements of the light scattering coefficients for 450, 550, and 700 nm, the particle number concentration ($D_{pa} > 0.5 \mu\text{m}$), and the particle size distribution from 0.5 to $12 \mu\text{m}$ in conjunction with satellite measurements were investigated during July 2012 in urban environment. The investigation of the air mass backward trajectories and the regional AOD distribution over Europe allowed determining the far located air pollution sources and their effect on the typical local aerosol physical and optical properties. It was determined that the cleanest air masses arrived from the Atlantic Ocean and Scandinavia. The trends observed in the AOD and the Ångström exponent were consistent with the dependences found in the size distributions. The major source of small particles occurred when the air mass crossed the industrialized areas of Europe or was sourced locally, pointing to the influence of anthropogenic particles related to both urban and industrial pollution. Inversely, the major contribution of coarse particles occurred when the dominant air masses were transported from Sahara dust plume extended across the Atlantic Ocean toward Great Britain. As

a result, the light scattering coefficient suddenly increased to 276 Mm^{-1} and the particle number concentration increased up to 118 cm^{-3} , while the Ångström exponent decreased to 1.4. The measurements of the optical and physical particle properties determined two dominating types of the aerosol particles dividing them into two sectors “the high scattering sector” and “the low scattering sector” described by three parameters $\alpha_H = 63.6^\circ$, $\alpha_L = 24.1^\circ$, and $\beta = 39.5^\circ$. It was evaluated that aerosol properties depended on the air mass properties. For example, “the high scattering sector” consists of the aerosol particles from the Mediterranean Sea region, while “low scattering sector” is formed by particles from the Atlantic Ocean.

The optical property characterization of the local aerosol particles cannot be done accurately based only on the satellite measurements of the AOD. The most detailed characterization can be obtained referring to the ground based measurements of the light scattering coefficient, the particle number concentration, and the particle size distribution.

Conflict of Interests

The authors declare that they have no competing interests as defined by this journal or other interests that might be perceived to influence the results and discussion reported in this paper.

Acknowledgment

This research was partially supported by FP7 TRANSPHORM.

References

- [1] C. A. Pope, D. W. Dockery, and J. Schwartz, “Review of epidemiological evidence of health effects of particulate air pollution,” *Inhalation Toxicology*, vol. 7, no. 1, pp. 1–18, 1995.
- [2] H. L. Horvath, A. Arboledas, F. J. Olmo et al., “Optical characteristics of the aerosol in Spain and Austria and its effect on radiative forcing,” *Journal of Geophysical Research*, vol. 107, no. 19, p. 4386, 2002.
- [3] D. Meloni, A. di Sarra, T. di Iorio, and G. Fiocco, “Influence of the vertical profile of Saharan dust on the visible direct radiative forcing,” *Journal of Quantitative Spectroscopy and Radiative Transfer*, vol. 93, no. 4, pp. 397–413, 2005.
- [4] M. Santese, F. De Tomasi, and M. R. Perrone, “Advection patterns and aerosol optical and microphysical properties by AERONET over south-east Italy in the central Mediterranean,” *Atmospheric Chemistry and Physics*, vol. 8, no. 7, pp. 1881–1896, 2008.
- [5] M. O. Andreae and P. J. Crutzen, “Atmospheric aerosols: biogeochemical sources and role in atmospheric chemistry,” *Science*, vol. 276, no. 5315, pp. 1052–1058, 1997.
- [6] Intergovernmental Panel on Climate Change (IPCC), *The Scientific Basis. Contribution of Working Group I to the Third Assessment Report of the Intergovernmental Panel on Climate Change*, Cambridge University Press, New York, NY, USA, 2001.
- [7] L. McInnes, M. Bergin, J. Ogren, and S. Schwartz, “Apportionment of light scattering and hygroscopic growth to aerosol composition,” *Geophysical Research Letters*, vol. 25, no. 4, pp. 513–516, 1998.

- [8] E. Mészáros, A. Molnár, and J. Ogren, “Scattering and absorption coefficients vs. chemical composition of fine atmospheric aerosol particles under regional conditions in Hungary,” *Journal of Aerosol Science*, vol. 29, no. 10, pp. 1171–1178, 1998.
- [9] L. W. Richards, S. H. Alcorn, C. McDade et al., “Optical properties of the San Joaquin Valley aerosol collected during the 1995 integrated monitoring study,” *Atmospheric Environment*, vol. 33, no. 29, pp. 4787–4795, 1999.
- [10] K. Chamailard, C. Kleefeld, S. G. Jennings, D. Ceburnis, and C. D. O’Dowd, “Light scattering properties of sea-salt aerosol particles inferred from modeling studies and ground-based measurements,” *Journal of Quantitative Spectroscopy and Radiative Transfer*, vol. 101, no. 3, pp. 498–511, 2006.
- [11] C. Kleefeld, C. D. O’Dowd, S. O’Reilly et al., “Relative contribution of submicron and supermicron particles to aerosol light scattering in the marine boundary layer,” *Journal of Geophysical Research*, vol. 107, no. 19, 2002.
- [12] H. Lyamani, F. J. Olmo, and L. Alados-Arboledas, “Light scattering and absorption properties of aerosol particles in the urban environment of Granada, Spain,” *Atmospheric Environment*, vol. 42, no. 11, pp. 2630–2642, 2008.
- [13] M. Z. Jacobson, “A physically-based treatment of elemental carbon optics: implications for global direct forcing of aerosols,” *Geophysical Research Letters*, vol. 27, no. 2, pp. 217–220, 2000.
- [14] P. J. Sheridan, E. Andrews, J. A. Ogren, J. L. Tackett, and D. M. Winker, “Vertical profiles of aerosol optical properties over central Illinois and comparison with surface and satellite measurements,” *Atmospheric Chemistry and Physics*, vol. 12, no. 23, pp. 11695–11721, 2012.
- [15] J. E. Penner, M. Andreae, H. Annegarn et al., “Aerosols, their direct and indirect effects,” in *Climate Change 2001: The Scientific Basis, Contribution of Working Group I to the Third Assessment Report of the Intergovernmental Panel on Climate Change*, J. T. Houghton, Y. Ding, D. J. Griggs et al., Eds., pp. 289–348, Cambridge University Press, Cambridge, UK, 2001.
- [16] H. Liao and J. H. Seinfeld, “Global impacts of gas-phase chemistry-aerosol interactions on direct radiative forcing by anthropogenic aerosols and ozone,” *Journal of Geophysical Research D: Atmospheres*, vol. 110, no. 18, Article ID D18208, 2005.
- [17] B. Zhuang, Q. Liu, T. Wang et al., “Investigation on semi-direct and indirect climate effects of fossil fuel black carbon aerosol over China,” *Theoretical and Applied Climatology*, vol. 114, no. 3–4, pp. 651–672, 2013.
- [18] N. Bellouin, O. Boucher, D. Tanré, and O. Dubovik, “Aerosol absorption over the clear-sky oceans deduced from POLDER-1 and AERONET observations,” *Geophysical Research Letters*, vol. 30, no. 14, p. 1748, 2003.
- [19] J. Zhang, S. A. Christopher, L. A. Remer, and Y. J. Kaufman, “Shortwave aerosol radiative forcing over cloud-free oceans from Terra: 2. Seasonal and global distributions,” *Journal of Geophysical Research D: Atmospheres*, vol. 110, no. 10, pp. 1–10, 2005.
- [20] S. A. Christopher, J. Zhang, Y. J. Kaufman, and L. A. Remer, “Satellite-based assessment of top of atmosphere anthropogenic aerosol radiative forcing over cloud-free oceans,” *Geophysical Research Letters*, vol. 33, no. 15, Article ID L15816, 2006.
- [21] A. K. Prasad, H. El-Askary, and M. Kafatos, “Implications of high altitude desert dust transport from Western Sahara to Nile Delta during biomass burning season,” *Environmental Pollution*, vol. 158, no. 11, pp. 3385–3391, 2010.
- [22] R. Gautam, Z. Liu, R. P. Singh, and N. C. Hsu, “Two contrasting dust-dominant periods over India observed from MODIS and CALIPSO data,” *Geophysical Research Letters*, vol. 36, no. 6, Article ID L06813, 2009.
- [23] M. Kulmala, A. Asmi, H. K. Lappalainen et al., “Introduction: European Integrated Project on Aerosol Cloud Climate and Air Quality Interactions (EUCAARI) integrating aerosol research from nano to global scales,” *Atmospheric Chemistry and Physics*, vol. 9, no. 23, pp. 2825–2841, 2009.
- [24] R. C. Levy, L. A. Remer, R. G. Kleidman et al., “Global evaluation of the Collection 5 MODIS dark-target aerosol products over land,” *Atmospheric Chemistry and Physics*, vol. 10, no. 21, pp. 10399–10420, 2010.
- [25] V. V. Salomonson, W. L. Barnes, P. W. Maymon, H. E. Montgomery, and H. Ostrow, “MODIS: advanced facility instrument for studies of the earth as a system,” *IEEE Transactions on Geoscience and Remote Sensing*, vol. 27, no. 2, pp. 145–153, 1992.
- [26] IPCC, *Climate Change 2014: Impacts, Adaptation, and Vulnerability, Part A: Global and Sectoral Aspects*, Contribution of Working Group II to the Fifth Assessment Report of the Intergovernmental Panel on Climate Change, edited by C. B. Field, V. R. Barros, D. J. Dokken et al., Cambridge University Press, New York, NY, USA, 2014.
- [27] J. Al-Saadi, J. Szykman, R. B. Pierce et al., “Improving national air quality forecasts with satellite aerosol observations,” *Bulletin of the American Meteorological Society*, vol. 86, no. 9, pp. 1249–1261, 2005.
- [28] A. van Donkelaar, R. V. Martin, M. Brauer et al., “Global estimates of ambient fine particulate matter concentrations from satellite-based aerosol optical depth: development and application,” *Environmental Health Perspectives*, vol. 118, no. 6, pp. 847–855, 2010.
- [29] J. Wang and S. A. Christopher, “Intercomparison between satellite-derived aerosol optical thickness and PM_{2.5} mass: implications for air quality studies,” *Geophysical Research Letters*, vol. 30, no. 21, article 2095, 2003.
- [30] A. Nemuc, L. Belegante, and R. Radulescu, “One year of sun-photometer measurements in Romania,” *Romanian Journal of Physics*, vol. 56, no. 3–4, pp. 550–562, 2011.
- [31] T. L. Anderson, D. S. Covert, S. F. Marshall et al., “Performance characteristics of a high-sensitivity, three-wavelength, total scatter/backscatter nephelometer,” *Journal of Atmospheric and Oceanic Technology*, vol. 13, no. 5, pp. 967–986, 1996.
- [32] T. L. Anderson and J. A. Ogren, “Determining aerosol radiative properties using the TSI 3563 integrating nephelometer,” *Aerosol Science and Technology*, vol. 29, no. 1, pp. 57–69, 1998.
- [33] C. Kleefeld, C. D. O’Dowd, S. O’Reilly et al., “Relative contribution of submicron and supermicron particles to aerosol light scattering in the marine boundary layer,” *Journal of Geophysical Research D: Atmospheres*, vol. 107, no. 19, article 8103, 2002.
- [34] K. Willeke and P. A. Baron, Eds., *Aerosol Measurement: Principles, Techniques, and Applications*, Van Nostrand Reinhold, New York, NY, USA, 1993.
- [35] B. B. Chen, L. G. Sverdlik, and S. A. Imashev, “Dynamics of accumulation mode particles at transboundary aerosol transport,” *Herald of the KRSU Series: Physics*, vol. 9, no. 11, pp. 73–85, 2009.
- [36] R. R. Draxler and G. D. Rolph, *HYSPLIT (Hybrid Single-Particle Lagrangian Integrated Trajectory) Model Access via NOAA ARL READY Website*, NOAA Air Resources Laboratory, Silver Spring, Md, USA, 2015, <http://ready.arl.noaa.gov/HYSPLIT.php>.

- [37] T. F. Hogan and T. E. Rosmond, "The description of the Navy Operational Global Atmospheric Prediction System's spectral forecast model," *Monthly Weather Review*, vol. 119, no. 8, pp. 1786–1815, 1991.
- [38] T. F. Hogan and L. R. Brody, "Sensitivity studies of the Navy's global forecast model parameterizations and evaluation of improvements to NOGAPS," *Monthly Weather Review*, vol. 121, no. 8, pp. 2373–2395, 1993.
- [39] Y. J. Kaufman, D. Tanré, L. A. Remer, E. F. Vermote, A. Chu, and B. N. Holben, "Operational remote sensing of tropospheric aerosol over land from EOS moderate resolution imaging spectroradiometer," *Journal of Geophysical Research D: Atmospheres*, vol. 102, no. 14, pp. 17051–17067, 1997.
- [40] L. Remer, R. Kleidman, R. Levy et al., "Global aerosol climatology from the MODIS satellite sensors," *Journal of Geophysical Research: Atmospheres*, vol. 113, no. D14, Article ID D14S07, 2008.
- [41] R. C. Levy, L. A. Remer, S. Mattoo, E. F. Vermote, and Y. J. Kaufman, "Second-generation operational algorithm: retrieval of aerosol properties over land from inversion of Moderate Resolution Imaging Spectroradiometer spectral reflectance," *Journal of Geophysical Research D: Atmospheres*, vol. 112, no. 13, Article ID D13211, 2007.
- [42] R. Levy, L. Remer, D. Tanré, S. Mattoo, Y. Kaufman, and D. Tanré, "Algorithm for remote sensing of tropospheric aerosol over dark targets from MODIS: collections 005 and 051: revision 2," MODIS Algorithm Theoretical Basis Document, 2009.
- [43] D. A. Chu, Y. J. Kaufman, C. Ichoku, L. A. Remer, D. Tanré, and B. N. Holben, "Validation of MODIS aerosol optical depth retrieval over land," *Geophysical Research Letters*, vol. 29, no. 12, 2002.
- [44] C. Ichoku, L. A. Remer, Y. J. Kaufman et al., "MODIS observation of aerosols and estimation of aerosol radiative forcing over southern Africa during SAFARI 2000," *Journal of Geophysical Research D: Atmospheres*, vol. 108, no. 13, article 8499, 2003.
- [45] P. B. Russell, R. W. Bergstrom, Y. Shinozuka et al., "Absorption Ångström Exponent in AERONET and related data as an indicator of aerosol composition," *Atmospheric Chemistry and Physics*, vol. 10, no. 3, pp. 1155–1169, 2010.
- [46] M. Vrekoussis, E. Liakakou, M. Koçak et al., "Seasonal variability of optical properties of aerosols in the Eastern Mediterranean," *Atmospheric Environment*, vol. 39, no. 37, pp. 7083–7094, 2005.
- [47] A. Aculinin, V. Smicov, B. Holben et al., "Variability of total column ozone content measured at the Kishinev site, Moldova," *Moldavian Journal of the Physical Sciences*, vol. 5, no. 2, pp. 240–248, 2006.
- [48] C. Chou, O. Stetzer, E. Weingartner, Z. Jurányi, Z. A. Kanji, and U. Lohmann, "Ice nuclei properties within a Saharan dust event at the Jungfraujoch in the Swiss Alps," *Atmospheric Chemistry and Physics*, vol. 11, no. 10, pp. 4725–4738, 2011.
- [49] C. D. O'Dowd, M. C. Facchini, F. Cavalli et al., "Biogenically driven organic contribution to marine aerosol," *Nature*, vol. 431, no. 7009, pp. 676–680, 2004.
- [50] S. Bauer, E. Bierwirth, M. Esselborn et al., "Airborne spectral radiation measurements to derive solar radiative forcing of Saharan dust mixed with biomass burning smoke particles," *Tellus, Series B: Chemical and Physical Meteorology*, vol. 63, no. 4, pp. 742–750, 2011.
- [51] K. Kandler, N. Benker, U. Bundke et al., "Chemical composition and complex refractive index of Saharan Mineral Dust at Izaña, Tenerife (Spain) derived by electron microscopy," *Atmospheric Environment*, vol. 41, no. 37, pp. 8058–8074, 2007.
- [52] G. Gangoiti, L. Alonso, M. Navazo, J. A. García, and M. M. Millán, "North African soil dust and European pollution transport to America during the warm season: hidden links shown by a passive tracer simulation," *Journal of Geophysical Research D: Atmospheres*, vol. 111, no. 10, Article ID D10109, 2006.
- [53] E. Gerasopoulos, M. O. Andreae, C. S. Zerefos et al., "Climatological aspects of aerosol optical properties in Northern Greece," *Atmospheric Chemistry and Physics*, vol. 3, no. 6, pp. 2025–2041, 2003.
- [54] M. R. Perrone and A. Bergamo, "Direct radiative forcing during Sahara dust intrusions at a site in the Central Mediterranean: anthropogenic particle contribution," *Atmospheric Research*, vol. 101, no. 3, pp. 783–798, 2011.
- [55] Report on the Research Work, *Assessment Large-Scale and Cross-Border Transfer Pollution in the Atmosphere with Use of Systems Remote Sensing and Data Global and Regional Measuring Networks*, Institute of Physics of Stepanov, Minsk, Belarus, 2010, <http://scat.bas-net.by/~lidarteam/Transboundary%20transport-ru/Report-2008.pdf>.
- [56] A. Papayannis, V. Amiridis, L. Mona et al., "Systematic lidar observations of Saharan dust over Europe in the frame of EARLINET (2000–2002)," *Journal of Geophysical Research*, vol. 113, Article ID D10204, 2008.

Research Article

Satellite Observed Aerosol Optical Thickness and Trend around Megacities in the Coastal Zone

Xuepeng Zhao

National Centers for Environmental Information (NCEI), NOAA/NESDIS, Asheville, NC 28801, USA

Correspondence should be addressed to Xuepeng Zhao; xuepeng.zhao@noaa.gov

Received 20 January 2015; Accepted 30 April 2015

Academic Editor: Liangfu Chen

Copyright © 2015 Xuepeng Zhao. This is an open access article distributed under the Creative Commons Attribution License, which permits unrestricted use, distribution, and reproduction in any medium, provided the original work is properly cited.

Nearly 30-year aerosol optical thickness (AOT) climate data record (CDR) derived from the operational satellite observations of National Ocean and Atmospheric Administration (NOAA) Advanced Very High Resolution Radiometer (AVHRR) is used to study the AOT trends over seventeen megacities in the coast zone (MCCZ). Linear trends are derived from monthly and seasonal mean AOT in the past three decades and used in the analysis. The results indicate the following: (1) AOT around a MCCZ in fast developing countries has relatively high value and a positive trend with a confidence level generally above 95%; (2) AOT around a MCCZ in industrialized countries has relatively low value and a negative trend with a confidence level generally above 95%; (3) AOT values and their trends show distinct seasonal variations in MCCZ, which can be explained somewhat by the seasonal variations of meteorological conditions. AOT trend is an effective index for examining the efficacy of air pollution control policies implemented for these megacities.

1. Introduction

About half of the world's population lives in urban areas today due to convenient living facilities and the opportunity of a better quality of life, driving the formation of many rapidly growing urban centers or agglomerations, called megacities. Here, a megacity is defined as a large urban agglomeration with populations exceeding 10 million inhabitants. The majority of these urban megacities are located in a coastal zone or a zone with distinct coastal influence [1], which are called megacities in the coastal zone (MCCZ) hereafter. The concentrations of people in MCCZ and the related human activities (e.g., construction, transportation, energy generation, industrial production, etc.) pose serious challenge to the ecological environment of MCCZ [1, 2]. For example, air and water pollutions associated with human activities have become one of the most imminent environmental issues of MCCZ in recent decades [3–6], especially in the developing countries where limited resources are available for addressing the pollution issues.

The scale of air and water pollutions in MCCZ can be hundreds to thousands of kilometers in the atmosphere and

tens to hundreds of kilometers in the ocean and has the potential to contribute significantly to climate change [1, 7–10]. Long-term continuous monitoring and analysis on the distribution and evolution of air pollutants are the necessary effort to better manage, control, and mitigate the air pollution in MCCZ [7, 11]. One primary reason for monitoring ambient air pollutants is to provide information for estimating their potential effects, particularly on environmental and human health. Considering that satellite remote sensing can detect air pollutants and track their transport from local and regional scales to the globe, long-term satellite observations of air pollution have been identified as an effective measurement to characterize air pollution in MCCZ [6, 7].

One of the most important ambient air pollutants is particulate matter (PM), which refers to tiny pieces of solid or liquid particles suspended in the air and is also called atmospheric aerosols. Aerosols in urban environment not only cause serious air quality and health issues but also serve as important cooling and warming agent for climate change due to its scattering and absorbing of solar and earth radiations [9] and serving as cloud condensation nuclei (CCN) [12]. Aerosol optical thickness (AOT) can be used

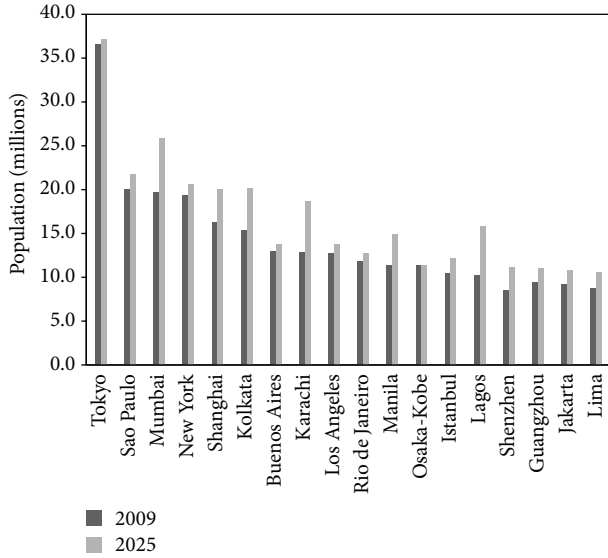


FIGURE 1: Identified seventeen megacities in the coastal zone (MCCZ) in the study and their population in 2009 and 2025, respectively.

as an effective optical measure of PM amount for urban air pollution. In general, a high or low AOT value corresponds to a high or low PM amount assuming most of the aerosols are near ground or in planetary boundary layer (PBL) in an urban environment. Thus, long-term observation of AOT over MCCZ from satellite can provide information on the changes and trends of air pollution, which can be used to evaluate the efficiency of the measures and policies implemented for air pollution control and air quality improvement in MCCZ.

In this paper, we will analyze AOT and its trend around MCCZ observed in the past three decades from the Advanced Very High Resolution Radiometer (AVHRR) onboard polar operational satellites of National Ocean and Atmospheric Administration (NOAA). The paper is arranged as follows: Section 2 introduces selected MCCZ and the AVHRR satellite AOT data; trend analysis approach is briefly described in Section 3; variation of monthly mean AOT and its trend for the selected MCCZ are studied in Section 4; seasonal features of AOT and its trend are examined in Section 5; summary and conclusions are given in the close section.

2. Selected MCCZ and Satellite Data

Seventeen urban centers in the coastal zone with inhabitants going to exceed 10 million in 2025 are selected as MCCZ in our current study. Figure 1 shows the population of these 17 MCCZ in 2009 and 2025, respectively, based on the data of United Nations [1, 13]. Among these megacities, there are five (Tokyo, Osaka-Kobe, New York, Los Angeles, and Istanbul) in developed countries and the rest are in developing countries. There are five megacities (Sao Paulo, Rio de Janeiro, Buenos Aires, Lima, and Jakarta) in the south hemisphere (SH) and the others are in the north hemisphere (NH). Fifteen out of the seventeen megacities are in the coastal zone of tropical

or subtropical regions and the other two (New York and Istanbul) are in the coasts of NH temperate zone.

Version 2 of NOAA operational AVHRR satellite AOT climate data record (CDR) [14, 15] is used in this study. AVHRR AOT CDR is derived over global water (or ocean) surface at $0.63 \mu\text{m}$ channel using a two-channel AVHRR aerosol retrieval algorithm [16] from the AVHRR clear-sky reflectance, which is determined from the NOAA Pathfinder Atmospheres-Extended (PATMOS-x) AVHRR all-sky reflectance and cloud probability CDR products [17]. The PATMOS-x AVHRR reflectance has been intercalibrated with MODIS reflectance and retrospectively calibrated among all the AVHRR sensors used in the AOT CDR production so that the calibration accuracy is improved to $\sim 3\%$, which is close to MODIS accuracy of $\sim 2\%$ [17].

Due to limited channels of AVHRR instrument, only aerosol retrieval over waters can be obtained and only AOT retrieved from $0.63 \mu\text{m}$ channel achieves a climate quality since the retrieval from wider $0.86 \mu\text{m}$ channel is contaminated by water vapor absorption, which is difficult to be accurately quantified, especially in the case of AOT trend detection. The retrieval algorithm has been validated by comparing with the AERONET ground AOT measurement [16, 18]; specifically, surface AOT observations from AERONET coastal stations had been used to validate our AOT retrieval algorithm and the aerosol model and surface reflectance were adjusted to achieve best validation results as demonstrated in our validation works [16, 18]. In our validation, satellite (ST) aerosol optical thickness values (τ_{st}) are matched up with the corresponding “truth” values derived from the same day surface AERONET sun-photometer (SP) observations (τ_{sp}) at coastal stations. They are statistically processed within an optimum space-time window from which scatter diagram of τ_{st} versus τ_{sp} is produced. Linear regression analyses are performed, predicting the satellite retrieved values of τ_{st} as a function of the SP values of τ_{sp} in the form of $\tau_{\text{st}} = A + B\tau_{\text{sp}}$. Retrieval algorithm performance can be evaluated from resulting statistical parameters of the linear regression: A (intercept), B (slope), δ (standard error), and R^2 (square of correlation coefficient). For example, a nonzero intercept tells us the retrieval algorithm is biased at low AOT values, which is mainly associated with improper assumptions about ocean surface reflection (including the contamination associated with sediment in Case II water in coastal regions) after sensor calibration error has been minimized through intercalibration. A slope that is different from unity (proportional error) indicates that there is some inconsistency between the aerosol microphysical model (mainly refractive index) used in the retrieval algorithm and that in the real world.

Corresponding input satellite reflectances and retrieval geometrical conditions are also collected in the match-up validation data set; thus, we were able to adjust the ocean surface reflectance and aerosol model and redo the AOT retrieval for the collected match-up data to obtain updated match-up τ_{st} data. Then we perform linear regression analyses again and obtain new statistical parameters of the linear regression: A , B , δ , and R^2 . This adjustment and linear regression are repeated until obtained A is nearly zero and B is close to unity.

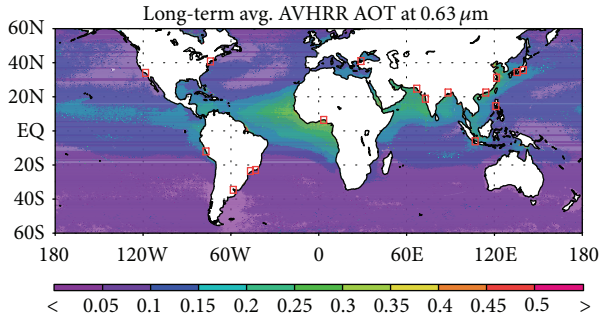


FIGURE 2: Global map of temporal averaged (1981–2009) monthly mean AOT along with the locations of seventeen MCCZ marked by red square boxes.

The corresponding surface reflectance and aerosol model are optimized and used in the retrieval algorithm. As a result, the surface contamination from various sources (including the contamination associated with sediment in Case II water in coastal regions) on the AOT retrieval is corrected and minimized in a collective way rather than individually. Please refer to [16, 18] for more detailed explanation.

The AOT values in the coastal regions shown in Figure 2 clearly demonstrate the effectiveness of removing the surface reflectance contamination; otherwise high AOT values will be over all the coast regions. The comparison with the MODIS satellite AOT observation [19] also indicated that our AOT retrieval over ocean has similar performance as the standard MODIS AOT retrieval if the same MODIS observed radiances are used as the input radiances. The algorithm had been applied to both previous and current versions of the PATMOS-x reflectance to generate long-term AOT data for the study of AOT long-term trend over global and regional scales [20, 21]. We will extend the study to local scale in this work.

Residual cloud contamination on AOT has been greatly reduced in version 2 AVHRR AOT CDR product compared to previous version and is more reliable for AOT trend study [15]. Global AVHRR AOT ($0.63 \mu\text{m}$) CDR product from 1981 to 2009 in 0.1×0.1 degree equal angle grid is used in this study. Two and a half years of data after the major volcano eruptions of El Chichón in March 1982 and Mt. Pinatubo in June 1991 are discarded in the trend analysis to remove the abrupt AOT perturbations [20].

Figure 2 shows the global map of temporal (1981–2009) averaged AOT along with the locations of seventeen MCCZ marked by red square boxes. It is seen that AOT values over the coastal oceanic surface around these MCCZ are generally higher than over the remote open ocean due to the downwind transport of aerosols originated from urban pollution. Thus, the changes and trends of AOT over the coastal ocean surface around these MCCZ can be used effectively to track the changes and trends of PM over these MCCZ.

3. AOT Linear Trend Analysis

In this paper, we only study the statistical linear tendency of AOT for selected MCCZ. The real tendencies of AOT

may be much more complex than the statistical linear model. However, the linear trend allows a simple approximation of the direction and magnitude of the changes in the data and may be adequate for many practical purposes. Results from the linear trend studies are not only commonly used by scientists but also familiar to policy makers and the public. Thus, it is important to examine the climate change issues under such a linear model. Actually, we have successfully applied this linear trend analysis on the investigation of global and regional AOT changes and trends in some previous studies [15, 20, 21].

Here, we only give a brief description on the linear trend analysis used in this study and detailed description of linear trend analysis can be found in the literature [22–24]. The linear change of a variable, such as AOT, is often measured with the linear trend (LT) in the unit of absolute (or percentage) changes per decade. AOT LT is the slope of the linear regression line for the time series of monthly averaged AOT. We adopt the commonly used decision rule that a detectable trend is indicated, at the 5% significance level or 95% confidence level, when $|LT/\sigma| > 2$ [23]. Here σ is the standard deviation of AOT LT. It is difficult to determine σ from the observational data directly so that, as a first-order approximation, we will use the standard deviation (ϵ) of monthly averaged AOT as σ after adjusting the unit of ϵ to match the unit of LT. We further name LT/σ ratio as the “significance” of AOT LT in this paper. A significance $>+2$ (or <-2) indicates the increasing (or decreasing) tendency detected is above 95% confidence level. For each MCCZ, AOT observation within $\pm 1^\circ$ latitude/longitude spatial window around the megacity is used for the analysis of AOT variation and trend. The spatial window is in square shape with the center located at MCCZ latitude/longitude listed in Table 1 and the four sides are 2° wide in both latitudinal and longitudinal directions. This optimal window size is determined from sensitive tests for both retaining the signal of city influence in AOT and providing sufficient observation sampling numbers for statistical analysis.

4. Monthly Mean AOT and Trend

As an example, the AOT time series of the two cities with the most distinct negative trend and positive trend, respectively, are shown in Figure 3. Table 1 summarizes the linear trend and its significance along with temporal averaged (1981–2009) AOT values for the seventeen MCCZ. It is seen that AOT in Jakarta, Mumbai, Karachi, Lagos, Buenos Aires, Shanghai, Kolkata, and Shenzhen have positive trends either above or close to 95% confidence level for the past three decades. These MCCZ are in the developing countries, where limited pollution control is performed due to lack of strategic planning and resources as well as relatively low public concern on the pollution issues compared to the concern on the improvement of living condition and convenience, such as job, housing, and transportation [3, 4, 7, 25].

Shanghai and Buenos Aires are the two cities with the highest temporal averaged AOT value (or climatology value) while Jakarta and Mumbai are the two cities with the most

TABLE 1: AOT linear trend (LT) and its significance (LT/σ) and temporal averaged (1981–2009) monthly mean AOT values for the seventeen MCCZ along with their geolocation and projected population in 2025.

Number	Megacity	AOT LT (1/decade)	Significance of LT	Averaged AOT	Geolocation (longitude, latitude)	Population in 2025 (million)
1	Tokyo	-0.092	-1.78	0.21	139.77°, 35.68°	37
2	Mumbai	0.489	4.85	0.44	72.82°, 18.90°	26
3	Sao Paulo	-0.231	-3.14	0.20	-46.63°, -23.55°	22
4	New York	-0.439	-7.66	0.17	-73.94°, 40.78°	21
5	Shanghai	0.333	1.98	0.78	121.43°, 31.20°	20
6	Kolkata	0.595	1.80	0.58	88.33°, 22.53°	20
7	Karachi	0.258	3.42	0.31	66.98°, 24.80°	19
8	Lagos	0.258	2.26	0.40	3.40°, 6.45°	16
9	Manila	-0.084	-1.61	0.13	120.98°, 14.58°	15
10	Buenos Aires	0.436	2.01	0.77	-58.37°, -34.58°	14
11	Los Angeles	-0.229	-5.99	0.12	-118.25°, 34.05°	14
12	Rio de Janeiro	-0.302	-4.92	0.18	-43.23°, -22.90°	13
13	Istanbul	-0.761	-12.85	0.20	28.83°, 40.97°	12
14	Osaka Kobe	0.005	0.10	0.21	135.50°, 34.53°	11
15	Shenzhen	0.173	1.45	0.42	114.13°, 22.53°	11
16	Jakarta	0.450	6.21	0.26	106.83°, -6.10°	11
17	Lima	0.059	1.08	0.25	-77.03°, -12.05°	11

distinct positive trend in AOT. This suggests that current air quality in Shanghai and Buenos Aires is much easier to reach the unhealthy level defined by World Health Organization (WHO) than in Jakarta and Mumbai but air quality degrades much faster with time in Jakarta and Mumbai than in Shanghai and Buenos Aires. There is a high potential that air quality will become worse in Jakarta and Mumbai than in Shanghai and Buenos Aires in the future if the trends stay the same.

AOT climatology value of Mumbai (0.44) is almost two times larger than that of Jakarta (0.26) and the magnitude of seasonal extremes observed in Figure 3(d) (Mumbai) is also larger than that in Figure 3(c) (Jakarta). This suggests that there is more chance that air quality may reach to WHO unhealthy level in Mumbai than in Jakarta even though the positive trend of AOT in Jakarta is more evident than in Mumbai. Thus, both AOT climatology value and AOT trend are information needed to better assess the air quality issue of a MCCZ.

AOT in Istanbul, New York, Los Angeles, Rio de Janeiro, and Sao Paulo have negative trend with a confidence level above 95% for the past three decades and their AOT climatology values are also at the low end of seventeen MCCZ AOT climatology values. These megacities are either in the developed countries (Istanbul, New York, and Los Angeles) with more stringent policies implemented for pollution emissions or in popular coastal tourism cities (Rio de Janeiro and Sao Paulo) where more stringent air pollution measures are implemented by the city government due to the concerns of tourism business and general public [2, 7, 25]. For the other cities, even though the monthly AOT show some trends

(either positive or negative), their significance is generally below 95% confidence level.

5. Seasonal Variation of AOT and Trend

Due to the seasonal changes of pollution emissions and meteorological conditions in a MCCZ, AOT and its trend may also display seasonal variations accordingly. Thus, examining the seasonal variations of AOT and its trend for a MCCZ should provide more insightful information on the pollution conditions and scenarios. The following seasonal analysis focuses on the eleven MCCZ where the positive or negative trend of monthly mean AOT discussed in the above section is at a confidence level close to or above 95%. The eleven megacities are Jakarta, Shanghai, Karachi, Mumbai, Lagos, Istanbul, New York, Los Angeles, Buenos Aires, Sao Paulo, and Rio de Janeiro.

Figure 4 shows the significance (LT/σ) of monthly and seasonal AOT linear trends and temporal averaged seasonal mean AOT values for the identified eleven megacities in a bar plot. Relatively high seasonal mean AOT values along with evident seasonal variations are observed in Shanghai, Karachi, Mumbai, Lagos, and Buenos Aires, especially in Shanghai and Buenos Aires. Air quality in Shanghai is strongly influenced by on-shore wind condition in later summer and earlier fall and off-shore wind condition in later winter and earlier spring, which produces low AOT in summer and fall relative to high AOT in winter and spring along with a positive trend above 95% confidence level in winter. For Buenos Aires, air quality is the worst in cold season due to stagnant wind and strong shallow

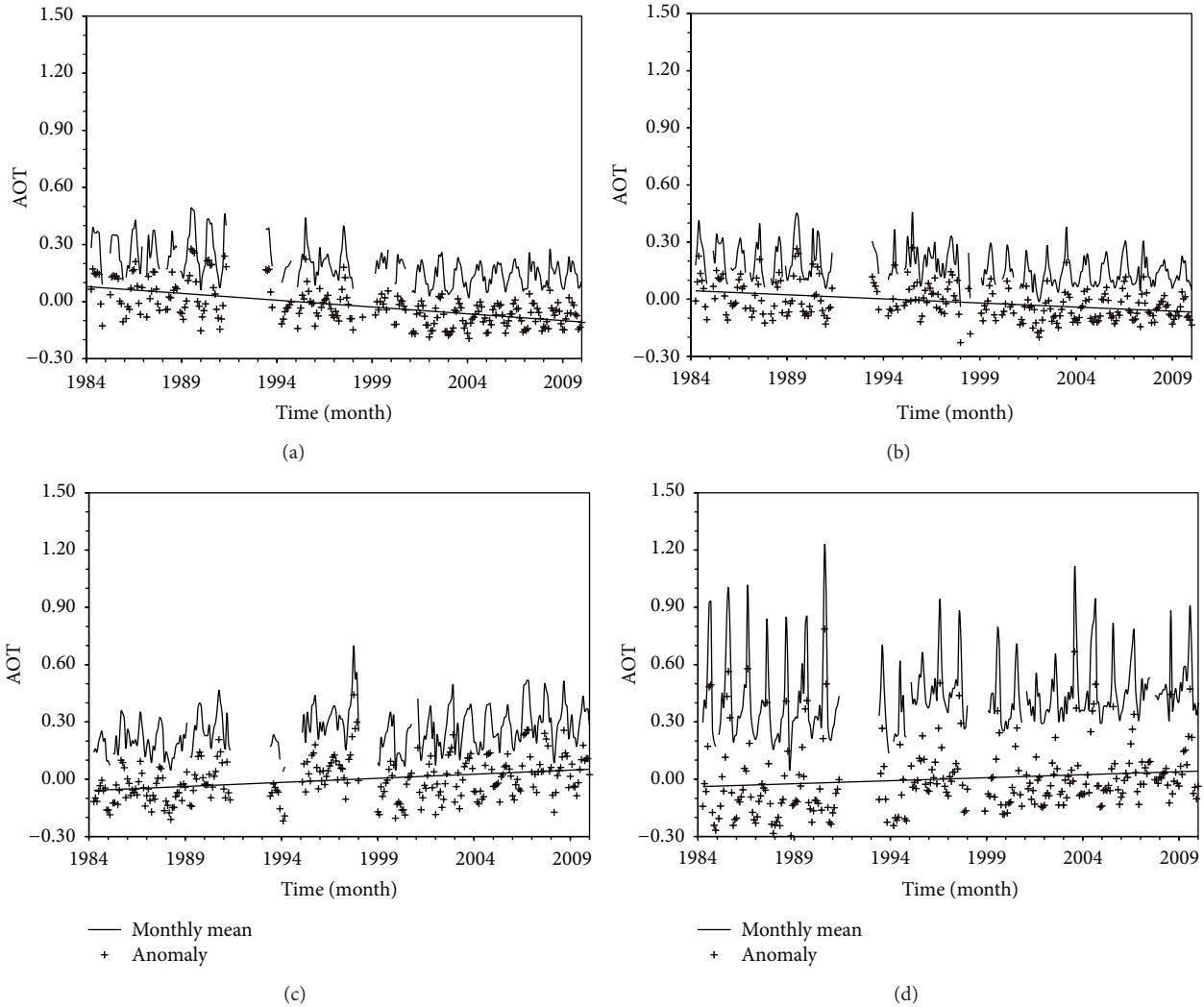


FIGURE 3: Examples of time series (dark curve) of monthly mean AOT for (a) Istanbul, (b) New York, (c) Jakarta, and (d) Mumbai. Plus symbols are the departure (or anomaly) from the climatology and the linear trend is shown as the dark straight line.

temperature inversion conditions but greatly improved in warm season due to moderate and strong winds buffeting the city throughout most of the summer, which explains the highest AOT in winter season. However, the seasonal trend is negative in winter and positive in summer but both are somewhat below 95% confidence level.

Air quality in Indian Peninsula is heavily influenced by Indian monsoon circulation and precipitation. As a result, local urban pollution in Mumbai and Karachi is much worse in winter than in summer due to the washout of pollutants by the strong precipitation associated with Indian summer monsoon, which results in distinct positive trends (above 95% confidence level) of seasonal mean AOT in nonmonsoon seasons for the two cities. However, due to the intrusion of dusty air in later spring and summer, which is transported from Arabian Peninsula and East Africa by monsoon circulation, seasonal mean AOT value is actually higher in summer and spring than in the other two seasons. Seasonal mean AOT in Lagos is higher in winter and spring than in summer and fall, which is consistent with the distinct dry (November to

April) and rainy (May to October) seasons in Lagos. However, the trends of season mean AOT are positive in all seasons but below 95% confidence level. In Jakarta, AOT is higher in summer and fall than in winter and spring. AOT trends are positive in all seasons and the confidence level in summer and fall is well above 95%.

For Istanbul, New York, and Los Angeles, AOT negative trends are above 95% confidence level for all four seasons and temporal averaged seasonal mean AOT values are at the low end of eleven MCCZ. This suggests that stringent pollution control and emission criteria implemented during the past three decades for these MCCZ in developed countries are highly effective for improving air quality for all seasons. The seasonal variations of AOT in Sao Paulo and Rio de Janeiro are very similar with high AOT in cold seasons (fall and winter) and low AOT in warm seasons (spring and summer). However, the variations of their seasonal AOT trend are different. For example, the highest (above 95% confidence level) and lowest (below 95% confidence level) negative seasonal trends are observed in summer and fall, respectively,

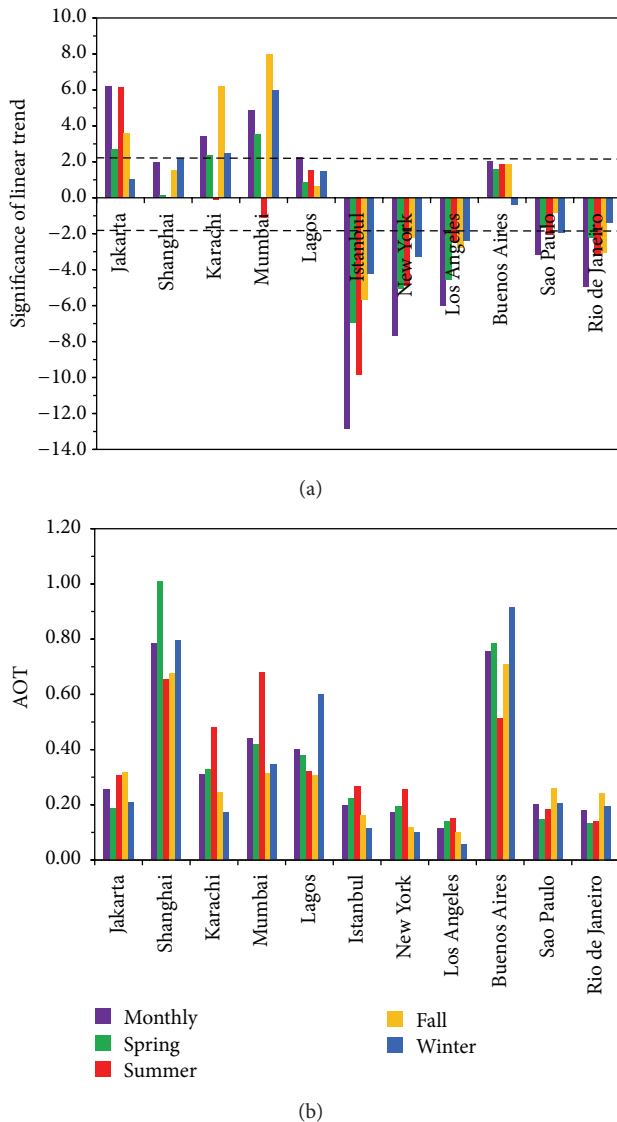


FIGURE 4: (a) The significance of linear trends of monthly and seasonal mean AOT and (b) temporal averaged seasonal mean AOT values for the eleven megacities where the positive or negative trend of monthly mean AOT is at a confidence level close to or above 95%.

in Sao Paulo, while the corresponding seasons are summer and winter, respectively, in Rio de Janeiro. Negative AOT trends in all four seasons (even though not all above 95% confidence level) for these two coastal tourism cities also suggest that the policy of air pollution control carried out by the two city governments during the past three decades is generally effective for improving air quality.

The above seasonal analyses of AOT variations and trends in the MCCZ suggest that seasonal variations of meteorological condition have a more direct effect on the AOT variations than on its trends.

6. Summary and Conclusion

Nearly 30-year AOT climate data record derived from NOAA AVHRR operational satellites observations is used to study

the AOT trends over seventeen megacities in the coast zone. Linear trend is derived from monthly and seasonal mean AOT in the past three decades and used in our analysis. AOT around the MCCZ in fast developing countries generally has positive trend with a confidence level above 95% and relatively high AOT value while AOT around the MCCZ in industrialized countries generally has negative trend with a confidence level above 95% and relatively low AOT value. AOT values and their trends show distinct seasonal variation, which can be explained somewhat by the seasonal variation of meteorological condition, especially for the variation of AOT values.

Combined analysis of AOT variations and trends is useful to reveal the air quality condition in a MCCZ and is effective for assessing the efficiency of the air pollution control policies and measures implemented. For a megacity with a higher AOT and distinct positive trend (e.g., Shanghai), it is relatively easy for air quality to reach and degrade to WHO unhealthy level, while for a megacity with a lower AOT and distinct negative trend (e.g., New York), it is relatively rare for air quality to reach and degrade to WHO unhealthy level. This study demonstrates that, similar to global and regional air pollution applications, continuous global long-term satellite observation of AOT is also useful for local urban air quality applications.

Conflict of Interests

The author declares that there is no conflict of interests regarding the publication of this paper.

Acknowledgments

This work is supported by the NOAA Climate Data Record (CDR) Program at National Centers for Environmental Information (NCEI). Constructive comments and suggestions from four anonymous reviewers are greatly appreciated.

References

- [1] R. von Glasow, T. D. Jickells, A. Baklanov et al., "Megacities and large urban agglomerations in the coastal zone: interactions between atmosphere, land, and marine ecosystems," *Ambio*, vol. 42, no. 1, pp. 13–28, 2013.
- [2] I. Sekovski, A. Newton, and W. C. Dennison, "Megacities in the coastal zone: using a driver-pressure-state-impact-response framework to address complex environmental problems," *Estuarine, Coastal and Shelf Science*, vol. 96, no. 1, pp. 48–59, 2012.
- [3] D. Mage, G. Ozolins, P. Peterson et al., "Urban air pollution in megacities of the world," *Atmospheric Environment*, vol. 30, no. 5, pp. 681–686, 1996.
- [4] S. K. Guttikunda, G. R. Carmichael, G. Calori, C. Eck, and J.-H. Woo, "The contribution of megacities to regional sulfur pollution in Asia," *Atmospheric Environment*, vol. 37, no. 1, pp. 11–22, 2003.
- [5] D. D. Parrish and T. Zhu, "Clean air for megacities," *Science*, vol. 326, no. 5953, pp. 674–675, 2009.

- [6] M. Kanakidou, N. Mihalopoulos, T. Kindap et al., "Megacities as hot spots of air pollution in the east mediterranean," *Atmospheric Environment*, vol. 45, no. 6, pp. 1223–1235, 2011.
- [7] M. J. Molina and L. T. Molina, "Megacities and atmospheric pollution," *Journal of the Air & Waste Management Association*, vol. 54, no. 6, pp. 644–680, 2004.
- [8] B. R. Gurjar and J. Lelieveld, "New directions: megacities and global change," *Atmospheric Environment*, vol. 39, no. 2, pp. 391–393, 2005.
- [9] V. Ramanathan, P. J. Crutzen, J. T. Kiehl, and D. Rosenfeld, "Atmosphere: aerosols, climate, and the hydrological cycle," *Science*, vol. 294, no. 5549, pp. 2119–2124, 2001.
- [10] M. G. Lawrence and J. Lelieveld, "Atmospheric pollutant outflow from southern Asia: a review," *Atmospheric Chemistry and Physics*, vol. 10, no. 22, pp. 11017–11096, 2010.
- [11] J. C. Chow, J. G. Watson, J. J. Shah et al., "Megacities and atmospheric pollution," *Journal of the Air & Waste Management Association*, vol. 54, no. 10, pp. 1226–1235, 2004.
- [12] J. D. Whitehead, G. McFiggans, M. W. Gallagher, and M. J. Flynn, "Simultaneous coastal measurements of ozone deposition fluxes and iodine-mediated particle emission fluxes with subsequent CCN formation," *Atmospheric Chemistry and Physics*, vol. 10, no. 1, pp. 255–266, 2010.
- [13] UN DESA, "World urbanization prospects: the 2009 revision," Tech. Rep., United Nations Department of Economic and Social Affairs and Population Division, 2010.
- [14] P. K. Chan, X.-P. Zhao, and A. K. Heidinger, "Long-term aerosol climate data record derived from operational AVHRR satellite observations," *Dataset Papers in Geosciences*, vol. 2013, Article ID 140791, 5 pages, 2013.
- [15] T. X. P. Zhao, P. K. Chan, and A. K. Heidinger, "A global survey of the effect of cloud contamination on the aerosol optical thickness and its long-term trend derived from operational AVHRR satellite observations," *Journal of Geophysical Research D: Atmospheres*, vol. 118, no. 7, pp. 2849–2857, 2013.
- [16] T. X.-P. Zhao, O. Dubovik, A. Smirnov et al., "Regional evaluation of an advanced very high resolution radiometer (AVHRR) two-channel aerosol retrieval algorithm," *Journal of Geophysical Research D: Atmospheres*, vol. 109, no. 2, Article ID D02204, 2004.
- [17] A. K. Heidinger, M. J. Foster, A. Walther, and X.-P. Zhao, "The pathfinder atmospheres-extended avhrr climate dataset," *Bulletin of the American Meteorological Society*, vol. 95, no. 6, pp. 909–922, 2014.
- [18] T. X.-P. Zhao, I. Laszlo, B. N. Holben, C. Pietras, and K. J. Voss, "Validation of two-channel VIRS retrievals of aerosol optical thickness over ocean and quantitative evaluation of the impact from potential subpixel cloud contamination and surface wind effect," *Journal of Geophysical Research D: Atmospheres*, vol. 108, no. 3, pp. 4106–4117, 2003.
- [19] T. X.-P. Zhao, I. Laszlo, P. Minnis, and L. Remer, "Comparison and analysis of two aerosol retrievals over the ocean in the Terra/Clouds and the Earth's Radiant Energy System—Moderate Resolution Imaging Spectroradiometer single scanner footprint data: 1. Global evaluation," *Journal of Geophysical Research D: Atmospheres*, vol. 110, no. 21, Article ID D21208, 15 pages, 2005.
- [20] T. X.-P. Zhao, I. Laszlo, W. Guo et al., "Study of long-term trend in aerosol optical thickness observed from operational AVHRR satellite instrument," *Journal of Geophysical Research D: Atmospheres*, vol. 113, no. 7, Article ID D07201, 2008.
- [21] X.-P. Tom Zhao, A. K. Heidinger, and K. R. Knapp, "Long-term trends of zonally averaged aerosol optical thickness observed from operational satellite AVHRR instrument," *Meteorological Applications*, vol. 18, no. 4, pp. 440–445, 2011.
- [22] G. C. Tiao, G. C. Reinsel, D. M. Xu et al., "Effects of auto-correlation and temporal sampling schemes on estimates of trend and spatial correlation," *Journal of Geophysical Research—Atmospheres*, vol. 95, no. D12, pp. 20507–20517, 1990.
- [23] E. C. Weatherhead, G. C. Reinsel, G. C. Tiao et al., "Factors affecting the detection of trends: statistical considerations and applications to environmental data," *Journal of Geophysical Research D: Atmospheres*, vol. 103, no. 14, pp. 17149–17161, 1998.
- [24] D. S. Wilks, *Statistical Methods in the Atmosphere Sciences*, Academic Press, San Diego, Calif, USA, 1995.
- [25] B. R. Gurjar, T. M. Butler, M. G. Lawrence, and J. Lelieveld, "Evaluation of emissions and air quality in megacities," *Atmospheric Environment*, vol. 42, no. 7, pp. 1593–1606, 2008.

Research Article

Operational Monitoring of Trace Gases over the Mediterranean Sea

Giuseppe Grieco,¹ Guido Masiello,² and Carmine Serio²

¹Agenzia Spaziale Italiana, Contrada Terlecchia, 75100 Matera, Italy

²Scuola di Ingegneria, Università degli Studi della Basilicata, Via dell'Ateneo Lucano, 85100 Potenza, Italy

Correspondence should be addressed to Giuseppe Grieco; giuseppe.grieco@est.asi.it

Received 18 February 2015; Revised 24 April 2015; Accepted 27 April 2015

Academic Editor: Liangfu Chen

Copyright © 2015 Giuseppe Grieco et al. This is an open access article distributed under the Creative Commons Attribution License, which permits unrestricted use, distribution, and reproduction in any medium, provided the original work is properly cited.

This paper describes the operational implementation of the processor φ -IASI over the Mediterranean sea. The φ -IASI model implements two physically based inversion algorithms for the sequential retrieval of (a) the thermodynamic state of the atmosphere and (b) the tropospheric content of CO, CO₂, CH₄, and N₂O from hyperspectral radiance observations of the Infrared Atmospheric Sounding Interferometer (IASI). The retrieval algorithm for trace gases exploits the concept of *partially scanned interferogram* technique, which is a tool mostly suited for Fourier transform spectrometers in the infrared. Minor and trace gases retrievals for July 2010 are presented and compared to in situ observations from five Mediterranean, permanent, stations of the Global Atmospheric Watch (GAW) network. The comparison evidences a good general consistency between satellite and in situ observations. IASI retrievals show a marked southeastern gradient, which is shown to be consistent with the general tropospheric circulation over the Mediterranean basin. These patterns are barely seen from in situ observations, a fact which stresses the importance of satellite (trace gases) data assimilation to improve the performance and quality of trace gases transport models.

1. Introduction

The Infrared Atmospheric Sounding Interferometer (IASI) is a Michelson interferometer developed by the European Agency for the Exploitation of Meteorological Satellites (EUMETSAT). It has been flying onboard the polar Metop A/B orbiting platforms since October 2006 [1]. IASI sounds the atmosphere in the infrared spectral band between 645 cm⁻¹ (15.5 μ m) and 2760 cm⁻¹ (3.6 μ m) with a spectral sampling of 0.25 cm⁻¹ with the aim of retrieving the thermodynamic state of the atmosphere and its chemical composition for both weather and climate applications. The high quality hyperspectral radiances acquired by IASI [1] allows us to retrieve the thermodynamic structure of the atmosphere with a vertical resolution of 1-2 Km and an accuracy of 1K for the atmospheric temperature, an accuracy of 0.5 K for the skin temperature, and an accuracy of 10–20% for what concerns the vertical structure of water vapor. These retrieval

accuracies meet the World Meteorological Organization (WMO) requirements and, generally, they can be achieved by applying physically based retrieval algorithms [2].

In this paper, we present an operational implementation of the physically based forward/inverse model, called φ -IASI [3, 4], for the Mediterranean Sea. The φ -IASI model is a physically based retrieval package for the estimation of the thermodynamic structure of the atmosphere (surface temperature (T_s), temperature (T), water vapour mixing ratio (H₂O), and ozone mixing ratio (O₃) profiles) and the tropospheric columnar content of minor and trace gases, namely, CO, CO₂, CH₄, and N₂O, from clear sky radiance measurements acquired by IASI.

The limb-sounding of upper and lower stratosphere trace species is amongst the main goals of many satellite missions, for example, Atmospheric Chemistry Experiment (see, e.g., <http://www.ace.uwaterloo.ca/>) and MIPAS (Michelson Interferometer for Passive Atmospheric Sounding) of the

European Space Agency (see, e.g., <https://earth.esa.int/web/guest/missions/esa-operational-eo-missions/envisat/instruments/mipas>). However, our study focuses on the retrieval of trace gases from IASI, which is a nadir-looking instrument.

The subject of remote sensing of atmospheric minor and trace gases from nadir-looking instruments on board polar satellites is not a new subject. Instruments used for this objective include the Japanese IMG (Interferometric Monitor for Greenhouse Gases) [5], the American AIRS (Atmospheric Infrared Radiometer Sounder) [6–8], the European IASI [9–17], and the Japanese GOSAT (Greenhouse Gases Observing Satellite) [18].

In this study we offer a different perspective focusing on the use of the partially scanned interferogram (PSI) methodology, first introduced by [19], and demonstrating its capability of achieving columnar contents of trace gases with an unprecedented precision [20]. IASI retrievals for July 2010 over the Mediterranean basin will be compared with in situ observations of the GAW (Global Atmospheric Watch) network. The retrieval exercise will also deserve to get better insight into understanding whether satellite observations of heavy molecules, such as CO_2 and N_2O , can track synoptic-scale weather patterns as claimed by Chahine et al. [7].

The paper is organized as follows. Section 2 gives a description of the modules of the φ -IASI package. Section 3 describes and discusses the results of a retrieval exercise for July 2010; the same section also deals with an analysis of the computing performance of the code. Conclusions are drawn in Section 4.

2. The φ -IASI Forward/Inverse Software Package

In this section we summarize the main methodological aspects regarding the algorithms implemented in φ -IASI. An in-depth description of φ -IASI and its accuracy and validation has been presented in many papers [2–4, 21], which the interested reader is referred to for further details.

The model φ -IASI is a MATLAB written software package which consists of seven modules which sequentially process the clear sky spectral radiance observations acquired by IASI. These include a scene analysis module to select only clear sky measurements; an Empirical Orthogonal Functions (EOF) statistical regression scheme to provide the first guess for the next module, which implements an iterative optimal estimation algorithm that we call δ -IASI [4]. The inverse module δ -IASI uses a physical radiative transfer model, which is provided by the module σ -IASI [3]. The two modules δ -IASI and σ -IASI are the core of the φ -IASI model. Once δ -IASI has provided the thermodynamic state of the atmosphere (T_s , T , H_2O , O_3); this state forms the input for each of the modules dedicated to the computation of the total columnar content of minor and trace gases, that is, CO , CO_2 , CH_4 , and N_2O . The flow chart of φ -IASI is shown in Figure 1. Further details about the individual modules are given below.

2.1. The Scene Analysis Module. The high spectral resolution of new advanced infrared sensors has resulted in better

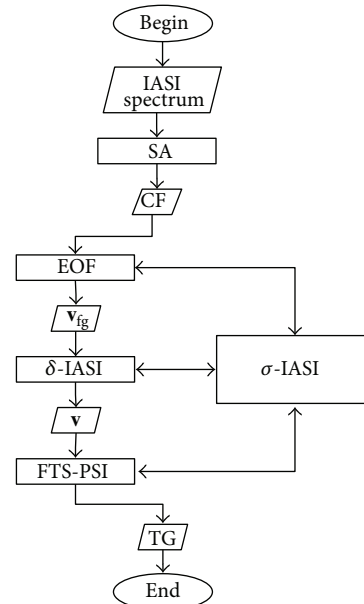


FIGURE 1: Flow chart of φ -IASI. The acronym SA stands for scene analysis and its output CF stands for cloud flag. \mathbf{v} stands for the thermodynamic state of the atmosphere (T_s , T , H_2O , O_3) while the subscript fg is the acronym for first guess. FTS-PSI stands for Fourier transform spectroscopy with partially scanned interferogram. Finally the acronym TG stands for trace gases. The double-way arrows connecting the modules EOF, δ -IASI, and FTS-PSI with σ -IASI mean that all these modules use the σ -IASI code as a subroutine.

coverage and significantly improved temperature and moisture soundings capabilities compared with the current situation. Infrared data from nadir-looking instruments, however, are frequently affected by clouds. Thus, observations must be processed for operational data assimilation and inversion for geophysical parameters by screening to remove cloud-contaminated soundings. This operation is performed with a *Scene Analysis* module, which is normally based on thresholding of a suitable radiance channels. The scene analysis module embedded in φ -IASI has been variously described in many papers. The most up-to-date version of the module can be found in [22].

2.2. The σ -IASI Code. The forward model embedded in φ -IASI is called σ -IASI [3]. This is a monochromatic forward module using a look-up table for the optical depth. The look-up table is derived from LBLRTM (Line-by-Line Radiative Transfer Model) model [23]. For the work here shown we have used LBLRTM version 12.2. The forward module is based on 60 pressure layers, spanning the atmosphere from the ground level to the top assumed to be at 0.005 hPa. The model computes spectral radiances and analytical Jacobian derivatives of any surface and/or atmospheric parameter. IASI radiances are obtained through convolution with the IASI Instrumental Spectral Response Function (ISRF).

2.3. The EOF Module. The EOF module is a statistically based algorithm for the retrieval of the thermodynamic state of

the atmosphere (T_s , T , H_2O , and O_3). The general analytic formulation of the problem is described in the work of Serio et al. [24], which the interested reader is referred to for more details. Basically, the module is based on a linear regression among atmospheric parameters and radiances, represented through a truncated expansion of EOF scores. In fact, the radiances are first transformed to EOF scores and a truncated expansion is used to reduce the dimensionality of the data space. The regression coefficients are computed on the basis of a suitable training data set. For the current implementation we use a set of (T_s , T , H_2O , O_3) state vectors derived from the ECMWF (European Centre for Medium-Range Weather Forecasts) analysis for July 2010. A total of 1147 state vectors were used, which uniformly cover the Mediterranean basin.

2.4. The δ -IASI Module. The δ -IASI module [4] implements an iterative algorithm for the optimal estimation of the thermodynamic state of the atmosphere. The algorithms simultaneously retrieves the state vector \mathbf{v} which, for sea surface, is made up of (T_s , T , H_2O , O_3). For sea surface emissivity we use the Masuda model [25].

The retrieval algorithm follows Rodgers optimal estimation [26] and uses an additional regularization parameter which improves the retrieval accuracy and convergence rate of the inverse scheme [15, 21]. The optimal estimator we use to get an estimate of the state vector \mathbf{v} from spectral radiances has been first derived by Carissimo et al. [4] and discussed at length by Grieco et al. [21] and Masiello et al. [27].

The δ -IASI estimator reads

$$(\gamma \mathbf{S}_a^{-1} + \mathbf{K}^t \mathbf{S}_\varepsilon^{-1} \mathbf{K}) \mathbf{x} = \mathbf{K}^t \mathbf{S}_\varepsilon^{-1} \mathbf{y}, \quad (1)$$

where the superscript t indicates the transpose operation. Without any loss of generality, we assume that we are in a region around the first guess in which problem (1) is linear. If not, the scheme has to be further iterated according to the usual Gauss-Newton scheme [4]. With this in mind, in (1), we have

$$\begin{aligned} \mathbf{x} &= \hat{\mathbf{v}} - \mathbf{v}_a; \\ \mathbf{y} &= (\mathbf{R} - \mathbf{r}_0) - \mathbf{K} \mathbf{x}_a; \quad \text{with } \mathbf{x}_a = \mathbf{v}_a - \mathbf{v}_0, \end{aligned} \quad (2)$$

where $\hat{\mathbf{v}}$, \mathbf{v}_a , and \mathbf{v}_0 are the parameters' state vector (estimated), the *a priori* or background vector, and the first guess state vector (the size of these vectors will be denoted by N). Furthermore, \mathbf{S}_ε in (1) is the observational covariance matrix and \mathbf{S}_a indicates a suitable smoothing operator, normally fixed to the covariance matrix of \mathbf{v}_a (e.g., [26]). \mathbf{R} is the vector (size M) of observed radiances, $\mathbf{r}_0 = F(\mathbf{v}_0)$, with F being the forward model. Furthermore, the $M \times N$ derivative matrix or Jacobian derivative, \mathbf{K} , is computed as

$$\mathbf{K} = \left. \frac{\partial F(\mathbf{v})}{\partial \mathbf{v}} \right|_{\mathbf{v}=\mathbf{v}_0}. \quad (3)$$

If we define

$$\tilde{\mathbf{S}}_\varepsilon = \gamma \mathbf{S}_\varepsilon, \quad (4)$$

then (e.g., [21]) (1) can be written in the equivalent form

$$(\mathbf{S}_a^{-1} + \mathbf{K}^t \tilde{\mathbf{S}}_\varepsilon^{-1} \mathbf{K}) \mathbf{x} = \mathbf{K}^t \tilde{\mathbf{S}}_\varepsilon^{-1} \mathbf{y}, \quad (5)$$

which says that scaling the background covariance by $1/\gamma$ has the same effect as scaling the observational covariance matrix by γ .

The meaning and use of the parameter γ have been discussed at length by Carissimo et al. [4] and Grieco et al. [21]. Basically, γ can improve the regularization of the inverse problem (1) and its tuning may allow us to trade off between accuracy and stability of the solution, $\hat{\mathbf{v}}$.

In fact, introducing the operator [4]

$$\mathbf{G} = \mathbf{S}_\varepsilon^{-1/2} \mathbf{K} \mathbf{S}_a^{1/2}, \quad (6)$$

the δ -IASI estimator can be put in the dimensionless form

$$(\mathbf{G}^t \mathbf{G} + \gamma \mathbf{I}) \mathbf{u} = \mathbf{G}^t \mathbf{z}; \quad \text{with } \mathbf{z} = \mathbf{S}_\varepsilon^{-1/2} \mathbf{y}; \quad \mathbf{u} = \mathbf{S}_a^{-1/2} \mathbf{x}, \quad (7)$$

whose solution, \mathbf{u} , is given by

$$\mathbf{u} = \mathbf{T} \mathbf{z} \quad (8)$$

with

$$\mathbf{T} = (\mathbf{G}^t \mathbf{G} + \gamma \mathbf{I})^{-1} \mathbf{G}^t. \quad (9)$$

Equation (7) describes a Tikhonov-type or *ridge regression* regularization problem. According to Tikhonov and Arsenin (see, e.g., [28]) the operator \mathbf{T} describes a regularization scheme with the norm of \mathbf{T} given by

$$\text{norm}(\mathbf{T}) \leq \frac{1}{2\sqrt{\gamma}}. \quad (10)$$

Within the context of Tikhonov theory [28], the regularization of the problem (7) (hence (1)) improves for $\gamma > 1$. From (10) it is also seen that the amount of smoothing (regularization) is independent of the details of \mathbf{S}_ε and \mathbf{S}_a , provided that they have inverse (so that we can define the operator \mathbf{G}). This is an important aspect of the inverse problem (1) because normally both \mathbf{S}_ε and \mathbf{S}_a are model approximations of the *truth*. Of course, the accuracy with which both \mathbf{S}_ε and \mathbf{S}_a are known affects the final estimate $\hat{\mathbf{v}}$ and its error analysis.

Finally, we stress that (7) also provides a fast and effective scheme for the computation of the estimate $\hat{\mathbf{v}}$. Based on the operator \mathbf{G} and (7) an algorithm can be developed [4, 21], which does not require the inversion of \mathbf{S}_a and, in case $\tilde{\mathbf{S}}_\varepsilon$ is diagonal, is fast and accurate because it just requires the singular value decomposition of the kernel $\mathbf{G}^t \mathbf{G}$.

2.5. The Minor and Trace Gases Modules: The FTS-PSI Based Retrieval Technique. The PSI based retrieval technique consists in transforming the radiance spectrum into the interferogram domain where we identify a region which is particularly sensitive to the geophysical parameter we want to retrieve. Once the resonant peak in the interferogram domain has been identified, the given gas is simultaneously retrieved

with the most important interfering parameters, normally ($T_s, T, \text{H}_2\text{O}$).

The PSI technique has been applied in several contexts and is particularly efficient when information content related to the given geophysical parameter is confined to a small portion of the interferogram radiance. This is the case, for example, of linear molecules, such as CO and CO_2 . In fact, the regularly spaced CO_2 absorption lines around $15 \mu\text{m}$ and of CO around $4.65 \mu\text{m}$ yield a resonant peak in the interferogram domain. To exemplify let us consider the case of CO. For CO the radiance spectrum shows a regular line spacing of $\approx 3.6 \text{ cm}^{-1}$; therefore, if we Fourier-transform the spectrum to the interferogram domain, we expect a resonant peak at an optical path difference (opd) of about the inverse of this value, that is, 0.28 cm. In order to better clarify this aspect, Figure 2 shows the interferogram around the expected resonance peak of CO for the US standard atmospheric profile [29] and for the same profile with a null concentration of CO. It can be seen that in the optical path difference interval between 0.2 and 0.3 the two interferograms are sensibly different, while they are quite similar outside this interval. This is an extreme example which gives an idea of the sensitivity of the interferogram radiance to the CO concentration near to the expected resonance peak.

The most important advantage of this technique is the improvement of the signal to noise ratio and the reduction of the influence of the interfering parameters in the final retrieval. The basics of the technique may be found in the work of Grieco et al. [20] and are here briefly summarized for the benefit of the reader.

For the purpose of the retrieval problem, the retrieved atmospheric parameters (these include the given gas and the set of the most important interfering factors, i.e., T_s, T , and H_2O) are represented through a parametric form of the profile:

$$q_i(p) = q_{0i}(p)(1 + f_{q_i}); \quad (11)$$

$$i = 1, \dots, n,$$

where n is the number of parameters to be retrieved, q_i is the vertical profile, p is the atmospheric pressure, q_{0i} is a suitable first guess profile, and f_{q_i} is the parameter to be retrieved. For the case of surface temperature, (11) just reduces to the scalar form

$$T_s = T_{s0}(1 + f_{T_s}). \quad (12)$$

Considering the first-order Taylor expansion of the interferogram radiance \mathbf{I} around first guess values, we have

$$\Delta \mathbf{I} = \mathbf{I} - \mathbf{I}_0 = \sum_{i=1}^n \mathbf{J}_i \mathbf{q}_{0i} f_{q_i}, \quad (13)$$

where, as for the radiance case, \mathbf{I} is the observed interferogram, \mathbf{I}_0 is the interferogram computed with the forward model at the first guess state vector, and \mathbf{J}_i is the Jacobian derivative of the interferogram radiance.

Equation (13) can be rearranged as follows [20]:

$$\Delta \mathbf{I} = \mathbf{A} \mathbf{f}, \quad (14)$$

where \mathbf{A} is the horizontal concatenation of $\mathbf{J}_i \mathbf{q}_{0i}$, $i = \dots, n$.

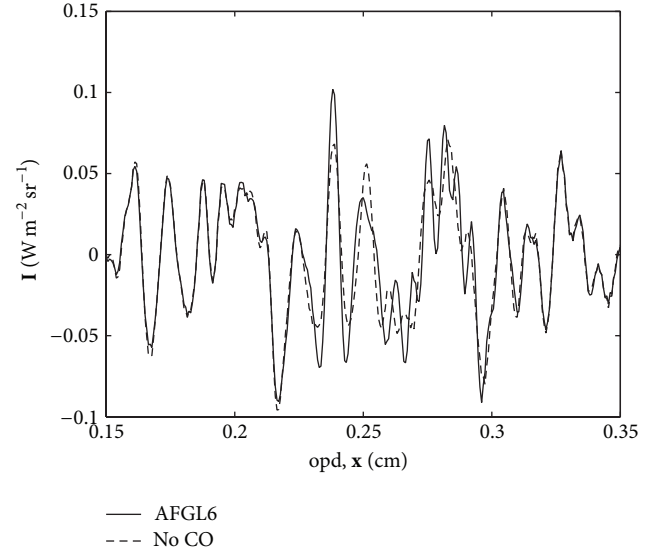


FIGURE 2: Interferogram radiance (\mathbf{I}) around the expected resonance peak of CO in $\text{Wm}^{-2}\text{sr}^{-1}$. The optical path difference (opd) is expressed in cm. AFGL6 stands for the US standard atmosphere, while “no CO” refers to the same atmospheric profile with a null CO concentration.

The vector \mathbf{f} is retrieved by means of an unconstrained least square algorithm, and an estimation of the total columnar content is carried out according to

$$\widehat{\mathbf{Q}}_i = (1 + \widehat{f}_{q_i}) \int_{p_s}^0 q_i(p) dp, \quad (15)$$

where \widehat{f}_{q_i} is the estimate of f_{q_i} and p_s is the surface pressure.

The usual least square *a posteriori* error analysis allows assessing the accuracy of the retrieval and the relative weight of the interfering parameters. Based on the *a posteriori* retrieval accuracy analysis, we have that the retrieved columnar content of the trace and minor gases has the error bars shown in Table 1. The details about the assessment of these values can be found in the work of Grieco et al. [20].

Figure 3 exemplifies the Jacobian derivative for CO mixing ratio, in the region around the interferogram resonant peak. The Jacobian derivative does not show any sharp peak all over the absorption spectral interval and most of the contribution comes from the pressure interval between 800 and 200 mb, which corresponds approximately to the region of the free troposphere. Similar results hold for the other gases considered in this study and are not shown for the sake of brevity.

3. Application to the Mediterranean Basin

The φ -IASI package has been applied to a dataset of ≈ 35000 IASI radiance spectra acquired over the Mediterranean basin for July 2010. This month has been selected because of the weather pattern over the Mediterranean region, which has been characterized by above normal surface temperatures associated with a relatively high frequency of blocking days.

TABLE 1: Accuracy of the retrieved total columns of the trace and minor gases for a single IASI field of view.

Gas species	Absolute accuracy	Relative accuracy
CO ₂	±3 ppmv	<1%
CO	±1.5 ppbv	≈1.5%
CH ₄	±13 ppbv	<1%
N ₂ O	±15 ppbv	≈5%

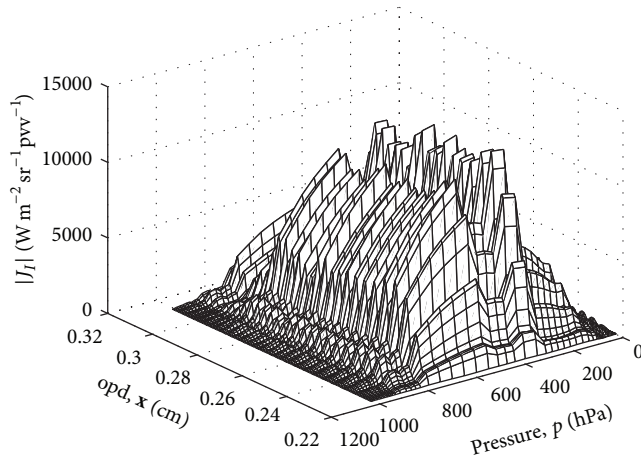


FIGURE 3: Mesh surface of J_I . The Jacobian derivative of the interferogram radiance with respect to the mixing ratio profile of CO.

Likewise, a particularly long blocking event has been experienced over Western Russia that has led to the occurrence of anomalously high temperatures over this region [30, 31]. Apart from the high temperatures, July 2010 showed the typical synoptic conditions [32, 33] of the Mediterranean summer (June to September), with high pressure over the Mediterranean Europe and a low-pressure through extending from the Persian Gulf through Iraq to the southeastern Mediterranean (see Figure 4).

It is now very well understood (e.g., Karnieli et al. [34] and the references therein) that this kind of weather pattern yields persistent northwesterly winds which causes long-range transport of air masses from southeastern and southwestern Europe into the eastern Mediterranean basin.

Arguing that atmospheric heavy molecules, such as CO₂ and NO₂, follow the dominant atmospheric circulation, Chahine et al. [7] demonstrated that satellite derived CO₂ data track weather patterns and can also be used to study the vertical and horizontal transports in the Earth atmosphere. Thus, according to Chahine et al. [7], because of the aforementioned summer weather pattern over the Mediterranean basin, we expect that CO₂ and N₂O should show a northwestern to southeastern pattern over the Mediterranean region. To study this effect, in this section, we will show and analyze trace gases retrievals from IASI data for July 2010.

To begin with, we briefly show and discuss patterns associated with retrievals of surface (T_s) and atmospheric parameters (T and O₃) derived with δ -IASI. Figures 5 and 6 show the maps of the retrieved atmospheric 500 hPa

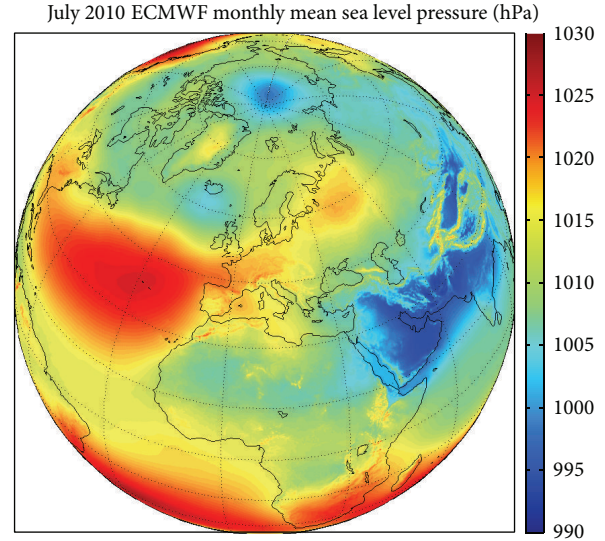


FIGURE 4: ECMWF analysis of the monthly sea level pressure for July 2010.

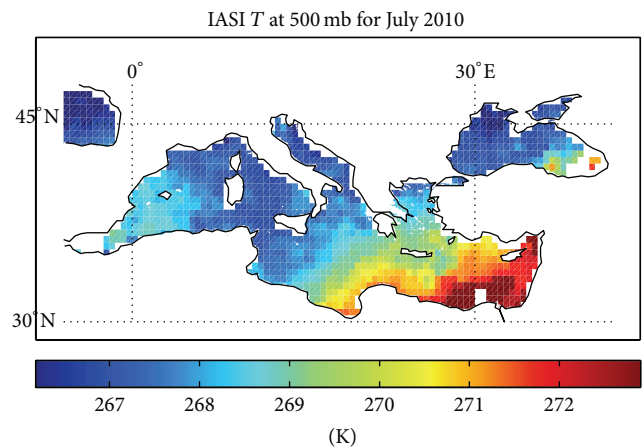


FIGURE 5: Retrieved atmospheric temperature at 500 mb for the month of July 2010. Data have been smoothed and rendered on a grid of $0.5^\circ \times 0.5^\circ$ (lat. \times lon.).

temperature and the total columnar ozone, averaged over the whole July period. These maps and all the following ones have been smoothed with a median filter and rendered on a regular grid of $0.5^\circ \times 0.5^\circ$. The value of each image pixel is the median value of the whole month distribution of all the values in the 2×2 neighborhood pixels around the corresponding pixel in the input image. The maps clearly show the transition from the European midlatitude air mass type to tropical one which characterizes the southeastern region of the Mediterranean basin. This transition is very well evidenced in the temperature and ozone maps and also testifies the quality of the retrieval. In addition, Figure 7 shows the sea surface temperature, with the expected northwestern southeastern gradient. This map evidences the relatively high sea surface temperature, which in most part of the Mediterranean basin exceeds 26°C (299 K).

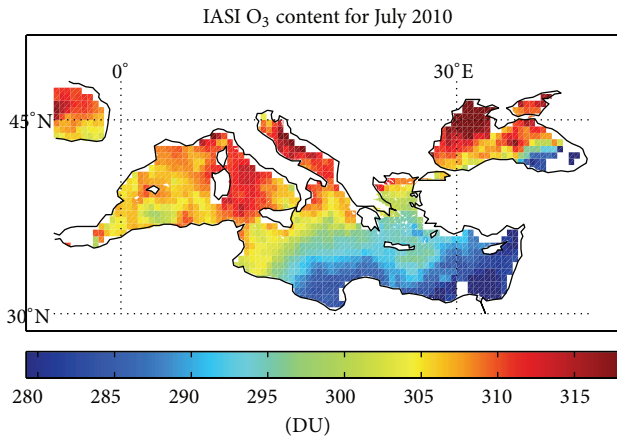


FIGURE 6: Retrieved atmospheric ozone content for the month of July 2010. Data have been smoothed and rendered on a grid of $0.5^\circ \times 0.5^\circ$ (lat. \times lon.).

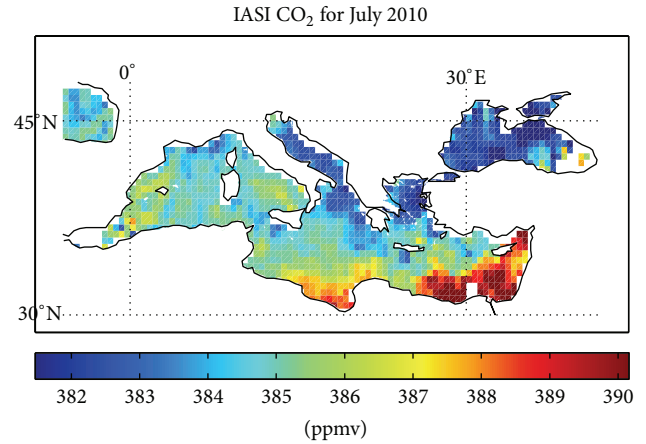


FIGURE 8: Retrieved tropospheric CO_2 content for the month of July 2010. Data have been smoothed and rendered on a grid of $0.5^\circ \times 0.5^\circ$ (lat. \times lon.).

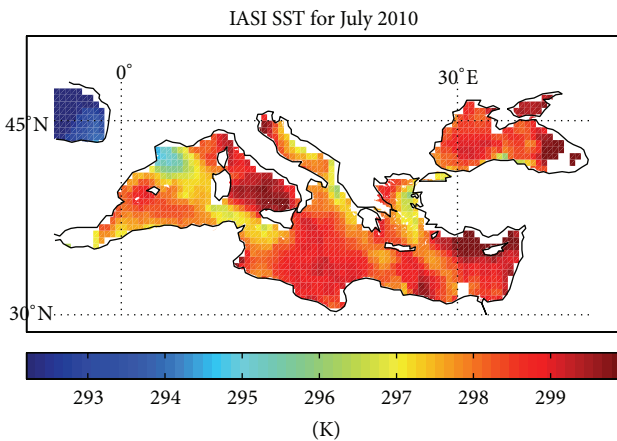


FIGURE 7: Retrieved sea surface temperature for the month of July 2010. Data have been smoothed and rendered on a grid of $0.5^\circ \times 0.5^\circ$ (lat. \times lon.).

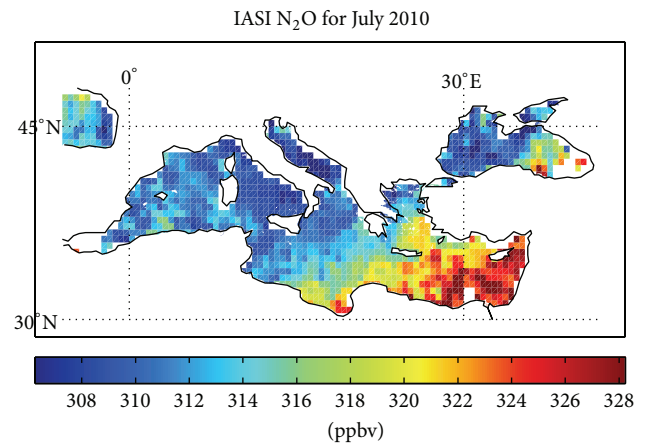


FIGURE 9: Retrieved tropospheric N_2O content for the month of July 2010. Data have been smoothed and rendered on a grid of $0.5^\circ \times 0.5^\circ$ (lat. \times lon.).

Figure 8 shows the retrieved tropospheric CO_2 content averaged over the whole period of July 2010. The most striking feature in this map is the marked northwestern-southeastern gradient, which is consistent with the large scale synoptic weather pattern for July 2010. Thus, Figure 8 supports Chahine et al.'s [7] finding that the retrieved CO_2 is capable of tracking the dominant atmospheric circulation. Similar results have been also found for N_2O (see Figure 9) and for methane (see Figure 10).

Finally, we show and discuss the comparison with in situ observations from the GAW stations of Begur (Spain), Lampedusa (Italy), Finokalia (Greece), Cairo (Egypt), and Sde Boker (Israel). It is important to remark that this comparison is not aimed at validating the retrievals. This matter has been addressed by Grieco et al. [20, 35], and the references therein. The present comparison is aimed at getting insight into understanding whether patterns and structures seen from satellite data are also shown by in situ observations.

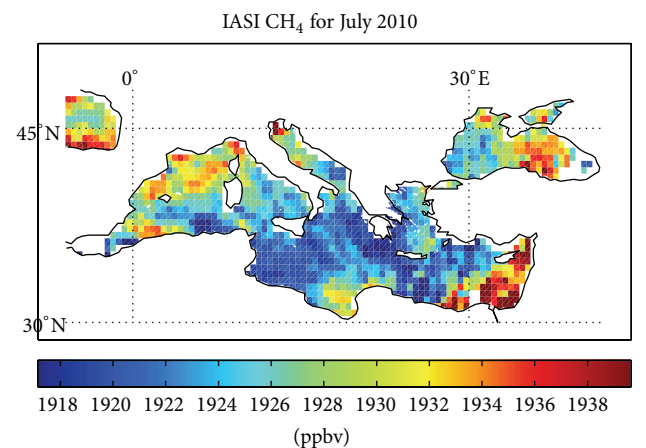


FIGURE 10: Retrieved tropospheric CH_4 content for the month of July 2010. Data have been smoothed and rendered on a grid of $0.5^\circ \times 0.5^\circ$ (lat. \times lon.).

TABLE 2: Time averaged values of the ground measurements (GM) and retrieved (IASI) columnar tropospheric content of trace gases.

	Begur		Lampedusa		Finokalia		Sde Boker		Cairo	
	GM	IASI	GM	IASI	GM	IASI	GM	IASI	GM	IASI
CO ₂ (ppmv)	385.7	382.5	385.7	386.8	383.5	386.4	—	—	386.8	392.1
CH ₄ (ppbv)	1834	1920	1860	1924	1865	1930	1890	1936	—	—

As already mentioned, these stations belong to the Global Atmosphere Watch (GAW) network and the data have been downloaded from the website of the World Data Centre for Greenhouse Gases. Figure 11 shows the geographical positions of the GAW stations. As it can be seen, they span all the Mediterranean basin. Three of them are seaside while Sde Boker and Cairo are about 100 Km far from the coast.

Table 2 compares the monthly average of in situ and IASI retrievals. The comparison is limited to CO₂ and CH₄ because these two gases have the largest density of monitoring (4 out of 5 GAW stations). There is a general consistency between in situ and satellite observations. However, systematic differences appear, which nevertheless are still consistent with the diverse atmospheric column sensed with in situ and satellite instruments. In fact, from Figure 3, we see that, conversely to in situ observations, IASI retrieval for atmospheric gases is sensitive to the free troposphere and cannot see the planetary boundary layer.

From the comparison of in situ observations and collocated satellite retrievals it can be seen that CO₂ and CH₄ concentrations tend to agree in showing a southeastward gradient, although it is fair to say that the gradient is much more marked for the satellite retrieval than in situ observations.

3.1. Performance of the Code. The performance of the code has been evaluated on a multiprocessor machine equipped with 6 physical and 6 virtual Intel i7 CPUs with a CPU clock rate equal to 3.33 GHz and a RAM memory which amounts to 24 GB. The time to invert a single IASI spectrum varies from about 8 seconds to 14 seconds, depending on the number of iterations the δ -IASI module performs. For the application discussed in this paper, the number of iterations ranges from 1 to 3 with an average number which is around 1.5. Obviously, the number of iterations depends on the quality of the first guess of the thermodynamic state of the atmosphere and this aspect is crucial for both the quality and the speed of the retrieval. For the application under examination, we can consider that the average time spent for the retrieval of a single IASI spectrum is about 10 seconds. Considering that the total number of IASI spectra over the Mediterranean basin for the whole month of July is about 35000 and that only about the 25% of the spectra have been classified as clear-sky and therefore processed by the physical inversion scheme, the computational time spent for the retrieval amounts to a little bit more than 24 hours. The availability of 6 physical CPUs reduced this time to few hours. Considering the implementation of the code for the whole globe, a number of 50 to 100 CPUs of the type described above should be enough to guarantee operability.

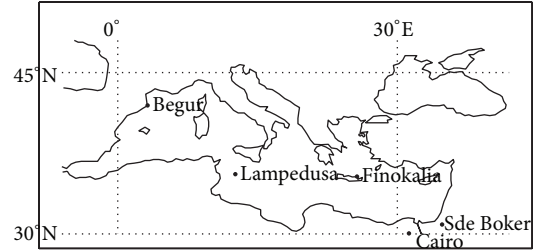


FIGURE 11: Map of the GAW stations.

The hardware equipment used for the evaluation of the performance of the code is available at the moment for few thousand Euros, which means that the computer technology is now mature enough and contextually cheap to allow the full exploitation of information content of hyperspectral satellite infrared sounders such as a IASI.

4. Conclusions

The operational implementation of the φ -IASI software package over the Mediterranean basin for the retrieval of the thermodynamic state of the atmosphere and of the free tropospheric columnar content of CO₂, CO, CH₄, and N₂O from the hyperspectral radiance measurements acquired by the Infrared Atmospheric Sounding Interferometer has been presented.

We have shown that φ -IASI can operationally retrieve skin temperature, T_s , atmospheric parameters (T , H₂O, and O₃), and minor and trace gases, namely, CO, CO₂, N₂O, and CH₄, at the scale of the Mediterranean basin.

The retrieval scheme has been exemplified through its application to IASI spectra recorded on July 2010. The retrieval results have been also compared to in situ observations from five GAW permanent stations. Considering that nadir-looking IASI retrievals are sensitive to the free troposphere, whereas in situ measurements sense the boundary layer, the comparison has shown a fair agreement of in situ observations with IASI observations. IASI retrieval for heavy molecules, noticeably CO₂ and N₂O, shows marked north-western to southeastern gradients with a relatively higher concentration over the eastern part of the Mediterranean basin. This behaviour is both consistent with biogenic activity of the Mediterranean sea [36] and the large scale synoptic weather circulation in July 2010 which transports air masses from southeastern and southwestern Europe into the eastern Mediterranean basin.

Our findings support previous results for CO₂ geospatial distribution [7] and also exemplify how satellite retrievals are complementary to in situ observations to study the vertical and horizontal transports in the Earth's atmosphere of gases such as CO₂, N₂O, and CH₄ which are of paramount interest in view of their crucial role within the anthropogenic greenhouse effect and hence global warming of the planet.

Conflict of Interests

The authors declare that there is no conflict of interests regarding the publication of this paper.

Acknowledgments

The measurements in Lampedusa and Sde Boker have been downloaded from the web page <http://www.esrl.noaa.gov/gmd/dv/iadv/> owned by NOAA/ESRL. The measurements in Begur and Finokalia have been supplied by the Laboratoire des Sciences du Climat et de l'Environnement (<http://www.lscce.ipsl.fr/>). The measurements in Cairo have been supplied by the Egyptian Meteorological Authority (<http://ema.gov.eg/>). This work has been partly supported by *The RITMARE Flagship Project* (CNR-MIUR). IASI has been developed and built under the responsibility of the Centre National d'Etudes Spatiales (CNES, France). It is flown onboard the Metop satellites as part of the EUMETSAT Polar System. The IASI L1 data are received through the EUMETCast near real time data distribution service.

References

- [1] F. Hilton, R. Armante, T. August et al., "Hyperspectral earth observation from IASI: five years of accomplishments," *Bulletin of the American Meteorological Society*, vol. 93, no. 3, pp. 347–370, 2012.
- [2] G. Masiello, C. Serio, A. Carissimo, G. Grieco, and M. Matricardi, "Application of φ -IASI to IASI: retrieval products evaluation and radiative transfer consistency," *Atmospheric Chemistry and Physics*, vol. 9, no. 22, pp. 8771–8783, 2009.
- [3] U. Amato, G. Masiello, C. Serio, and M. Viggiano, "The σ -IASI code for the calculation of infrared atmospheric radiance and its derivatives," *Environmental Modelling & Software*, vol. 17, no. 7, pp. 651–667, 2002.
- [4] A. Carissimo, I. De Feis, and C. Serio, "The physical retrieval methodology for IASI: The δ -IASI code," *Environmental Modelling and Software*, vol. 20, no. 9, pp. 1111–1126, 2005.
- [5] H. Shimoda and T. Ogawa, "Interferometric monitor for greenhouse gases (IMG)," *Advances in Space Research*, vol. 25, no. 5, pp. 937–946, 2000, Remote Sensing and Applications: Earth, Atmosphere and Oceans.
- [6] M. Chahine, C. Barnet, E. T. Olsen, L. Chen, and E. Maddy, "On the determination of atmospheric minor gases by the method of vanishing partial derivatives with application to CO₂," *Geophysical Research Letters*, vol. 32, no. 22, Article ID L22803, pp. 1–5, 2005.
- [7] M. T. Chahine, L. Chen, P. Dimotakis et al., "Satellite remote sounding of mid-tropospheric CO₂," *Geophysical Research Letters*, vol. 35, no. 17, Article ID L17807, 2008.
- [8] W. W. McMillan, C. Barnet, L. Strow et al., "Daily global maps of carbon monoxide from nasa's atmospheric infrared sounder," *Geophysical Research Letters*, vol. 32, no. 11, pp. 1–4, 2005.
- [9] C. Crevoisier, A. Chédin, H. Matsueda, T. MacHida, R. Armante, and N. A. Scott, "First year of upper tropospheric integrated content of CO₂ from IASI hyperspectral infrared observations," *Atmospheric Chemistry and Physics*, vol. 9, no. 14, pp. 4797–4810, 2009.
- [10] P. Ricaud, J.-L. Attié, H. Teysseire et al., "Equatorial total column of nitrous oxide as measured by IASI on MetOp-A: Implications for transport processes," *Atmospheric Chemistry and Physics*, vol. 9, no. 12, pp. 3947–3956, 2009.
- [11] A. Boynard, C. Clerbaux, P.-F. Coheur et al., "Measurements of total and tropospheric ozone from IASI: comparison with correlative satellite, ground-based and ozonesonde observations," *Atmospheric Chemistry and Physics*, vol. 9, no. 16, pp. 6255–6271, 2009.
- [12] L. Clarisse, P. F. Coheur, A. J. Prata et al., "Tracking and quantifying volcanic SO₂ with IASI, the September 2007 eruption at Jebel at Tair," *Atmospheric Chemistry and Physics*, vol. 8, no. 24, pp. 7723–7734, 2008.
- [13] L. Clarisse, C. Clerbaux, F. Dentener, D. Hurtmans, and P.-F. Coheur, "Global ammonia distribution derived from infrared satellite observations," *Nature Geoscience*, vol. 2, no. 7, pp. 479–483, 2009.
- [14] C. Clerbaux, A. Boynard, L. Clarisse et al., "Monitoring of atmospheric composition using the thermal infrared IASI/MetOp sounder," *Atmospheric Chemistry and Physics*, vol. 9, no. 16, pp. 6041–6054, 2009.
- [15] G. Masiello and C. Serio, "Simultaneous physical retrieval of surface emissivity spectrum and atmospheric parameters from infrared atmospheric sounder interferometer spectral radiances," *Applied Optics*, vol. 52, no. 11, pp. 2428–2446, 2013.
- [16] D. Hurtmans, P.-F. Coheur, C. Wespes et al., "FORLI radiative transfer and retrieval code for IASI," *Journal of Quantitative Spectroscopy and Radiative Transfer*, vol. 113, no. 11, pp. 1391–1408, 2012.
- [17] T. Kerzenmacher, B. Dils, N. Kumps et al., "Validation of IASI FORLI carbon monoxide retrievals using FTIR data from NDACC," *Atmospheric Measurement Techniques*, vol. 5, no. 11, pp. 2751–2761, 2012.
- [18] D. Wunch, P. O. Wennberg, G. C. Toon et al., "A method for evaluating bias in global measurements of CO₂ total columns from space," *Atmospheric Chemistry and Physics*, vol. 11, no. 23, pp. 12317–12337, 2011.
- [19] T. G. Kyle, "Temperature soundings with partially scanned interferograms," *Applied Optics*, vol. 16, no. 2, pp. 326–333, 1977.
- [20] G. Grieco, G. Masiello, M. Matricardi, and C. Serio, "Partially scanned interferogram methodology applied to IASI for the retrieval of CO, CO₂, CH₄ and N₂O," *Optics Express*, vol. 21, no. 21, pp. 24753–24769, 2013.
- [21] G. Grieco, G. Masiello, M. Matricardi, C. Serio, D. Summa, and V. Cuomo, "Demonstration and validation of the φ -IASI inversion scheme with NAST-I data," *Quarterly Journal of the Royal Meteorological Society*, vol. 133, no. 3, pp. 217–232, 2007.
- [22] U. Amato, L. Lavanant, G. Liuzzi et al., "Cloud mask via cumulative discriminant analysis applied to satellite infrared observations: scientific basis and initial evaluation," *Atmospheric Measurement Techniques*, vol. 7, no. 10, pp. 3355–3372, 2014.
- [23] S. A. Clough, M. W. Shephard, E. J. Mlawer et al., "Atmospheric radiative transfer modeling: a summary of the AER codes,"

- Journal of Quantitative Spectroscopy and Radiative Transfer*, vol. 91, no. 2, pp. 233–244, 2005.
- [24] C. Serio, G. Masiello, and G. Grieco, *EOF Expression Analytical Model with Applications to the Retrieval of Atmospheric Temperature and Gas Constituents Concentrations from High Spectral Resolution Infrared Observations*, chapter 2, Nova Science Publishers, 2013.
- [25] K. Masuda, T. Takashima, and Y. Takayama, “Emissivity of pure and sea waters for the model sea surface in the infrared window regions,” *Remote Sensing of Environment*, vol. 24, no. 2, pp. 313–329, 1988.
- [26] C. D. Rodgers, *Inverse Methods for Atmospheric Sounding: Theory and Practice*, vol. 2, World Scientific Publishing, Singapore, 2000.
- [27] G. Masiello, C. Serio, and P. Antonelli, “Inversion for atmospheric thermodynamical parameters of IASI data in the principal components space,” *Quarterly Journal of the Royal Meteorological Society*, vol. 138, no. 662, pp. 103–117, 2012.
- [28] A. N. Tikhonov and V. Y. Arsenin, *Solutions of Ill-Posed Problems*, Winston & Sons, Washington, DC, USA, 1978.
- [29] G. P. Anderson, S. A. Clough, F. X. Kneizys, J. H. Chetwynd, and E. P. Shettle, “Agl atmospheric constituent profiles (0–120 km),” Tech. Rep., Air Force Geophysics Laboratory, Hanscom AFB, Bedford, Mass, USA, 1986.
- [30] D. Barriopedro, E. M. Fischer, J. Luterbacher, R. M. Trigo, and R. García-Herrera, “The hot summer of 2010: redrawing the temperature record map of Europe,” *Science*, vol. 332, no. 6026, pp. 220–224, 2011.
- [31] B. A. Revich, “Heat-wave, air quality and mortality in european russia in summer 2010: preliminary assessment,” *Human Ecology*, no. 7, pp. 3–9, 2011.
- [32] Great Britain Meteorological Office, *Weather in the Mediterranean*, Great Britain Meteorological Office, London, UK, 2nd edition, 1962.
- [33] Y. Goldreich, *The Climate of Israel: Observation, Research and Applications*, Springer, New York, NY, USA, 2003.
- [34] A. Karnieli, Y. Derimian, R. Indoitu et al., “Temporal trend in anthropogenic sulfur aerosol transport from central and eastern Europe to Israel,” *Journal of Geophysical Research D: Atmospheres*, vol. 114, no. 15, Article ID D00D19, 2009.
- [35] G. Grieco, G. Masiello, C. Serio, R. L. Jones, and M. I. Mead, “Infrared atmospheric sounding interferometer correlation interferometry for the retrieval of atmospheric gases: the case of H₂O and CO₂,” *Applied Optics*, vol. 50, no. 22, pp. 4516–4528, 2011.
- [36] F. D’Ortenzio, D. Antoine, and S. Marullo, “Satellite-driven modeling of the upper ocean mixed layer and air-sea CO₂ flux in the Mediterranean Sea,” *Deep Sea Research Part I: Oceanographic Research Papers*, vol. 55, no. 4, pp. 405–434, 2008.

Research Article

Dominant Modes of Tropospheric Ozone Variation over East Asia from GOME Observations

Yi Liu,^{1,2} Yuli Zhang,^{1,3} Yong Wang,¹ Chuanxi Liu,^{1,2} Zhaonan Cai,¹
Paul Konopka,⁴ and Rolf Müller⁴

¹Key Laboratory of Middle Atmosphere and Global Environment Observation (LAGEO), Institute of Atmospheric Physics, Chinese Academy of Sciences, Beijing 100029, China

²Joint Center for Global Change Studies (JCGCS), Beijing 100875, China

³University of Chinese Academy of Sciences, Beijing 100049, China

⁴Institute of Energy and Climate Research: Stratosphere (IEK-7), Forschungszentrum Jülich, 52425 Jülich, Germany

Correspondence should be addressed to Zhaonan Cai; caizhaonan@mail.iap.ac.cn

Received 4 February 2015; Accepted 17 April 2015

Academic Editor: Xiaozhen Xiong

Copyright © 2015 Yi Liu et al. This is an open access article distributed under the Creative Commons Attribution License, which permits unrestricted use, distribution, and reproduction in any medium, provided the original work is properly cited.

The variation in tropospheric ozone over East Asia was analyzed using tropospheric column ozone data measured by the Global Ozone Monitoring Experiment (GOME) satellite. An empirical orthogonal function (EOF) analysis was carried out to derive the dominant modes of the variation in the tropospheric ozone volume-mixing ratio (TOVMR). The EOF1 mode, which explained 61.5% of the total variance, showed a same-sign distribution over all of East Asia, with a belt of enhanced ozone concentrations around 40°N. The principal component of EOF1 (PC1) suggested that photochemical ozone production together with Brewer-Dobson circulation and subtropical westerly jet plays important roles in modulating the seasonal variation of the TOVMR; ozone-rich air produced by photochemical processes was transported from the stratosphere to the troposphere by BD circulation and this ozone-rich air was then blocked by the subtropical westerly jet and accumulated north of the jet. The EOF2 mode explained 29.2% of the total variance with an opposite-sign pattern on the north and south side of 35°N. When anticyclonic circulation transported ozone-poor air from the upwelling area over the Bay of Bengal towards the Tibetan Plateau during the onset of the Asian summer monsoon, tropospheric ozone in this region decreased dramatically.

1. Introduction

Tropospheric ozone has been considered a greenhouse gas for some time [1]. It has strong effects on radiative forcing [2] and is an important component of the photochemical reactions that occur in the boundary layer [3]. Increasing ozone concentrations in this layer threaten human health and surface ecosystems [4]. Therefore, studies into the spatiotemporal characteristics of tropospheric ozone and its drivers are important theoretically and practically.

With the rapid development of the Asian economies in recent decades, air pollution has increased dramatically [5] and influenced atmospheric chemistry, radiation, and dynamics at regional and global scales. Some air pollutants can directly or indirectly affect ozone concentrations, by influencing the photochemical reactions that generate ozone

in the troposphere. Dramatic changes in the concentrations of ozone and its precursors have caused international concern; this has inspired research, including into the effects of increasing air pollution in Asia on ozone concentrations and climate [6], extreme tropospheric ozone events [7], the production, distribution, and evolution of tropospheric ozone [8], cross-tropopause ozone fluxes over east Asia [9, 10], long-range transport of ozone in the East Asian Pacific Rim region [11], tropospheric ozone during the Asian summertime monsoon [12], and tropospheric ozone modeling over Asia [13].

Recently, Randel et al. [14] suggested that tropospheric pollution could be transported into the stratosphere by the Asian summer monsoon and further influence the global atmosphere and climate. However, there are few ozonesonde stations in East Asia and long-term continuous ozone profile

measurements are especially limited. Because of the lack of sufficient ozonesonde measurements, most researchers who study ozone concentrations over Asia have had to rely on satellite datasets, or limited ground-based measurements.

In this study, the dominant modes of tropospheric ozone variation over Asia were investigated, using empirical orthogonal function (EOF) analysis. Tropospheric column ozone derived from satellite measurements was used to examine the mechanism (photochemistry and transport) behind this variation of the tropospheric ozone over Asia. Section 2 describes the data and methods used. Section 3 describes the seasonality of tropospheric ozone. Section 4 analyzes the dominant modes of the tropospheric ozone variation and their mechanisms. Conclusions are summarized in Section 5.

2. Data and Methods

2.1. Satellite Ozone Measurements. The Global Ozone Monitoring Experiment (GOME), on board the European Space Agency (ESA) Remote Sensing-2 (ERS-2) satellite, measured radiance backscattered from the Earth's atmosphere over a wavelength range of 240–790 nm. GOME had a moderate spectral resolution of 0.2–0.4 nm and high signal-to-noise ratios in ozone absorption bands, making it possible to retrieve the vertical distribution of ozone from the troposphere to the stratosphere [15]. The ozone profile and tropospheric column ozone (TCO) were retrieved from GOME measurements by performing extensive calibration and improvements in the Liu forward model [16–18]. Tropopause pressure reanalysis data from the National Centers for Environmental Prediction (NCEP) were used to separate the stratosphere and troposphere.

The retrieved ozone profiles agreed well with measurements from ozonesonde, Total Ozone Mapping Spectrometer (TOMS), and Stratospheric Aerosol and Gas Experiment II (SAGE-II) [16, 19]. Validation with ozonesonde from 33 stations between 75°N and 71°S during 1996–1999 showed that the retrieved TCO profiles captured most of the temporal variability in ozonesonde TCO; the mean biases were mostly within 3 DU (15%) and the 1σ standard deviations were within 3–8 DU (13–27%). We compared GOME ozone profiles to ozonesonde measurements over three stations in China, including Beijing (39.8°N, 116.47°E) from September 2002 to June 2003, Lhasa (29.7°N, 91.1°E) from June to October in 1998 and 1999, and Xining (36.63°N, 101.75°E) from April to August 1996 [20]. In the middle and lower troposphere, the bias was within $\pm 10\%$ over Beijing and $\pm 5\%$ over Lhasa and Xining; in the upper troposphere and lower stratosphere (UTLS), the GOME data had biases of $\pm 10\%$ over Beijing and positive biases of 10% over Lhasa and 5% over Xining; in the middle stratosphere, the GOME retrievals compared well to ozonesonde values over Lhasa but had a negative bias of 10% over Xining and a positive bias of up to 20% over Beijing. The mean biases of the TCO were less than 10% over these three stations.

The spatial resolution of GOME retrievals is normally $960 \times 80 \text{ km}^2$. We mapped the swath data from orbits onto a 2° latitude \times 2.5° longitude grid and derived monthly averaged

data for March 1996 to June 2003. The TCO was converted from Dobson units to the mean tropospheric ozone volume mixing ratio (TOVMR, in ppbv unit), using the method described by Ziemke et al. [21].

2.2. Definition of Westerly Jet Occurrence. The definition of westerly jet occurrence was based on the methods of Schiemann et al. [22], with the difference being that the wind data used here was in potential temperature (θ) coordinates rather than pressure coordinates. A four-dimensional index field of jet occurrence, $J(t, x, y, \theta)$, was set to either zero or one, where t , x , and y refer to time, latitude, and longitude, respectively. It was set to one when the horizontal velocity $V(t, x, y, \theta) = [u(t, x, y, \theta), v(t, x, y, \theta)]$ satisfied

$$|V|_{t,x}(y, \theta) \text{ is a local maximum,} \quad (1a)$$

$$|V| \geq 30 \text{ ms}^{-1}, \quad (1b)$$

$$u \geq 0 \text{ ms}^{-1} \quad (1c)$$

and to zero otherwise. Subscripts denote fixed dimensions; that is, J identifies the maxima of the horizontal wind speed in latitude-theta cross sections. The jet identification was carried out between 280 and 400 K, using the European Centre for Medium-Range Weather Forecasts (ECMWF) meteorological ERA-interim reanalysis [23], at time intervals of 6 hours during 1996–2003.

2.3. Definition of Monsoon Index. The Monsoon-Hadley index (MHI), which is based on the anomalous meridional wind shear, was used as a suitable monthly mean monsoon index to describe the intensity of the South Asian (Indian) summer monsoon circulation [24]:

$$\text{MHI} = V_{850}^* - V_{200}^*, \quad (2)$$

where V_{850}^* and V_{200}^* are the regional and temporal mean meridional wind anomalies, at 850 hPa and 200 hPa, respectively, over the monsoon region (10°N–30°N, 70°E–110°E) during April–August.

2.4. Empirical Orthogonal Function (EOF) Analysis. EOF analysis decomposes the space-time field into a set of orthogonal spatial patterns along with a set of associated, uncorrelated, time indices or principal components (PCs) in a linear fashion. The EOF technique aims to find a new set of variables that capture most of the observed variance from the data, through linear combinations of the original variables, or reduce the large number of variables of the original data to a few variables. It has proven to be a powerful tool for identifying dominant modes of climate variability and tracer analysis [25]. In this study, EOF analysis was applied to the monthly mean TOVMR dataset over East Asia (80°E–140°E, 10°N–50°N) from March 1996 to June 2003 to retrieve the dominant spatiotemporal modes of tropospheric ozone over East Asia.

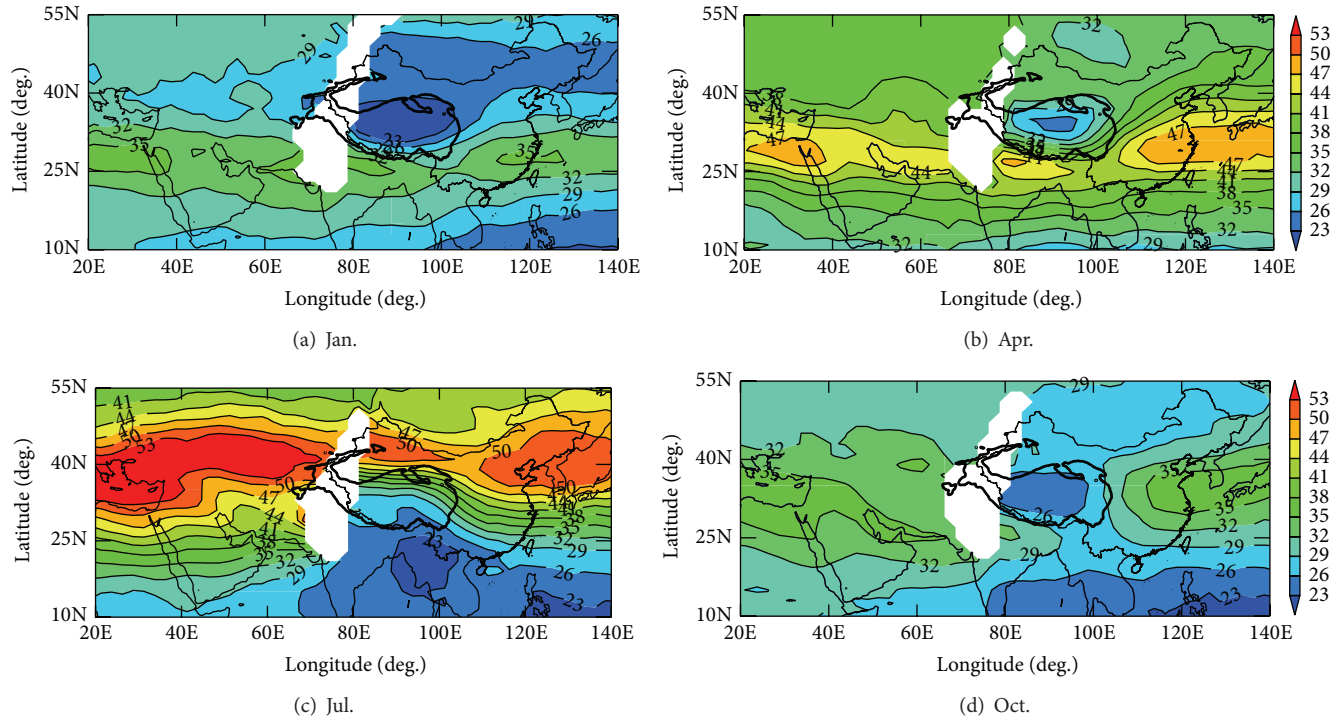


FIGURE 1: Monthly mean tropospheric column ozone (TCO) (unit: Dobson unit (DU)) from GOME (Global Ozone Monitoring Experiment) measurements between March 1996 and June 2003. GOME data are unavailable over the white area due to the lack of downlinking of GOME data to ground stations. The dark thick contours are coastline and the edge of Tibetan Plateau.

3. The Seasonality of Tropospheric Ozone

In winter (Figure 1(a)), high values of TCO (>32 DU) were present along a zonal belt around 30°N and there were low values of TCO (<26 DU) over the Tibetan Plateau and northern China. In spring (Figure 1(b)), TCO was enhanced (>47 DU) along a zonal belt around 30–35°N, due to stratosphere–troposphere exchange (STE), which predominantly occurs at this time of the year within this zonal belt [26]. In summer (Figure 1(c)), the belt of enhanced TCO (greater than 50 DU) moved northward to around 40°N. Here, TCO shows the highest values throughout the year. Some studies have attributed this large increase in ozone in summer to its photochemical production, which is enhanced by the presence of anthropogenic pollution, biogenic volatile organic compounds, and NO_x [26, 27]. In autumn (Figure 1(d)), the TCO rapidly decreased and the belt of high TCO moved back towards the lower latitudes. GOME data were not available over Northern India and west of the Himalayas due to a lack of downlinking of GOME data to ground stations; thus these areas are shown in white in Figure 1.

Note that TCO was lower over the Tibetan Plateau than over other regions in the same latitudes in East Asia during the year. This tropospheric ozone anomaly is sufficiently shown to be clearly noticeable even in total ozone column measurements [28]. The anomaly low TCO over the Tibetan Plateau mainly occurs because of both the unique topography of the area and the tropopause height, which together determine the vertical extent of the tropospheric air column. With

elevations up to almost the middle troposphere, the Tibetan Plateau (which extends over 27°N–45°N, 70°E–105°E at an average elevation of ~4 km) has a much shorter tropospheric air column over it than that in other regions at the same latitude. Further, the tropopause pressure over the Tibetan Plateau is lower, which means the tropopause is higher (Figure 2) over this region than at similar latitudes elsewhere in East Asia; this is especially true in summer (Figure 2(c)) as a result of the onset of Asian summer monsoon. Therefore, in order to reduce the influence of topography and tropopause height on tropospheric ozone, as detailed in the methods, the TCO was converted to TOVMR by using the tropopause and surface pressure data from NCEP.

The seasonality of TOVMR (Figure 3) is similar to that of TCO (Figure 1), except over the Tibetan Plateau, where TOVMR is higher than in other regions of the same latitude in East Asia. By excluding the effects of topography and tropopause height, TOVMR has certain advantages over TCO in studying the tropospheric ozone over East Asia. So, the spatiotemporal variations of tropospheric ozone over East Asia were investigated using TOVMR and are described in the following.

4. EOF Analysis of TOVMR

The two dominant spatial modes of monthly mean TOVMR from March 1996 to June 2003 over East Asia (80°E–140°E, 10°N–50°N) retrieved by EOF analysis (EOF1 and EOF2; Figures 4(a) and 4(b), resp.), along with their associated time

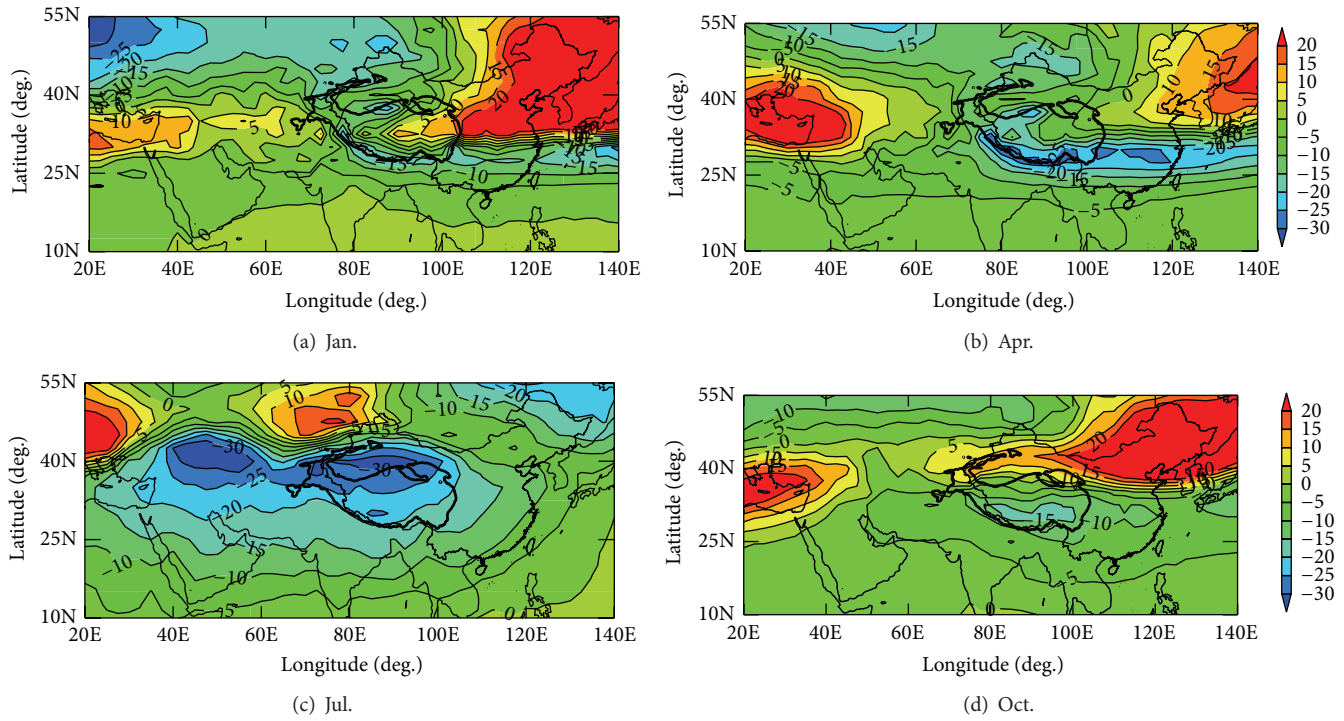


FIGURE 2: The same as Figure 1, but for zonal deviations of tropopause pressure (unit: hPa).

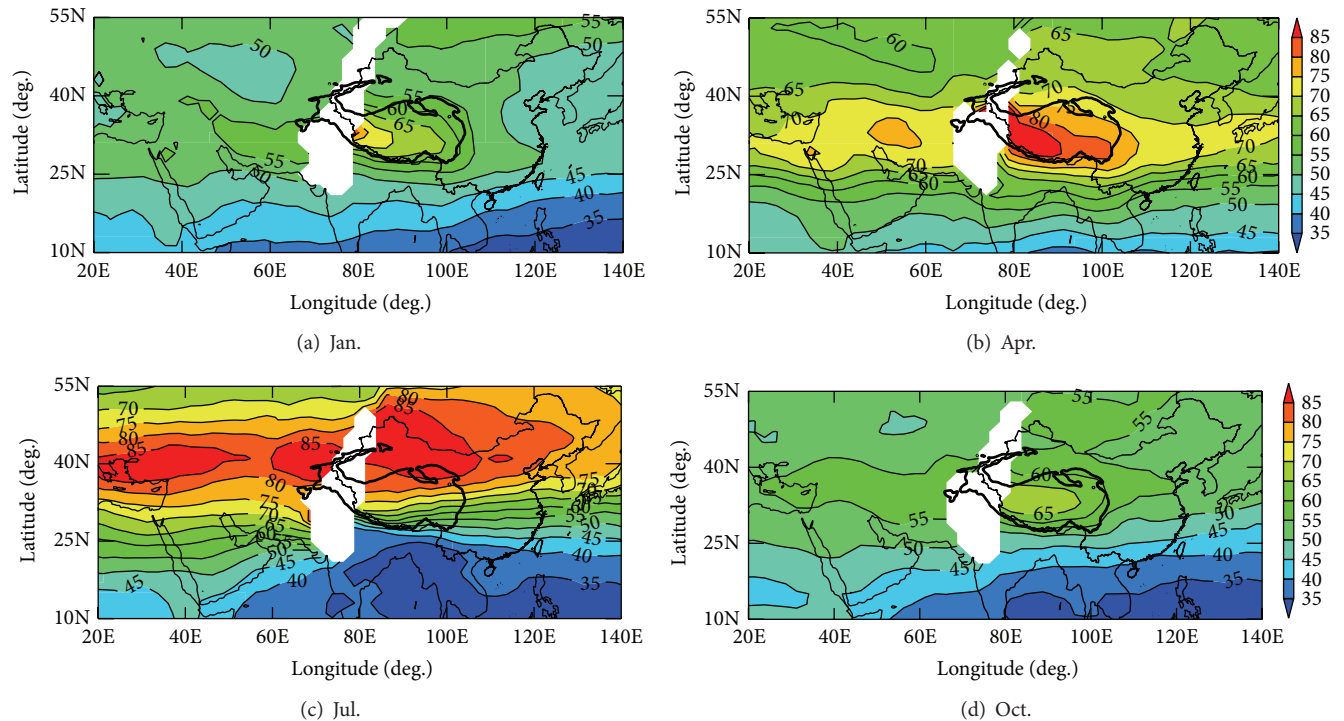


FIGURE 3: The same as Figure 1, but for tropospheric ozone volume mixing ratio (TOVMR, unit: ppbv).

series (PC1 and PC2; Figures 4(c) and 4(d), resp.), together explained ~90% of the spatiotemporal ozone variability in East Asia. This means that the major characteristics of tropospheric ozone were captured by these two modes. Both modes satisfied North's criteria [29] and have actual physical meaning.

4.1. *The First EOF Mode (EOF1).* The EOF1 (Figure 4(a)) explained 61.5% of the variance in ozone variability, with same-sign values over the entire East Asia, suggesting that the main variability in TOVMR over the entire region is very likely dominated by the same mechanism. The PC1 time series suggested that the maxima occur in May-June and the

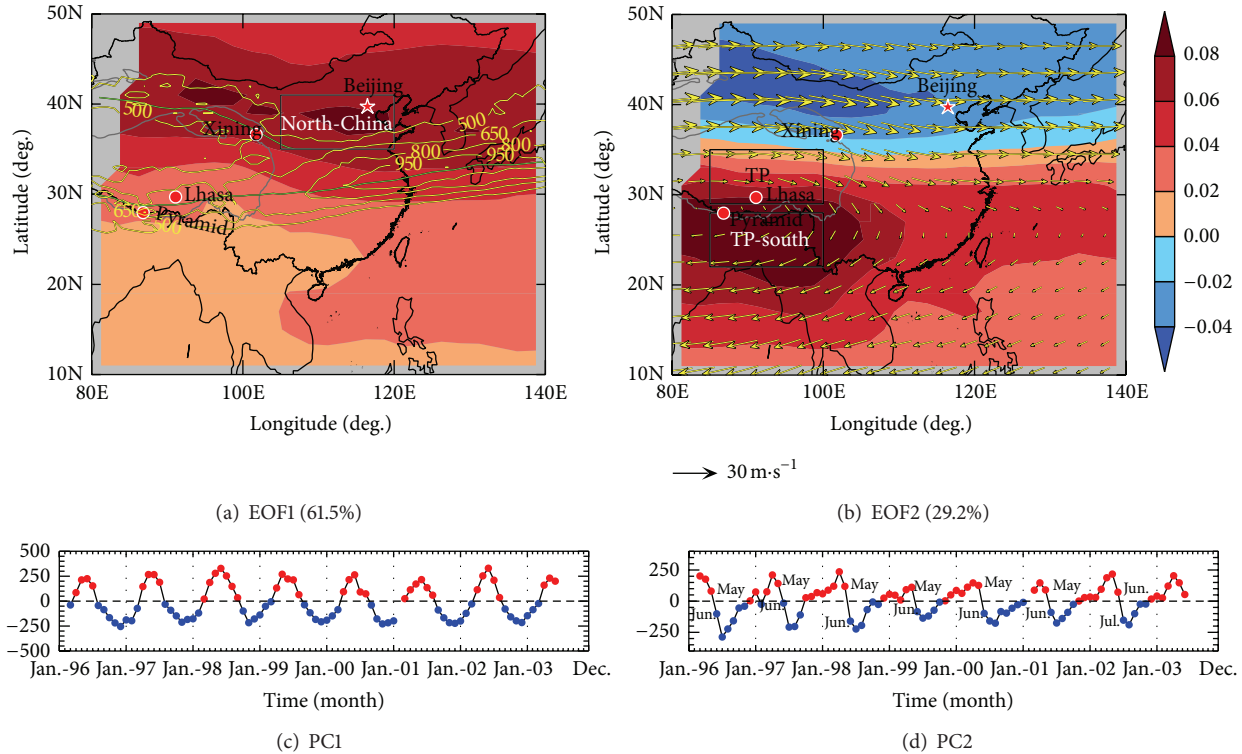


FIGURE 4: Two dominant patterns retrieved from EOF analysis ((a) EOF1, (b) EOF2) of monthly mean TOVMR (color shaded) and their corresponding time series ((c) PCI, (d) PC2; red: positives, blue: negatives) between March 1996 and June 2003. The yellow contours in (a) are total westerly jet occurrence counts based on 6-hourly ERA-interim data, and the thick green lines show the position of maximum occurrence. Summer (June–August) winds at 200 hPa for the same period are shown by vectors in (b). The red star is the location of Beijing and the red dots are locations of Lhasa, Xining, and Pyramid (Nepal); they are four ozonesonde stations. The square in (a) is the area of northern China; the square in (b) is southern Tibetan Plateau and the area to the south of Tibetan Plateau.

minima in November–December (Figure 4(c)). This indicates that the contribution of photochemical ozone production plays a significant role in modulating the seasonal variation of the averaged ozone concentration in the troposphere. However, the maxima did not occur in July–August when photochemical production was even stronger. We suspect that some dynamical processes must also be responsible for the formation of EOF1. It is noted that there was a belt of high values of EOF1 around 40°N (Figure 4(a)). The latitudinal location of the high-value belt is very close to that of the downward branch of the Brewer–Dobson circulation (BDC) in the midlatitudes, which is regarded to be a dominant avenue for stratosphere-to-troposphere ozone transport [30, 31]. Additionally, as a horizontal barrier which weakens the north-south exchange, the subtropical westerly jet further maintains the ozone-rich air, brought by the downward transport of the BDC, around 40°N. In the following sections, the correlations between the PCI time series and the seasonal variation of BDC and westerly jet are analyzed.

4.1.1. The Correlation between EOF1 and BDC Intensity. The BDC is the meridional transport circulation system, which implies upward motion of air in the tropics and downward motion in the subtropics. Dobson [32] successfully explained the meridional distribution of ozone and water vapor by using

the BDC, which is mainly driven by stratospheric planetary waves. As a representation of the planetary wave forcing, the vertical component of the Eliassen–Palm- (EP-) flux (EP-Fz) drives the BDC and further affects the meridional transport of ozone [33]. In the following text, we describe how we used the EP-Fz to study the relationship between the BDC and ozone variability in the region that had high levels of TOVMR in the EOF1 mode.

The three-dimensional EP-flux [34] was calculated based on the monthly mean ERA-interim zonal wind and temperature data. The mean EP-Fz within the region of high TOVMR values in EOF1 mode (100 hPa, 80–140°E, 35–45°N) was used to characterize the ozone transport from the stratosphere to the troposphere by the BDC. The EP-Fz was high in winter and low in summer (Figure 5(a)), suggesting that the BDC transports more ozone-rich air from lower latitudes to the higher latitudes in stratosphere in winter. However, the maximal tropospheric ozone occurred 5–7 months after the EP-Fz maximum, indicating that once stratospheric ozone has been transported from tropics to midlatitudes by the BDC, it takes several months to be transported through the tropopause and into the troposphere in the subtropics [30]. The lagged correlations between the EP-Fz and GOME tropospheric ozone (Figure 5(b)) indicate that the maximal tropospheric ozone seen in PCI occurred five months after the EP-Fz

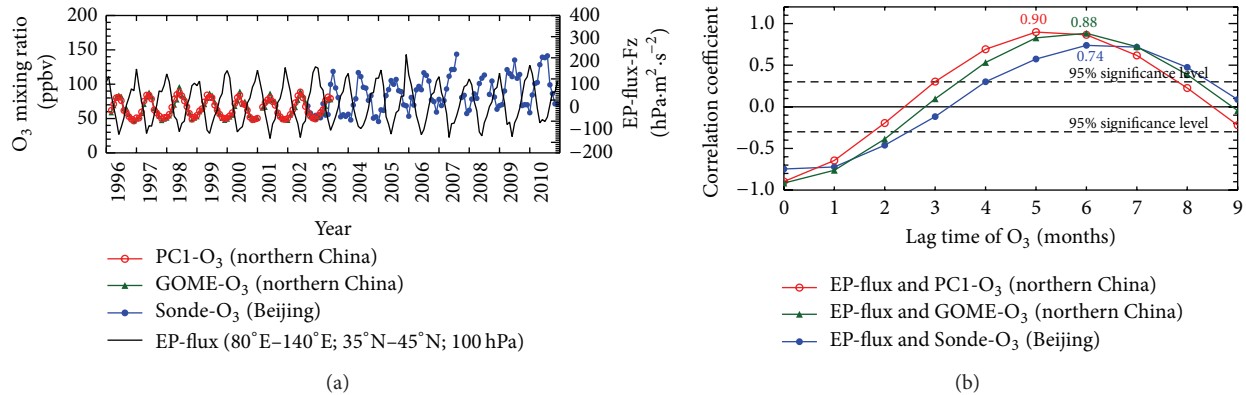


FIGURE 5: (a) Time series of the regional mean (80°E – 140°E ; 35°N – 45°N) vertical EP-flux at 100 hPa between January 1996 and December 2010, PC1 decomposed from GOME TOVMR (PCI-O₃) and GOME TOVMR (GOME-O₃) between March 1996 and June 2003 over northern China, and ozonesonde observed tropospheric ozone mixing ratio (Sonde-O₃) over Beijing from September 2002 to December 2010. (b) Lag correlation coefficients between EP-flux and the time series of ozone (red: PCI-O₃ over northern China; green: GOME ozone over northern China; blue: ozonesonde over Beijing).

maximum ($r = 0.9$), and the maximal GOME ozone (without EOF analysis) occurred six months after the EP-Fz maximum ($r = 0.88$). Based on the ozonesonde measurements over Beijing, which is located in the region of high TOVMR values in EOF1 mode, the maximal tropospheric ozone over Beijing occurred six months after the EP-Fz maximum ($r = 0.74$). The lagged correlations between the EP-Fz and tropospheric ozone (both satellite and ozonesonde) were significant at the 95% confidence level, suggesting that the BDC does play an important role in the formation of the tropospheric ozone pattern seen in EOF1.

4.1.2. The Correlation between EOF1 and the Subtropical Westerly Jet. According to previous studies [35–37], the subtropical westerly jet can block the horizontal ozone exchange between high and low latitudes. Separated by high topography, the two maxima of the subtropical westerly jet occurrence (green lines in Figure 4(a)) exist on the northern and southern edges of the Tibetan Plateau. However, the high values of TOVMR in the EOF1 pattern only existed on the northern edge of the Tibetan Plateau; here, the ozone-rich air brought by the downward transport of the BDC from the stratosphere is blocked by the subtropical westerly jet and accumulates north of the jet.

As a result of BDC transportation and blocking effort of subtropical westerly jet, the high ozone produced by photochemical peaked in May-June. Although photochemical production was even stronger in the later July-August, the weakening of BDC transportation and the strength of subtropical westerly jet led to the decrease in ozone during this period.

4.2. The Second EOF Mode (EOF2). The EOF2 mode explained 29.2% of the variance, with an opposite-sign pattern on either side of 35°N (Figure 4(b)). The high values of TOVMR seen in EOF2 were mainly located to the south of the Tibetan Plateau and in the Bay of Bengal. The positive maxima of PC2 (Figure 4(d)) occurred in spring (April-May),

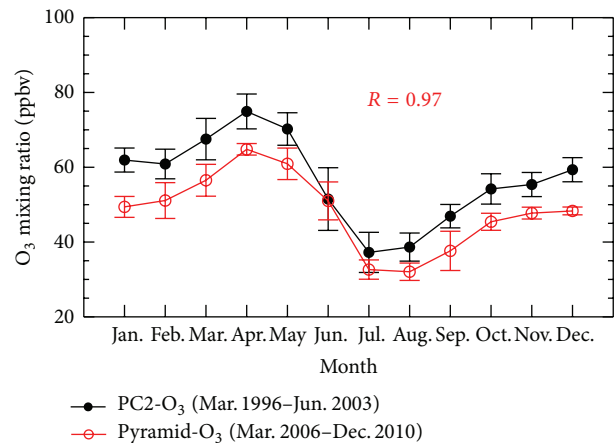


FIGURE 6: Seasonality of surface ozone at Pyramid station (Pyramid-O₃) from March 2006 to December 2010 and the regional mean (within $\pm 1^{\circ}$, centered at Pyramid station) PC2 decomposed from GOME TOVMR (PC2-O₃) between March 1996 and June 2003. Error bars are standard deviations ($\pm\sigma$).

and the negative minima occurred in summer (July-August). So, it can be concluded that tropospheric ozone, over the areas to the south of the Tibetan Plateau and in the Bay of Bengal, is higher in spring and lower in summer.

The PC2 changed rapidly from positive to negative in May-June, indicating that the tropospheric ozone over the area to the south of the Tibetan Plateau and in the Bay of Bengal decreased dramatically during this period. Since this region is located within the area of the summer monsoon anticyclone, which begins during May-June, the Asian summer monsoon could be the main reason for the observed EOF2 mode.

There were similar trends ($r = 0.97$) between the PC2 pattern and surface observations from Pyramid, Nepal (5079 m a.s.l.; located on the southern edge of the Tibetan Plateau) (Figure 6). Because PC2 describes tropospheric ozone and the Pyramid observations only recorded surface

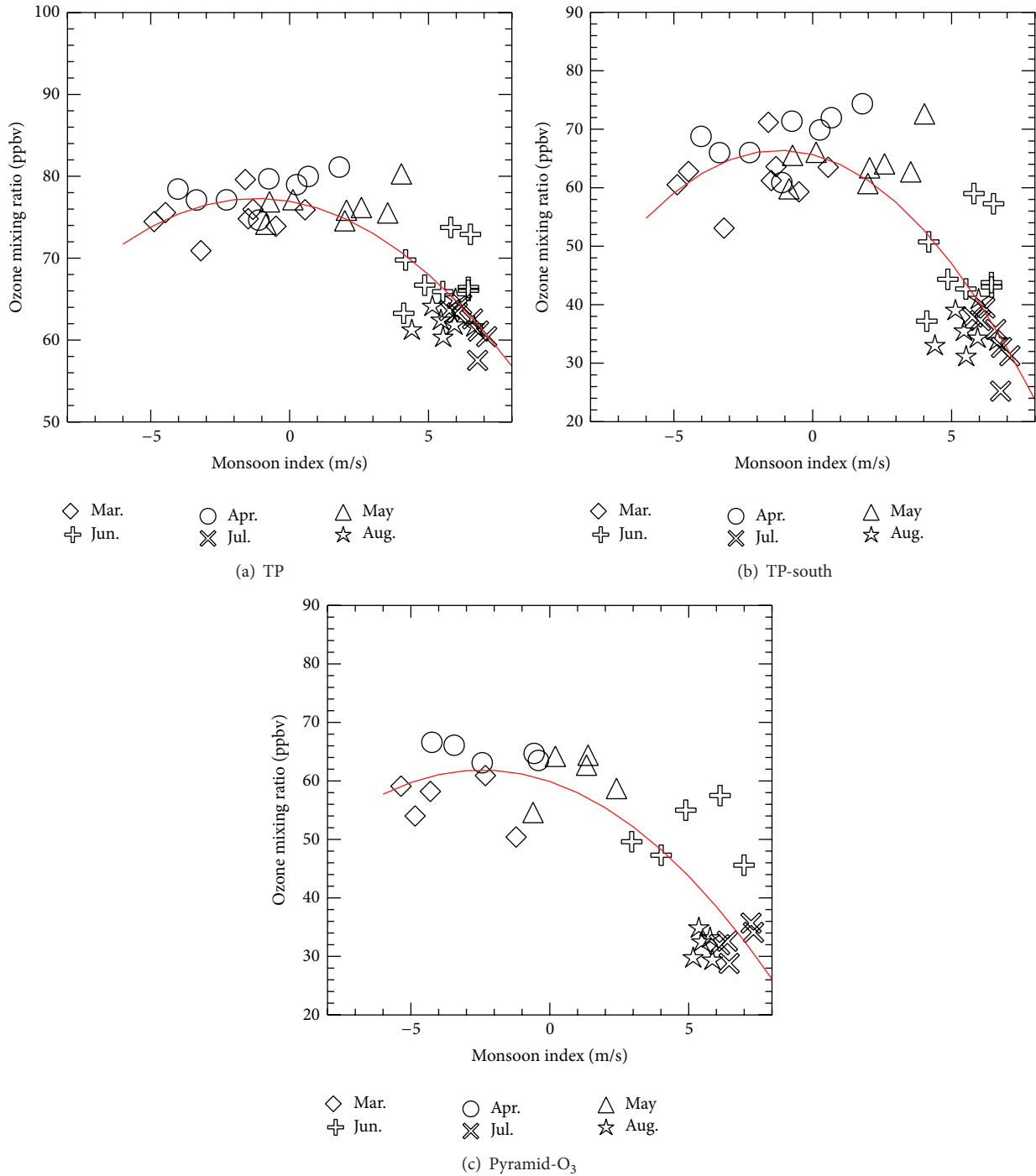


FIGURE 7: Correlation between the Indian Monsoon index and PC2-O₃ over (a) the Tibetan Plateau and (b) south of the Tibetan Plateau between March 1996 and June 2003, and (c) the correlation between the Indian Monsoon index and surface observations of ozone from Pyramid between March 2006 and December 2010.

ozone concentrations, PC2 was generally higher than the ozone observations from Pyramid, except in June, when they were almost equal. This equality can be attributed to the onset of the Asian summer monsoon, which transports air containing less ozone into the region in June; as a result, the tropospheric ozone is reduced and becomes almost equivalent to the surface ozone.

A minimum ozone concentration has been shown to occur in the middle troposphere over the Tibetan Plateau in June, simultaneous with the onset of the Asian summer monsoon [38]. It was suggested that the monsoon anticyclone causes air containing less ozone to be transported from the lower to middle and higher troposphere, by strong upward movements over the Bay of Bengal, driving the air

to the Tibetan Plateau. The tropospheric ozone over Pyramid rapidly decreased to be almost equal to surface observations during this process (Figure 6). Blocked by the westerly jet on the northern side of the Tibetan Plateau, the ozone accumulates over the southeast of the Plateau. The existence of this ozone minimum in the middle troposphere over the Tibetan Plateau is consistent with the ozone minimum over Pyramid, resulting from the onset of the Asian summer monsoon.

The PC2 over the Tibetan Plateau and to the south of the Tibetan Plateau and the surface ozone observations from Pyramid appear closely related to the South Asian summer monsoon (Figures 7(a)–7(c), resp.). However, the relationships between the monsoon and ozone at each location were not simply linear. During March–May, the enhanced photochemistry and ozone exchange between the stratosphere and troposphere over the Tibetan Plateau increased the tropospheric ozone. With the onset of the Asian summer monsoon, during the months May–June, the tropospheric ozone levels over the Tibetan Plateau and to the south of the Tibetan Plateau dramatically decreased, as explained above. Further, the increase in precipitation, due to enhanced convection during the summer monsoon, also played a role in the decrease in ozone.

5. Conclusions

The spatiotemporal characteristics of tropospheric ozone over East Asia were analyzed using tropospheric ozone data from the GOME satellite and meteorological datasets from the ERA-interim reanalysis dataset. Generally, the TCO was the lowest in winter and the highest in summer, with a TCO minimum present over the Tibetan Plateau. There was a belt of high TCO, which occurred at 30°N in winter and moved northward to 40°N in summer. To reduce the influence of topography and the tropopause height on TCO, we calculated the average ozone concentration in the troposphere (TOVMR). The seasonality of TOVMR was similar to that of TCO, except that the TOVMR over the Tibetan Plateau was the highest in East Asia throughout the year.

EOF analysis was applied to characterize the spatiotemporal variations in TOVMR. The two dominant spatial patterns (EOF1 and EOF2) explained ~90% of the total variance in TOVMR. The EOF1 mode, which explained 61.5% of the total variance, showed a same-sign distribution over all of East Asia, with a belt of enhanced ozone concentrations around 40°N. The PC1 time series showed that the averaged ozone concentration in the troposphere was higher in summer and lower in winter, indicating the contribution of photochemical ozone production. Further analysis suggested that the high-value belt of ozone concentrations around 40°N was highly related to the vertical transport of ozone-rich air from the stratosphere to the troposphere by the downward branch of the BDC. This ozone-rich air is then blocked by the subtropical westerly jet and accumulates to the north of the jet.

The EOF2 mode explained 29.2% of the total variance, with an opposite-sign pattern on the northern and southern

sides of 35°N. The high values of TOVMR in EOF2 were located to the south of the Tibetan Plateau and in the Bay of Bengal. Tropospheric ozone over this region decreased dramatically in May–June, when the anticyclonic circulation transports ozone-poor air from the upwelling area over the Bay of Bengal towards the Tibetan Plateau during the onset of the Asian summer monsoon. The high correlations between the Monsoon-Hadley index (MHI) and ozone over three locations in this region confirmed the dominant contribution of the Asian summer monsoon to the EOF2 mode.

To quantify the relative contributions of photochemistry and transport to the tropospheric ozone budget and its seasonal variation shown in EOF1, a numerical study based on the chemistry transport models should be performed in the future.

Conflict of Interests

The authors declare that there is no conflict of interests regarding the publication of this paper.

Acknowledgments

This work was funded by the National Science Foundation of China (Grant nos. 41305127 and 41105025) and the Dragon 3 Programme (ID: 10577). The authors thank Dr. Xiong Liu for providing the GOME data. The European Centre for Medium-Range Weather Forecasts (ECMWF) is acknowledged for meteorological data support.

References

- [1] J. Fishman, S. Solomon, and P. J. Crutzen, “Observational and theoretical evidence in support of a significant in-situ photochemical source of tropospheric ozone,” *Tellus*, vol. 31, no. 5, pp. 432–446, 1979.
- [2] T. K. Berntsen, G. Myhre, F. Stordal, and I. S. A. Isaksen, “Time evolution of tropospheric ozone and its radiative forcing,” *Journal of Geophysical Research D: Atmospheres*, vol. 105, no. 7, pp. 8915–8930, 2000.
- [3] H. Levy II, “Normal atmosphere: large radical and formaldehyde concentrations predicted,” *Science*, vol. 173, no. 3992, pp. 141–143, 1971.
- [4] V. P. Aneja and Z. Li, “Characterization of ozone at high elevation in the eastern United States: trends, seasonal variations, and exposure,” *Journal of Geophysical Research*, vol. 97, no. 9, pp. 9873–9888, 1992.
- [5] X. Tie, G. P. Brasseur, C. Zhao et al., “Chemical characterization of air pollution in Eastern China and the Eastern United States,” *Atmospheric Environment*, vol. 40, no. 14, pp. 2607–2625, 2006.
- [6] T. Berntsen, I. S. A. Isaksen, W.-C. Wang, and X.-Z. Liang, “Impacts of increased anthropogenic emissions in Asia on tropospheric ozone and climate: a global 3-D model study,” *Tellus, Series B: Chemical and Physical Meteorology*, vol. 48, no. 1, pp. 13–32, 1996.
- [7] J. H. Kim and H. Lee, “What causes the springtime tropospheric ozone maximum over Northeast Asia?” *Advances in Atmospheric Sciences*, vol. 27, no. 3, pp. 543–551, 2010.
- [8] K. Yamaji, T. Ohara, I. Uno, H. Tanimoto, J.-I. Kurokawa, and H. Akimoto, “Analysis of the seasonal variation of ozone in

- the boundary layer in East Asia using the Community Multi-scale Air Quality model: what controls surface ozone levels over Japan?" *Atmospheric Environment*, vol. 40, no. 10, pp. 1856–1868, 2006.
- [9] M. L. Buker, M. H. Hitchman, G. J. Tripoli, R. B. Pierce, E. V. Browell, and M. A. Avery, "Resolution dependence of cross-tropopause ozone transport over east Asia," *Journal of Geophysical Research: Atmospheres*, vol. 110, no. 3, Article ID D03107, 2005.
- [10] Y. Wang, P. Konopka, Y. Liu et al., "Tropospheric ozone trend over Beijing from 2002–2010: ozonesonde measurements and modeling analysis," *Atmospheric Chemistry and Physics*, vol. 12, no. 18, pp. 8389–8399, 2012.
- [11] H. Liu, D. J. Jacob, L. Y. Chan et al., "Sources of tropospheric ozone along the Asian Pacific Rim: an analysis of ozonesonde observations," *Journal of Geophysical Research: Atmospheres*, vol. 107, no. 21, article 4573, 2002.
- [12] J. Worden, D. B. A. Jones, J. Liu et al., "Observed vertical distribution of tropospheric ozone during the Asian summertime monsoon," *Journal of Geophysical Research D: Atmospheres*, vol. 114, no. 13, Article ID D13304, 2009.
- [13] K. Yamaji, T. Ohara, I. Uno, J. I. Kurokawa, P. Pochanart, and H. Akimoto, "Future prediction of surface ozone over east Asia using Models-3 Community Multiscale Air Quality Modeling System and Regional Emission Inventory in Asia," *Journal of Geophysical Research D: Atmospheres*, vol. 113, no. 8, Article ID D08306, 2008.
- [14] W. J. Randel, M. Park, L. Emmons et al., "Asian monsoon transport of pollution to the stratosphere," *Science*, vol. 328, no. 5978, pp. 611–613, 2010.
- [15] K. V. Chance, J. P. Burrows, D. Perner, and W. Schneider, "Satellite measurements of atmospheric ozone profiles, including tropospheric ozone, from ultraviolet/visible measurements in the nadir geometry: a potential method to retrieve tropospheric ozone," *Journal of Quantitative Spectroscopy and Radiative Transfer*, vol. 57, no. 4, pp. 467–476, 1997.
- [16] X. Liu, K. Chance, C. E. Sioris et al., "Ozone profile and tropospheric ozone retrievals from the Global Ozone Monitoring Experiment: algorithm description and validation," *Journal of Geophysical Research: Atmospheres*, vol. 110, no. 20, Article ID D20307, 2005.
- [17] X. Liu, K. Chance, C. E. Sioris et al., "First directly retrieved global distribution of tropospheric column ozone from GOME: comparison with the GEOS-CHEM model," *Journal of Geophysical Research: Atmospheres*, vol. 111, no. D2, 2006.
- [18] X. Liu, K. Chance, and T. P. Kurosu, "Improved ozone profile retrievals from GOME data with degradation correction in reflectance," *Atmospheric Chemistry and Physics*, vol. 7, no. 6, pp. 1575–1583, 2007.
- [19] X. Liu, K. Chance, C. E. Sioris, T. P. Kurosu, and M. J. Newchurch, "Intercomparison of GOME, ozonesonde, and SAGE II measurements of ozone: demonstration of the need to homogenize available ozonesonde data sets," *Journal of Geophysical Research D: Atmospheres*, vol. 111, no. 14, Article ID D14305, 2006.
- [20] Z. Cai, Y. Wang, X. Liu, X. Zheng, K. Chance, and Y. Liu, "Validation of GOME ozone profiles and tropospheric column ozone with ozonesonde over China," *Journal of Applied Meteorological Science*, vol. 20, pp. 337–345, 2009 (Chinese).
- [21] J. R. Ziemke, S. Chandra, and P. K. Bhartia, "Cloud slicing": a new technique to derive upper tropospheric ozone from satellite measurements," *Journal of Geophysical Research: Atmospheres*, vol. 106, no. 9, pp. 9853–9867, 2001.
- [22] R. Schiemann, D. Lüthi, and C. Schär, "Seasonality and inter-annual variability of the westerley jet in the Tibetan Plateau region," *Journal of Climate*, vol. 22, no. 11, pp. 2940–2957, 2009.
- [23] D. P. Dee, S. M. Uppala, A. J. Simmons et al., "The ERA-Interim reanalysis: Configuration and performance of the data assimilation system," *Quarterly Journal of the Royal Meteorological Society*, vol. 137, no. 656, pp. 553–597, 2011.
- [24] B. N. Goswami, V. Krishnamurthy, and H. Annamalai, "A broad-scale circulation index for the interannual variability of the Indian summer monsoon," *Quarterly Journal of the Royal Meteorological Society*, vol. 125, no. 554, pp. 611–633, 1999.
- [25] A. Hannachi, I. T. Jolliffe, and D. B. Stephenson, "Empirical orthogonal functions and related techniques in atmospheric science: a review," *International Journal of Climatology*, vol. 27, no. 9, pp. 1119–1152, 2007.
- [26] J. R. Ziemke, S. Chandra, B. N. Duncan et al., "Tropospheric ozone determined from Aura OMI and MLS: evaluation of measurements and comparison with the Global Modeling Initiative's Chemical Transport Model," *Journal of Geophysical Research D: Atmospheres*, vol. 111, no. 19, Article ID D19303, 2006.
- [27] J. Fishman, A. E. Wozniak, and J. K. Creilson, "Global distribution of tropospheric ozone from satellite measurements using the empirically corrected tropospheric ozone residual technique: identification of the regional aspects of air pollution," *Atmospheric Chemistry and Physics*, vol. 3, no. 4, pp. 893–907, 2003.
- [28] P. Kiss, R. Müller, and I. M. Jánosi, "Long-range correlations of extrapolar total ozone are determined by the global atmospheric circulation," *Nonlinear Processes in Geophysics*, vol. 14, no. 4, pp. 435–442, 2007.
- [29] G. R. North, T. L. Bell, R. F. Cahalan, and F. J. Moeng, "Sampling errors in the estimation of empirical orthogonal functions," *Monthly Weather Review*, vol. 110, no. 7, pp. 699–706, 1982.
- [30] J. R. Holton, P. H. Haynes, M. E. McIntyre, A. R. Douglass, R. B. Rood, and L. Pfister, "Stratosphere-troposphere exchange," *Reviews of Geophysics*, vol. 33, no. 4, pp. 403–439, 1995.
- [31] Y. Liu, C. X. Liu, H. P. Wang et al., "Atmospheric tracers during the 2003–2004 stratospheric warming event and impact of ozone intrusions in the troposphere," *Atmospheric Chemistry and Physics*, vol. 9, no. 6, pp. 2157–2170, 2009.
- [32] G. M. B. Dobson, "Origin and distribution of the polyatomic molecules in the atmosphere," *Proceedings of the Royal Society of London A: Mathematical, Physical and Engineering Sciences*, vol. 236, no. 1205, pp. 187–193, 1956.
- [33] W. J. Randel, F. Wu, and R. Stolarski, "Changes in column ozone correlated with the stratospheric EP flux," *Journal of the Meteorological Society of Japan*, vol. 80, no. 4 B, pp. 849–862, 2002.
- [34] R. A. Plumb, "On the three-dimensional propagation of stationary waves," *Journal of the Atmospheric Sciences*, vol. 42, no. 3, pp. 217–229, 1985.
- [35] C. Liu, Y. Liu, Z. Cai, S. Gao, D. Lu, and E. Kyrölä, "A Madden-Julian oscillation-triggered record ozone minimum over the Tibetan plateau in December 2003 and its association with stratospheric 'low-ozone pockets,'" *Geophysical Research Letters*, vol. 36, no. 15, Article ID L15830, 2009.

- [36] C. Liu, Y. Liu, Z. Cai et al., “Dynamic formation of extreme ozone minimum events over the Tibetan Plateau during northern winters 1987–2001,” *Journal of Geophysical Research D: Atmospheres*, vol. 115, no. 18, Article ID D18311, 2010.
- [37] J. Bian, “Features of ozone mini-hole events over the Tibetan Plateau,” *Advances in Atmospheric Sciences*, vol. 26, no. 2, pp. 305–311, 2009.
- [38] Y. Liu, Y. Wang, X. Liu, Z. Cai, and K. Chance, “Tibetan middle tropospheric ozone minimum in June discovered from GOME observations,” *Geophysical Research Letters*, vol. 36, Article ID L05814, 2009.